

Magmatism and Glacial Cycles: Coupled Oscillations?

Jonathan M.A. Burley

Thesis submitted to the University of Oxford
for the degree of Doctor of Philosophy



Department of Earth Sciences

and

University of Oxford

Trinity 2017

Supervised by Prof. Richard F. Katz

Abstract

The Earth's climate system is driven by varying insolation from the Sun. The dominant variations in insolation are at 23 and 40 thousand year periods, yet for the past million years the Earth's climate has glacial cycles at approximately 100 kyr periodicity.

These cycles are a coupled variation in temperature, ice volume, and atmospheric CO₂. Somehow, the Earth system's collective response to 23 and 40 kyr insolation forcing produces 100 kyr cycles.

Generally it has been assumed that the causative mechanisms are a combination of ice dynamics (high ice reflectivity controlling temperature) and ocean circulation (changing carbon partitioning between the deep ocean and the atmosphere, and heat transport to the poles).

However, these proposed mechanisms have not yet resulted in a compelling theory for all three variations, particularly CO₂.

This thesis explores the role of volcanic CO₂ emissions in glacial cycles. I calculate that glacial-driven sea level change alters the pressure on mid-ocean ridges (MORs), changing their CO₂ emissions by approximately 10%. This occurs because pressure affects the thermodynamics of melt generation.

The delay between sea level change and the consequent change in MOR CO₂ emissions is several tens-of-thousands-of-years, conceptually consistent with a coupled non-linear oscillation that could disrupt glacial cycles from a 40 kyr mode to a multiple of that period.

I develop an Earth system model to investigate this possibility, running for approximately one million years and explicitly calculating global temperatures, ice sheet configuration, and CO₂ concentration in the atmosphere. The model is driven by insolation, with all other components varying in response (and according to their own interactions).

This model calculates that volcanism is capable of causing a transition to ~100 kyr glacial cycles, however the required average volcanic CO₂ emissions are barely within the 95% confidence interval. Therefore it is possible for volcanic systems and glacial cycles to form a 100 kyr coupled oscillation, but not probable.

Acknowledgements

Firstly, the legally-mandated boilerplate: The research leading to these results has received funding from the European Research Council under the European Union's Seventh Framework Programme (FP7/2007-2013) / ERC grant agreement number 279925. The University of Oxford Advanced Research Computing (ARC) facility was used in this work (doi:10.5281/zenodo.22558).

More personally, I would like to thank Richard Katz for his guidance over the past few years, which would take an unreasonable amount of space to detail here, and for never leaving me in any doubt that his door was open if there was interesting science to discuss. All members of my lab group have provided help that changed my thesis in some form: Tobias Keller, Teresa Kyrke-Smith, David Rees-Jones, Sander Rhebergen, Andrew Turner, and Meng Tian.

Discussions with Peter Huybers (and extensive inspiration from his publications) greatly improved the quality of my climate work. James Moore applied his terrifying competence in Mathematica to help me attack some modelling problems, and we planned a very exciting project that sadly could not fit within the time constraints of this thesis.

A series of academics have given kindly of their time over the years, and their comments and aid have removed obstacles from my research whether they know it or not. Many of these may not remember talking to me, but I remember them: C. Ballentine, D. Battisti, W. Broecker, A. Donohoe, A. Ekman, I. Hewitt, M. Hirschmann, P. Kelemen, K. Krüger, C. Langmuir, J. Maclennan, K. Nisancioglu, C. Proistosescu, D.Pyle, R. Rickaby, A. Ridgewell, I. Riipinen, C. Rowan, B. Rose, N. Trefethen, A. Wells and R. Zeebe.

For maintaining a semblance of normality over the final period of my thesis I would like to thank my reliable Tuesday quiz group: Aidan, Drew, Moizza, and Phil. Catherine Laporte-Oshiro's love and support have been invaluable rather longer than that, and her efforts in the final month of my writeup have been above and beyond what could be expected.

Finally, Carol Burley is responsible for making this possible in a thousand little ways over the decades.

Contents

Abstract	iii
Acknowledgements	v
Contents	vii
Contents	viii
1 Theoretical Foundations	1
1.1 Overview and Extended Abstract	1
1.2 Glacial Cycles	4
1.2.1 Ice Sheet Physics	6
1.2.2 Orbital Parameters and Forcing	7
1.2.3 History of Glacial Theories	16
1.3 Mantle Dynamics	21
1.3.1 CO ₂ in the Mantle	28
1.3.2 Mid-Ocean Ridges	28
1.3.3 Arc Volcanism	31
1.4 Summary	33
2 MOR CO₂ Emissions Modulated by Glacial Cycles	35
2.1 Introduction	36
2.2 The Model	40
2.3 Results	46
2.3.1 Constant Sea Level & Baseline Emissions	47
2.3.2 Single Sudden Change in Sea Level	50
2.3.3 Oscillating Sea Level	55
2.3.4 Reconstructed Pleistocene Sea Level	58
2.3.5 Global Mid-Ocean Ridges	59
2.4 Discussion	64
2.5 Summary	68
2.6 Subsequent Literature	69
Appendices	75
2.A Supporting Materials	75
2.A.1 MOR CO ₂ Emissions Response to Changing Melting Rate	75
2.A.2 Depth of First Silicate Melting: z_m	77
2.A.3 Upper Boundary of the Melting Region: z_l	78
2.A.4 Width of the Melting Region: x_w	80
2.A.5 Degree of Melting: F	81
2.A.6 Corner Flow Solution	85

3	The C-VICE Model	89
3.1	Introduction	89
3.2	The Model System	96
3.2.1	Energy Balance Model	98
3.2.2	Ice Sheet Model	104
3.2.3	Carbon Model	107
3.2.4	Coupling and Initialising the Model	114
3.3	Results: Basic Model Behaviour	116
3.3.1	Mid-Ocean Ridge CO ₂ Response to Sinusoidal Sea Level	116
3.3.2	Dynamics of Coupled EBM & Ice Sheet	119
3.3.3	Forcing with Historical CO ₂ Values	120
3.3.4	Forcing with Individual Historical Values	121
3.4	Results: Volcanic Interactions	123
3.4.1	Varying Mid-Ocean Ridge Lag	123
3.4.2	Full Model Behaviour	126
3.5	Discussion	129
3.6	Summary	134
	Appendices	137
3.A	Supporting Materials	137
3.A.1	EBM Modifications	137
3.A.2	Calculating Radiative CO ₂ Forcing	140
3.A.3	Calculating Other Radiative Forcing	142
3.A.4	Model Timestep and Resolution	144
3.A.5	Varying Bed Relaxation Timescale: τ_b	145
3.A.6	Linear Kinetics	147
3.A.7	Convolution: Analytical Solution for Sinusoidal Sea Level	149
3.A.8	Controls on Ice Sheet Mass Balance	151
3.A.9	Tuning C Feedback Strength	153
3.A.10	Model Response to Noise	156
4	Final Conclusions	159
4.1	Summary	159
4.1.1	Model Results and Predictions	160
4.1.2	Reflections on Modelling Complex Systems	163
4.1.3	Concluding Remarks	164
	Bibliography	167

Chapter 1

Theoretical Foundations

This thesis began with the question “*could glacial cycles and volcanism form a feedback loop?*”. The logic behind that question — how glacial cycles could influence volcanism, how volcanism could influence glacial cycles, and why might we think this occurs — is explained in subsequent sections of this chapter. I begin with a top-level overview.

The purpose of this overview is to sketch out the history of this thesis’ question from the perspective of those involved in the work, and provide awareness of the key papers and thoughts that guided the process. However in the interests of brevity, it does not justify all assumptions made nor clarify all terms used; subsequent sections of this chapter provide the detailed background information.

1.1 Overview and Extended Abstract

Glacial cycles are temperature oscillations in the Earth’s surface system, and thus understanding them means understanding controls on the energy balance of the Earth. The three main variables that can change the Earth’s energy balance are 1) ice extent; 2) insolation, the distribution of solar energy on the Earth’s surface; and 3) the physical composition of the atmosphere, particularly CO₂ and H₂O concentrations. Of these three variables, only insolation is an external driver of the Earth’s climate system; ice sheets and atmospheric composition evolve over time in response to global conditions.

However, the evolution of atmospheric composition is not fully understood. Atmospheric CO₂ concentration varies by about 100 ppmv on a 100 kyr timescale for the past

million years, requiring nearly 800 Gt of CO₂ be cycled in and out of the atmosphere. Neither the 100 kyr timescale nor the total CO₂ mass are readily explained; we will first consider the mass problem. Potentially this CO₂ could come from several CO₂ reservoirs connected to the atmosphere — there are 147,000 GtCO₂ in oceans and ocean sediments, and 9,200 GtCO₂ in the biosphere and soils [Stocker, 2013] — but models and data do not support 800 GtCO₂ transfers from these reservoirs.

Another reservoir of CO₂ is the ‘solid Earth’, the carbon-bearing rocks and mantle, containing the equivalent of $\sim 200,000,000$ GtCO₂ [Dasgupta and Hirschmann, 2010]. This reservoir vents to the atmosphere through volcanic activity, and removes from the atmosphere through chemical weathering of (some) CO₂-reactive rocks. If these processes vary on a glacial-cycle-timescale, then perhaps the solid Earth influences glacial cycles. Chemical weathering of rock is temperature dependent, with higher temperatures leading to faster reactions and faster removal of CO₂ from the atmosphere [Velbel, 1993]. Chemical weathering thus acts as a negative feedback, however the changes in CO₂ removal rate are so small that they take around one million years to significantly alter atmospheric CO₂ concentrations [Le Hir et al., 2009], making this unimportant on 100 ka glacial timescales. Global volcanism was thought to be a stable emitter of CO₂ (although individual large eruptions give stochastic noise on centennial timescales), such that a particular continental configuration had a predictable volcanic CO₂ output until plate tectonics created new volcanic margins — an effect on the 10’s-of-Myr timescale, far longer than glacial timescales. However, it has recently been shown that assumptions about volcanic emissions stability were incorrect.

Huybers and Langmuir [2009] suggested that subaerial volcanic CO₂ emissions varied globally in response to glacial cycles, based on amalgamated global records of subaerial volcanic eruption frequency (back to the last glacial maximum). The data shows at least a 50% increase in eruption frequency during a deglaciation. This was not the first time glacial volcanic variability had been proposed, MacLennan et al. [2002] showed magma eruption volumes (per unit time) in Iceland increased by over a factor of 30 in the first thousand years following deglaciation. The increase in eruption volume and frequency is reasonable physical behaviour; the loss of ice sheets during a deglaciation reduces pressure

on volcanoes, promoting eruptions by 1) reducing confining pressure on magma chamber structures (promotes fracture and dyking), and 2) increasing mantle melting. However, [Huybers and Langmuir \[2009\]](#)'s novel suggestions were the globally significant increase in volcanism, and that this might in turn alter volcanic CO₂ emissions. Increased subaerial volcanic CO₂ emissions during deglaciation can help close the glacial cycles' 800 GtCO₂ budget, but this was not the only plausible source of volcanic CO₂ variability.

Mid-ocean ridge volcanoes experience variable pressure during a glacial cycle as ocean level rises and falls by 100 m; perhaps this pressure change also causes mid-ocean ridge volcanoes to alter their eruptive behaviour in a similar manner to subaerial volcanoes? [Huybers and Langmuir \[2009\]](#) assumed that this process would occur for MORs on the same timescale as for subaerial volcanism, changing CO₂ emissions for a few thousand years following deglaciation (a rapid sea level rise). This assumption was not obviously correct to those more familiar mid-ocean ridge mantle dynamics; in fact it seemed improbable. A typical mid-ocean ridge has a melting region extending 100 km beneath it and about 200 km wide, overlaid by a thin crust (7 km deep) and an ocean 1000's of kilometres wide. When sea level changes, the thin crust has effectively zero elastic resistance. Therefore changing sea level will change pressure throughout the full depth and width of the melting region. Glacial sea-level-change changes the melting rate by about 10%. It is thought that mantle melt takes 30–100 kyrs to flow from the base of the melting region to the surface, therefore (at first estimate) any CO₂ effects from sea-level-induced mantle melting should be spread over 10's-of-kyrs. (Chapter 2 of this thesis details my work in transforming this sketched idea into a quantified prediction of mid-ocean ridge CO₂ emissions).

If this longer timescale effect is true, then MOR CO₂ emissions can help address the second oddity in the CO₂ record, why CO₂ varies on a 100 kyr timescale.

The timescale problem of CO₂ is thus: given that solar insolation is the only external driver of the climate system, we should expect climate to follow variations in insolation. It does not. The dominant variation in insolation is a 40 kyr cycle, but CO₂ varies in 100 kyr cycles. The only reason for climate not to follow insolation is if the Earth system has an internal oscillation (or, similarly, inertia) acting on a $\gtrsim 40$ kyr timescale and dominating

insolation's effect. However, it is difficult to imagine how the oceans, atmosphere, or ice sheets could achieve this and induce a 100 ka CO₂ cycle. Mid-ocean ridges, with their slow response time overlapping with the 40 kyr insolation period, are arguably capable of doing so.

Overall, reflecting on the initial three queries — how could glacial cycles influence volcanism, how could volcanism influence glacial cycles, and why might we think this occurs — we see evidence for glacial cycles influencing subaerial volcanism, and plausible reasons for this to affect their CO₂ emissions rate. Physical arguments suggest that MORs should also be affected. If volcanic emissions of CO₂, a long-lifetime greenhouse gas, are changing then volcanism could affect glacial cycles. Depending on the timescale and magnitude of these bi-directional effects, there could be a feedback loop where volcanism and glacial cycles significantly alter each other's behaviour.

In the following sections I discuss the necessary information for understanding and modelling these processes. Section 1.2 covers glacial cycles, the mechanisms of their major influences, and their history. Section 1.3 covers the mantle dynamics supplying melt and CO₂ to volcanoes, and how we expect these processes to vary in response to glacial cycles. Finally, section 1.4 summarises the key messages of this chapter.

1.2 Glacial Cycles

Glacial periods are defined by large ice sheets spreading across the Earth's continents. When glacial periods regularly alternate with ice-free interglacial periods, the sequence is called a glacial cycle. In this section I describe the physics behind glaciation, the key features of the Quaternary glacial cycles, and the rough scientific history behind glaciation. This will explain why the causal mechanism of the observed ~100 kyr glacial cycles of the last million years has not yet been discovered.

The geological record shows alternating glacial and interglacial periods over the last 2.5 Myrs, a period called the Quaternary glacial. Our certainty in the geological record is based on two major components: the deep sea sediment stack [Imbrie et al., 1984, Lisiecki and Raymo, 2005] and the Antarctic ice core record [Bereiter et al., 2015].

The deep sea stack is a record of foraminiferal $\delta^{18}\text{O}$ values — the isotopic oxygen

ratio of carbonate-shelled microorganisms. Foraminifera's $\delta^{18}\text{O}$ ratio is a function of local temperature and of the $\delta^{18}\text{O}$ of the surrounding ocean water. In turn, ocean water $\delta^{18}\text{O}$ is a function of global ice volume. Thus foraminiferal $\delta^{18}\text{O}$ is a record of both temperature and ice sheet volume. The deep sea stack uses deepwater forams and consequently is a record of ocean deepwater temperature and global ice volume over the past 5.3 Myrs [Lisiecki and Raymo \[2005\]](#). The ice cores record a wider suite of parameters over the past 800 kyrs [[Bereiter et al., 2015](#)], the most important of which are atmospheric CO_2 concentration and Antarctic air temperature.

The deep sea stack's $\delta^{18}\text{O}$ record begins at 5.3 Ma with 40 kyr oscillations. These oscillations are interpreted as changes in global temperature, however the cold extremes did not cause ice sheets to form. The amplitude of $\delta^{18}\text{O}$ oscillations increases at ~ 2.5 Ma, representing both a larger temperature variation and an ice volume signal, thus marking the start of the Quaternary glacial period. From 2.5–1 Ma the $\delta^{18}\text{O}$ record remains at a 40 kyr period, however at 1 Ma the $\delta^{18}\text{O}$ record changes to a ~ 100 kyr cycle.

The ice core record gives us a secondary data source for the past 800 kyrs, with $\delta^{18}\text{O}$ and δD isotope methods showing a ~ 100 kyr temperature cycle that matches the temperature timeseries inferred from the deep sea stack record. Furthermore, the ice core record of CO_2 concentration in the atmosphere is closely correlated with temperature, with low CO_2 concentration corresponding to cold temperatures.

Collectively, these are the key observable features of the Quaternary glacial: 40 kyr glacial cycles from 2.5–1 Ma, and ~ 100 kyr glacial cycles from 1 Ma-to-present. Variations in global ice volume and deep-sea temperature are known for this entire time period, and variations in CO_2 concentration in the atmosphere are known for the past 800 kyrs. There are other observations that use different proxy measurements to infer paleo-climate properties, but none of these provide significantly more information than presented above; for the purposes of introduction, I will merely say that other diverse proxies agree with the outline of 40-then-approximately-100 kyr cycles. With this outline of ice sheet history in place, we now discuss the physics behind how and why an ice sheet forms.

1.2.1 Ice Sheet Physics

The core physics behind ice sheets are intuitive: an ice sheet begins to form when a region gains more ice during winter snowfall than ice is melted during summer, causing net accumulation. As ice accumulates, the stresses on the ice cause it to flow outwards from the accumulating region (equivalently, the region above the ‘snowline’). This flow can maintain ice in regions where more ice is melted than accumulates through snowfall. An ice sheet reaches a steady state when the ice mass annually melted away at its edges matches the ice mass accumulated annually through snowfall. Thus the steady state is a balance of net accumulating regions above the snowline, and net melting regions below the snowline.

Mountain glaciers are an example of this balance in action; a high, cold region of a mountain accumulates snow over time, until ice flows downhill into warmer regions where the ice melts. Modern mountain glaciers are even an example of the basic dynamics of ice sheets: anthropogenic warming of the planet has increased the melting rates of glaciers without a similar increase in annual snowfall and thus these miniature ice sheets are in retreat.

Continent-scale ice sheets are larger scale examples of mountain glaciers with a significant difference — they are large enough to change the radiative properties of the Earth such that its climate changes. Figure 1.1 shows the basic schematics of an ice sheet.

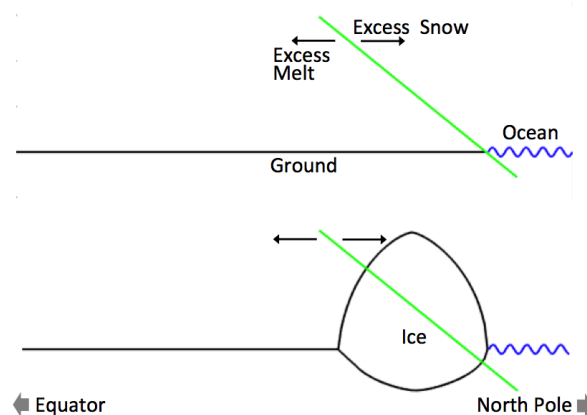


Figure 1.1: Cartoon of ice sheet growth southwards from the Arctic ocean. Green line denotes the snowline, inclined due to reduction of temperature with altitude. Upper panel shows the snowline barely intersecting land; there is no ice sheet. The lower panel shows the result of the snowline moving southwards: a large ice sheet depressing the ground beneath it.

When external forcing cools the planet such that the snowline intersects with the

ground surface, an ice sheet starts to accumulate. If favourable conditions continue, the ice sheet spreads across 100's of kilometres. Ice reflects more solar radiation than bare ground/vegetation (higher albedo), thus reducing the amount of solar radiation absorbed by the Earth and consequently cooling the planet. This cooling is a positive feedback favouring further ice sheet expansion. The ice sheet thus expands until this positive feedback is counteracted by the increasing difficulty of expanding ice sheets to warmer, lower latitudes, or by an external forcing.

The albedo forcing is not just a positive feedback for an advancing ice sheet, it is also a positive feedback for a retreating ice sheet; decreasing ice cover reveals darker, less reflective ground that absorbs more solar radiation than the ice sheet, warming the Earth and prompting further ice retreat. Therefore ice sheets should retreat in response to an external forcing (warmth or precipitation) that triggers significant reductions in ice cover.

A second positive feedback is ground height. Temperature in the lowest 10 km of the atmosphere decreases linearly with altitude. Therefore, as the ice sheet advances and thickens, its upper surface is elevated into colder air (reducing melting). Conversely, for a mature ice sheet where ice has depressed the bedrock beneath it (see figure 1.1), any retreat of the ice sheet lowers the upper surface into warmer air (increasing melting).

This physical picture gives an idea of the key controls on ice sheet growth/retreat: melting and snow precipitation. Anything that affects these, affects the ice sheet. Albedo feedbacks can explain some ice sheet behaviour, but not all; there is a need for external forcings to trigger changes that albedo can reinforce. From this framework, we can discuss the physics of one of the potential ice sheet forcings in more detail.

1.2.2 Orbital Parameters and Forcing

Glossary	
Aphelion	Point in an orbit furthest from the sun
Perihelion	Point in an orbit closest to the sun
Semi-major axis	Half of the longest axis through an orbit. Directly proportional to the energy of an orbit, thus is a conserved quantity.
Solstice	Midpoint of a season. Summer/winter solstices are the longest/shortest days of the year respectively

This section explains how variations in Earth’s three main orbital parameters cause variations in insolation. The focus is on understanding and quantifying insolation changes caused by each orbital effect. I use simple physical models looking at trigonometric approximations of orbital effects, discussing each in its own subsection, leading to the conclusion that the three orbital parameters can be understood as two net insolation forcings: obliquity-forcing causing more extreme seasons at high latitudes, and precession-index-forcing causing insolation to change evenly across the planet.

Variable	Range	Units	Description
d_0	150	Gm	Semi-major axis: half of the Earth’s longest orbital axis
ϵ	22.1–24.5	degree	Obliquity: angle between the Earth’s rotation axis and orbital axis
e	0.003–0.058	–	Eccentricity of the Earth’s orbit
$\tilde{\omega}$	0 – 360	degree	Precession: true longitude of the perihelion from vernal equinox
$e \sin \tilde{\omega}$	-0.056–0.055	–	Precession Index: relative change from semi-major axis length at summer solstice
ϕ	0–90	degree	Latitude: angle from the equator

Table 1.1: Insolation parameters over the past million years. The value range may change slightly if considering other time periods.

1.2.2.1 Obliquity

Obliquity ϵ denotes the angle between the Earth’s rotation axis and orbital axis, or equivalently the angle between the plane of the Earth’s equator and the plane of the Earth’s orbit around the Sun, currently 23.4° . As the Earth orbits the sun, this axial tilt means that the northern and southern hemispheres are alternatively tilting towards the sun and away from it. The northern and southern hemisphere seasons are defined by this axial tilt, with summer occurring when the hemisphere is tilted towards the Sun (and winter when it is tilted away).

Summer warming is driven both by sunlight being spread over a smaller area of the Earth’s surface in summer than in winter — increasing the W/m^2 insolation — and by the increased daylight hours. These effects can be simply represented at leading order; figure 1.2 shows the geometry for calculating the change in insolation intensity with obliquity and latitude, ϕ , at summer solstice. Insolation intensity relative to the maximum

is the cosine of the angle between a point on the sphere and the orbital plane. Thus, at a given latitude, summer solstice insolation is proportional to $\cos(\phi - \epsilon)$, and winter insolation $\cos(\phi + \epsilon)$.

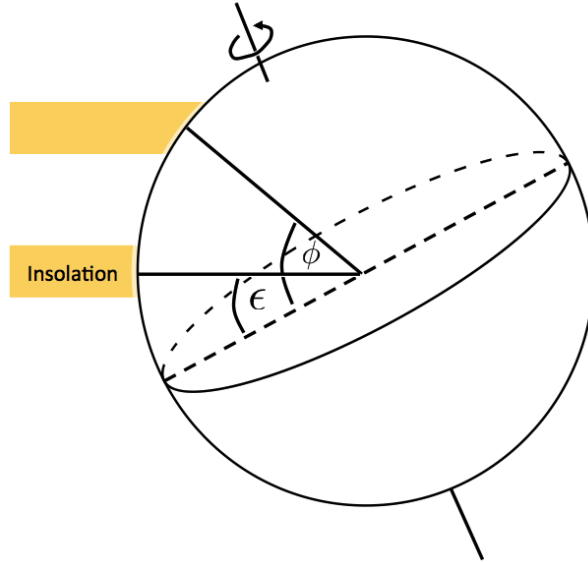


Figure 1.2: Sketch illustrating the geometry for changing insolation intensity with respect to obliquity. An equivalent incoming cross-section of sunlight is spread across a larger area of the earth for higher angles from the orbital plane. The high-latitude insolation beam is spread over an area $\cos(\phi - \epsilon)$ times larger than the beam in the orbital plane.

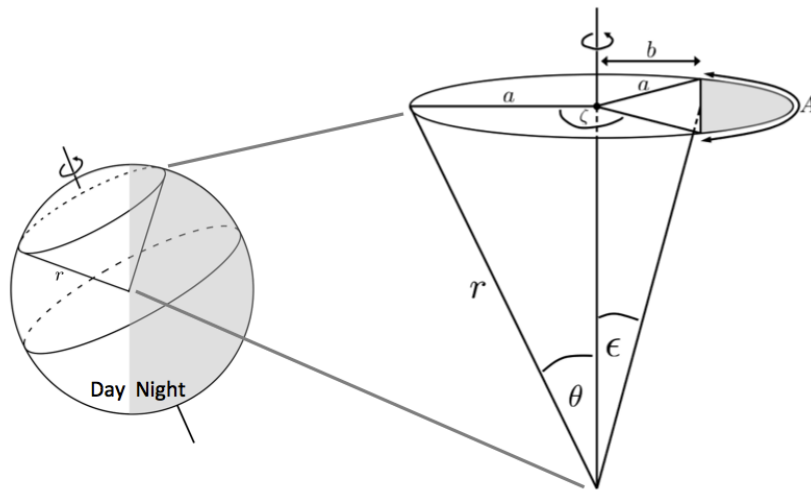


Figure 1.3: Sketch illustrating the geometry for changing daylight length with respect to obliquity. The right-hand sketch is a fixed-latitude great circle, according to the tilted Earth, with obliquity ϵ , shown on the left-hand side. θ is the complementary angle to latitude, ϕ . The ratio of daytime to nighttime at summer solstice can be defined by the angle ζ . Winter solstice ζ is equal to night time angle at summer solstice, equal to $\pi - \zeta_{\text{Summer}}$

Figure 1.3 shows the geometry for calculating daylight ratio at summer solstice, where $\theta = \pi/2 - \phi$ radians, r is planet radius, a is the radius of the great circle, A is the arc

length representing nighttime, and 2ζ is the subtended daytime angle. The day-to-night ratio at the solstices is ζ/π , with ζ given by

$$\zeta = \arccos(\mp \tan \epsilon \tan \theta) \quad , \quad (1.1)$$

where \mp gives the summer and winter solstice values respectively.

Applying these calculations for Oxford at 51.8°N , the insolation at summer solstice noon is $3.4\times$ higher than at winter solstice noon, and daylight hours increase by a factor of 2.1 (specifically, $7.6 \rightarrow 16.4$ hours). This is a spatial and temporal redistribution of insolation: because the Earth has axial tilt, solar radiation becomes more intense at high latitudes during summer, and there is a matching insolation reduction in winter; thus the net annual insolation at each latitude is unchanged. Increasing obliquity (larger axial tilt) makes these seasonal effects stronger, causing hotter summers and colder winters.

To be clear, the equations above are correct for two quantities at summer and winter solstice: Noon insolation, and day length. These cannot be multiplied together to get daily insolation as we need to account for how, as the Earth rotates during the day, insolation intensity changes. Making this calculation is somewhat tedious, does not provide physical insight, and is a published result [Berger et al., 1993], so let us merely consider the end result. The correct, generalised equation for obliquity's daily insolation forcing at summer solstice is

$$R_{\text{Obl}} = \pm \zeta \sin(\phi) \sin(\epsilon) + \cos(\phi) \cos(\epsilon) \sin(\zeta) \quad , \quad (1.2)$$

where R_{Obl} is the fractional change in radiative forcing due to obliquity, and \pm gives the summer and winter solstice values respectively. Thus the W/m^2 forcing is SR_{Obl} , where S is the solar constant.

In the past million years, the Earth's axial tilt varied between 22.1° and 24.5° , with a 41 kyr period [Berger and Loutre, 1991]. For summer solstice at 65°N , the maximum obliquity, compared to minimum obliquity, has a 3.8% higher peak insolation, 11.4% longer daytime, and 8.6% higher daily insolation.

1.2.2.2 Eccentricity

The Earth's orbit around the Sun is slightly elliptical, however the ellipse is not constant, varying from more circular to less circular. The more elliptical the orbit, the higher its eccentricity e , with a circular orbit being $e = 0$ and maximum ellipsis $e = 1$. The Earth's orbit ranged over $e = 0.003$ – 0.058 in the past million years. By definition, the change

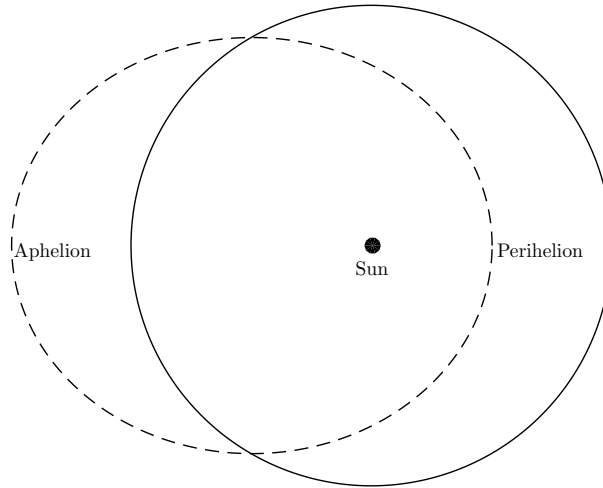


Figure 1.4: Exaggerated example of Earth's eccentricity changes: orbits with eccentricity of 0 (solid line) and 0.6 (dashed line) and constant semi-major axis d_0 . Labels mark the Sun and the maximum (aphelion) and minimum (perihelion) points in the orbit.

in distance from the Sun between perihelion and aphelion, in units of the semi-major axis, is double the eccentricity value. Changing distance from the Sun has two effects on Earth's climate: 1) closer orbits have higher insolation — the W/m^2 radiation flux from the Sun at a particular distance d is the Sun's total power output divided by the area of a sphere $4\pi d^2$, therefore insolation scales with the inverse square of orbital distance. This acts to warm the planet with decreasing orbital distance. 2) closer orbits have higher velocities — the speed of an elliptical orbit scales with $(2d_0/d - 1)^{\frac{1}{2}}$, thus the Earth moves faster when closer to the Sun, and slower when further away. This acts to reduce the length of the eccentricity-induced perihelion warm period, and extend the length of the eccentricity-induced aphelion cool period.

Qualitatively, we expect a larger annual warming effect than annual cooling effect (insolation increase scales with a higher power of d). This intuition is correct, the (fractional) net annual change in insolation is $1/\sqrt{(1 - e^2)}$, slightly warming the Earth at higher eccentricity.

We can calculate all these eccentricity effects: maximum eccentricity (0.058) gives the Earth a 26% difference in insolation over the course of a year (spatially uniform), and a 12% difference in orbital speed. The difference in perihelion effects from minimum to maximum eccentricity are a 12% insolation and 5.6% orbital speed change. Finally, the difference in net annual insolation is 0.17%.

The eccentricity variation has a predominantly 100 kyr period, as shown in figure 1.5b, although it can be split out into 95, 125, and 413 kyr components [Berger and Loutre, 1991].

However, there is a complication in understanding the overall effect of eccentricity on the Earth’s energy balance — how does eccentricity interact with obliquity? Eccentricity affects insolation and orbital speed, and obliquity affects insolation and day-length (to simplify discussion, we can consider that obliquity affects average daily insolation). In the eccentricity discussion above, we assumed that a slower orbital velocity at aphelion was, effectively, a cooling effect because it extended the time period when the Earth was receiving less insolation. However, obliquity can increase insolation in mid–high latitudes’ summer by more than eccentricity decreases it, therefore if aphelion coincides with summer (for one hemisphere) the slower orbital velocity is acting as a net annual warming effect in high latitudes on that hemisphere.

Clearly there is a need to describe the alignment between summer and perihelion, bringing us to our third orbital parameter: precession.

1.2.2.3 Precession

The precession parameter $\tilde{\omega}$ is an angle recording the alignment between northern-hemisphere summer (Earth is leaning towards the sun) and perihelion (orbital point closest to the Sun); the ‘true longitude of the perihelion from vernal equinox’. This is the (right-handed) angle in the orbital plane between the vernal equinox (northern hemisphere mid-spring) and perihelion. The angle tells us whether eccentricity’s insolation effect is reinforcing obliquity’s northern hemisphere insolation effect, according to $\sin \tilde{\omega}$. However, this precession angle only records if the insolation effects are in phase, not how strong they are. Therefore a precession index was designed to include this information, choosing to embed

the strength of the eccentricity:

$$\text{Precession Index} = e \sin \tilde{\omega} . \quad (1.3)$$

Qualitatively, this precession index is a measure of eccentricity-based insolation effects during obliquity's maximum annual insolation (*i.e.* northern hemisphere summer solstice). Specifically, $e \sin \tilde{\omega}$ records change in the Earth–Sun distance at summer solstice due to eccentricity, in units of the orbit's semi-major axis. If perihelion coincides with northern-hemisphere-summer-solstice when there is large eccentricity, then the precession index is very positive. If perihelion coincides with northern hemisphere winter solstice when there is large eccentricity, then the precession index is very negative. The same solstice/perihelion alignments at low eccentricity give slightly large and slightly small precession indices. To be clear, the precession index is not a perfectly accurate measure of eccentricity forcing at the summer solstice — recall forcing scales with the inverse square of orbital distance, thus a factor of $(1 - e)^{-2}$ would be preferable to e . However, despite the flaw, this precession index has become the standard. Importantly, the timing information in the precession index is correct: the peaks and troughs occur at times of maximum and minimum eccentricity forcing on summer solstice.

The precession index combines signals with two frequencies; e at 100 kyrs, and $\sin \tilde{\omega}$ at 23 kyrs. Consequently the precessional index timeseries is similar to a beat frequency, with a 23 kyr sinusoid oscillating within a 100 kyr envelope (see figure 1.5c). In detail the behaviour is more complex; eccentricity variations include 413 kyr variability and are not sinusoidal. Regardless, a two-sine beat frequency gives a useful conceptual understanding of precession index behaviour.

Moving from conceptual to exact calculations, the combined radiative effect of precession and eccentricity at solstices, R_{PE} , can be calculated from elliptical equations (using insolation proportional to distance squared), giving

$$R_{\text{PE}} = \left(\frac{1 \pm e \sin(\tilde{\omega})}{1 - e^2} \right)^2 , \quad (1.4)$$

which reduces to $(1 \mp e)^{-2}$ when eccentricity and obliquity are in phase.

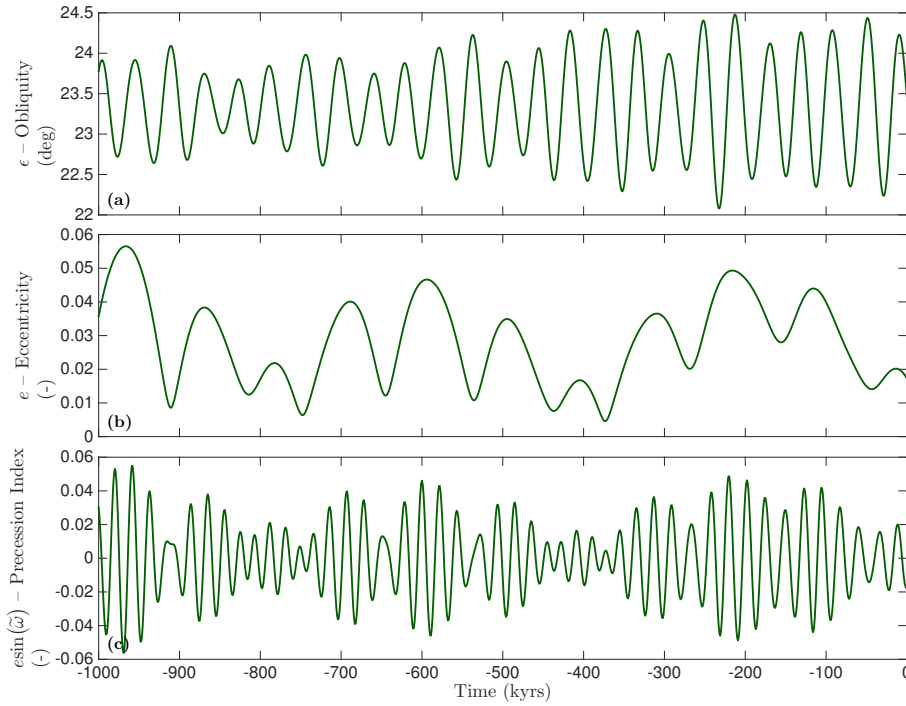


Figure 1.5: Insolation parameters over the past million years. Note that these values do not scale with the W/m^2 insolation forcing or calorific half-year, they only tell us when each forcing effect is at maximum and whether that forcing is larger or smaller than its other local maxima. For instance, eccentricity is plotted as e , but eccentricity-driven peak perihelion insolation scales with $(1 - e)^{-2}$.

Physically, precession does not alter the insolation distribution of the Earth, it merely describes the interaction between two processes that do alter insolation — obliquity and eccentricity. R_{PE} calculates eccentricity-driven-insolation-change’s reinforcement of the obliquity-driven-insolation-change at northern hemisphere summer solstice. Figure 1.6 shows how NH peak daily insolation is a combination of precession index and obliquity forcing.

However, having discussed the physics of the three orbital parameters, I highlight a final complication: peak summer insolation is not a sufficient indicator of the world’s glacial state. As discussed in section 1.2.1, the glacial system is a balance between ‘annual snowfall’ and ‘annual melting’, neither of which are directly proportional to peak summer insolation. Why not? To simplify for the sake of summary, precipitation scales exponentially with air temperature — warmer air can hold more water vapour — and thus longer, colder winters don’t change snowfall much because the competing effects cancel somewhat (longer = more snow, colder = less snow). Therefore annual melting is the dominant control on mass balance.

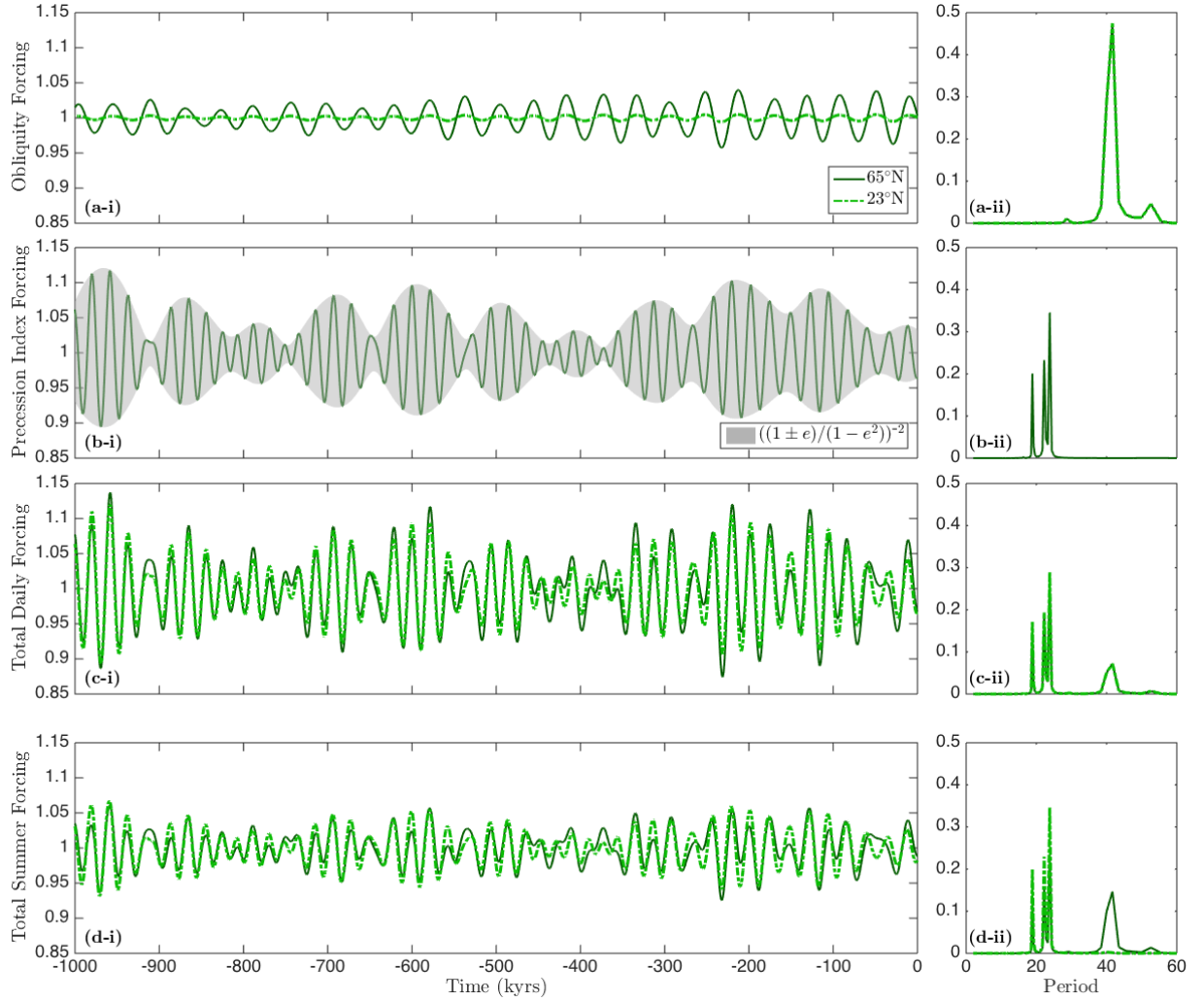


Figure 1.6: The (i) column shows relative forcing at (a)–(c) summer solstice, and (d) half-year summer. The value 1 denotes the average over the past million years. The (ii) column shows a Discrete Fourier Transform (DFT) power spectra scaled so the terms sum to 1. For readability, terms above the 60 kyr period are not shown. Row (a) shows obliquity forcing R_{Obl} for 65°N and 23°N tropic of Cancer. Row (b) shows the precession index forcing R_{PE} in green — the insolation effect of eccentricity at northern hemisphere summer solstice — and the eccentricity forcing as a grey envelope. This insolation change is independent of latitude. The final two panels show the combined insolation forcing from both effects, retaining the same line styles for the 65°N and 23°N values. Row (c) shows the total maximum daily insolation forcing $R_{\text{Obl}}R_{\text{PE}}$ and row (d) shows the summer half-year forcing calculated by a full orbital code. For summer half-year forcing, obliquity forcing dominates precessional forcing above 72°.

Annual snow melt is directly proportional to the excess energy put into trying to raise ice sheet temperature above 0°C. This ‘excess energy’ is the integral, over a year, of local thermodynamic quantities.

Peak daily summer insolation does not reflect excess energy well. When the precession index is high, NH peak summer insolation is high (increasing melting), but summer is shorter due to faster orbital velocity at perihelion (reducing melting). Studies calculating

melting over a year show this orbital velocity effect is significant [Huybers and Tziperman, 2008], reducing the influence of eccentricity and the precession index on glacial cycles. Therefore measures of peak daily insolation overstate the importance of the precession index on glacial state.

Figure 1.6c,d illustrate this. Due to the reduced precession index effect on half-year insolation, the amplitude of forcing changes are smaller in figure 1.6d than figure 1.6c. Furthermore, the obliquity cycle has double the power in figure 1.6d (sum of approximately 40 kyr terms are 25% vs. 13% for 65°N, and 5% vs. 3% for 23°N).

In summary, orbital parameters collectively altered the Earth's summer insolation by $\pm 5\%$ in the past million years (figure 1.6d), with a mixed 23 and 40 kyr signal at high latitudes, and a predominant 23 kyr signal at low latitudes.

1.2.3 History of Glacial Theories

The first evidence of glacial events entered scientific literature in the mid-1800's, with work describing glacial moraines, erratic boulders and glacial striations far beyond the range of 1800's glaciers. The conclusion: in the past, glaciers covered far more of Europe and North America, forming large ice sheets. Evidence suggested the ice sheets were a relatively recent feature, occurring in the last 10–30 kyrs. Furthermore, hot and cold events seemed to be repeating in cycle, although the period of the repetition was unknown.

No existing view of the Earth's evolution could explain these features. The change in conditions over the last 10–30 kyrs was too rapid, and cyclical climate behaviour was thought to be impossible.

Two causative physical mechanisms were proposed for this extensive European glaciation: greenhouse theories and astronomical theories. The greenhouse theories hypothesised that the variable atmospheric concentration of gases with infrared absorption spectra (greenhouse gases) controlled ice sheets; the astronomical theories hypothesised variability in the Earth's orbital parameters controlled ice sheets.

Greenhouse theories were derived from the hypothesis that the physical composition of the atmosphere affects planetary temperature. Specifically, that gases with absorption and emission spectra overlapping the Earth's peak blackbody frequency band would reduce

thermal emissions to space and increase Earth's temperature. Researchers of the 1800's (correctly) identified water vapour and CO₂ as the most important molecules in this process.

The landmark paper [Arrhenius \[1896\]](#) used estimates of variable atmospheric absorption of infrared radiation (in response to varying water and CO₂) to calculate the temperature change of the Earth in response to variable CO₂ concentration. His results suggested a 2–3 K reduction in European temperatures for a 30–40% decrease in CO₂ concentration (close to modern estimates, although as we will discuss the underlying calculations were incorrect). Furthermore, he identified several qualitative features important to glacial hypotheses: there are reservoirs of CO₂ that far exceed the atmospheric CO₂ inventory, thus atmospheric CO₂ concentration could be significantly altered over time through small flux imbalances of these reservoirs; water vapour saturation is temperature-dependent, thus water vapour forcing will reinforce temperature changes; changing the concentration of a greenhouse gas (by $x\%$) has a greater effect when that radiative frequency band is undersaturated.

This theory's headlines are consistent with the current understanding of greenhouse gases. However, the original works were inaccurate in the exact details of radiative transfer, treating the atmosphere as a single layer with a variable, incomplete absorption of infrared radiation. This is incorrect; the atmosphere is optically thick to infrared radiation, fully absorbing infrared radiation emitted in any direction; infrared emissions to space occur from high, low-density atmosphere (that is optically thin to infrared radiation transmitted towards space). Increased greenhouse gas concentration means the atmosphere becomes optically thin at a lower density, thus the optically thin layer is higher and colder, reducing the Earth's infrared emissions to space. Consequently, the Earth has a net energy imbalance, absorbing more than it is emitting, and will warm until the outgoing radiative emissions match the incoming. Fortunately, the incorrect treatment used by early researchers retains the roughly logarithmic scaling of longwave forcing with greenhouse gas concentration [[Myhre et al., 1998](#)], so the understanding derived from their results was roughly correct.

The astronomical theories hypothesised that the variations in the Earth's orbit caused

glacial cycles. Specifically, variations in the Earth’s precession, obliquity, and eccentricity could change how solar insolation was distributed spatially over the planet’s surface and temporally over the course of a year [Croll, 1867]. It was qualitatively believed that these redistributions of energy would affect ice sheets, but exact quantitative calculations of their effects were not made until 1941 [Milankovitch, 1941], thus it was not known which of precession, obliquity and eccentricity should be dominant drivers of glacial cycles. Regardless, the qualitative concepts had sufficient merits to be taken seriously.

For instance, variations in these three orbital parameters are cyclical, offering a ready explanation for the inferred repetition of hot/cold climates in Europe [Geikie, 1874]; insolation calculations also stated whether northern and southern hemisphere glacials should be synchronous, which was increasingly testable against field evidence. Furthermore, exact dates for orbital maxima/minima could be defined — pre-1900 astronomy could accurately define Earth’s orbital parameters for ~ 300 kyrs into the past (modern research: >20 Myrs [Laskar et al., 2004]) — facilitating comparisons against the ‘known’ time of the last glacial maximum.

The 1950s saw a significant advance in geological climate data, with the development of ocean-sediment corers that extracted 10–20 m of sediment (previous limits were ≤ 1 m). These were the first continuous datasets recording global variability over 100’s of kyrs. Initial analysis looked at variations in carbonate volume fraction of the sediment [Arrhenius, 1953], but within a few years isotopic analysis of the core’s $\delta^{18}\text{O}$ oxygen ratio by Emiliani [1955] provided proof of temperature cycling. Initially, the exact timing of these cycles remained elusive; the most recent ~ 100 kyrs could be dated by Thorium-isotopes, and deeper-time records were extrapolated assuming constant sedimentation rate. Thus the magnitude of $\delta^{18}\text{O}$ events were accurate throughout the record, the timing of most recent 100 kyrs were reasonably accurate, and timings prior to that were of unknown accuracy.

Partly in recognition of the timing limitations, Emiliani’s work began the “Marine Isotope Stage” (MIS) nomenclature, where isotope timeseries were demarcated by particular $\delta^{18}\text{O}$ minima, with the expectation that the exact time of the minima would change, but literature could maintain continuity by referring to the features rather than the timing of

those features.

The end result of oxygen isotope data in the 1950's was that the last 100 kyrs showed a single glacial cycle (with just enough inflection between MIS 2–4 that it could be a pair of 40 kyr cycles if you squint at the graph) and the remaining extrapolated time record was dominated by a 40 kyr cycle. The 40 kyr cycling was consistent with Milankovitch's calculations predicting an obliquity-driven glacial record, and the data was considered to agree with this hypothesis.

However, as the timing record of the last million years improved, the idea of late-Pleistocene 40 kyr glacial cycles became less favourable [Hays et al., 1969, Broecker and Donk, 1970, Shackleton and Opdyke, 1973].

The next major synthesis of material was Hays et al. [1976], which compared improved ocean sediment $\delta^{18}\text{O}$ timeseries of the past 450 kyrs with orbital calculations. Specifically, Hays showed the ocean sediment timeseries had a power spectrum clustered to three orbital periods: 10% at 23 kyr, 25% at 41 kyr, and 50% at, roughly, 100 kyr. This was strong evidence that orbital effects paced glacial cycles, although it left several questions unanswered.

A purely statistical reading of Hays et al. [1976] $\delta^{18}\text{O}$ timeseries would say 100 kyr eccentricity variations control glacial cycles, as they have twice the $\delta^{18}\text{O}$ spectral power of any other orbital term, however the physics of orbital calculations emphatically disagrees. Eccentricity is an orbital parameter that varies at 100 ka but it does not change seasonal insolation at that periodicity. Instead it modulates the amplitude of precession index forcing at 23 kyr periods (see figure 1.6b). Any proposed causal mechanism invoking 100 kyr eccentricity maxima must explain why the associated large precession index maximum caused deglaciation, whilst the adjacent (also relatively large) precession index maxima did not, and why the subsequent large precession index minima did not induce glaciation. Even then, consecutive eccentricity maxima have different magnitudes (up to a factor of two difference in relative forcing), but glacial cycles remain about 100 kyr, meaning deglaciation cannot simply trigger at a threshold insolation value.

A further complication is that high latitude summer insolation is altered by obliquity more than it is by maximum amplitude precession index forcing. Therefore we must

explain why a system with forcing that varies from dominant 40 kyr to moderately less dominant 40 kyr (due to increased 23 kyr forcing on a 100 kyr interval) produces a 100 kyr response.

Orbital calculations thus show that insolation forces the Earth system on a mixed 23 and 40 kyr cycle. The only way astronomical forcing could result in a 100 kyr glacial cycle is if the Earth system has a highly non-linear response to astronomical forcing — as recognised in [Hays et al. \[1976\]](#), although they sensibly refrain from suggesting mechanisms.

Mechanisms aside, the observation was the late-Pleistocene glacial record correlates best with eccentricity and the precession index maxima. This is difficult to align with the ‘summer half-year at 65°N’ insolation metric that best represents the driving physics acting on ice sheets. However the metric ‘peak summer insolation’ has a higher variation from precession index forcing, thus better correlates with the glacial record. Consequently, it became more common to use ‘peak summer insolation’ in papers.

The peak summer insolation metric has remained dominant in literature, driven by the implicit assumption that the deglaciation–eccentricity correlation is statistically significant, and that this statistical significance dominates the lack of sensible eccentricity-linked causal mechanism.

However, more recent work suggests the glacial record is roughly as well represented by deglaciations on every 2nd or 3rd obliquity cycle as on 4th or 5th precessional cycle [[Ridgwell et al., 1999](#)]. Therefore, all three orbital parameters have statistical fits to glacial records; although different parameters have varying degrees of physical plausibility regarding how the associated orbital forcing could affect glacial cycles. Unfortunately, these fits and plausibilities cannot be calculated to give exact probabilities. Considering these probabilities subjectively, I disagree with the assumption that eccentricity-mediated effects control glacial cycles.

Overall, astronomical theories must clearly abandon assumptions of linearity. The late-Pleistocene Earth does not respond linearly to insolation. The answer must lie in Earth system dynamics, with the evolution of greenhouse gases and ice sheet motion leading to a glacial response that contains orbital periodicity, but not a linear response

to insolation.

In fact, models combining Greenhouse forcing, astronomical forcing and ice sheets are, within limits, reasonably successful. Models of ice sheet evolution and Earth temperature can, if driven by the known orbital parameters and CO₂ record, output an ice sheet response that matches the glacial record [[Ganopolski and Calov, 2011](#), [Abe-Ouchi et al., 2013](#)].

However, the limits of such models are substantial: atmospheric CO₂ evolves over time in response to physical processes cycling CO₂ between reservoirs. Driving the model with CO₂ and allowing ice to evolve in response is cheating; CO₂ and ice co-evolve in response to insolation forcings and subsequent feedbacks. No model has yet explained how insolation can drive the evolution of the Earth's CO₂ and ice in a manner that matches the historical data of the past 3 Ma.

1.3 Mantle Dynamics

The mantle spans 3,000 km between Earth's outer core and crust and unsurprisingly the term mantle dynamics has a very broad range of potential applications. We focus on the subset of mantle dynamics relevant to extracting CO₂ from the mantle and releasing it into the atmosphere — namely two-phase mantle dynamics in the upper ~100 km of the mantle, where a few percent of the convecting solid mantle melts, forming the liquid magma that is erupted at mid-ocean ridges and subaerial volcanoes. This section discusses the key physical properties of the mantle, the equations governing its flow and evolution, and how CO₂ moves through this system.

The mantle is a solid, consisting of single-crystal grains locked together in a matrix. Throughout the Earth, the mantle is at a high temperature (close to its melting point) and under significant pressure gradients, enabling creep and the motion of crystal dislocations. These processes enable plastic deformation, and the solid mantle flows on geological timescales, moving up to a few cm/yr in response to deviatoric stresses.

When the mantle upwells, such as beneath mid-ocean ridges, it experiences a reduction in pressure leading to both an adiabatic cooling (doing work as it expands slightly) and a reduction in solidus temperature. The solidus temperature reduces at a faster rate than

the mantle cools, and for adiabatic upwelling the mantle exceeds its melting temperature about 60 km beneath the crust¹. This creates mantle melt. Melting continues as the mantle ascends. The generated melt occupies the vertices and edges of the solid mantle grains, forming up to a few percent of the mantle by volume. This fluid forms an interconnected porous network, allowing the melt to percolate through the solid. Percolating melt moves at about 1 m/yr, nearly two orders of magnitude faster than the solid mantle. This melting process and migration drives volcanism and MORs.

A second route to melting the mantle through reducing its solidus temperature is to change its chemical composition (similar to adding salt to ice). In the mantle, the prominent solidus-influencing chemical species are water or CO₂. At subduction zones, water is emitted from the subducting plate, inducing melts that feed the subduction zone's volcanic arc.

To be clear, mantle processes are somewhat more complicated than the picture I sketch above. However, the sketch is a reasonable framework for understanding mantle behaviour. Solid and liquid components are comingled, both flow in response to pressure gradients, the liquid moves faster than the solid, and the dominant cause of melting is the reduction in solidus temperature. More detailed discussion can wait until after the dynamic equations are defined.

The foundation paper for two-phase mantle dynamics is [McKenzie \[1984\]](#), which laid out fundamental equations to describe the dynamics of partially molten rock, accounting for the motion of liquid mantle through the network of boundaries along solid mantle grains. McKenzie was not the first person to use fluid dynamics in a geophysical context [[Sleep, 1974](#), [Walker et al., 1978](#), [Ahern and Turcotte, 1979](#), [Stolper et al., 1981](#)], but his 1984 paper was the first synthesis of all the necessary component equations. The core difficulty in the synthesis is taking the full set of processes controlling motion in a two-phase fluid, and reducing them to solvable equations in a physically justified manner.

Mantle liquid and solid flow occur due to mantle-grain-scale processes, so there is

¹This depth of first melting depends on the chemical composition of the mantle. 60 km is the dry peridotite melting boundary — peridotite being a major rock component of the mantle, and dry denoting a lack of water. The presence of water or CO₂ (as interstitial elements in the mantle's atomic lattice) substantially lowers the melting temperature, such that wet peridotite with 0.01% water by weight melts at about 110 km, and 0.01 wt % carbon-bearing peridotite at about 160 km [[Keller et al., 2017](#)]

a micro-macro problem in formulating useful equations. For instance, fluid flow along grain edges is akin to Poiseuille flow along a series of pipes — where volume flow rate is proportional to radius to the 4th power — implying the flow is highly dependent on the radius of pathways along individual grain edges. Do we need to know the exact porous network at a microscale to understand fluid flow, or can we get representative behaviour at a macroscale according to bulk system properties at that macroscale? Fortunately, yes, bulk property macroscale models are accurate. We assume representative volume elements (RVEs) containing sufficient mantle grains to have a representative average of grain properties (temperature, density, etc...) and to capture isotropic behaviour of properties that are anisotropic at the grain scale (viscosity, edge network) but isotropic over multiple, randomly-orientated grains. RVEs are also small enough that mantle properties vary across the element, at most, linearly.

The McKenzie equations are conservation of mass, momentum (equivalently, due to the insignificance of inertial terms, a force balance), and energy. We begin with conservation of mass for fluid and solid, asserting that the rate of change of phase mass is equal to the outflow of that phase from a point plus the rate that phase is melting/freezing:

$$\frac{\partial \rho_f \phi}{\partial y} = -\nabla \cdot [\rho_f \phi \mathbf{v}_f] + \Gamma, \quad (1.5)$$

$$\frac{\partial \rho_m (1 - \phi)}{\partial y} = -\nabla \cdot [\rho_m (1 - \phi) \mathbf{v}_m] - \Gamma, \quad (1.6)$$

where f, m subscripts denote fluid and matrix (ie. solid) mantle properties, ρ is density, ϕ is porosity volume fraction, \mathbf{v} is velocity, and Γ is the rate of mass transfer from the solid to the fluid phase (the melting rate).

Conservation of momentum for the fluid component is treated with a modified Darcy's law for fluid moving through a porous network under laminar flow. Darcy's law is a simplification of Navier-Stokes, taking the average momentum balance of a Newtonian fluid; neglecting inertial effects and friction forces within the fluid [Bear and Bachmat, 1990]. Our equation asserts that the fluid segregates from the solid according to the pressure gradients and buoyancy forces acting on the fluid, with a volume flux modulated

by permeability and fluid viscosity.

$$\phi(\mathbf{v}_f - \mathbf{v}_m) = \frac{K_0 \phi^n}{\mu \phi_0^n} [\nabla P_f - \rho_f \mathbf{g}] \quad , \quad (1.7)$$

where K_0 is the permeability at reference porosity ϕ_0 , μ is the fluid viscosity, n is the permeability exponent (permeability is $K = K_0(\phi/\phi_0)^n$), P_f is pressure in the fluid, and \mathbf{g} is gravitational acceleration.

Conservation of momentum for the solid component asserts that pressure gradients in the melt are balanced by viscous shear and compaction stresses in the melt, and by gravitational forces:

$$\nabla P_f = -\nabla \cdot \eta (\nabla \mathbf{v}_m + \mathbf{v}_m^T) + \nabla \left[\left(\zeta - \frac{2\eta}{3} \right) \nabla \cdot \mathbf{v}_m \right] - \bar{\rho} \mathbf{g} \quad , \quad (1.8)$$

where T denotes a matrix transpose, $\bar{\rho} = \rho_f \phi + \rho_m(1 - \phi)$ is the phase averaged mantle density, ζ is the bulk viscosity and η the shear viscosity of the matrix. In writing equation 1.8, we have used $P_f - P_m = \zeta \nabla \cdot \mathbf{v}_m$, which states that the difference in pressure between the fluid and mantle is equal to the outflow of fluid from a volume element, multiplied by the resistance of the mantle to compaction and dilation. This was done to eliminate the solid pressure from the system of equations (if the relationship between P_f and P_m is not defined and used in this fashion, the system of dynamical equations is under-defined).

Finally, conservation of energy. A mantle element contains energy equal to its sensible and latent heat, chemical potential, potential energy (both gravitational and compressional), and kinetic energy. However, mantle motion is slow, so kinetic energy and changes thereof are negligible and can be discarded. Therefore changes in sensible heat are caused by energy transfers from latent heat or the potentials.

In formulating the energy equation, it is convenient to approximate that the density, thermal expansion coefficient α , thermal diffusivity k , and heat capacity c_p of the mantle solid and melt are identical, and state them as bulk parameters. The net effect of these simplifications is that changes in the energy of a volume element can be calculated by considering only temperature (and porosity, if the element is not in thermodynamic

equilibrium), rather than also painstakingly calculating changes in these other parameters. Furthermore, we can define a mantle potential temperature $\mathcal{T} = T e^{-\alpha g z / c_p}$, the temperature an element of mantle would have if it were raised adiabatically to the surface without melting. This is useful because mantle upwelling is adiabatic below the depth of first melting. Thus the mantle potential temperature of a parcel of mantle is constant unless sensible heat is transferred by diffusion, or from the latent heat reservoir, allowing us to write energy conservation

$$\rho c_p \frac{D\mathcal{T}}{Dt} = k \nabla^2 \mathcal{T} - e^{\alpha g z / c_p} L \Gamma \quad , \quad (1.9)$$

$$\rho c_p \left(\frac{\partial \mathcal{T}}{\partial t} + \bar{\mathbf{v}} \cdot \nabla \mathcal{T} \right) = k \nabla^2 \mathcal{T} - e^{\alpha g z / c_p} L \Gamma \quad , \quad (1.10)$$

where $\bar{\mathbf{v}} = \phi \mathbf{v}_m + (1 - \phi) \mathbf{v}_f$ is the mean phase velocity, and L is the latent heat of fusion.

Equations (1.5), (1.6), (1.7), and (1.8) describe the motion of a two-phase system consisting of a porous solid and its melt. Equation (1.10) calculates the temperature of the system. These five coupled equations can be solved for the five unknowns ϕ , \mathbf{v}_m , \mathbf{v}_f , P , and T . However, the variables K , ρ_m , ρ_f , Γ , η , ζ , and μ need to be specified using constitutive equations. Having each variable depend on T and P leads to ferocious complexity, and is rarely solvable analytically. Therefore, it is helpful to use simplified constitutive relations according to the problem at hand, making judicious approximations to remove unnecessary complexity and highlight the most important processes in a problem. Common choices are constant viscosities, constant densities, and either constant (non-zero) melting rate or constant porosity and zero melting rate.

For my research area, the melting rate Γ is the variable most in need of complete physical treatment. The simplest plausible expression is to assume the only source of energy driving melting is upwelling²:

$$\Gamma = (\mathbf{v}_m \cdot \mathbf{k}) \Pi \quad , \quad (1.11)$$

²Recall that upwelling mantle cools adiabatically at a slower rate than the mantle solidus temperature reduces, therefore energy is made available for melting as the mantle upwells

where \mathbf{k} is a unit vector in the vertical direction and Π is melt productivity³ with units of kg of melt per m³ of mantle per metre of upwelling.

Equation (1.11) requires an expression for Π , the simplest being a constant value. This would give a steady melt production as an element of mantle upwells, a reasonable first-order approximation of upwelling (once the mantle is above its solidus temperature). However, a constant melt productivity ignores important thermodynamic and petrological facts about the complex mix of chemical species in the mantle. It cannot determine conditions for which melting begins, nor predict phase depletion (whereby melting stops when a particular species is exhausted), nor predict the reduction in melting temperatures when volatiles are added to the mantle. In short, it excludes any phase change due to non-isentropic changes in temperature.

Correcting Π to include these effects is not simple. Even assuming equilibrium thermodynamics, a completely accurate Π would have to summarise the entire thermo-chemistry of the (chemically diverse) mantle; predicting how much melting occurs when energy is added to an element of mantle with a particular chemical composition (in contact with melt of a different composition) at a particular temperature and pressure. A dynamic simulation incorporating even the basic elements of this must track the chemical composition of the mantle and solve thermodynamical equations every timestep, adding significant complexity to calculations.

Most of the complexity can be avoided if we consider a single-component mantle, whereby the solidus temperature has a single, well-defined value at a particular pressure. Assuming a linear solidus with respect to pressure (and approximating adiabatic cooling as linear with respect to P), we get a system with no melting until the solidus and adiabatic temperatures crossover at a particular, fixed pressure (equal to some depth). Above this depth, for every unit decrease in pressure ΔP , there will be a unit amount of melting, thus the melt productivity Π is constant.

If we wish to consider the mantle as a mix of chemical components, then the fixed-pressure onset of melting will remain, but the melt and temperature calculations after

³Melt productivity can be expressed as $\Pi = \rho \frac{\partial F}{\partial z}$, where F is the degree of melting, a unitless parameter ranging from 0–1 as an element of mantle becomes completely melted. Both F and Π are extremely concepts in mantle dynamics; although F is more commonly used in literature.

than point will alter. A two-component mantle's solidus is also dependent on the relative amounts of the two components in the solid. Any melt selectively carries away the more fertile component, dynamically altering melting conditions. Therefore this system requires the previously mentioned tracking of chemical composition and its inherent complexity.

The complexity is such that thermodynamically-based two-component melting was not included in mantle dynamics until long after McKenzie [1984] (Ribe [1985a] modelled a two-component 1D melting system but this was not built upon for 23 years). Binary phase loop methods developed following Katz [2008] allowed the calculation of two-component mantle systems [Katz, 2010, Hewitt, 2010] (similar to metal alloys, the mantle solidus increases as a fertile component is leached into the fluid phase) and three-component systems [Keller and Katz, 2016].

Multi-component mantle models can develop qualitatively different behaviours to single-component models. For instance: melting via changing the chemical composition of the mantle, thus replicating the known reduction in mantle solidus temperature when water or CO₂ are present. This is important both for my interest in volcanic CO₂ emissions, and because this concept is required to understand arc volcanism (primarily driven by water released from downwelling lithosphere at the adjacent subduction zone).

This melting in response to compositional changes is called 'reactive melting', and can have significant dynamic effects on the mantle. Buoyantly upwelling fluid mantle can become undersaturated in a soluble component (relative to the solid it is percolating through) inducing a melting reaction in which the soluble component is transferred from the solid to the liquid. This can drive a runaway melting process — the reactive melt instability — whereby upwelling melt can induce melting, increasing porosity and allowing faster melt flow upwards (inducing more melting, etc...), eventually forming a high-porosity channel. However, the details of such channels are a topic of active research and slightly outside the scope of our introduction. I will merely mention that they may exist under real mantle conditions, but are not essential to understanding the overall behaviour of volcanism.

Below, we discuss the first-order picture of MOR and arc volcanism derived from the McKenzie equations, describing the mantle flow and the CO₂ flux through the system.

Subsequently, we will highlight where these simplifications diverge from reality, and describe what more complete versions of these equations predict for mantle behaviour.

1.3.1 CO₂ in the Mantle

This section lays out CO₂'s basic chemical and physical characteristics in the mantle. It states that CO₂ will move with mantle melt as soon as any melt is present, justifying later sections' strong focus on mantle melt and how it flows to volcanoes for eruption into the surface carbon system.

In the upper mantle, CO₂ is a scarce element, forming about 0.001% of the mantle by mass⁴ (the 2- σ range of CO₂ is 30–250 ppmw [Le Voyer et al., 2017]). CO₂ is a highly incompatible element that dislikes being incorporated into solid mantle; the concentration of CO₂ in the melt is 1800 times higher than in the solid mantle when the two phases are in equilibrium (the partitioning coefficient is $D^{\text{solid/melt}} = 0.00055 \pm 0.00025$ with 2- σ error [Rosenthal et al., 2015]).

This very high incompatibility means carbon dioxide's route through the mantle is simply defined. Initially, CO₂ moves with the solid mantle. When the first melting occurs, the entirety of the mantle CO₂ load is transferred to the melt. The CO₂ moves with the melt, either erupting to the surface (if the melt reaches a volcanic system), or being reincorporated into the solid Earth (if the melt freezes).

Therefore, to understand CO₂ emissions, we must understand where melt is first generated (acquiring its CO₂ content), and how it subsequently travels to the volcanic system.

1.3.2 Mid-Ocean Ridges

Beneath mid-ocean ridges (MORs) the motion of the solid mantle is vertical upwelling beneath the ridge, with horizontal spreading off to the side, a characteristic pattern called 'corner flow'. This flow also focuses melt towards the ridge. The physical basis for corner flow is:

⁴Mantle chemical conditions may be such that the upper 250 km of the mantle contains CO₂ and deeper mantle with lower oxygen fugacity has pure carbon. However, my primary interest is volcanic CO₂ emissions. Given that all mantle carbon becomes CO₂ before erupting, I choose to consistently use CO₂ in my mass calculations (rather than carbon). The reader may interpret this as "CO₂ mass equivalent".

- The sinking oceanic lithosphere at subduction zones is about 80 kg/m^3 denser than the surrounding asthenosphere [Schellart, 2004], so the slab is pulled downwards under gravity.
- The descending slab pulls the oceanic lithosphere behind it⁵, this motion is accommodated by the crust rifting and spreading apart at MORs.
- The moving lithosphere drags the underlying mantle, pulling the upper layers of the mantle sideways, away from the MOR.
- To fill the space created by the mantle dragged sideways, solid mantle upwells directly underneath the ridge.
- This solid mantle flow creates pressure gradients that suck mantle melt towards the ridge (within a characteristic lengthscale), a process called ‘active focusing’.

Figure 1.7 demonstrates corner flow under a mid-ocean ridge. The calculations underlying this figure assume a constant porosity (melt volume fraction), isoviscous mantle, and that the crust is wedge-shaped.

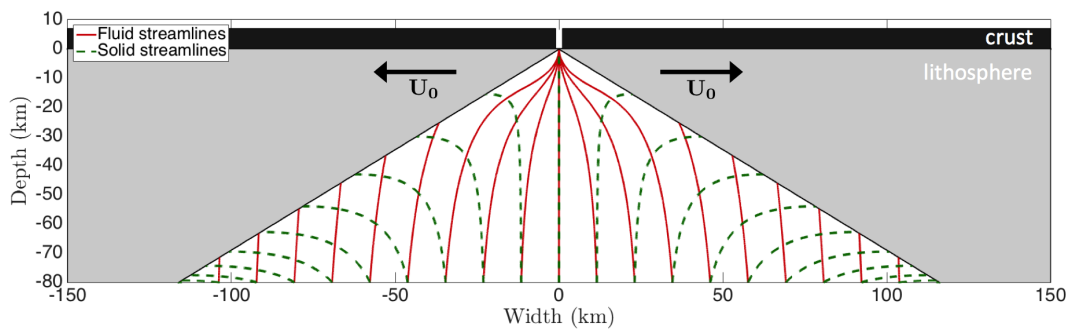


Figure 1.7: Corner flow solution for a mid-ocean ridge with half-spreading rate U_0 of 3 cm/yr , calculated following Spiegelman and McKenzie [1987]. The characteristic lengthscale for active focusing is 28 km , and fluid mantle is focused to the ridge from a 40 km width.

These assumptions are simple, but provide a useful foundation on which to build a more complete picture of MORs — what changes as we consider more processes?

Figure 1.8 demonstrates the difference presented by models using a thermodynamic melting scheme, variable viscosity and a lithosphere derived from local mantle conditions.

⁵Oceanic crust is moved by a combination of ‘slab pull’, whereby the descending slab yanks the crust behind it because it is physically attached to that crust, and ‘slab suction’ whereby the descending slab stirs mantle currents that drag the nearby crust by shear traction. These forces are equal within an order of magnitude [Conrad and Lithgow-Bertelloni, 2002], but the exact balance is a matter of debate. Regardless, it is clear the negative buoyancy of descending slabs powers the motion of the oceanic plate.

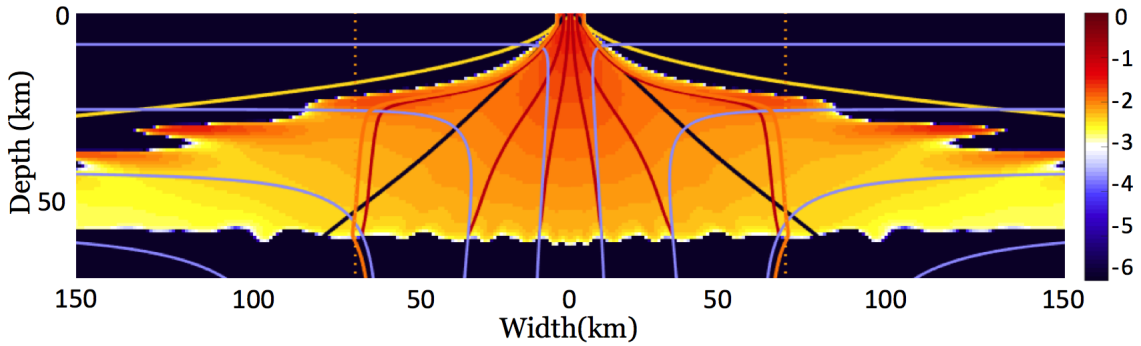


Figure 1.8: Mid-ocean ridge simulation for a half-spreading rate of 3 cm/yr, (pers.comm. T. Keller, using the model in Keller et al. [2017]). The colourbar shows porosity (melt volume fraction) in units of \log_{10} , and the yellow line marks the 1200°C isotherm. Streamlines are shown for melt (red) and solid (light blue) flow, and melt focusing width (orange). Fluid mantle is focused to the ridge from a 75 km width, 87% wider than a corner flow model predicts.

Some of the obvious changes are not that important to the carbon dynamics (*e.g.* the cold ocean cooling the mantle via conduction changes lithosphere profile substantially, but this has little effect on mantle motion within the melting region).

A few of the more important alterations are: 1) Porosity is not constant. As discussed in section 1.3, melting begins when the solidus crosses the local mantle temperature at some depth, rather than being omnipresent. Therefore we track melt (and its CO_2) from a particular depth. 2) Melt that meets the lithosphere is not necessarily incorporated into that lithosphere. The lithosphere is a cold, impermeable barrier to melt; some melt is frozen into the lithosphere, but some melt is deflected along this impermeable barrier towards the ridge, a process called ‘passive focusing’. This passive melt focusing, compared to active forcing alone, expands the focusing width of the melting region considerably (an 87% increase in our simplified scenario).

To summarise, MORs have melting in a region whose lower surface is defined by a fixed pressure boundary, and some of melt generated there is transported to the ridge. As discussed in section 1.3.1, the CO_2 content of the upwelling mantle will instantly transfer to the melt and be transported with it.

Glacial cycles change sea level, causing a change in pressure on the MOR system. Given that the entirety of melt generation and transport at the MOR are pressure dependent, there are several plausible mechanisms for sea-level change to alter the rate of CO_2 emissions from the MOR. My calculations in chapter 2 will show the dominant mechanism for CO_2 variations is the changing depth of first melting.

1.3.3 Arc Volcanism

Arc volcanoes are volcanic systems associated with subduction zones whereby a line of volcanoes occur in the overriding plate, set back about 100 km from the subduction trench. The solid mantle motion in this region is controlled by the negatively buoyant descending slab, producing the flow shown in figure 1.9

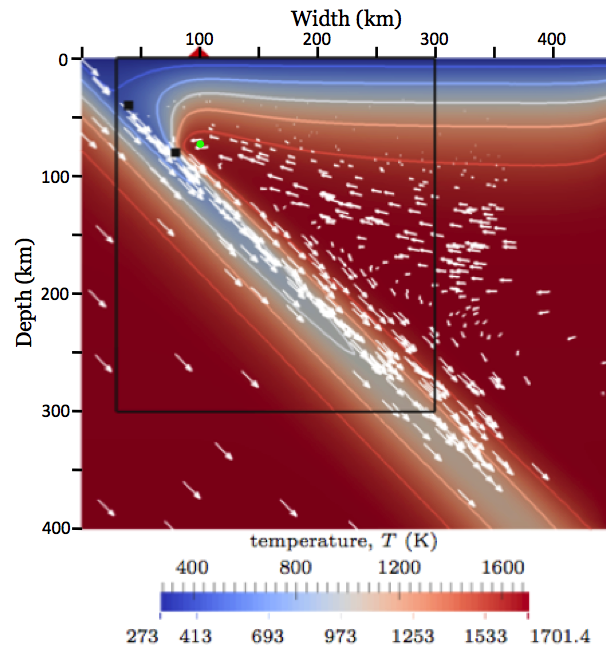


Figure 1.9: Calculated dynamics for subducting oceanic slab modified from [Wilson et al. \[2014\]](#). White arrows denote solid mantle flow, the green dot marks the nose of the mantle wedge, the red triangle marks the average volcano location, and the colourmap gives temperature. The temperature model used for this figure is primitive, considering only heat advection by solid mantle flow and conduction; thus missing advection by magma, and latent heat. These simplifications may underestimate the temperature by 200–300 K above the nose of the mantle wedge [[Rees Jones et al., 2017](#)] (about 50km beneath the volcano).

Similar to mid-ocean ridges, arc volcanism is driven by mantle melt, however the source of this melting is dissimilar. In MORs, the energy excess for melting comes from the solidus dropping below the local mantle temperature during the ascent of solid mantle; in arc volcanism, the energy excess comes from the descending slab releasing water and CO_2 , two volatiles that vastly reduce the solidus temperature of the mantle.

Water in the descending slab is initially stored in hydrous minerals; as the slab descends, the increasing pressure changes the mineral stability, causing some minerals to release their water content [[Rupke et al., 2004](#)]. At 100 km depth, the first mineral dehydrates; the released water induces mantle melting and that buoyant melt rises toward the volcanic system. In rising, the melt passes through the hot mantle in the nose of the

wedge, which may provide further melt when in contact with the hydrated fluids (reactive melting).

This melt moves vertically upward, impinging on the crust beneath the volcanic system. To reach the volcano and erupt, the melt transects the crust. How exactly the melt transects the crust is not entirely understood by modelling [Keller et al., 2013], but petrological and field evidence suggest that melt proceeds through dykes, with intermittent pauses in mush and chamber regions [Pinel and Jaupart, 2004, Rawson et al., 2016a].

As with MORs, we can understand the CO₂ moving through this system by tracking the melt from source to sink. There are three sources of CO₂ in the arc system: CO₂ in the subducted slab's sediments, CO₂ in the solid mantle wedge, and (potentially) carbonate rock units in the crust. The CO₂ from the sediments is present in the volatile-rich incipient melt rising from the slab. CO₂ in the wedge is rinsed out of the solid mantle by the passing melt (recall CO₂ is highly incompatible). The mantle wedge is depleted in carbon, so the majority of CO₂ in the melt is derived from the subducted sediments. Finally, melt transversing the lithosphere may encounter rock units that can be thermally metamorphosed by magma to release CO₂ (*e.g.* limestone and dolomite at Etna [Gerlach, 1991] and Popocatépetl [Goff et al., 2001]), but this seems to be unusual and not worth considering in the general case.

The CO₂ mass added to the melt by these processes is not dependent on the pressure changes caused by changing ice sheets during glacial cycles. Regardless of pressure, all the sediments' CO₂ load will enter the melt and extra pressure-driven melting is unlikely to change the volume of mantle drained of CO₂ in the wedge. Therefore the only way to alter CO₂ emissions is to alter the rate at which melt (and its CO₂ load) erupts from the ridge system.

The dyking and fracture system that moderates melt flow through the crust is pressure sensitive. Removing a load from the surface would reduce confining pressures, promoting fracture and magma eruption, qualitatively consistent with the increase post-glacial eruption rates suggested in Huybers and Langmuir [2009]. Therefore there are plausible mechanisms for arc volcanism's CO₂ emissions to vary with glacial cycles.

1.4 Summary

The purpose of this chapter was to familiarise a reader with the context for this PhD, and provide the essential background for the theoretical work in upcoming chapters. I began by discussing glacial cycles as a feature of the Earth’s climate that has emerged over the past 3 Ma⁶, and the observed features that we struggle to explain: the cycles transitioning from 40 kyr to \sim 100 kyr periods about 1 Ma, the continued stability of those 100 kyr cycles, and why CO₂ varies in a 100 kyr sawtooth during this period. I suggested that volcanic CO₂ emissions might vary in a manner consistent with some of these unexplained features.

Understanding this suggestion required some background of both glacial cycle physics, and mantle processes that would lead to volcanic variability.

For glacial cycles, I began with ice sheets — they are controlled by a mass balance between snowfall and melting, and have a strong positive feedbacks through albedo variations.

Ice sheet melting is controlled by temperature, and the following subsections looked at the two potential causes of this change: 1) varying CO₂ and water vapour concentration in the atmosphere, and 2) varying insolation, according to changes in the Earth’s orbit.

The orbital variations suggest 23 kyr or 40 kyr periods should dominate glacial cycles, and therefore do not readily explain the observed 100 kyr cycles that currently dominate Earth’s climate.

Models combining orbital forcing with the known CO₂ record (*i.e.* a 100 kyr sawtooth in CO₂) can replicate 100 kyr glacial cycles, but such models merely shift the question from “*why do we have 100 kyr cycles in ice volume?*” to “*why do we have 100 kyr cycles in CO₂?*”. Therefore to explain glacial cycles we must explain how insolation changes cause the Earth system to respond with a 100 kyr variation in atmospheric CO₂ concentration.

For volcanic variability, we covered the McKenzie equations, a set of conservation equations applicable to mantle dynamics, and discussed some of the constitutive relation-

⁶This is, of course, not the only glacial series that has occurred. There are seven identified sets of strong glacial activity in the Earth’s history: Quaternary, Karoo, Andean-Saharan, Ediacaran, Cryogenian, Huronian, Pongola. However this thesis only focuses on the most recent, Quaternary, glacial series. Given that we don’t fully understand this glacial — for which we have good data — trying to interpret glacial epochs for which we have little data would be over-reaching.

ships that must be applied to make these equations solvable. Using simplified versions of the McKenzie equations, we looked at the leading-order behaviour governing mid-ocean ridges (MOR) and arc volcanism.

The subsequent chapters build on this foundational knowledge. Chapter 2 quantifies the variations in MOR CO_2 caused by glacially-driven sea level change, providing estimates of both their magnitude and the lag period between sea-level and the consequent CO_2 change. Chapter 3 develops a million-year climate model that calculates the Earth's glacial state under insolation forcing, physically modelling the response of (and interactions between) Earth's temperature, ice sheets, and atmospheric CO_2 concentrations.

Chapter 2

MOR CO₂ Emissions Modulated by Glacial Cycles

This chapter is based on the published paper:

“ J.M.A. Burley & R. F. Katz. Variations in Mid-Ocean Ridge CO₂ Emissions Driven by Glacial Cycles. *Earth and Planetary Science Letters* 2015.”

Whilst the underlying model is the same as in the published paper, there are changes throughout this chapter to improve readability and provide clarification of points that were not possible in the tight word limit of *EPSL*.

An extra appendix section has been added to discuss the degree of melting, plots have been extended to cover higher mantle permeability, new plots added to illustrate important behaviours, and discussion considers the original paper's assumptions and results in light of subsequent publications. Fortunately, the assumptions made in the paper have been supported by subsequent results.

Table 2.1: Glossary of key diagnostics in this chapter.

Variable	Units	Definition
Local		
$\mathcal{E}_{\text{CO}_2}$	MtCO ₂ /yr per m	MOR CO ₂ emissions rate per metre of ridge (with a particular spreading rate)
$\bar{\mathcal{E}}_{\text{CO}_2}$	MtCO ₂ /yr per m	Baseline MOR CO ₂ emissions rate; the CO ₂ flux rate in the absence of sea level change.
E_{CO_2}	%	Percentage change in MOR CO ₂ emissions for a ridge (with a particular spreading rate)
Global		
$\mathcal{G}_{\text{CO}_2}$	MtCO ₂ /yr	Global MOR CO ₂ emissions
$\bar{\mathcal{G}}_{\text{CO}_2}$	MtCO ₂ /yr	Baseline global MOR CO ₂ emissions.

2.1 Introduction

Glacial cycles transfer $\sim 5 \times 10^{19}$ kg of water between the oceans and ice sheets [Tushingham and Peltier, 1991], leading to accumulation and ablation of kilometres of ice on the continents and sea-level change of ~ 100 m. In Iceland, for example, the pressure change associated with melting of the ice sheet since the last glacial maximum had well-documented consequences for the volcanic activity [Sigvaldason et al., 1992, Jull and McKenzie, 1996, Maclennan et al., 2002] and lava geochemistry [Maclennan et al., 2002]. More broadly, continental volcanism in both the northern and southern hemispheres shows increased activity associated with the last deglaciation [Gardeweg et al., 1998, Jellinek et al., 2004, Huybers and Langmuir, 2009]. Huybers and Langmuir [2009] and Lund and Asimow [2011] hypothesised that the pressure variations caused by changing sea level during glacial cycles would affect mid-ocean ridge (MOR) volcanism. Crowley et al. [2015a] documented variations of bathymetry near the Australian-Antarctic ridge that are possible evidence of such glacial effects changing the volume of melt emitted at MORs.

A simple argument shows that variations in crustal thickness and sea-floor relief should be expected to result from sea-level variation. The melting rate of a parcel of mantle beneath a MOR is proportional to its depressurisation rate. As the parcel upwells, it depressurises due to the decreasing height of rock above it. The rate of change of pressure due to upwelling is the gravitational acceleration g times the mantle density times the upwelling rate (~ 3 cm/yr). Sea-level variation can modify this depressurisation rate: the pressure change due to varying sea level is the product of g , water density and the

rate of change of sea level (up to 100 m in 10 kyr or 1 cm/yr). Water is about one third the density of the mantle and sea-level changes can be equivalent to one third the mantle upwelling rate, implying that sea-level changes can modify depressurisation rates, and hence melting rates, by up to $\pm 10\%$. [Crowley et al. \[2015a\]](#) apply a paleo-sea-level reconstruction to a simulation of MOR melting and melt transport, with melting rates varying according to the variable pressure exerted by sea level. This leads to varying melt flux at the ridge, predicting variations in crustal thickness consistent with bathymetric observations of sea-floor relief.

Given this evidence for glacial cycles affecting MOR melt production, it is reasonable to consider if, as in Iceland [[MacLennan et al., 2002](#)], the chemistry of the lavas is also affected. To investigate this we develop a model of the transport of a highly incompatible element from the asthenosphere through the melting region to the MOR. Highly incompatible elements partition strongly into the melt, rather than remaining in the residual solid. Approximating this as complete incompatibility creates useful simplifications in modelling. For instance, a completely incompatible element's path through the melting region is entirely determined by the motion of the melt, without any need to consider that element in the solid or partitioning between phases. Furthermore, for small perturbations to the melting rate (such as those caused by sea-level change) the mass-flow rate of the element through the MOR is constant (see appendix [2.A.1](#)).

In a simple model of melting beneath a mid-ocean ridge, a parcel of mantle upwells adiabatically beneath the ridge axis, cooling slightly due to its expansion. The pressure-dependent solidus temperature of that parcel decreases as it ascends; at some depth (or, equivalently, pressure), the temperature of the parcel is equal to its solidus temperature. This depth, thought to be around 60 km, is called the depth of first silicate melting. With further upwelling, the parcel's temperature exceeds the solidus and it partially melts. As soon as the first increment of melt is produced, 100% of the completely incompatible element that was locally present in the solid mantle is transferred to the melt. Because the mantle is permeable and the melt is less dense than the residue, the melt ascends faster than the solid, segregating from its source. Melt segregation and transport of incompatible elements thus begins at a pressure-dependent depth. More specifically, melt

segregation begins at a fixed pressure, but the depth corresponding to this pressure can change.

Variations in sea level cause pressure changes in the mantle and, therefore, will cause the depth of first silicate melting (and initiation of melt segregation) to rise and fall. The rate at which mantle crosses this melt-segregation-boundary and delivers its content of incompatible elements to the melting region is the mantle upwelling rate minus the rate of upward motion of the boundary. We assume that there is no isostatic rebound associated with sea-level change and hence the mantle upwelling rate is constant. So in this model, variations in the depth of first silicate melting cause variations in the flux of an incompatible element. For example: as sea level falls, the depth of first melting increases, upwelling mantle crosses into the melting region faster, and the flux of incompatible element increases; the reverse is true for sea-level rise. Any perturbation to the melting rate within the melting region does not alter the mass of the incompatible element in the melt, it only dilutes (or concentrates) the element. Variations in melt-transport-rate associated with melting perturbations are a secondary effect and are not considered in detail here (though see appendix 2.A.1).

A more nuanced view of melting may disagree with this simple story in some of the details, especially with the inclusion of volatile elements that are present in small concentrations in the mantle. Experimental evidence suggests that CO₂-rich melt forms at ~ 250 km depth [Dasgupta et al., 2013] and has a low viscosity that rises sharply with silica content [Kono et al., 2014]. If such carbon-rich melts can segregate from the solid mantle it would complicate the role of the transition to silicate melting at around 60 km. However, it remains an open question whether oxygen fugacity allows such melts to form and, if they do form, whether such tiny melt fractions can segregate from the solid mantle. Dasgupta et al. [2013] suggests carbonatite melt fractions reach ~ 0.03 wt% deep in the mantle below ridges, which is at the lowest limit of carbonatite melt interconnectivity of 0.03–0.07 wt% in ~ 0.05 mm olivine grains [Minarik and Watson, 1995]. The additional presence of water might increase the melt fraction to 0.06–0.1 wt% [Dasgupta et al., 2013] by 150 km depth, but the threshold for interconnectivity of such melts is not known. In our calculations, we assume that these melt fractions do not segregate from the solid

mantle until the onset of volatile-free peridotite melting at ~ 60 km raises the melt fraction, creating an interconnected, permeable network of pores.

Among the highly incompatible elements, we focus on carbon despite its active role in the thermodynamics of melt production because variations in CO_2 emissions from the solid Earth are potentially important to understanding past variation of the climate. The solid Earth contains 10^{10} – 10^{11} Mt carbon [Dasgupta and Hirschmann, 2010], orders of magnitude more than the atmosphere (0.6×10^6 MtC [Solomon et al., 2007]) and the oceans (4×10^7 MtC [Solomon et al., 2007]). Solid-Earth carbon emissions from MORs are estimated as ~ 25 MtC/yr [Coltice et al., 2004, Cartigny et al., 2008, Marty and Tolstikhin, 1998] and from arc volcanoes ~ 20 MtC/yr [Coltice et al., 2004]. As the largest reservoir, the solid Earth’s carbon budget is known to control atmospheric carbon on multi-Myr timescales; geological ages show a correlation between volcanic activity and atmospheric CO_2 concentration [Budyko et al., 1987]. Hence there is evidence for both MOR volcanism being affected by glacial cycles and for the effect of volcanic CO_2 emissions on atmospheric CO_2 concentration. While we focus on CO_2 in our model, the same theory applies equally to other highly incompatible elements such as U, Th, Nb, Ba, and Rb.

The model is developed under the guiding principle that it should be simple enough that the connections between the assumptions and the outputs are readily traceable. The full model is assembled from independent, decoupled parts that capture the key physics with minimal complexity. Mantle flow is modelled by the passively-driven corner-flow solution [Batchelor, 1967, Spiegelman and McKenzie, 1987]; lithospheric temperature structure and thickness is computed with a half-space cooling model [Turcotte and Schubert, 2002]. To quantify melt generation and transport we use one-dimensional compaction columns [Ribe, 1985b, Hewitt, 2010] that are based on conservation of energy, mass, and momentum at steady state in a homogenous, two-component mantle. The outline of the melting region is given by a parameterised solidus [Katz, 2008]. A focusing width is applied such that melt focused to the ridge produces a maximum crustal thickness of 7 km. A detailed discussion of the assumptions made in deriving the model is presented in the following sections.

To summarise the results, the model predicts that a section of MOR with a half-spreading rate at 3 cm/yr will see a change in the rate of efflux of highly incompatible elements (*e.g.*, CO₂) of $\sim 10\%$ for a linear sea-level change of 100 m in 10 kyrs. For reconstructed sea level data and the present distribution of plate spreading rates, the model predicts global MOR emissions to deviate from the mean by up to $\pm 12\%$. These results are sensitive to the permeability of the mantle, which is a primary control on the rate of melt transport. There are good constraints on how permeability scales with porosity, but its absolute value at a reference porosity (1% here) is uncertain. We consider a broad range of values that includes the most extreme estimates.

Section 2.2 details the model used to predict CO₂ emissions for a section of mid-ocean ridge; parameter values are stated in table 2.2. The behaviour of the model is demonstrated for simple scenarios of sea-level variation in sections 2.3.1–2.3.3, and the model is applied to the global MOR system under a reconstructed sea-level history in sections 2.3.4 and 2.3.5. The results are discussed in section 2.4, the key conclusions stated in section 2.5, and I consider the results in light of subsequent literature in section 2.6.

2.2 The Model

Our goal is to develop a method to compute the CO₂ emission rate $\mathcal{E}_{\text{CO}_2}$ (mass per unit time per unit length of ridge) from a segment of ridge. To achieve this we require a model of CO₂ flux into the melting region and also of its transport to the ridge. We approximate the behaviour of CO₂ as perfectly incompatible, and hence there is no exchange of CO₂ between phases during melt transport. Therefore CO₂ transfers into the melt as soon as the mantle crosses the lower boundary of the melting region, and is carried by that melt to the ridge. Melt upwelling rates are slower with increasing distance from the ridge axis, so depending upon where the CO₂ crosses the lower boundary, it will take different amounts of time to reach the ridge. Consequently, the CO₂ load arriving at the ridge at a given time t is a sum of CO₂ crossing the melt boundary at a range of previous times.

Thus the rate of ridge emission of CO₂ can be quantified by integrating the mass flux into the base of the melting region f_{CO_2} (mass per cross-sectional-area per time) and using

the travel time from the base of the melting region to the ridge. This is formulated as

$$\mathcal{E}_{\text{CO}_2}(t) = 2 \int_0^{x_f} f_{\text{CO}_2}(t_s, x, U_0) dx \quad , \quad (2.1)$$

where x is the horizontal distance from the ridge axis, x_f is the maximum distance over which melt is focused to the ridge axis, U_0 is the half-spreading rate, and t is time. A parcel of melt arriving at the ridge axis at time t was produced by mantle that crossed into the melting region at time t_s . The travel time of melt from the base of the melting region to the ridge is represented as τ , which varies with lateral distance x from the ridge axis. Hence the source time is $t_s(x) = t - \tau(x)$. The factor of two in eqn. (2.1) arises from the symmetry of the melting region across the ridge axis, a sketch of half the melting region is shown in figure 2.1.

Solving equation (2.1) ultimately requires equations (dependent on only x and t) defining mantle upwelling rate, the shape of the melting region and the travel time of melt through the melting region. We define these equations below.

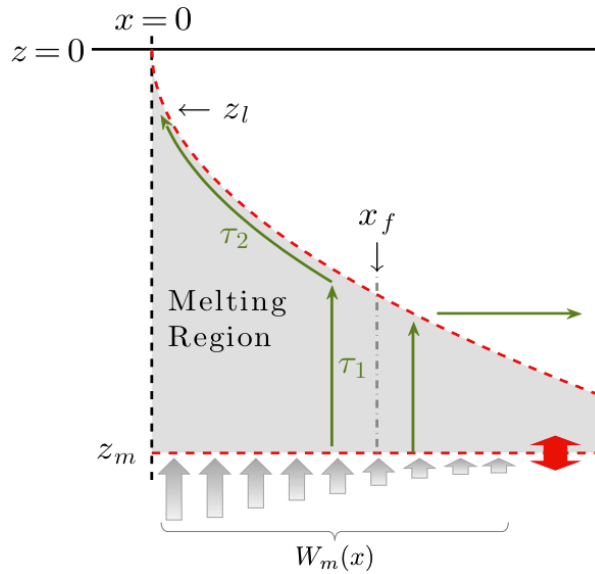


Figure 2.1: Sketch of the melting region. Two example melt streamlines are shown in green. Mantle upwelling rate into the base of the melting region W_m is represented by grey arrows, the size of which shows the decreasing magnitude of W_m with distance from the ridge axis. The red arrow indicates the variability of z_m with respect to time, expressed in equation (2.6) (all other boundaries are steady state). The melt streamlines on either side of the maximum focusing distance x_f show melt flow to the ridge or frozen into the lithosphere.

Equation (2.1) requires an expression for f_{CO_2} . This is a product of the rate at which mantle material crosses the depth of first silicate melting z_m and the CO_2 concentration in

that material. For generality, we consider an expression that allows for volatile-enriched incipient partial melting beneath the depth of first silicate melting, though we will later exclude this scenario from consideration. Thus, f_{CO_2} is written as

$$f_{\text{CO}_2}(t_s, x, U_0) = \left(W_m(x, U_0) - \frac{dz_m(t_s)}{dt} \right) (1 - \phi) \mathcal{C}_{\text{CO}_2}^{\text{solid}} + \left(w_m - \frac{dz_m(t_s)}{dt} \right) \phi \mathcal{C}_{\text{CO}_2}^{\text{melt}}, \quad (2.2)$$

where $W_m(x, U_0)$ is the upwelling rate of the mantle, w_m is the upwelling rate of incipient melt, $\mathcal{C}_{\text{CO}_2}$ is a mass concentration of CO₂, and ϕ is the volume fraction of melt; all of these are evaluated at depth z_m and distance x from the ridge axis. The first term in parentheses on the right-hand side of the equation is the rate at which mantle crosses into the melting region. The concentrations and melt fraction may be considered steady-state, constant values as long as the rate at which material crosses the depth of first silicate melting is always positive or zero; specifically $w_m \geq W_m \geq \max(\dot{z}_m(t))$. Even the fastest sea-level changes on record, meltwater pulses during the last deglaciation, satisfy these conditions for most MORs: 20 m sea level change in 500 years gives $\dot{z}_m = 1.3$ cm/yr. However, meltwater pulse events are not resolved in the reconstructed sea-level series that we consider in this paper [Siddall et al., 2010], so the conditions $w_m \geq W_m \geq \max(\dot{z}_m(t))$ are true with only occasional exceptions for the slowest spreading ridges. With these conditions satisfied and assuming that either $\phi(z_m) = 0$ or that $w_m = W_m$, equation (2.2) can be simplified to

$$f_{\text{CO}_2}(t_s, x, U_0) = \left(W_m(x, U_0) - \frac{dz_m(t_s)}{dt} \right) \mathcal{C}_{\text{CO}_2}. \quad (2.3)$$

Here we should interpret $\mathcal{C}_{\text{CO}_2}$ as the mass concentration of CO₂ in the solid mantle plus co-moving incipient melt, if it is present.

The flux of CO₂ in equation (2.3) depends on the solid mantle upwelling rate at the depth of first silicate melting. Approximating this as passive (plate-driven) flow of isoviscous rock, mantle upwelling is given by the corner flow solution [Batchelor, 1967, Spiegelman and McKenzie, 1987]. The vertical component of this solution, evaluated at

$z = z_m$, can be written as

$$W_m(x, U_0) = \frac{2U_0}{\pi - 2\alpha_c - \sin 2\alpha_c} \left(\frac{1}{1 + \frac{x^2}{z_m^2}} - \sin^2(\alpha_c) \right), \quad (2.4)$$

where the lithosphere is represented as a wedge with angle α_c to the horizontal. We follow Spiegelman and McKenzie [1987] in computing the wedge angle to approximately match the plate thickness at a specified distance from the axis. We define this angle such that the wedge intersects the upper boundary of the melting region z_l at the maximum width of melting region x_w ; $\alpha_c = \tan^{-1}(z_l/x_w)$; see appendix 2.A.4 for details. This definition of the wedge angle ensures that the lithospheric wedge does not overlap with the melting region, and that the upwelling rate is small but non-zero at the extreme width of the melting region ($0 \leq W_m(x_w) \ll U_0$).

An expression for the depth of first melting z_m is needed in equations (2.3) and (2.4). Taking decompression as the only influence on local mantle temperature prior to melting, we model the depth of first melting as the intersection between an adiabatic temperature profile and the solidus temperature profile. We approximate both profiles as linear with respect to depth (details in appendix 2.A.2) to obtain

$$z_m = - \left(\frac{\tilde{T} - T_{S_{\text{ref}}}}{\gamma\rho g - \frac{\alpha g \tilde{T}}{c}} \right) + \frac{\rho_w}{\rho} S, \quad (2.5)$$

where \tilde{T} is the mantle potential temperature, $T_{S_{\text{ref}}}$ is the solidus temperature at reference mantle composition and surface pressure, γ is the Clausius-Clapeyron slope for the mantle, ρ is the mantle density, α is the coefficient of thermal expansion, c is the specific heat capacity, S is the sea-level deviation from a long-term mean, and ρ_w is the density of water. The first term in equation (2.5) is the dry peridotite melting depth of $\simeq 60$ km, and the second term is the shift in melting depth due to sea-level. The only time-dependent variable in equation (2.5) is the sea level S , so differentiating gives

$$\frac{dz_m}{dt} = \frac{\rho_w}{\rho} \frac{dS}{dt}. \quad (2.6)$$

Equations (2.5) and (2.6) collectively state that silicate melting begins at a fixed pressure,

but the depth corresponding to this pressure varies as sea level rises and falls: $\Delta z_m = \frac{\rho_w}{\rho} \Delta S$.

The source time t_s used in equations (2.1) and (2.3) depends on the travel time of melt to the ridge from any point x along the base of the melting region. For simplicity, we consider melt flow as following a vertical path from the base to the top of the melting region, then following a high porosity channel along the impermeable top of the melting region to the ridge axis, as illustrated by streamlines τ_1 and τ_2 in figure 2.1. This is a reasonable approximation of numerically modelled streamlines for homogenous mantle [*e.g.*, Katz, 2008], where buoyancy forces drive vertical fluid flow in the majority of the melting region, with the compaction pressure only becoming large enough to deflect melt flow from the vertical within a few kilometres of melt-impermeable boundaries [Sparks and Parmentier, 1991]. We consider flow along the high porosity channel as instantaneous, motivated by the high flow rates expected there, as compared to vertical flow rates in the rest of the melting region [Katz, 2008]. To compute the travel time from the base of the melting region to the base of the lithosphere, we use a 1D compaction column from Hewitt [2010]. This model assumes Darcy flow and thermodynamic equilibrium for a two-component, homogenous mantle with a constant Clausius-Clapeyron slope. Following the reduced model of Crowley et al. [2015a], we assume that small variations in melting rates due to sea-level change do not significantly affect melt velocity or travel time. Furthermore, in computing τ we take z_m as constant, because changes in z_m due to sea level are only tens of metres, changing τ by $\ll 1\%$. This gives a travel time

$$\tau(W_m, z_t, z_m) = \phi_0 \left(\frac{\eta_f}{K_0 \Delta \rho g} \right)^{\frac{1}{n}} \left(\frac{\rho}{\Pi W_m} \right)^{1 - \frac{1}{n}} \left[n (z_t - z_m)^{\frac{1}{n}} \right], \quad (2.7)$$

where η_f is the mantle melt viscosity, K_0 is the permeability of the mantle at the 1% reference porosity ϕ_0 , $\Delta \rho$ is the density difference between the solid and melt, n is the porosity exponent in the permeability relation ($n \approx 2.7 \sim 3$, Miller et al. [2014]), $z_t(x, U_0)$ is the depth of the upper boundary of the melting region, and Π is the adiabatic melt productivity (kg of melt produced per m³ per m upwelling). This productivity is given by Hewitt [2010] as a ratio of thermodynamic parameters, and we retain the same parameter values here.

To close the model we need an expression for the upper boundary of the melting region $z_l(x)$. This boundary is located where the local temperature equals the solidus temperature, which is controlled by the thickness of the conductively cooled boundary layer that forms the lithosphere. [Crowley et al. \[2015a\]](#) also included the effects of adiabatic decompression and latent heat removal, but this leads to an expression for $x_l(z)$ that cannot be inverted. However, as shown in appendix [2.A.3](#), the depth of this melting boundary is approximated by an isotherm of the half-space cooling model, which can be expressed as $z_l(x)$. This isotherm is hotter than the low-pressure solidus, but the temperature difference compensates for the change in solidus temperature with respect to depth. We use

$$z_l(x, U_0) = 2\sqrt{\frac{\kappa x}{U_0}} \operatorname{erfc}^{-1} \left(\frac{\tilde{T} - T_l}{\tilde{T} - T_0} \right), \quad (2.8)$$

where T_l is the temperature of the upper boundary of melting region, assumed to be constant. T_0 is the temperature of the ocean floor, and κ is the thermal diffusivity of the mantle. Note that although we have neglected adiabatic decompression and latent heat of melting in equation [\(2.8\)](#), these are accounted for in the melting calculations.

Parameter	Value		Parameter description
c	1200	J/kg/K	Specific heat
$\mathcal{C}_{\text{CO}_2}$	0.645	kg/m ³	CO ₂ mass per m ³ of mantle (derived from 215ppm by weight)
dF/dz	0.0037	km ⁻¹	Rate of change of melt fraction with depth.
g	10	m/s ²	Gravitational acceleration
K_0	10 ⁻¹³ –10 ⁻¹¹	m ²	Permeability at 1% porosity
K	$K_0(\phi/\phi_0)^n$	m ²	Permeability
L	4×10^5	J/kg	Latent heat of the mantle
L_{MOR}	61 000	km	Total length of the mid-ocean ridge system
n	3	-	Porosity exponent in the permeability relation
S	[various]	m	Sea level, stated as deviation from long-term mean
\dot{S}	[various]	cm/yr	Rate-of-change-of-sea-level with respect to time
\tilde{T}	1648	K	Potential temperature of the mantle
T_0	273	K	Ocean floor temperature
T_{sref}	1554	K	Reference solidus temperature
U_0	≤ 8	cm/yr	Plate half-spreading rate
x_f	10–70	km	Width of region, at z_m , from which melt is focused to the ridge
x_w	10–350	km	Width of melting region
z_m	60	km	Depth of first melting
α	3×10^{-5}	K ⁻¹	Thermal expansion coefficient for the mantle
γ	60×10^{-9}	K/Pa	Clausius-Clapeyron slope of the mantle
η_f	1	Pa s	Mantle melt viscosity
κ	10 ⁻⁶	m ² /s	Thermal diffusivity
Π	0.01	kg/m ⁴	Adiabatic melt productivity, kg of melt per m ³ of mantle per metre of upwelling
ρ	3300	kg/m ³	Mantle density
ρ_c	2900	kg/m ³	Oceanic crust (mean) density
ρ_w	1000	kg/m ³	Freshwater density
$\Delta\rho$	500	kg/m ³	Density difference between liquid and solid mantle
ϕ_0	0.01	-	Reference porosity (volume fraction)

Table 2.2: Parameter values for calculations.

2.3 Results

Below we demonstrate the behaviour of the model by a series of examples, then consider global CO₂ emissions for reconstructed sea level. We begin by modelling a unit length of mid-ocean ridge in the absence of sea-level change. This defines the baseline state of the model that we compare against when applying sea-level forcing. The first dynamic example is a single, linear sea-level change, which illustrates key characteristics of the model and emphasises the importance of the melt travel time. The emissions curve for

this example approximates the Green’s function for the model: the response to a step-change in sea level. We next consider simple, periodic sea level curves, demonstrating the system’s response to an oscillatory forcing as a function of the frequency of that forcing. We then compute the model’s response to a reconstructed Pleistocene sea-level record.

Building on these calculations for a single section of mid-ocean ridge, we calculate predictions for a global model, created by summing sections with appropriate spreading rates over the full MOR system. We demonstrate this composite model by considering the global emissions response to a single sea-level change and then to the reconstructed Pleistocene sea-level curve. The global response to a single sea-level change gives us a Green’s function that is the basis for MOR CO₂ emissions in the Earth system model I build in the next chapter.

2.3.1 Constant Sea Level & Baseline Emissions

Baseline emissions $\bar{\mathcal{E}}_{\text{CO}_2}$ are defined as the steady-state emission rate of CO₂ from the MOR for constant sea level. This represents the background state, which is disturbed after sea-level change.

Figure 2.2 shows baseline emissions as a function of plate spreading rate and demonstrates that, in the absence of changing sea level, CO₂ emissions per metre of ridge are approximately proportional to the half-spreading rate U_0 . A faster spreading rate drives faster mantle upwelling, bringing more CO₂ into the melting region. Faster spreading rates also increase the width of the melting region (see supporting material 2.A.4), leading to more melt and more CO₂ being focused to the ridge axis. However, not all melt produced is focused to the MOR; at some lateral distance, melts are frozen back into the lithosphere, rather than travelling to the ridge axis [e.g., Katz, 2008]. We incorporate this detail by enforcing a maximum focusing width x_f such that melt focused to the MOR will produce crust ≤ 7 km thick in steady state, consistent with observations [White et al., 1992, Bown and White, 1994]. Crustal thickness is calculated as the volume flow rate of melt to the ridge axis (m³ per metre along MOR axis) times the density ratio of basaltic melt to oceanic crust, divided by the half-spreading rate. At half-rates $U_0 \geq 1$ cm/yr, the focusing width is smaller than the width of the melting region. With the imposition of

this limit on melt focusing, there is a slight change in the slope of the baseline emission curve at $U_0 = 1$ cm/yr (fig. 2.2a)¹

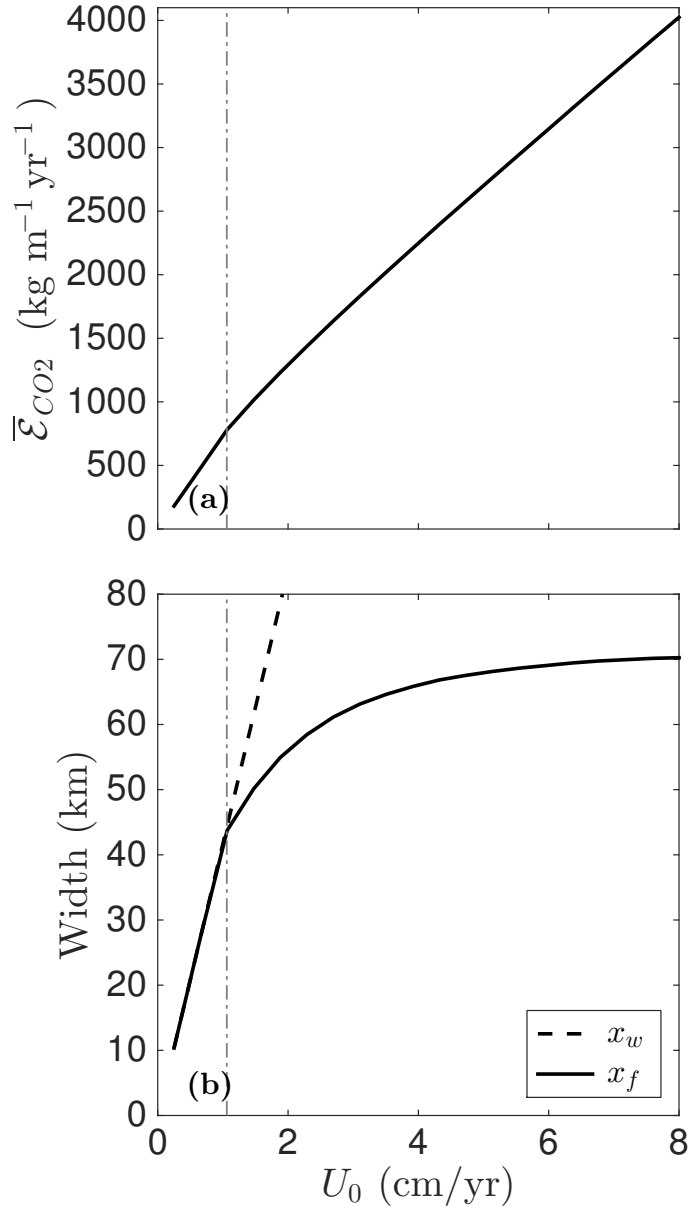


Figure 2.2: (a) Ridge CO₂ emissions for constant sea level $\bar{\mathcal{E}}_{CO_2}$, and (b) focusing width x_f and full width x_w of the melting region; all shown for varying half-spreading rate. Focusing width is equal to the width of the melting region when crustal thickness is less than 7 km ($U_0 \leq 1$ cm/yr), and is otherwise limited such that crustal thickness does not exceed 7 km. The switch between these behaviours is marked by the grey dotted line at 1 cm/yr. \mathcal{E}_{CO_2} is computed with CO₂ concentration in the mantle of 215 ppmw.

For the range of U_0 on Earth of up to 8 cm/yr, figure 2.2(a) shows baseline emissions of up to 4000 kg m⁻¹ yr⁻¹. This is calculated using 0.65 kg CO₂ per m³ of upwelling mantle (215 ppm CO₂ by weight, hereafter ppmw).

The average concentration of CO₂ in MOR source mantle \mathcal{C}_{CO_2} is generally stated as 50-200 ppmw [to one standard deviation, *e.g.* Dasgupta, 2013, Cartigny et al., 2008, Saal et al., 2002b, Marty and Tolstikhin, 1998, Salters and Stracke, 2004]. These source mantle CO₂ concentrations are inferred by four methods: (i) Cartigny et al. [2008] start

¹This model system makes interesting predictions about the degree of melting at MOR, which is discussed in supporting material 2.A.5

with Nb concentration in MOR basalts (MORB), use Nb/C ratios, and assume an average degree of melting to calculate a CO₂ concentration in the source mantle. (ii) Saal et al. [2002b] use MORB melt inclusions to measure CO₂ concentrations in the erupting mantle immediately prior to degassing, then assume an average degree of melting to calculate a CO₂ concentration in the source mantle. (iii) Marty and Tolstikhin [1998] use ³He concentrations in the ocean to infer a ³He efflux from MORs. Then they apply a He/C ratio to estimate carbon efflux from MORs, which is matched to a CO₂ concentration in the erupting mantle using a (completely degassed) crustal formation rate of 21 km³/yr. CO₂ in the source mantle is then calculated by assuming an average degree of melting to generate MORB. (iv) Salters and Stracke [2004] start from major elements in the mantle and use a chain of element ratios to derive a CO₂ concentration in the depleted mantle. For all these approaches, CO₂ concentration in the mantle is derived using several assumptions and has large uncertainties. The global MOR efflux of CO₂ is calculated using fewer assumptions and has less uncertainty.

Therefore I choose to state the results in this chapter based on matching this model to the global MOR efflux of CO₂, requiring a concentration of CO₂ in the source mantle of 215 ppmw (section 2.3.5). This is effectively substituting our average degree of melting into other's calculations, and gives a result slightly higher than prior estimates of $\mathcal{C}_{\text{CO}_2}$ (for a details, see section 2.A.5). For simplicity, we use the 215 ppmw $\mathcal{C}_{\text{CO}_2}$ throughout this chapter, but restate key results for the 125 ppmw value. This changes CO₂ emissions by a factor of 1.7, as emissions scale linearly with $\mathcal{C}_{\text{CO}_2}$ (see eqn.(2.3)).

Subsequent sections present scenarios of changing sea-level. In these sections, plots depict emissions in terms of percentage difference from baseline emissions for the appropriate half-spreading rate; these percentage values apply to all highly incompatible elements and for any $\mathcal{C}_{\text{CO}_2}$. This is calculated as

$$\begin{aligned} E_{\text{CO}_2}(t) &= \frac{\mathcal{E}_{\text{CO}_2} - \bar{\mathcal{E}}_{\text{CO}_2}}{\bar{\mathcal{E}}_{\text{CO}_2}} , \\ &= \frac{\int -\dot{z}_m(t_s) dx}{\int W_m dx} . \end{aligned} \quad (2.9)$$

Percentage results can be converted to CO₂ mass by multiplying with the appropriate

baseline emissions from figure 2.2. The deviations from the baseline emission rate are a consequence of non-zero \dot{z}_m in equation (2.3). By definition, total emissions are equal to this deviation summed with baseline emissions.

2.3.2 Single Sudden Change in Sea Level

Imposition of a sudden sea-level change exposes the behaviour of the model. We use a steep, linear ramp, which gives a box function in \dot{S} . We will investigate the temporal response in MOR CO₂ emissions rate, and the total CO₂ mass emitted, explaining the processes driving each of these behaviours.

2.3.2.1 Emissions Rate Response

Figure 2.3 shows the predicted MOR CO₂ emission rate E_{CO_2} resulting from this sea level forcing. CO₂ emissions remain at the baseline level for ~ 90 kyrs after the change in sea level and then there is a sharp rise in E_{CO_2} , representing an 8% increase in emission rate. This delayed response is due to the travel time of CO₂ from the base of the melting region to the ridge. After the 8% peak, E_{CO_2} falls sharply to about 3%, followed by a slow decay until 130 kyrs, after which there is a linear drop back to the baseline level over the duration of the box-pulse in \dot{S} . The origin of this emissions pattern in figure 2.3(c) is explored in figure 2.4.

Figure 2.4 demonstrates how the shape of the emission response curve in figure 2.3(c) is a consequence of the travel time τ and its variation with respect to distance x from the ridge axis. This travel time, shown in figure 2.4(c), ranges between τ_{min} for melts originating in the mantle beneath the ridge axis and τ_{max} for distal melts that are focused laterally. The mixture of melts that arrives at the ridge at time t contains CO₂ that was transported in melts that initiated along the base of the melting region at all $x < x_f$. These deep melts formed and began to segregate from their source at times in the past $t - \tau(x)$. The CO₂ content of the segregated melt is different to the baseline case according to the \dot{S} value at $t - \tau(x)$. Therefore, we can calculate the deviation from the baseline by considering the rate of sea-level change (alternatively, \dot{z}_m) acting on the melting region when each element of melt first segregated. This is represented in figure 2.4(c), and the

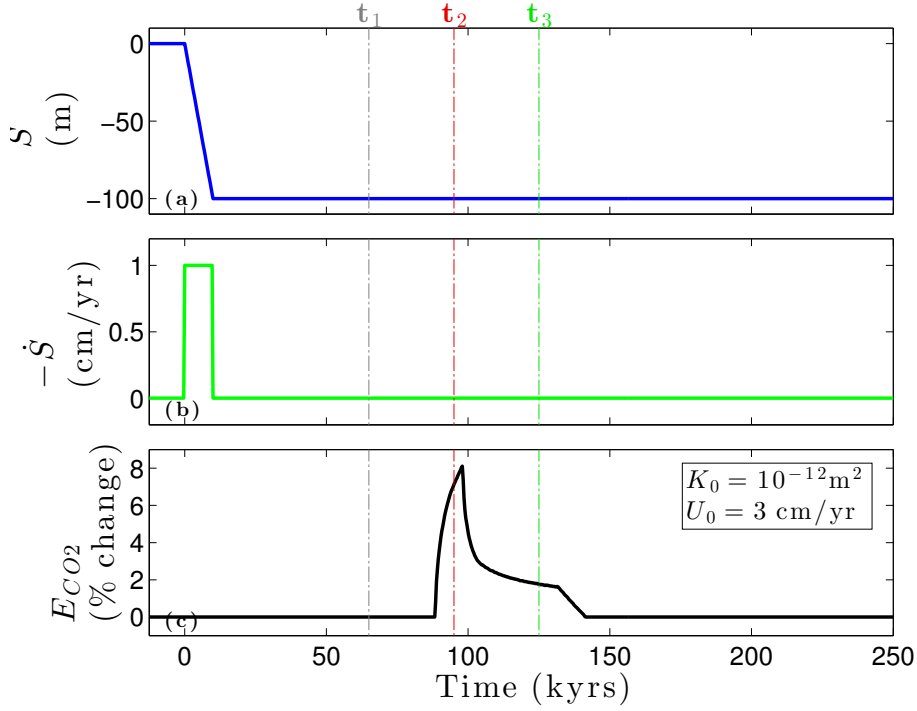


Figure 2.3: Single step change in sea level. Plots show (a) sea-level change, (b) the negative rate of sea-level change, and (c) CO₂ emissions from a section of mid-ocean ridge, measured as percentage change from baseline emissions. The plate half-spreading rate and the permeability constant at 1% porosity are U_0 and K_0 , respectively. The three times marked on the plots correspond to (a-i,ii,iii) in figure 2.4. Negative \dot{S} is plotted so that peaks in \dot{S} and consequent peaks in E_{CO_2} point in the same direction.

integral of this plot with respect to x is directly proportional to E_{CO_2} in figure 2.3.

The E_{CO_2} response is clarified by again considering a sharp, linear drop of sea level that occurs over the interval $0 \leq t \leq 10$ kyrs. The drop in sea level causes the depth of the base of the melting region to increase, importing additional CO₂ into the melting regime. In panels (a-i), (a-ii), and (a-iii) of fig. 2.4 we see the box pulse receding into the past as time progresses over $t_1 < t_2 < t_3$ (figure 2.3c shows E_{CO_2} at these times). The start and end times of the pulse are projected onto $\tau(x)$ in panel (b). At t_1 , the projection lines do not intersect $\tau(x)$, meaning that the CO₂ perturbation generated by \dot{S} has not yet reached the ridge axis. Therefore the emissions curve in figure 2.3(c) remains at the baseline level. At t_2 , the projection lines span τ_{\min} ; the shallow slope of $\tau(x)$ near τ_{\min} means that CO₂ from a broad (30 km) region affected by the \dot{S} pulse is arriving at the ridge axis at t_2 . This causes the spike in emissions shown in figure 2.3(c). At t_3 , the interval of sea-level change has receded far into the past. The only CO₂ perturbation in melts arriving at the ridge is in distal melts from the base of the melting region at 50 to 58 km off-axis.

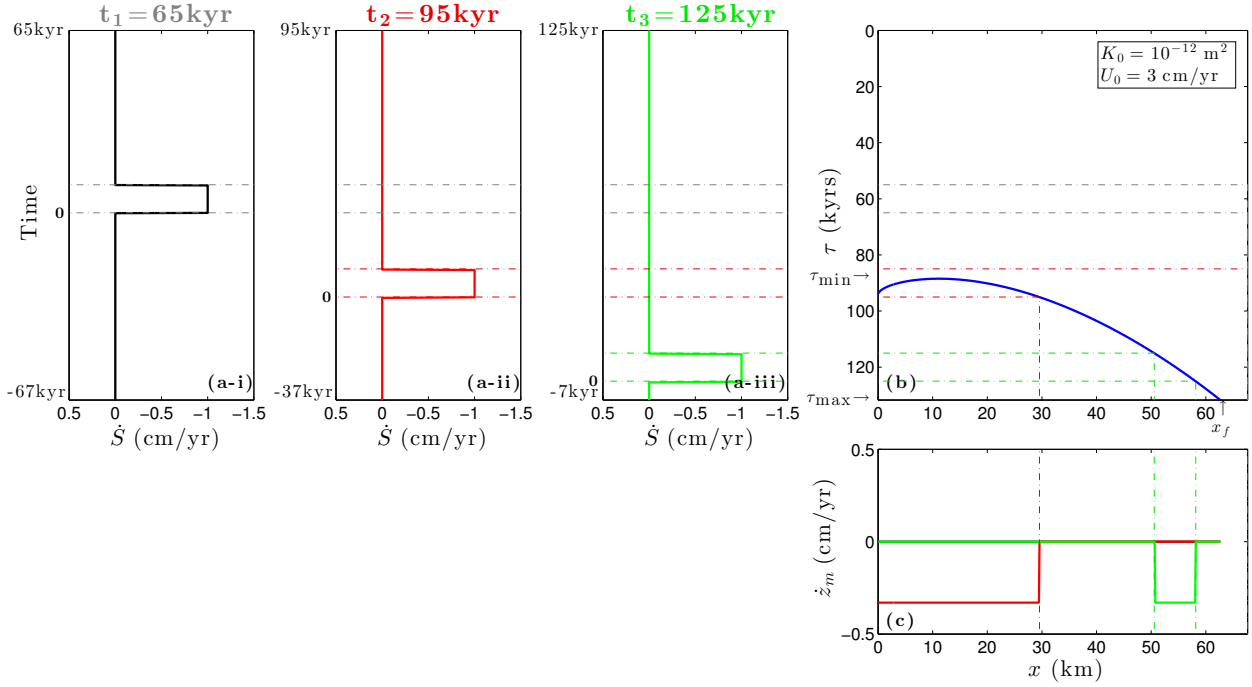


Figure 2.4: The effect of a linear change in sea level on ridge CO₂ emissions. The three points in time shown in black, red, and green show the state of the system 65, 95, and 125 kyrs after the pulse began. Plots show: **(a-i,ii,iii)** rate of sea-level change from present into the past, for the three points in time marked in figure 2.3. **(b)** Travel time of melt from the base of the melting region to the ridge, increasing downwards. Travel time at $x = 0$ is slightly greater than τ_{\min} because the sharp increase in lithospheric thickness within a few km of the ridge increases the column height; the effect of this increase in height exceeds the effect of faster on-axis upwelling. **(c)** Rate-of-change of the depth of first melting that acted on the melt currently arriving at the ridge axis, when that melt began to segregate. Dashed lines mark how the travel time converts $\dot{S}(t)$ to $\dot{z}_m(x)$. The integral of a coloured line from 0 to x_f in panel (c) is directly proportional to E_{CO_2} at the corresponding time in figure 2.3(c). This is expressed by the integral of \dot{z}_m with respect to x in equation (2.3). A video animating this plot and E_{CO_2} over time is hosted at <https://tinyurl.com/JB-EPSLvid>.

The narrowness of this band translates to a reduced (but non-zero) value of E_{CO_2} at t_3 in fig. 2.3(c). As the sea-level drop recedes further into the past, the emission rate drops to zero because the very distal melts (from $x > x_f$) are not focused to the ridge axis. This process is animated in a video hosted at <https://tinyurl.com/JB-EPSLvid>.

In the limit of vanishing duration of sea-level change, the pulse of \dot{S} approximates to a Dirac delta function. Hence the E_{CO_2} response shown in figure 2.3(c) is an approximation of the Green's function. Conceptually, the emissions response for any sea-level time series could be approximated by convolution with a Green's function approximation like figure 2.3(c).

From this discussion, it is clear that changes to $\tau(x)$ will alter how MOR emissions respond to changing sea-level. Equation (2.7) for travel time shows that plate half-spreading

rate U_0 and permeability constant K_0 are the key parameters affecting the melt travel-time τ . Higher values of either lead to shorter travel times, giving a higher peak in E_{CO_2} over a shorter time period, with this peak occurring sooner after the causative sea-level change. This is explored in more detail in section 2.3.3.

2.3.2.2 Total CO₂ Change

Whilst the focus of this chapter is elucidating how sea-level-drives change in MOR CO₂ emissions and the temporal pattern of that change, this system has a clear reservoir interpretation that can clarify the role of the MOR response to sea level in determining CO₂ mass in the atmosphere. This interpretation is useful for understanding the climate effects in later chapters, so we discuss it here in preparation

The layer of mantle near the bottom of the melting region is a reservoir that can either contain carbon (when outside of the melting region) or be depleted of carbon (when inside the melting region). The details of melt transport through the melting region complicate the picture somewhat, but ultimately we are linking a layer of mantle — that can be variably depleted in CO₂ — to the atmosphere. Change the CO₂ mass in the reservoir, and you change the mass of CO₂ in the atmosphere. This is explained below, and is illustrated in figure 2.5.

First, we approximate that the baseline MOR emissions rate of CO₂ to the atmosphere is exactly compensated by CO₂ drawdown effects². Therefore any increase or decrease in MOR CO₂ emissions changes atmospheric CO₂ mass. Considering figure 2.4 and its video, we see that the total emissions for a single change in sea level is calculated by integrating equation 2.9 over $0 < t < \tau_{\text{max}}$ and multiplying by $\bar{\mathcal{E}}_{\text{CO}_2}$.

Mathematically this integral only depends on U_0 and the total sea level change. Physically, greater sea level change causes greater change in the depth of first melting ($\Delta S = \frac{\rho_w}{\rho} \Delta z_m$) therefore increasing the thickness of the region flushed of CO₂; larger U_0 leads to a greater focusing width x_f therefore increasing the width of the region flushed of CO₂. The total emissions scale linearly with the depth and width of this flushed region,

² This approximation is justified by the long-term steady state of atmospheric CO₂ concentration over the past million years — if mean volcanic emissions were not exactly compensated, there would be a drift in mean atmospheric CO₂ concentration superimposed on the 100 kyr glacial cycle.

Figure 2.5: Single step change in sea level. Plots show (a) sea-level change, (b) the negative rate of sea-level change, and, for the range of permeabilities shown, (c) CO₂ emissions from a section of mid-ocean ridge, measured as percentage change from baseline emissions, and (d) the total excess CO₂ emitted per metre of ridge. The grey marker guides the reader to the equivalent point in figure 2.6.

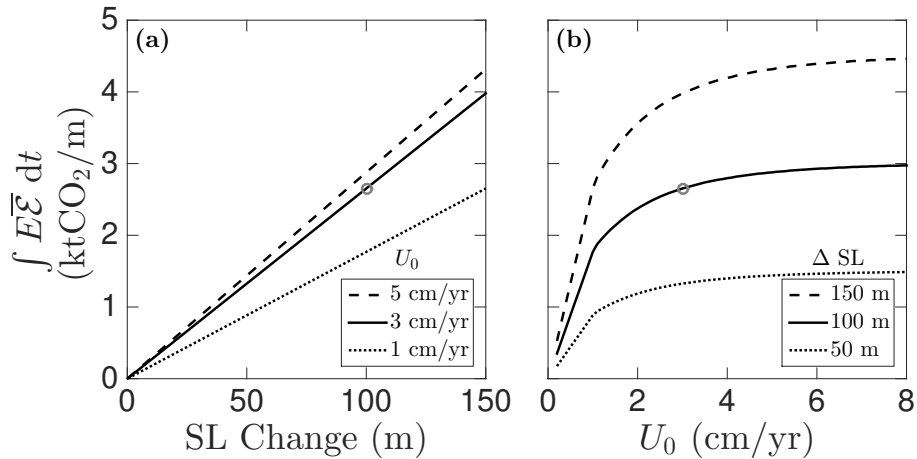
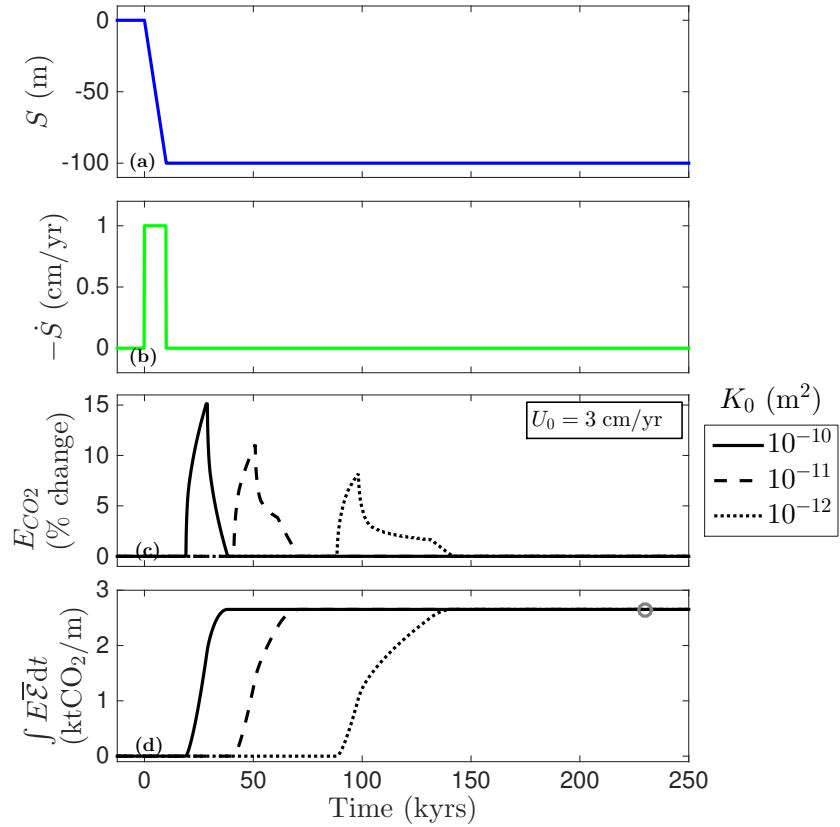


Figure 2.6: Plots show total excess CO₂ emitted per metre of ridge for a single step change in sea level across (a) varying sea-level change, and (b) varying plate spreading rate U_0 . The grey marker guides the reader to the equivalent point in figure 2.5.

thus there is a linear dependence on ΔSL and a dependence U_0 that scales like $x_f(U_0)$ in figure 2.2. These scalings are shown in figure 2.6.

Considering this framework on a global scale, as in section 2.3.5, we have a reservoir 61,000 km long, with an average width of 122 km, and a depth of approximately 30 m (depending on sea level change). Therefore the total potential size of this reservoir is 145 GtCO₂, a mass equivalent to a 19 ppmv change in atmospheric CO₂ concentration.

2.3.3 Oscillating Sea Level

We now consider oscillatory sea level and discuss the concepts of lag and admittance.

Figure 2.7 shows a pair of oscillating sea level scenarios and their predicted E_{CO_2} variation. The left column (i) shows a time series of alternating box-pulses in \dot{S} ; the right column (ii) shows a sinusoidal sea-level variation.

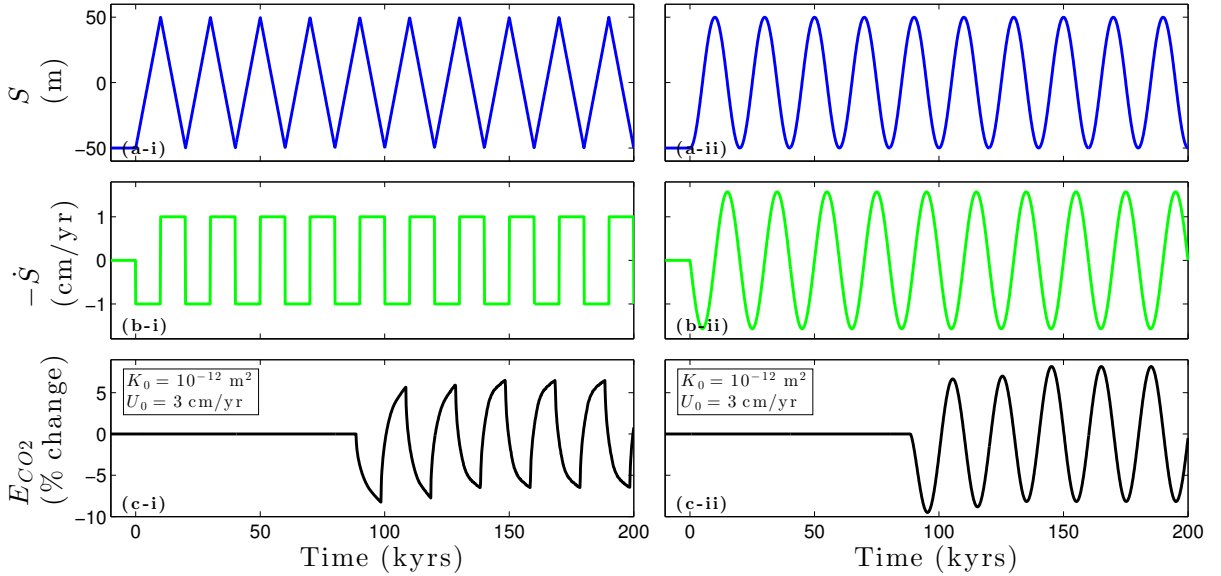


Figure 2.7: Sawtooth and sine waves in sea level starting at $t = 0$. Plots show (a) sea-level, (b) negative rate of sea-level change, (c) CO_2 emissions from a section of mid-ocean ridge. Considering the left column, each box-pulse in \dot{S} produces an emissions peak/trough as in figure 2.3(c) with interference where they overlap, giving the net result seen in (c-i). The steady upward shift in the E_{CO_2} -peaks until ~ 150 kyr is due to this overlap. If the first box-pulse in \dot{S} had been in the opposite direction, E_{CO_2} peaks in (c) would be mirrored across $E_{\text{CO}_2} = 0$.

Figure 2.7(c-i) has an oscillating series of peaks in E_{CO_2} resulting from a series of \dot{S} box-pulses in figure 2.7(b-i). This \dot{S} series is equivalent to summing single box-pulses from figure 2.3(b), with suitable offset and amplitude. Similarly, the CO_2 emissions can be represented as a sum of offset emissions spikes from single, linear changes in sea level. The train of emissions peaks in figure 2.7(c-i) and (c-ii) stabilises in amplitude after $t \approx \tau_{\text{max}}$; this transient represents the spin-up time of the model, associated with the tail of excess emissions shown in fig. 2.3.

Figure 2.7(ii) shows sinusoidal sea level and provides the context to define the lag metric. Lag \mathcal{L} is the time between a peak in \dot{S} and the corresponding peak in emissions. Because the time interval around τ_{min} kyrs before t has the largest influence on E_{CO_2} at

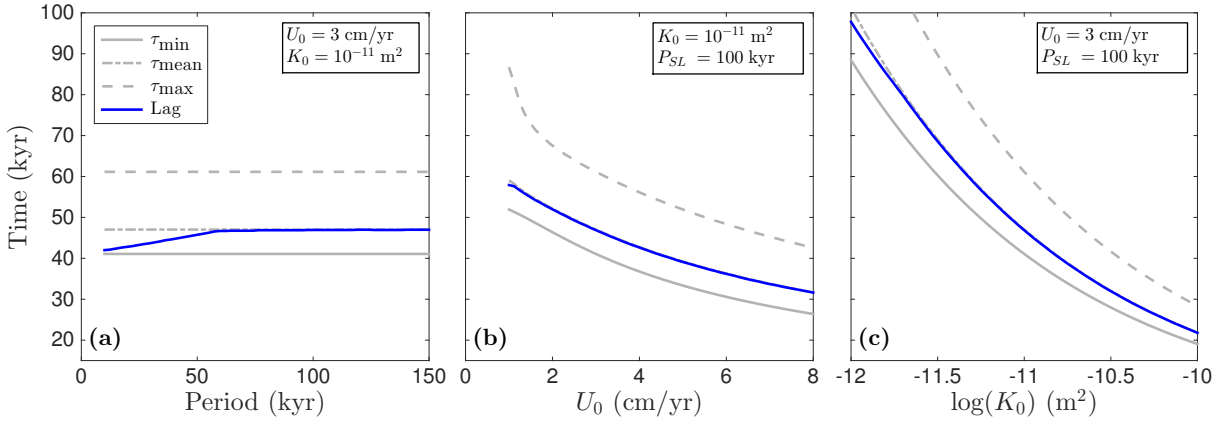


Figure 2.8: Lag and travel time for varying (a) sinusoidal sea-level period, (b) half-spreading rate, and (c) permeability constant. The lag is calculated as the time between a peak in $-\dot{S}$ and the corresponding peak in E_{CO_2} for sinusoidal sea level.

t , the E_{CO_2} signal should lag \dot{S} by about τ_{\min} . However, the lag will not be exactly τ_{\min} , as the influence of \dot{S} on E_{CO_2} is felt up to τ_{\max} years after the change in sea level. Thus the exact value of lag will be slightly greater than τ_{\min} and we expect this difference to depend on the period of sea-level oscillation relative to $\tau_{\max} - \tau_{\min}$. In particular, when the sea-level period significantly exceeds $2(\tau_{\max} - \tau_{\min})$, the lag becomes equal to the mean melt-transport time τ_{mean} . Figure 2.8 shows lag, τ_{\min} , τ_{mean} , and τ_{\max} for varying half-spreading rate, permeability constant, and sinusoidal sea-level period. We note that $\tau_{\min} \leq \mathcal{L} \leq \tau_{\text{mean}} \ll \tau_{\max}$ and therefore we assume $\mathcal{L} \approx \tau_{\min}$ with a small, systematic error.

Sinusoidal variation of sea level also provides a context in which compute admittance. Admittance is the ratio of the response amplitude to the forcing amplitude as a function of the sinusoidal forcing period. We define two versions of admittance: absolute admittance, with units of kilograms CO₂ per metre of ridge per year per 100 m of sea-level change, and relative admittance, with units of percentage change from baseline emission rate per 100 m of sea-level change. The latter is the absolute admittance divided by the baseline emission rate. Figure 2.9 shows absolute and relative admittance and how they vary with changing sea-level period, half-spreading rate, and permeability constant. We discuss both the trends and the oscillations of these curves, starting with absolute admittance.

Absolute admittance (panels (a) and (b) of figure 2.9) depends on the period of sea-level oscillation, the permeability, and to a lesser extent, on the half-spreading rate. We consider these in turn. Shorter periods of sea-level variation at constant amplitude give

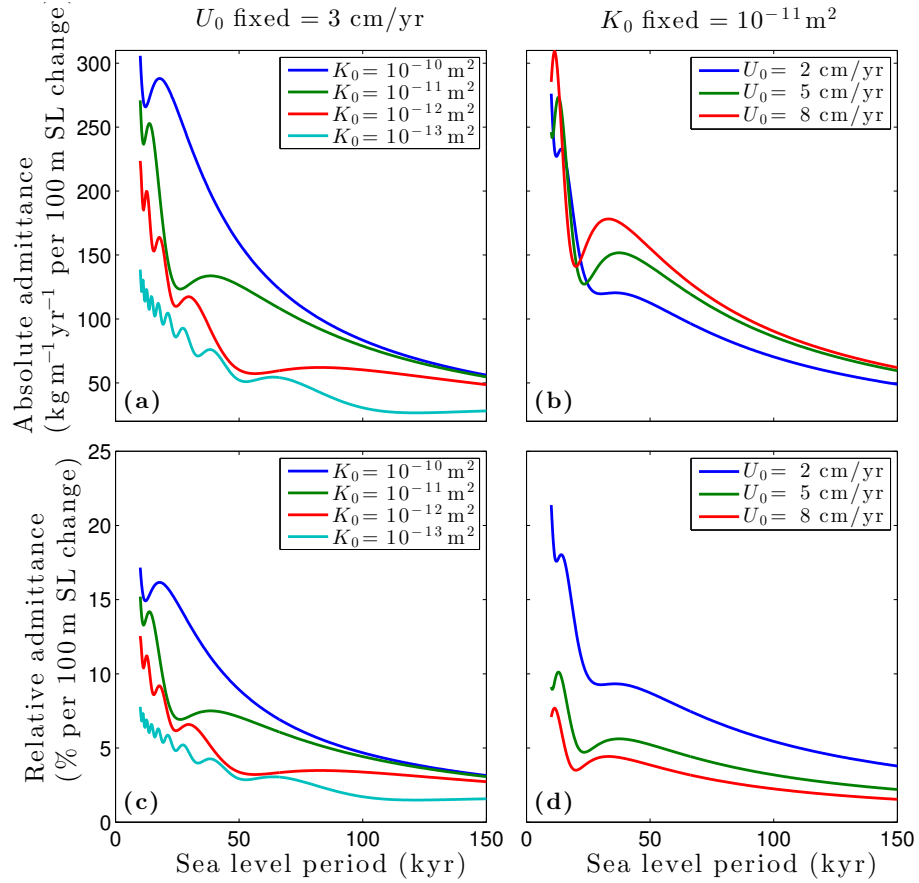


Figure 2.9: Absolute and relative admittance for varying half-spreading rate, permeability, and sinusoidal sea-level period. Plots hold either U_0 or K_0 fixed. The magnitude of sea-level change is constant for all periods.

larger values of $|\dot{S}|$ and $|\dot{z}_m|$, and hence increase the temporal variation of f_{CO_2} . This causes increased deviation of ridge emissions from baseline. Both increased spreading rate U_0 , and increased mantle permeability K_0 reduce the melt travel-time from the base of the melting region — recall that U_0 determines mantle upwelling rate W_m and equation (2.7) for melt travel-time is dependent on both K_0 and W_m . A reduced melt travel-time implies a smaller difference between τ_{max} and τ_{min} , and therefore a focusing of CO_2 from the base of the melting region to the ridge axis over a shorter interval in time.

Relative admittance is equal to the absolute admittance normalised by the baseline emissions rate. The baseline depends on half-spreading rate but not on permeability (fig. 2.2(a)). We therefore see a difference between absolute and relative admittance in figure 2.9(b) and (d). For slow-spreading ridges, which have a low baseline emissions rate, the normalised variance (and hence the relative admittance) is larger.

The oscillations superimposed on the primary admittance trend are not physically

significant, but are readily explained. They arise from variation in the number of sea-level half-cycles that fit into the time interval from $t - \tau_{\max}$ to $t - \tau_{\min}$; this is the time interval over which $\dot{S}(t - \tau)$ can contribute CO₂ emissions at time t . For oscillatory sea level, each positive or negative peak in \dot{S} has an opposing emissions effect relative to the prior negative or positive peak. If there is an unmatched peak affecting the bottom of the melting region, the amplitude of E_{CO_2} variations is larger and the admittance is higher.

Broadly, the patterns of admittance and lag imply that, in terms of CO₂ emission variation, the dominant sea-level changes will be those with large amplitude and short period changes. The emissions variation associated with such changes will lag the forcing by approximately τ_{\min} . The modelled magnitude and lag of E_{CO_2} changes are affected by both K_0 and U_0 .

2.3.4 Reconstructed Pleistocene Sea Level

The simple scenarios of sea-level variation presented above give insight into the behaviour of the model, but are not representative of the variations that have occurred naturally, over the past million years. We move, therefore, to a model forced by the time-series of reconstructed global sea level from Siddall et al. [2010], shown in figure 2.10(a). Other reconstructions exist, but the differences between them are small enough that I follow Crowley et al. [2015a] and consider only this one. Siddall et al. [2010] record data every 3 kyrs and, based on their reconstruction, the highest rates of sea-level change (fig. 2.10(b)) meet the condition $\max(\dot{z}_m(t)) < W_m$ required for validity of equation (2.3).

Figure 2.10(c) shows the result of applying reconstructed sea level to ridge E_{CO_2} . There is a $\pm 10\%$ range in E_{CO_2} for moderate half-spreading rate and permeability. The E_{CO_2} curve is, qualitatively, a smoothed, offset version of $-\dot{S}$ — as expected from E_{CO_2} being approximated by convolving $-\dot{S}$ with the emissions response in figure 2.3(c). Within this framework, we now consider how to apply the model to global MOR emissions.

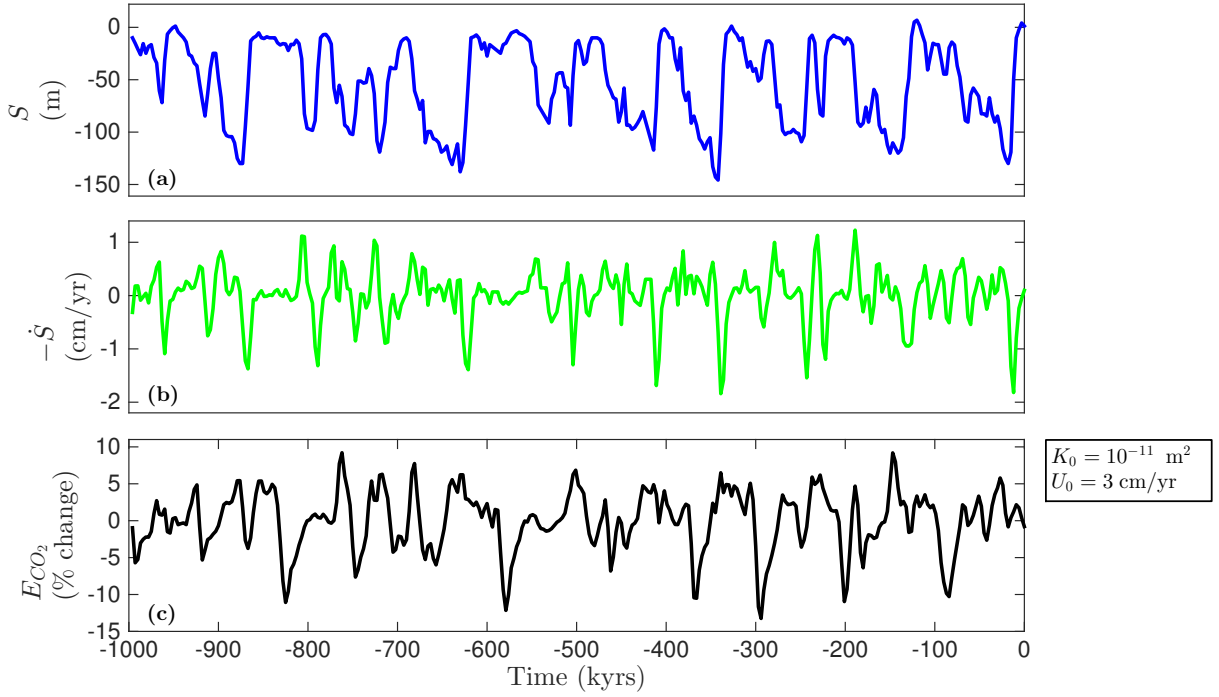


Figure 2.10: Reconstructed sea level. Plots show (a) sea-level change, (b) the negative rate of sea-level change, and (c) CO₂ emissions from a section of mid-ocean ridge. The lag is ~ 60 kyrs.

2.3.5 Global Mid-Ocean Ridges

The global MOR system is composed of ridge segments spreading at different rates, ranging from the ultra-slow Gakkell ridge to the fast East Pacific Rise. The baseline emissions depend on the half-spreading rate, as does the character of the emissions response to sea-level change. The global response to sea-level change should therefore be computed as the segment-scale response, integrated over the global MOR system,

$$\mathcal{G}_{\text{CO}_2}(t, K_0) = \int_0^{L_{\text{MOR}}} \mathcal{E}_{\text{CO}_2}(t, K_0, U_0(l)) dl, \quad (2.10)$$

where $\mathcal{G}_{\text{CO}_2}$ is global MOR emissions of CO₂ in kg/yr, l is arc length along the ridge, and L_{MOR} is the total length of the MOR system. This integral can be approximated by discretising the half-spreading rate into bins U_{0i} and summing the local response in each bin. A weighting is applied to each entry in the sum to account for the total length of segments with half-spreading rates in that bin. The sum is written as

$$\mathcal{G}_{\text{CO}_2}(t, K_0) = \sum_{i=1}^N \mathcal{E}_{\text{CO}_2}(t, K_0, U_{0i}) L_i(U_{0i}), \quad (2.11)$$

where N is the total number of spreading rate intervals to sum over and $L_i(U_{0i})$ is the total length of MOR in a particular spreading-rate bin. The local emission rate $\mathcal{E}_{\text{CO}_2}$ in each bin is computed by adopting the average half-spreading rate of the bin and assuming that sea-level change is eustatic — the same for all segments globally.

Gale et al. [2013] provide a catalogue of segment lengths and spreading rates for the global MOR system; the total ridge length is 61000 km with a mean half-spreading rate of 2.5 cm/yr. A histogram of these data is plotted in figure 2.11(a). Figure 2.11(b) shows, for each spreading-rate bin, the baseline emissions rate per metre of ridge. Panel (c) shows the product of ridge length and emissions rate per metre, giving the total emissions rate associated with each spreading rate bin. These are summed in accordance with eqn. (2.11) to give the total baseline global response. The global baseline emission rate thus predicted is 53 Mt CO₂ per year assuming a sub-ridge mantle CO₂ concentration of 125 ppmw. This can be compared to other estimates of 91 ± 45 MtCO₂/yr [Coltice et al., 2004, Cartigny et al., 2008, Marty and Tolstikhin, 1998]. If we instead constrain the model to have baseline emissions of 91 MtCO₂/yr, it requires a sub-ridge mantle CO₂ concentration of 215 ppmw (0.65 kg per m³).

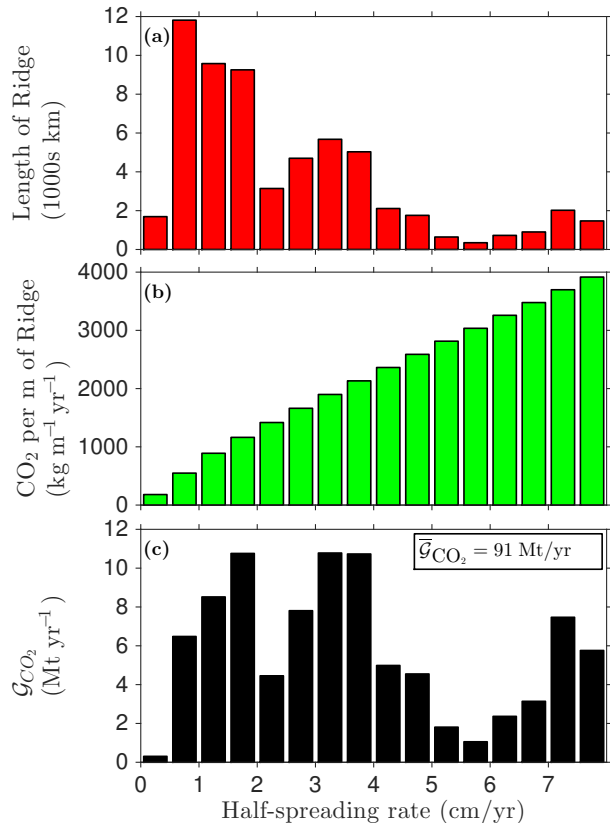


Figure 2.11: Quantities associated with discrete bins of half-spreading rate. (a) The total length of MOR [Gale et al., 2013]. (b) Baseline emissions per metre of MOR from our model. (c) Baseline global CO₂ emissions as the product of quantities in panels (a) and (b). Calculated for 0.65 kg CO₂ per m³ of upwelling mantle (215 ppmw). Baseline emissions are independent of K_0 .

Before applying the reconstructed sea-level forcing to the weighted global emissions sum in eqn. (2.11), we consider the simple sea-level forcing that was used to probe the behaviour of E_{CO_2} in fig. 2.3. This linear ramp in sea level is applied to compute the global emissions response in figure 2.12(a) for a range of mantle permeabilities. Global emissions in figure 2.12(a) are, unsurprisingly, more complex than the E_{CO_2} equivalent, as they consist of a summation of N E_{CO_2} peaks from figure 2.3, weighted according to the ridge length in each bin and offset due to the variation in τ with U_{0i} . Compared with figure 2.3, $\mathcal{G}_{\text{CO}_2}$ has a smaller percentage difference in the rate of CO_2 emissions and is spread out over a longer time-period.

Finally, we apply the reconstructed sea-level time series to the global model. Figure 2.12 shows $\mathcal{G}_{\text{CO}_2}$ for reconstructed sea level, calculated and plotted for a set of four values of the permeability constant K_0 in panels (d-i)–(d-iv). These curves demonstrate a reduction in $\mathcal{G}_{\text{CO}_2}$ range from 16 MtCO_2/yr for $K_0 = 10^{-10.5} \text{ m}^2$ to 2.1 MtCO_2/yr for $K_0 = 10^{-13} \text{ m}^2$. The reduction in $\mathcal{G}_{\text{CO}_2}$ range occurs because K_0 affects the range of τ_{min} that is implicit in the global sum in eqn. (2.11). A large value of K_0 gives higher overall permeability, shorter melt-transport times, and a global range in τ_{min} that is smaller. Therefore the emissions response to a box-pulse in \dot{S} (fig. 2.12(a)) is temporally concentrated and attains a higher peak value. Hence, larger K_0 causes greater amplitude of variation in $\mathcal{G}_{\text{CO}_2}$ for reconstructed sea level.

Figure 2.12 also demonstrates the expected behaviour whereby any of the (di–iv) panels can be replicated by convolving \dot{S} with the appropriate curve from panel (a), as these curves represent Green’s functions for the global MOR emissions response to sea level change.

To demonstrate the significance of these emissions variations, figure 2.13 shows the cumulative relative MOR emissions. These are the integral of the timeseries in figure 2.12d minus the baseline emissions, therefore showing the total change in atmospheric CO_2 mass caused by the variable volcanic emissions (assuming that the baseline earth system is in CO_2 equilibrium, a reasonable approximation given that there is no systematic drift in atmospheric CO_2 over the past million years). These cumulative emissions show a similar trend to $\mathcal{G}_{\text{CO}_2}$; larger K_0 causes greater variations in atmospheric CO_2 mass.

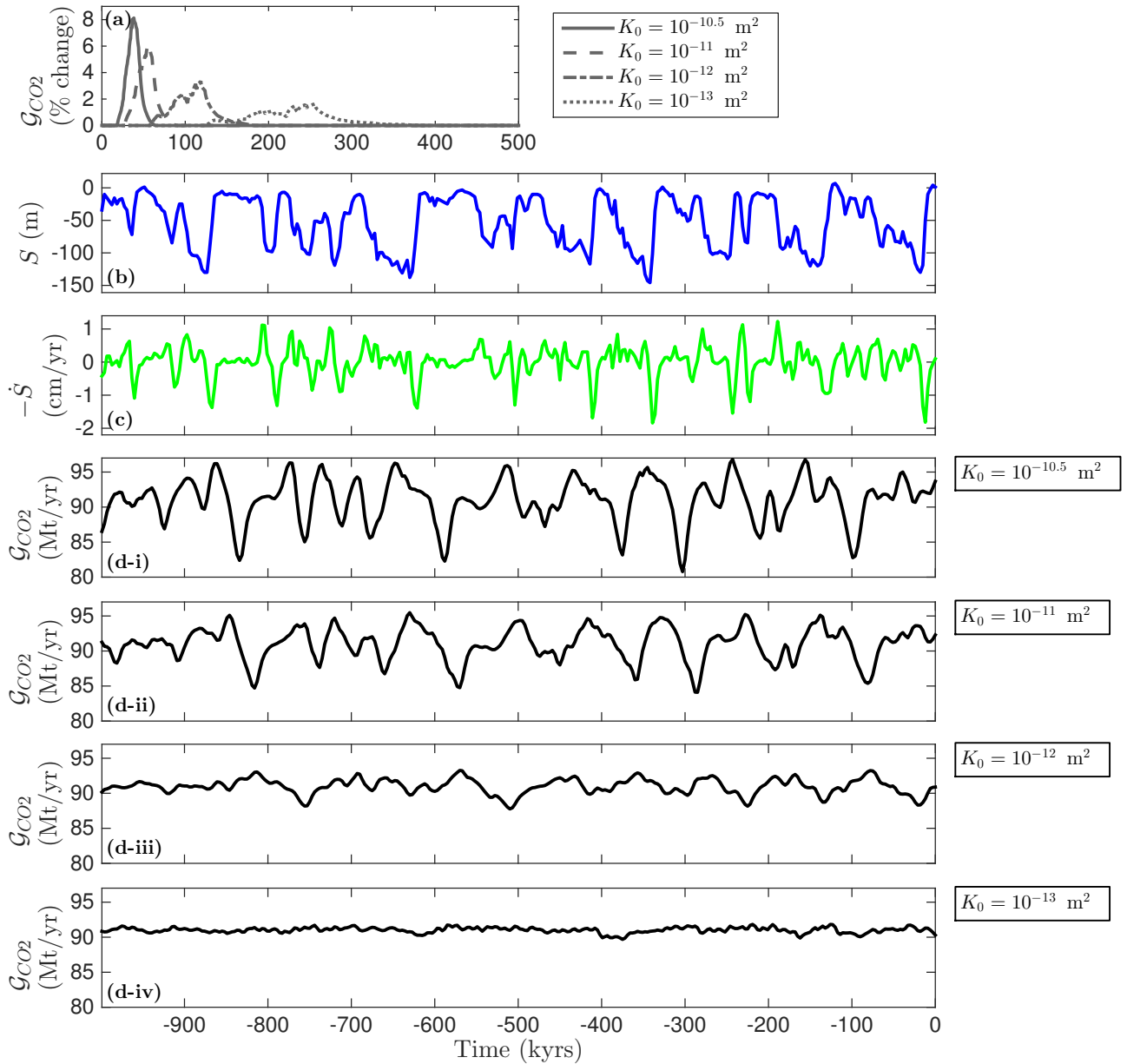


Figure 2.12: Global MOR emissions. Panel (a) shows CO₂ emissions from the global MOR system for a step change in sea-level identical to that of fig. 2.3(a). Subsequent panels consider reconstructed sea level and its effect. (b) Reconstructed sea level; (c) the negative rate of sea-level change; and (d-i)–(d-iv) CO₂ emissions from the global MOR system. The sea level time-series has been applied further back in time than shown, such that the left-most point in \mathcal{G}_{CO_2} is affected by more than τ_{\max} kyrs of prior sea-level change. For (d-i,ii,iii,iv) the lags in \mathcal{G}_{CO_2} are, respectively, 38 kyrs, ~ 60 kyrs, ~ 120 kyrs, and ~ 250 kyrs.

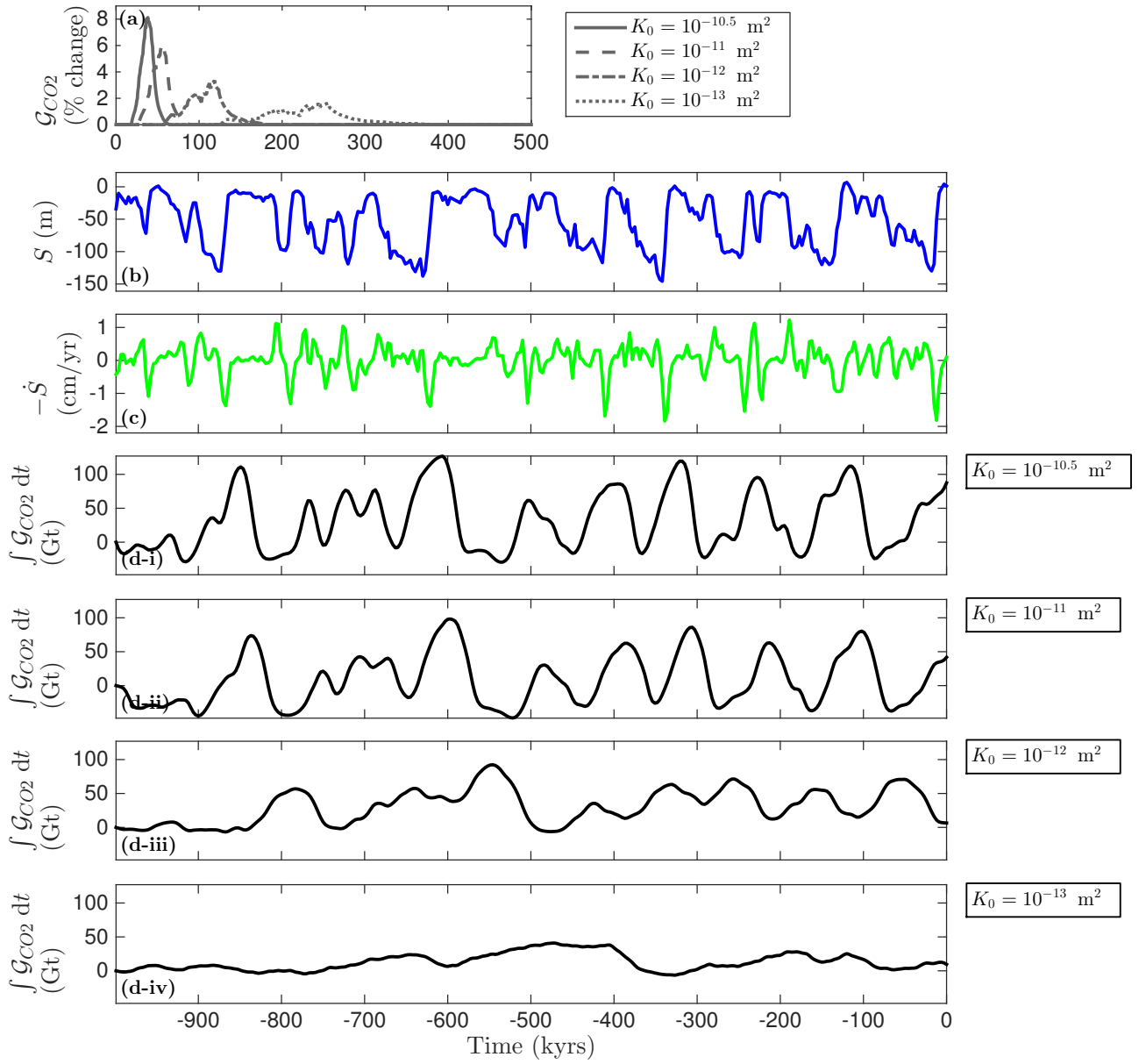


Figure 2.13: Global MOR emissions. Panels (a)–(c) as in figure 2.12. Panels (d-i)–(d-iv) show the cumulative CO₂ emissions (relative to baseline) from the global MOR system.

2.4 Discussion

This model calculates both baseline MOR CO₂ emissions $\bar{\mathcal{E}}_{\text{CO}_2}$ and the change in MOR CO₂ emissions caused by sea level change. Integrating these quantities over the global MOR system gives global totals. The model uses a system of equations based on the essential physics of melt generation and transport underneath a MOR, and the path of CO₂ through the melt system to the ridge.

This model framework predicts MOR CO₂ emissions will vary by $\pm 10\%$ during glacial cycles (depending on melt permeability); the change in MtCO₂/yr emissions this causes will depend upon the assumed baseline MOR CO₂ emissions.

We constrained the model to produce global baseline emissions $\bar{\mathcal{G}}_{\text{CO}_2}$ of 91 MtCO₂ per year (25 Mt carbon per year). This requires setting CO₂ concentration in the source mantle to 215 ppmw (0.65 kgCO₂/m³), within 1- σ error of $\mathcal{C}_{\text{CO}_2}$ estimates from analyses of mid-ocean ridge basalts [Coltice et al., 2004, Cartigny et al., 2008, Marty and Tolstikhin, 1998]. However, note that our prediction is not independent of MORB studies because our choice of global baseline emissions is partly based on observed MORB chemistry. If we instead choose to constrain the model to the mean published $\mathcal{C}_{\text{CO}_2}$, we calculate baseline CO₂ emissions of 53 MtCO₂/yr.

The relationship between $\bar{\mathcal{G}}_{\text{CO}_2}$ and $\mathcal{C}_{\text{CO}_2}$ is a function of both the mean degree of melting across the global MOR system F_G (uncertain) and the global melt volume (well-defined, 21 km³/yr [White et al., 1992]). Therefore the statements in the previous paragraph are equivalent to the difference in F_G between our model and geochemical analyses being less than the 1- σ uncertainty in those analyses. Compensating for the difference in F_G brings our models into agreement (see section 2.A.5).

The ranges in global CO₂ emissions under reconstructed variation of past sea level (fig. 2.12 for 215 ppmw CO₂) are between 2–16 MtCO₂/yr for mantle permeabilities at 1% porosity of 10⁻¹³–10^{-10.5} m². These idealised predictions assume that 100% of CO₂ transported to the ridge axis is degassed into the oceans, rather than retained in the crust or mantle. This may, in fact, be rather accurate; Cartigny et al. [2008] estimated that over 80% of CO₂ in primitive MORB is degassed near the ridge axis. Furthermore, 100% degassing is assumed in the papers that calculate the source mantle CO₂ concentration

and global CO₂ emissions. Any change to assumed degassing fraction would mean the source mantle CO₂ concentration must be changed to maintain the same global MOR CO₂ emissions rate.

Uncertainty in mantle permeability translates to uncertainty in both the amplitude of variations and the lag of global CO₂ emissions from MORs. There are various experimental constraints on mantle permeability [*e.g.* Miller et al., 2014, Connolly et al., 2009b]; these tend to agree on the scaling with porosity, but disagree on the magnitude of K_0 . Furthermore, permeability is sensitive to grain size, a parameter that is poorly known for the mantle beneath MORs [although see Turner et al., 2015]. Our chosen range of K_0 is intended to accommodate these uncertainties, as well as represent an effective permeability for melt transport that may be channelised into high-porosity, high-permeability dunite channels [*e.g.* Jull et al., 2002b, Kelemen et al., 1995]. Our K_0 range of 10^{-13} – $10^{-10.5}$ m² encompasses a change in the amplitude of $\mathcal{G}_{\text{CO}_2}$ variation by a factor of 5, a difference in lag of 200 kyrs, and qualitative difference in the time-series of $\mathcal{G}_{\text{CO}_2}$ (fig. 2.12). Therefore K_0 represents a leading source of uncertainty in the model. Uranium series disequilibria may provide an independent constraint on magma travel time from the base of the melting region [*e.g.* Jull et al., 2002b], although interpreting the various species in the decay chain is fraught with complexity. Preservation of ²³⁰Th disequilibrium (half-life of 75 kyrs) suggests a permeability of $K_0 \geq 10^{-12}$ m², and community consensus similarly favours K_0 at the higher end of our considered range.

Our model is based on the assumption that melt travels vertically from the depth of first melting to the top of the melting region and is then focused along a sloping, high-porosity decompaction channel to the ridge axis [Sparks and Parmentier, 1991]. The travel time of the vertical flow is modelled by a 1D compaction column; we assume that transport in the decompaction channel is instantaneous. The systematic error introduced by the latter assumption is zero on the ridge axis ($x = 0$), and increases with distance x from the ridge axis. This means τ plotted in figure 2.4(b) is more accurate at small x , but increasingly underestimates τ for larger x . Therefore, assuming τ_{min} is accurately modelled, τ_{max} is probably too small, such that E_{CO_2} in figure 2.3 should have a longer tail on the right of the graph. However, long tails have little effect on the resultant E_{CO_2}

pattern for complex sea-level changes or on the $\mathcal{G}_{\text{CO}_2}$ pattern for reconstructed sea level. Therefore the overall effect of including a finite travel time along the high porosity channel would be to make a small adjustment to the E_{CO_2} response. This suggests that assuming instantaneous travel time along the channel has little effect on the results of the model.

Another assumption made is that travel time is constant with respect to time, despite changes in melting rate (and thus, porosity) caused by changing sea-level. This follows the approach in the reduced model of [Crowley et al. \[2015a\]](#), where the perturbations in porosity were taken as negligible disturbances to the travel time in a steady-state compaction column solution from [Hewitt \[2010\]](#).

A more significant assumption underpinning the model is that carbon dioxide behaves as a perfectly incompatible tracer — meaning that carbon concentration does not affect the mantle’s physical or thermodynamic properties. However, carbon is not a trace element. In contrast, experiments by [Kono et al. \[2014\]](#) document the very low viscosity of incipient, carbon-rich melts present at small melt fraction below the base of the silicate melting region. The experiments also show that viscosity rises sharply as the carbon is diluted by silicate melting. It would be challenging to capture this variability in models, especially since the wetting properties (and hence the mobility) of carbon-rich melts are poorly constrained.

A more significant concern, however, is that treating volatiles as trace elements neglects their thermodynamic effect on melting. Small mantle concentrations of carbon affect the depth at which melting begins, though the melt fractions produced by this incipient melting are probably less than a few tenths of a percent [[Dasgupta et al., 2013](#)]. Our model assumes that these melts do not segregate until the onset of silicate melting. At such small porosity, it is unclear whether these carbonated melts can percolate. However, water-induced melting at the wet peridotite solidus of $\sim 90\text{--}120$ km [[Asimow and Langmuir, 2003](#), [Dasgupta et al., 2013](#)] increases the melt fraction. Again, the threshold of interconnectivity for such melts is not known, so it is possible that such deep, hydrous melts do not segregate, or do so very slowly. If the ^{230}Th disequilibrium observed in young MOR lavas originates with melt segregation in the presence of garnet [[Stracke et al., 2006](#)], it would support the hypothesis of efficient segregation of hydrous melts (although other hypotheses

also fit the observations). Overall, our model depends only on the presence of a pressure-dependent boundary that separates non-segregating melts, below, from segregating melts, above. The sharpness that is required of this boundary is unclear.

Finally, our model assumes a chemically and thermally homogenous mantle, which is certainly not true of the natural system [*e.g.*, Dalton et al., 2014]. No data exists that would allow us to accurately incorporate small-scale ($\lesssim 100$ km) heterogeneity in model. If such heterogeneity is pervasive at scales of ~ 10 km or smaller, it would affect the style of melt transport [Katz and Weatherley, 2012], with fertile regions creating pathways for rapid melt transport through the melting region. It may be the case that this is captured by a high effective permeability, though this is probably not a testable hypothesis. Large-scale heterogeneity would leave the mantle homogenous over the scale at which we calculate E_{CO_2} , so the underlying melt transport model would be unaffected, though parameters would need to be adjusted according to the oceanic region. It seems likely that such variations would cancel in the integral for global CO_2 emissions rate.

Previous authors have suggested that changing sea level might affect MOR CO_2 emissions almost instantaneously [Huybers and Langmuir, 2009, Lund and Asimow, 2011, Tolstoy, 2015]. Their assumption is that changes in pressure instantaneously affect melting rates, MOR volcanic productivity and therefore, assuming constant CO_2 concentration in the erupted melt, MOR CO_2 emissions. We disagree with the assumption that CO_2 concentrations would be constant. CO_2 is highly incompatible and therefore additional melting acts to dilute the constant mass of CO_2 in the melt. However, after including these effects, our model can calculate whether changing sea level affects MOR CO_2 emissions (see appendix 2.A.1). To leading order there is no effect; the reduced (or increased) concentration of CO_2 in the melt counteracts the increased (or reduced) rate of melt delivery to the ridge axis.

We would like to be able to compare the model to data, but there is no dataset of global MOR CO_2 flux over time. Atmospheric CO_2 concentration from Antarctic ice cores [Bereiter et al., 2015] is an existing dataset that might record some influence of $\mathcal{G}_{\text{CO}_2}$. However, there are many strong, nonlinear controls on atmospheric CO_2 and the relationship between $\mathcal{G}_{\text{CO}_2}$ and atmospheric CO_2 will not necessarily be constant over

time.

A potential avenue for future research would be to collect volcanic glass from the sea floor perpendicular to the MOR and analyse the concentration of a highly incompatible element in those glasses (*e.g.* Nb, Rb, Ba, Th...); thus generating a record of incompatible elements over time. If my calculations are correct, there would be clear Milankovitch frequencies in the concentration of highly incompatible elements in volcanic glass. The VOICE cruise of the Juan de Fuca ridge in 2014 discovered shards of volcanic glass in the lower parts of sediment cores [Langmuir, 2014], so this research is possible, albeit time-consuming and expensive³.

The MOR carbon flux may vary over time in other ways that we have not considered here. For instance, it is plausible that the intensity of hydrothermal circulation varies with sea level, driven by variations in melt supply [Lund and Asimow, 2011, Crowley et al., 2015a]. If this is the case, hydrothermal variations would have a different lag than that of CO₂ emissions. Hydrothermal systems have been proposed as both a CO₂ sink, with hot seawater transforming basalts to clay [Gysi and Stefansson, 2012], and a CO₂ source, with hydrothermal fluids transporting CO₂ from magma to the ocean [Sakai et al., 1990]. The rate of both these processes might scale with hydrothermal circulation, although it is not clear whether the net effect would be to increase or decrease MOR CO₂ emissions.

2.5 Summary

The model presented above calculates the efflux of a highly incompatible chemical component from a mid-ocean ridge, and how that efflux would vary with changes in sea level. It is based on a description of melt transport through a homogenous mantle and assumes perfect incompatibility of the component. This leads to a simple but physically consistent model of chemical transport through the melting region beneath a ridge. The model calculates total melt supply rate and global background emissions of CO₂ that are consistent with data and prior estimates.

In the model, changing sea level affects the depth of first silicate melting; this alters

³Furthermore, there are technical difficulties in consistently penetrating sediment cores close to bedrock when the thickness of the sediment layers varies considerably over axial ridge crests.

the rate at which CO_2 enters the melting region, segregates from its mantle source, and (some time later) arrives at the ridge axis and is degassed into the ocean.

The global MOR emission rate of CO_2 is predicted to vary by up to 11.2% when the model is forced with reconstructed Pleistocene sea level variation (5.8 MtCO_2/yr for 125 ppmw $\mathcal{C}_{\text{CO}_2}$; 10.0 MtCO_2/yr for 215 ppmw $\mathcal{C}_{\text{CO}_2}$). There is uncertainty in the predicted magnitude and timing (relative to sea-level forcing) of this effect, as two parameters of the model — $\mathcal{C}_{\text{CO}_2}$ and K_0 — are weakly constrained by existing data. However, within reasonable ranges of the model parameters, the amplitude of global MOR CO_2 emission-rate variation will remain on the order of several MtCO_2/yr . The total difference in the mass of CO_2 emitted from MORs during sea-level driven deviations from global baseline CO_2 is up to ~ 130 Gt CO_2 for high permeability and 215 ppmw $\mathcal{C}_{\text{CO}_2}$ (see figure 2.12(d-i)). This is 6% of the pre-industrial CO_2 mass in the atmosphere of 2190 Gt, or 0.1% of pre-industrial CO_2 in the oceans [IPCC: Solomon et al., 2007, fig 7.3].

Our results indicate that the CO_2 emissions from mid-ocean ridges are temporally variable in response to sea-level change. These results align with the hypothesis of Huybers and Langmuir [2009]; however, whereas they assumed an immediate emissions response, we show that the mid-ocean ridge CO_2 emissions response lags the sea-level forcing by approximately the minimum travel time of CO_2 through the melting region — at least 35 kyrs. Therefore MOR CO_2 emissions cannot feed back into the sea-level change that caused them; instead these CO_2 emissions will enter the climate system during the next glacial cycle.

As will be discussed further in the next chapter, this ability to transfer information from one glacial cycle to the next is vital to decoupling glacial cycles from the 40 kyr insolation cycle.

2.6 Subsequent Literature

Following this work's publication in 2015, there have been a handful of papers whose findings are relevant to my analysis.

Most important are assessments of volatile melting beneath MORs — at what depth are chemical conditions oxidising enough to allow CO_2 (elemental carbon has no effect

on the mantle solidus) and the consequent carbonatite melts? Are there also hydrous melts? Are these combined melts segregating from the solid mantle? In my model, the mechanism for E_{CO_2} variability is a fixed-pressure boundary, ~ 60 km deep, at which melt segregates from the solid mantle. If carbonatite melts segregate at a different, deeper boundary it would make the model inaccurate.

The Hammouda and Keshav [2015] review of carbon chemistry in the mantle concluded that carbon melts are expected above 150 km depth, however they provide no further constraints on the melt fraction nor whether it will segregate from the solid mantle.

Keller et al. [2017] (hereafter KKH17) provide the first constraint on the dynamics of MORs in the presence of water and CO₂: coupling two-phase mantle dynamics to an idealised thermodynamic model of mantle melting in the presence of water and carbon dioxide. Figure 2.14 shows the key schematic features of their model. Two of these features are pertinent to my model: firstly, the volatile melts above 160 km depth are constrained by thermodynamics to very low porosities (10^{-5} – 10^{-3} prior to dry peridotite melting at 60 km depth). These low-porosity melts have low velocities, arriving at the dry peridotite melting boundary with Darcy fluxes of less than 0.1 mm/yr.

Secondly, the (fixed-pressure) dry peridotite melting boundary z_m is associated with a sharp increase in melt segregation velocity, with the boundary demarcated by reactive infiltration channels.

Therefore the essential physical behaviours required for my model are preserved: there is a pressure-dependent boundary that separates (relatively) non-segregating melts, below, from segregating melts, above. The MOR system calculated in Keller et al. [2017] is consistent with the physical simplifications I make in my model.

Furthermore, KKH17 support other aspects of my model. 1) They calculate focusing width x_f as an emergent property, and their x_f closely matches that derived in figure 2.2. 2) Our baseline emissions are similar, which (combined with agreement on x_f) supports my analysis of the global mean degree of melting \bar{F}_G in section 2.A.5. And finally, 3) baseline CO₂ emissions are constant over time; $\bar{\mathcal{E}}_{\text{CO}_2}$ is not significantly affected by the emergent heterogeneities produced by reactive channels.

Unfortunately, the grid-resolution of KKH17's numerical model is larger than the

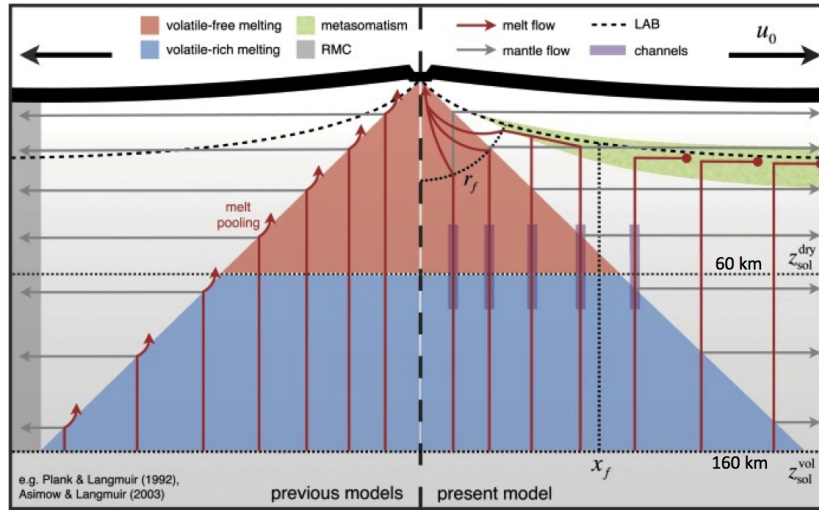


Figure 2.14: Summary of melt focusing beneath a MOR; left-hand-side presents a simplified standard model, compared to the KKH17 model on the right-hand-side. Shaded areas show volatile-bearing (blue) and volatile-free (red) domains of decompression melting; reactive channelling (purple); and the area of crystallisation and metasomatism (green). Dotted lines mark depths of first melting for volatile-bearing, $z_{\text{sol}}^{\text{vol}}$, and volatile-free mantle, $z_{\text{sol}}^{\text{dry}}$; lateral melt focusing distance x_f ; and active focusing radius r_f . Melt (red) and solid (grey) flow paths are strongly simplified. RMC is Residual Mantle Crystallisation. Figure taken from Keller et al. [2017].

glacially-driven Δz_m in my model, meaning my results cannot be replicated (they require behaviour beyond the KKH17 model’s spatial resolution).

Another important paper is Le Voyer et al. [2017], which provides both a review of previous estimates of carbon concentration in the mantle, and some new data for a range of elements in melt inclusions from the Mid-Atlantic ridge. They discuss probable $\mathcal{C}_{\text{CO}_2}$ values from the full suite of information available, leading to a parameter range and mean value similar to that assumed in this chapter.

The final directly relevant paper is Hasenclever et al. [2017], which uses numerical models of mantle flow and melting to calculate the glacially-induced variations in MOR and hotspot CO_2 emissions. It is a flawed paper, but let us start by giving it credit for its correct and useful contributions. The paleotimeseries data collated in the paper is wide-ranging and handles errors well, and the volcanic model calculates baseline emissions of 96 and 127 MtCO_2/yr for MORs and hotspots respectively, thus the model is accurately tuned to data-based constraints.

Hasenclever et al. [2017] calculates an increase in emissions of 13% following deglaciation, with a lag time of $\simeq 10$ kyrs. However, there are some considerable flaws in how they

achieve this, which invalidate their predictions. The paper fails to explain methods, uses some incorrect data, and tunes the model in a potentially unphysical fashion. However it is difficult to be certain because the paper fails to tell us relevant information. I will begin by discussing their mechanism for their variable emissions.

Their increase in volcanic CO₂ emissions is driven by an eruption-volume:CO₂-emissions correlation. This is achieved by having a CO₂ partitioning coefficient of 0.01, which is about a factor of 20 too large⁴ [Rosenthal et al., 2015] (as shown in section 2.A.1, for perfectly incompatible CO₂, increased melting does not alter the CO₂ emissions rate; thus the eruption-volume:CO₂-emissions correlation is spurious).

With the 0.01 CO₂ partitioning coefficient, CO₂ is added to the melt by depressurisation-driven melting in the lowest 20km of the melting region [Hasenclever et al., 2017, fig4]. We must infer from this that (during a sea-level fall) a mantle volume element releases all its CO₂ into the melt faster, but the total CO₂ released from a mantle volume element during upwelling through the melt region is unchanged.

Therefore, we must assume the model has an increase in magma upwelling rate associated with the increased melting (otherwise there wouldn't be any CO₂ signal in their model). The corollary is that there must be a subsequent decrease in CO₂ emissions. This is not mentioned in the paper.

Unlike this chapter's model, Hasenclever et al. [2017] has no CO₂ effect from the changing depth of first melting, presumably because the numerical model's resolution is too low to capture this effect.

Overall, I cannot find evidence to support their mechanism for volcanic CO₂ emissions changes. Let us now consider their lag time.

The lag time in their model is not physically justified; there is no discussion of melt motion through the melting regime. However, the authors do state "*[the] climate relevance of these CO₂ flux estimates will critically depend on how quickly CO₂ is transported from the melting region to the atmosphere*", so it is a little surprising that they don't discuss such an important factor. A previous publication of the M2TRI model treated fluid by

⁴Furthermore, CO₂ is treated as a trace element rather than a volatile, ignoring its effect on mantle melting. Hasenclever et al. [2017] also state that having a large CO₂ partitioning coefficient is a "moderate estimate" when in fact (under their assumptions) larger partitioning coefficients increase the change in CO₂ emissions

diffusion [Hasenclever et al., 2011], so perhaps they do that? Regardless, they do not explain how the model generates the travel time that drives their results, merely stating that the travel time has a value consistent with uranium-series disequilibria.

When considering the longer melt travel time from my publication Burley and Katz [2015] the authors state “*This time lag is, however, likely to be smaller when transient effects and processes related to intermediate magma storage in, for example, the axial melt lens at MOR or magma chambers at hotspot volcanoes are considered*”. Firstly, those are all magma storage processes that would **increase** the travel time rather than shorten it. Secondly, I cannot imagine any process reducing the melt travel times by 75% compared to my model, short of overhauling the fundamental assumptions of mantle dynamics or changing permeability by two orders of magnitude.

Despite these flaws, Hasenclever et al. [2017] raises an interesting point about the variability of hotspot CO₂ emissions. Mantle dynamics in this setting are not well constrained; high volatile content and potential temperatures may invalidate simple approximations made at MORs. Important complicating factors are, *i*) the potential for hotspot plumes to be partially molten at all depths [Harðardóttir et al., 2017, Yuan and Romanowicz, 2017, Zhao, 2001]. This would invalidate the changing-depth-of-first-melting mechanism for CO₂ variability, meaning there is no fixed-pressure boundary controlling CO₂ flux into the melt, and *ii*) extensive magma chamber systems [Harðardóttir et al., 2017, Larsen et al., 2001].

Therefore, neither my model, nor Hasenclever et al. [2017] are applicable at hotspots. Instead, a potential mechanism for glacially-driven variability at hotspots is the venting of existing reservoirs due to depressurisation promoting dyking and fracture. This aligns with the mechanisms for subaerial volcanic variability identified in chapter 3, and is consistent with observations of the eruption volume in arc settings and hotspots having a similar lag time from deglaciation [MacLennan et al., 2002, Kutterolf et al., 2013, Rawson et al., 2016b].

No other papers are directly relevant to my model. However, *1*) some literature has emerged supporting the glacial variability of MOR systems, with data showing that MOR hydrothermal activity is varying at the last glacial maximum [Middleton et al., 2016, Lund

and Asimow, 2011] — although no-one has yet published a mechanical explanation for such variations. 2) A steadily increasing number of papers confirm glacial variability in subaerial volcanic systems [Rawson et al., 2016b] with some modelling efforts inspired by the approach used here [Sternai et al.].

Overall, the work presented in this chapter has remained relevant since its publication, and is correct under our current knowledge.

Appendix

2.A Supporting Materials

2.A.1 MOR CO₂ Emissions Response to Changing Melting Rate

The model presented in section 2.2 calculates that changing sea-level causes a change in MOR CO₂ emissions rate by changing the depth of first silicate melting (and consequent effects on the rate at which CO₂ is transferred from the solid mantle to the melt). However, this model does not consider that changing sea-level also affects the rate of melting beneath the MOR. Variations in melting rate will affect porosity and melt fraction, leading to changes in melt upwelling rate and CO₂ concentration in the melt. These are clearly pertinent to the rate of CO₂ emissions from the MOR.

This section models the effect of changing melting rate on CO₂ emissions, demonstrating the leading order effect is nil.

Following the model used in the main text, the CO₂ emissions rate $\mathcal{E}_{\text{CO}_2}$ from a one-dimensional column in the melting region is:

$$\mathcal{E}_{\text{CO}_2} = RC_{\text{CO}_2}^{\text{melt}} \quad , \quad (2.12)$$

where R is the rate at which melt upwells per unit cross-sectional area ($\text{kg m}^{-2} \text{s}^{-1}$), and $C_{\text{CO}_2}^{\text{melt}}$ is the mass concentration of CO₂ in the melt, both defined at the top of the column. Both R and $C_{\text{CO}_2}^{\text{melt}}$ are affected by changing pressure and its consequent effects on melting rate.

Increased melting rate has two effects. Firstly, it increases porosity, which induces faster melt upwelling (increasing R). Secondly, it dilutes CO₂ in the melt, reducing $C_{\text{CO}_2}^{\text{melt}}$

(CO₂ is highly incompatible, thus its mass in the melt stays constant regardless of changes to the total melt mass). These two effects act in opposition, and the net result on $\mathcal{E}_{\text{CO}_2}$ is not immediately obvious. However, it can be evaluated by calculating the rate of change of $\mathcal{E}_{\text{CO}_2}$ in response to changing pressure,

$$\frac{d\mathcal{E}_{\text{CO}_2}}{dt} = \frac{dR}{dt} \mathcal{C}_{\text{CO}_2}^{\text{melt}} + \frac{d\mathcal{C}_{\text{CO}_2}^{\text{melt}}}{dt} R . \quad (2.13)$$

This calculation requires expressions for $\mathcal{C}_{\text{CO}_2}^{\text{melt}}$, R and their derivatives. Taking CO₂ as perfectly incompatible,

$$\mathcal{C}_{\text{CO}_2}^{\text{melt}} = \frac{\mathcal{C}_{\text{CO}_2}}{F} , \quad (2.14a)$$

$$\frac{d\mathcal{C}_{\text{CO}_2}^{\text{melt}}}{dt} = -\frac{\mathcal{C}_{\text{CO}_2}}{F^2} \frac{dF}{dt} , \quad (2.14b)$$

where F is the degree of melting. For a linearised solidus, following [Katz \[2008\]](#) [Hewitt \[2010\]](#), this is

$$F = \frac{\Pi}{\rho^2 g} (P - P_m) , \quad (2.15a)$$

$$\frac{dF}{dt} = \frac{\Pi \rho_w}{\rho^2 g} \frac{dS}{dt} , \quad (2.15b)$$

where P is pressure, P_m is the pressure at first silicate melting and we have used $\dot{P} = \rho_w \dot{S}$.

R is the product of the local porosity ϕ and melt upwelling velocity w . For a compaction column, following [Hewitt \[2010\]](#), these are

$$w = \left(\frac{K_0 \Delta \rho g}{\eta_f} \right)^{\frac{1}{n}} \left(\frac{\Pi W_m}{\rho^2} \right)^{1-\frac{1}{n}} (P - P_m)^{1-\frac{1}{n}} , \quad (2.16a)$$

$$\phi = \left(\frac{K_0 \Delta \rho g}{\eta_f} \right)^{-\frac{1}{n}} \left(\frac{\Pi W_m}{\rho^2} \right)^{\frac{1}{n}} (P - P_m)^{\frac{1}{n}} , \quad (2.16b)$$

where all the parameters have been previously defined and are stated in [table 2.2](#). Thus

$R = \phi w$ and its time-derivative are

$$R = \left(\frac{\Pi W_m}{\rho^2} \right) (P - P_m) \quad , \quad (2.17a)$$

$$\frac{dR}{dt} = \left(\frac{\Pi W_m \rho_w}{\rho^2} \right) \frac{dS}{dt} \quad . \quad (2.17b)$$

Substituting equations (2.14a), (2.14b), (2.15b), (2.17a), and (2.17b) into equation (2.13) then rearranging gives

$$\begin{aligned} \frac{d\mathcal{E}_{\text{CO}_2}}{dt} &= \left(1 - \frac{\Pi(P - P_m)}{\rho^2 g F} \right) \frac{C_{\text{CO}_2} \Pi W_m \rho_w}{\rho^2 F} \frac{dS}{dt} \quad , \\ &= 0 \quad , \end{aligned} \quad (2.18)$$

where, following eqn (2.15a), the term inside parentheses is $1 - F/F = 0$. Therefore, to leading order⁵, the instantaneous effect of changing sea-level on MOR CO₂ emissions (through changes to melting rate and eruption volume) is zero. Thus, suggestions that MOR CO₂ emissions should scale with eruptive volume are likely incorrect; it is only more compatible elements that increase emissions rates with increased melting.

However, the argument presented above is a simplification. For instance it assumes all melt that reaches the ridge is erupted instantaneously. A more detailed model might consider magma reservoirs at the MOR which could be vented by abrupt changes in pressure. However, such ventings would only be fluctuations against the background supply of CO₂ to the ridge, which (as shown above) does not vary with melting rate.

2.A.2 Depth of First Silicate Melting: z_m

The depth of first silicate melting occurs at the intersection of the local mantle temperature, which is adiabatic prior to first melting, and solidus temperature. We take a standard adiabatic temperature expression and approximate it with a Taylor series truncated at

⁵The leading order in question is assuming that F is a linear function of pressure (dF/dP is constant). This is a good approximation, whose physical basis is that the maximum degree of melting is only 22%, thus the top of the melting regime corresponds to a very linear part of the solidus' binary phase loop. Other simplifications in our two-phase compaction column, like constant viscosity and linear temperature profile, are also accurate — particularly over the small changes in quantity considered here — so this result is robust to increases in model complexity.

first order in pressure to obtain

$$T(z) = \tilde{T} - \frac{\alpha g \tilde{T}}{\rho c} (\rho z - \rho_w S) \quad , \quad (2.19)$$

where symbols are as defined in the main text and we have added a pressure term for varying sea level. The mass of a column of water is $\rho_w S$, provided the thermal expansion of the ocean is much less than S . Fortunately, oceanic thermal expansion causes less than 1% of total glacial sea-level change [McKay et al., 2011]. Freshwater density is used for ρ_w , as salt remains in the ocean when water is removed, and ocean water inputs are fresh. Coordinates are upwards-positive with origin at the MOR, therefore z is negative and increasing sea level S is positive. We model the solidus temperature following Katz [2008] and Hewitt [2010], using a solidus that is linear in pressure and a single composition parameter. We consider pressure terms due to the mass of mantle above the solidus, and sea-level deviations from reference conditions. This gives

$$T_{\text{Solidus}} = T_{S_{\text{ref}}} - \gamma g (\rho z - \rho_w S) \quad . \quad (2.20)$$

We ignore bulk ocean+atmospheric weight as this is accounted for in $T_{S_{\text{ref}}}$. Setting T_{Solidus} in eqn. (2.20) equal to $T(z)$ in eqn. (2.19) and solving for depth we obtain eqn. (2.5) in the main text.

2.A.3 Upper Boundary of the Melting Region: z_l

The upper boundary of the melting region, like the lower boundary, is a region where the solidus temperature matches the local mantle temperature. However, the controls on mantle temperature are slightly different. Local mantle temperature in the melting region can be modelled as the adiabatic temperature profile (eqn. (2.19)) plus terms for (i) thermal energy lost to latent heat during melting of $(z - z_m)\Pi L/\rho c$, and (ii) conduction near the cold ceiling (*i.e.*, the ocean floor) from the half-space cooling model. This approach assumes superposition of temperature fields without cross terms correcting for deviations from the assumptions of each model (*e.g.*, half-space cooling assumes a constant background temperature with respect to depth). Matching this to solidus temperature from

equation (2.20) gives

$$T_{S_{\text{ref}}} - \gamma\rho gz = \tilde{T} - \frac{\alpha g \tilde{T}}{c} z - \frac{\Pi L}{\rho c} (z - z_m) - (\tilde{T} - T_0) \operatorname{erfc} \left(\frac{z}{2} \sqrt{\frac{U_0}{\kappa x}} \right), \quad (2.21)$$

where L is the latent heat capacity of the mantle.

Equation (2.21) cannot be rearranged to give z as a function of x . However, as shown in equation (2.22), we can get x as a function of z ,

$$x_l(z, U_0) = \frac{U_0 z^2}{4\kappa} \left(\operatorname{erfc}^{-1} \left[\frac{\gamma\rho g - \alpha g \tilde{T}/c - \Pi L/\rho c}{\tilde{T} - T_0} (z - z_m) \right] \right)^{-2}. \quad (2.22)$$

Crowley et al. [2015a] show that this equation accurately matches the melting region calculated by numerical models of the MOR. The accuracy of $x_l(z, U_0)$ justifies the superposition of temperature fields assumption, and makes equation (2.22) a reference to benchmark against when formulating $z_l(x, U_0)$.

To get z in terms of x , we discard all depth-dependent temperature terms in equation (2.21) except half-space cooling. This approach is equivalent to plotting an isotherm in a half-space cooling model. Thus

$$z_l(x, U_0) = 2 \sqrt{\frac{\kappa x}{U_0}} \operatorname{erfc}^{-1} \left(\frac{\tilde{T} - T_l}{\tilde{T} - T_0} \right). \quad (2.23)$$

Figure 2.A.1 compares equation (2.23) to the benchmark (eqn. (2.22)). For a lithospheric boundary temperature of ~ 1550 K — close to the solidus temperature of mantle — equation (2.23) is a poor approximation of the real melting region. However, unphysically high boundary temperatures of $\gtrsim 1640$ K give good approximations of the melting region; the higher boundary temperature compensates for the temperature effects not explicitly accounted for. Therefore, we use equation (2.23) with $T_l = 1643$ K to approximate the upper boundary of the melting region.

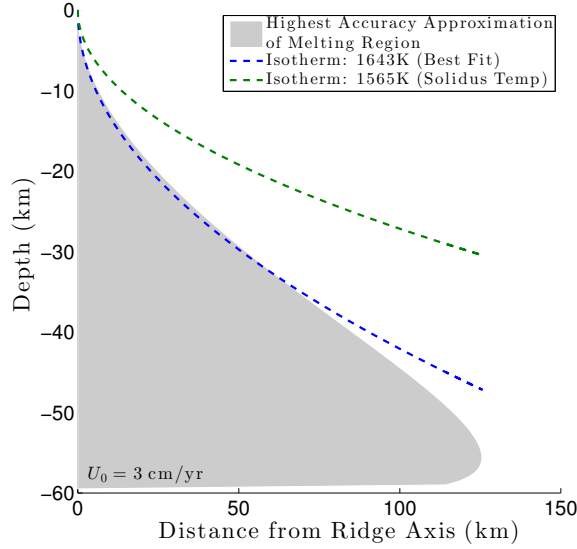


Figure 2.A.1: Melting region calculated by equation (2.22), compared to isotherms of the half-space cooling solution for 1565 K (a realistic solidus temperature) and 1643 K (a best fit isotherm). The 1643 K isotherm is used as the upper boundary of the melting region for this paper. All curves are calculated for a mantle potential temperature of 1648 K, surface temperature of 273 K and a half-spreading rate of 3 cm/yr. Plotted quantities all scale similarly with U_0 and thus isotherms have the same relative error across all spreading rates.

2.A.4 Width of the Melting Region: x_w

Equation (2.22) shows a finite width of the melting region defined by $dx_l/dz = 0$ (see figure 2.A.1 at $z \simeq 55$ km, $x \simeq 130$ km). The derivative of equation (2.22) is

$$\frac{dx_l(z)}{dz} = \frac{U_0 z}{4\kappa} \left(\frac{2 \operatorname{erfc}^{-1}(B(z - z_m)) - \sqrt{\pi} B e^{[\operatorname{erfc}^{-1}(B(z - z_m))]^2}}{[\operatorname{erfc}^{-1}(B(z - z_m))]^3} \right), \quad (2.24)$$

$$\text{where: } B = \frac{\gamma \rho g - \alpha g \tilde{T}/c - \Pi L/\rho c}{\tilde{T} - T_0}. \quad (2.25)$$

We have not found an analytical solution to equation (2.24) for $dx_l/dz = 0$. However, computational investigation of equation (2.22) for varying U_0 shows that the depth of the widest point of the melting region, z_w , is constant. Calculating x_l at this fixed depth gives the maximum width of the melting region, x_w . Thus,

$$\max(x_l) = x_w = \frac{U_0 z_w^2}{4\kappa} (\operatorname{erfc}^{-1}[B(z_w - z_m)])^{-2}. \quad (2.26)$$

2.A.5 Degree of Melting: F

Sections 2.3.1 & 2.4 state that the mean degree of melting causes the discrepancy between the concentration of CO_2 in the source mantle, $\mathcal{C}_{\text{CO}_2}$, and global CO_2 emissions, $\mathcal{G}_{\text{CO}_2}$, in my model compared to data-based geochemical calculations such as Marty and Tolstikhin [1998], Saal et al. [2002b], Salters and Stracke [2004], Cartigny et al. [2008]. This section covers how the degree of melting is calculated, and resolves the discrepancy. In the process, we discover first order differences between the dynamic predictions of the degree of melting, and common literature assumptions.

The degree of melting, F , is parameter denoting (for a particular point in the mantle) what fraction of the mantle has been melted; it is related to our adiabatic productivity parameter by $\Pi = \rho_m dF/dz$. Assuming equilibrium thermodynamics and a linearised solidus, dF/dz is constant and F is directly proportional to $z - z_m$. It is generally accepted that the degree of melting over a full 60 km of upwelling through the melting region is 20–25% [Langmuir et al., 1992a] — a representative example is shown in figure 2.A.2 — and our model matches this, with a maximum F of 22.2 %.

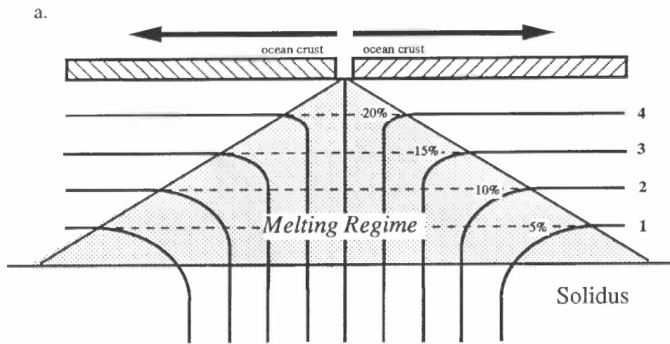


Figure 2.A.2: Conceptual sketch of F across a melting region. Solid lines are mantle streamlines. Taken from Langmuir et al. [1992a].

The mean degree of melting for melts at the extracted at a ridge segment \bar{F}_R is calculated by integrating over the focusing width of the melting system x_f

$$\bar{F}_R(U_0) = \frac{\int_0^{x_f} F_l \phi_l w_l dx}{\int_0^{x_f} \phi_l w_l dx} , \quad (2.27)$$

where F_l is the degree of melting, ϕ_l is porosity, and w_l is the melt upwelling rate; all defined at the upper boundary of the melting region z_l . Therefore $\phi_l w_l$ is the volumetric flux of melt through the top of the melting column, and equation (2.27) is a weighted mean of melts arriving at the ridge axis. In the interests of intercomparability, I will state

that my \bar{F}_R is equivalent to the bulk degree of melting F_B [Plank et al., 1995], but I use a different terminology and calculation method to more clearly focus on the physics and express the difference between local and global mean degrees of melting.

Figure 2.A.3 shows \bar{F}_R for a range of U_0 . We see that \bar{F}_R is dependent on U_0 , and that \bar{F}_R is higher than expected from looking at figure 2.A.2. We will begin by discussing the latter. High \bar{F}_R occurs for two reasons: Firstly, our model generally has a focusing distance less than the full width of the melting region, thus discarding low- F melts from the wings of the melting regime. Secondly, the on-axis regions produce more melt per unit time than off-axis regions, so the average melt is skewed towards the on-axis value.

The first reason has been discussed previously [e.g. Langmuir et al., 1992b, fig 50], although subsequent works generally discard this effect for simplicity. The second reason, however, is a consequence of compaction models for melt dynamics, and is less appreciated in literature. Collectively these act make the mean-degree-of-melting-of-extracted-melts higher than the mean-degree-of-melting-at-the-base-of-the-lithosphere.

Again considering figure 2.A.3, \bar{F}_R increases with U_0 because of two effects increasing the ratio of high- F melts extracted: 1) x_f/x_w reduces with increasing U_0 (see figure 2.2b), discarding an increasing fraction of melts from the wings of the melting region, and 2) W_m increases on-axis relative to off-axis (see figure 2.A.4), increasing the rate at which mantle enters the melting region on-axis vs. off-axis. This increases the proportion of on-axis high- F melts.

For melts generated in the focusing region, effect (2) is absent and effect (1) dominates, causing a large dependence of \bar{F}_R on spreading rate (figure 2.A.3 solid line). If melts are assumed to focus to the ridge from the entire melting region, effect (1) is absent and effect (2) induces a moderate dependence of \bar{F}_R on spreading rate (figure 2.A.3 dashed line).

The dependence of \bar{F}_R on U_0 is a topic of debate in petrology. On the one hand, it is supported by several observations of MOR melt compositions varying with spreading rate [e.g. Niu and Hekinian, 1997, Hellebrand et al., 2001, Rubin and Sinton, 2007], but on the other hand, the global dataset of MOR samples compiled and reinterpreted in Gale et al. [2013], Dalton et al. [2014] prefers to assign compositional variability to upwelling temperature rather than spreading rate. This null-result for spreading rate has

subsequently been challenged as failing to eliminate hotspot influence correctly [Regelous et al., 2016], or based on flawed metrics and failing to consider the non-independence of factors influencing melt composition [Niu, 2016].

I cannot comment on geochemical arguments with greater expertise than the authors of the papers referenced; however, I will say that from a dynamical perspective that it is hard to conceive of a MOR system that creates a steady 7 km of crust for $U_0 > 1$ cm/yr without a variable efficiency of melt focusing, and consequently \bar{F}_R as a function of U_0

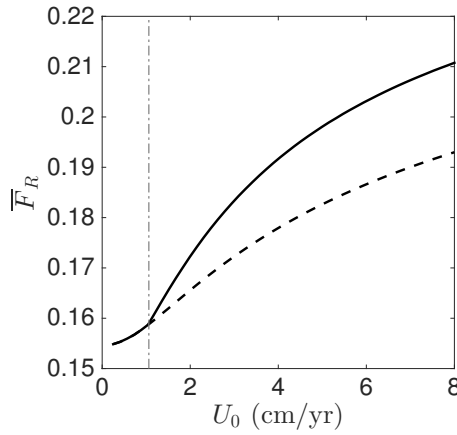


Figure 2.A.3: Mean degree of melting at the MOR (for constant sea-level), for a range of spreading rates. Data shown for melts extracted within the focusing width x_f (solid line), and for melts extracted from the full width of the melting region x_w (dashed line). The range of melts produced is in reasonable agreement with the Na-based constraints of 10-23% [Klein and Langmuir, 1987]

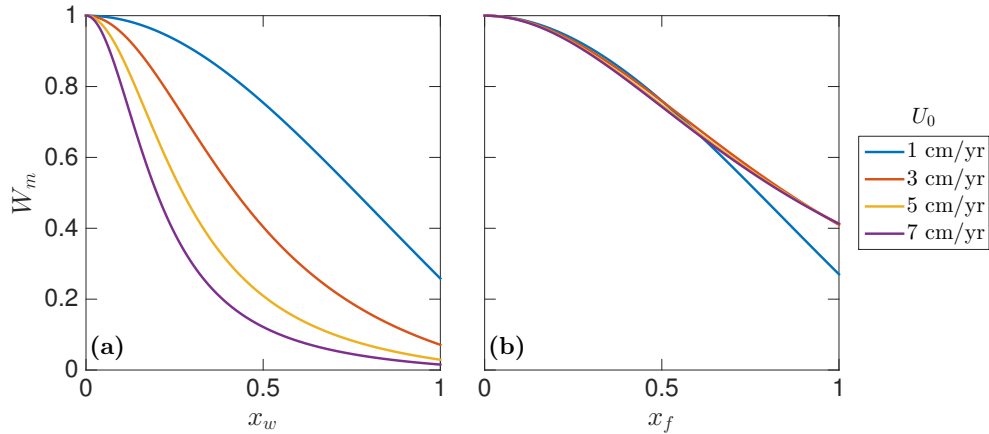


Figure 2.A.4: Mantle upwelling rate W_m for a range of spreading rates U_0 across (a) the full width of the melting region x_w and (b) the focusing width of the melting region x_f . All axes are normalised to max=1 for each U_0 . Note that applying our focusing width removes the variation in normalised W_m .

Integrating F_R over the global MOR system gives the global mean degree of melting

\bar{F}_G :

$$\bar{F}_G = \frac{\int_0^{L_{\text{MOR}}} \bar{F}_R V_R \, dl}{\int_0^{L_{\text{MOR}}} V_R \, dl} , \quad (2.28)$$

$$\bar{F}_G \simeq \sum_{i=1}^N \bar{F}_R(U_{0i}) V_R(U_{0i}) L_i(U_{0i}) , \quad (2.29)$$

where V_R is the volumetric mantle flow rate of a ridge (km³ of melt per metre of ridge per year), and similarly to equation (2.11), we approximate the integral with a summation of N spreading-rate intervals from the Gale et al. [2013] dataset.

Equation 2.29 calculates $\bar{F}_G = 0.187$, substantially higher than the 0.1 assumed in geochemical calculations [Marty and Tolstikhin, 1998, Saal et al., 2002b, Salters and Stracke, 2004, Cartigny et al., 2008].

Geochemical analyses infer carbon concentration in the mantle source from properties of erupted material via $C_{\text{CO}_2}^{\text{erupt}} = C_{\text{CO}_2}^{\text{source}}/F$. Therefore, using a systematically low value of $F = 0.1$ skews these calculations. Applying a correction factor of 0.187/0.1, my predicted global CO₂ emissions from 125 ppmw source mantle are 99 MtCO₂/yr (rather than 53 MtCO₂/yr), close to the expected value of 91 MtCO₂/yr.

In summary, MOR mantle dynamics enforce a dependence of \bar{F}_R on spreading rate, and a MOR melting region that generates a maximum degree of melting of 20–25% beneath the ridge is inconsistent with a global mean degree of melting $\bar{F} = 10\%$ according to any current understanding of mantle dynamics. Therefore MOR geochemical analyses are relating surface melts to the source mantle using simplified, inaccurate melting models⁶. The simplest solution to this dichotomy is to assert a lower degree of maximum melting, or a higher concentration of CO₂ in the source mantle; more complex solutions could try to invoke high-volatile melt focusing from the wings of the melting regime, but these are not supported by the latest MOR simulations [Keller et al., 2017].

The dependence of \bar{F}_R on U_0 is not directly relevant to the core investigation of this chapter, nor the overall thesis, however it is potentially relevant to ongoing debates within petrology.

⁶In the interests of balance, I will state that dynamic models use simplified geochemical constraints that are also somewhat inaccurate.

2.A.6 Corner Flow Solution

This section briefly outlines the corner flow solution and the changes I made to dimensionalise the classic solution of Spiegelman and McKenzie [1987], change the boundary conditions, and convert the equations into a more readily interpreted equation system.

The corner flow solution is a special case solution of the McKenzie equations [McKenzie, 1984] designed to illustrate the leading order behaviour of the mantle at mid-ocean ridges. To replicate the diverging plates which drive mantle motion at the MOR, it imposes a boundary condition where a pair of wedge-shaped lithosphere blocks are moving apart at $2U_0$, with no-slip condition with the solid mantle (*i.e.* solid mantle moves horizontally at U_0 cm/yr at these boundaries).

To simplify the resulting dynamics, corner flow assumes constant porosity and viscosity. The system is most easily solved using a polar coordinate scheme with the origin at the MOR (as imposed boundary conditions are straight lines from the MOR), giving a solution in terms of radius r and angle θ for the solid velocity W and the fluid velocity w :

$$W_r(\theta, U_0) = U_0 C_0 (\sin^2 \theta \cos \theta - \cos \theta + \theta \sin \theta) \quad , \quad (2.30a)$$

$$W_\theta(\theta, U_0) = U_0 C_0 (-\sin^2 \theta \sin \theta + \theta \cos \theta) \quad , \quad (2.30b)$$

$$w_r(r, \theta, U_0) = W_r - C_0 w_0 \left(\frac{\cos \theta}{C_0} + \frac{2 \cos \theta}{r^2} \right) \quad , \quad (2.30c)$$

$$w_\theta(r, \theta, U_0) = W_\theta - C_0 w_0 \left(\frac{\sin \theta}{C_0} - \frac{2 \sin \theta}{r^2} \right) \quad , \quad (2.30d)$$

where $_{r,\theta}$ denote flow in the radial and azimuthal directions respectively, $C_0 = 2/(\pi - 2\alpha - \sin(2\alpha))$ is a constant, and $w_0 = K_0 \rho g (1 - \phi_0) / \mu \phi_0$ is the percolation velocity — the constant rate at which melt separates from the solid under buoyancy forces. As defined in section 2.2, U_0 is the half-spreading rate, and α is the wedge angle.

These equations are correct, however they are not particularly intuitive. The natural language for the solve is polar coordinates, but given the resulting flow pattern is mostly near-vertical and near-horizontal (figure 1.7), the natural language in which to express that solution is Cartesians.

Conversion to Cartesians is done using the standard forms:

$$W_z = -W_r \cos \theta + W_\theta \sin \theta \quad ,$$

$$W_x = +W_r \sin \theta + W_\theta \cos \theta \quad ,$$

$$\theta = \arctan \left(\frac{-x}{z} \right) \quad ,$$

$$r^2 = x^2 + z^2 \quad ,$$

where x, z denote flow in the horizontal and vertical directions respectively, and upwards is defined as positive.

After rearranging, we can express (2.30a)–(2.30d) as

$$W_x(x, z, U_0) = U_0 C_0 \left(-\arctan \left(\frac{x}{z} \right) + \frac{x}{z \left(1 + \frac{x^2}{z^2} \right)} \right) \quad , \quad (2.31a)$$

$$W_z(x, z, U_0) = U_0 C_0 \left(\frac{1}{\left(1 + \frac{x^2}{z^2} \right)} - \sin^2 \alpha \right) \quad , \quad (2.31b)$$

$$w_x(x, z, U_0) = W_x + w_0 \frac{4C_0 L^2 x z}{(x^2 + z^2)^2} \quad , \quad (2.31c)$$

$$w_z(x, z, U_0) = W_z - w_0 \left(1 + \frac{2C_0 L^2 (z^2 - x^2)}{(x^2 + z^2)^2} \right) \quad . \quad (2.31d)$$

Equation (2.31b) is used to calculate the upwelling rate at the base of the melting region W_m (eq 2.4). None of the others are used directly in this thesis, but it would be wasteful to not include the full equation set here, as this Cartesian formulation is useful for understanding basic ridge dynamics.

For instance, equation (2.31d) has a clear physical interpretation where the melt moves at the mantle velocity W_z plus a phase separation velocity due to buoyancy w_0 , unless acted upon by compaction forces (the third term), which remain small until the melt approaches within compaction length L of the lithosphere.

Finally, the wedge angle is defined by $\alpha = \arctan(z_l/x_\alpha)$ taking a straight line from the origin through the expected lithospheric thickness z_l at some horizontal distance x_α away from the ridge axis (*i.e.* the depth of an isotherm from a half-space cooling solution, section 2.A.3).

Spiegelman and McKenzie [1987] selected x_α equal to L (18–30 km). This is a non-

trivial calculation as L is dependent on α . More importantly, it is not a good physical constraint. Melt regions are 40–300 km wide (eqn. (2.26)), and extrapolating linearly from the thermal conditions within 30 km of the ridge predicts lithosphere well over 100 km thick for the edge of the melting region at fast-spreading ridges — physically impossible. I instead choose α to match z_l at the focusing distance x_f (see sections 2.3.1, 2.A.3 for details), giving physically reasonable lithospheric thickness for the full width over which melt flows to the ridge.

Chapter 3

The C-VICE Model

This chapter presents a Combined Volcanism, Ice sheet, CO₂ and Energy balance model (C-VICE), which is the basis of an upcoming publication. The model treats the Earth system as forced by insolation alone; ice sheets, global temperature, and CO₂ concentration in the atmosphere vary dynamically in response to insolation (and the couplings between these systems).

The following sections lay out the details of this pseudo-2D climate model covering a strip of land from the equator to the north pole. Along this strip, the energy balance model calculates equilibrium atmosphere and surface temperatures according to the current insolation, ice sheet configuration, and CO₂ concentration in the atmosphere. In response to the current temperature and precipitation, the ice sheet advances or retreats. Atmospheric CO₂ changes in response to temperature change and volcanic emissions. The MOR volcanic emissions follow the theoretical predictions made in chapter 2, and subaerial (arc) volcanism is treated with a data-based model we derive in this chapter.

3.1 Introduction

Following the mid-Pleistocene transition, glacial cycles changed from 40 kyr cycles to longer 80 or 120 kyr cycles [Lisiecki and Raymo, 2005, Elderfield et al., 2012]. The 40 kyr glacial cycles are broadly accepted as being driven by cyclical changes in Earth's orbital parameters and the consequent insolation changes — Milankovitch cycles. However, Milankovitch forcing does not readily explain the >40 kyr glacial cycles that occur after the

mid-Pleistocene transition. These >40 kyr cycles therefore require that internal dynamics in the Earth system create a glacial response that is not linearly related to insolation [Tziperman et al., 2006].

Any proposed mechanism to extend glacial cycles' periods beyond 40 kyrs must give the Earth's climate system a memory on the order of 10s-of-kyrs, creating either a response that counteracts the 40 kyr Milankovitch forcing (allowing the Earth to 'skip' beats in the 40 kyr forcing) or a climate state with sufficient inertia — low climate sensitivity — that it is not affected by 40 kyr obliquity forcing [Imbrie and Imbrie, 1980]. The atmosphere/ocean has typical adjustment timescales on the order of 1000 years, thus oceanic theories for glacial cycles rely on other, long-timescale processes (*e.g.* weathering [Toggweiler, 2008]) to trigger arbitrary rules-based switches in the oceanic carbon system at tens-of-thousands-of-years intervals. Hence, it is difficult to envision how the ocean and atmosphere system could disrupt 40 kyr glacial cycles with a counteraction or inertia response; other mechanisms must be involved.

Hypothesised mechanisms of climate-inertia include: Antarctic ice sheets limiting deepwater ventilation [Ferrari et al., 2014], erosion of regolith to high-friction bedrock creating a thicker Laurentide icesheet [Clark and Pollard, 1998], ice-sheet calving instabilities [Pollard, 1983], and sea-ice limiting precipitation over ice sheets [Gildor and Tziperman, 2000]. However, none of these are universally accepted.

More recently, Abe-Ouchi et al. [2013] proposed a model of ~ 100 kyr glacial cycles for the past 400 kyrs. They modelled a 3D ice sheet forced by insolation and a prescribed CO_2 timeseries, using parameterised changes to temperature and precipitation derived from snapshots of a GCM (General Circulation Model). The reason for their ~ 100 kyr cycles is the climate-inertia of the Laurentide ice sheet: when the ice sheet is small it grows or remains stable in response to orbit-induced and CO_2 -induced climate perturbations, however at a larger size the Laurentide becomes unstable to such perturbations and will rapidly retreat in response to a warming event.

The large Laurentide ice-sheet's instability to warming perturbations is due to isostatic lithospheric adjustments forming a depression underneath an old ice sheet [Oerlemans, 1980, Pollard, 1982]. The retreat of the ice sheet is also a retreat downslope (in the isostatic

depression), continually exposing the ice sheet to warmer air, a positive feedback.

The [Abe-Ouchi et al. \[2013\]](#) model is not unique in producing 100 kyr cycles, [Ganopolski and Calov \[2011\]](#) manage the same in a slightly lower complexity model with an instability to warming perturbations derived from increased dust feedback when the Laurentide moves far enough south to encounter sediment-rich locations. [Ganopolski and Calov \[2011\]](#) state that any non-linear feedback on ice retreat could likely produce the same behaviour (although isostatic lithospheric adjustments are not sufficient in their model).

But, even in the framework of 100 kyr ice-sheet hysteresis, an explanation of late-Pleistocene glacial cycles must also explain why CO₂ minima (of the appropriate magnitude) occur on 100 kyr periods. Both the [Abe-Ouchi et al. \[2013\]](#) and [Ganopolski and Calov \[2011\]](#) models calculate approximate 100 kyr cycles when CO₂ is fixed around 220 ppmv. This fixed, glacial CO₂ value makes the Laurentide ice sheet unstable to orbital variations at ~ 90 msle (metres sea-level equivalent) global ice volume. Fixed atmospheric CO₂ values significantly above or below 220 ppmv prevent the ~ 100 kyr cycles from emerging.

Furthermore, whilst the [Abe-Ouchi et al. \[2013\]](#) fixed-CO₂ scenario has a predominant 100 kyr cycle, the resulting sea-level timeseries has departures from the geological record that are not present when prescribing CO₂: *i*) the power spectrum's 23 kyr and 40 kyr signals have similar strength, rather than a 1:2 ratio. *ii*) the last deglaciation and MIS11 deglaciation are small, leaving large ice-sheets at peak 'interglacial'. Thus, even a carefully selected fixed CO₂ value does not allow a model to replicate glacial behaviour; suggesting there is a need to incorporate a dynamic CO₂ response to fully understand glacial cycles.

For over a century [[Arrhenius, 1896](#)], it has been known that the $\sim 2,200$ Gt of CO₂ in the atmosphere is connected to much larger carbon reservoirs — there are 147,000 GtCO₂ in oceans and ocean sediments, and 9,200 GtCO₂ in the biosphere and soils, and 200,000,000 GtCO₂ in the mantle [[Stocker, 2013](#), [Dasgupta and Hirschmann, 2010](#)] — and that an imbalance in fluxes between them could alter atmospheric CO₂ concentration. Despite this, exact mechanisms behind ~ 100 kyr variations in atmospheric CO₂ concentration are unknown. Several theories for ocean–atmosphere CO₂ partitioning exist, some calculate close to the magnitude of glacial CO₂ change, however none make compelling dynamic predictions

for the timing of the observed atmospheric CO₂ record, nor the oceanic carbonate record [Broecker et al., 2015].

The line of argument for ocean–atmosphere CO₂ partitioning theories, simplified somewhat to summarise here, involves changing surface ocean and deep water exchange locations and volumes (and consequent changes in ocean carbonate chemistry). These can cumulatively change atmospheric CO₂ concentration by roughly 80 ppmv, be it by reorganising ocean currents [Toggweiler, 1999], ice sheets altering ocean ventilation [Ferrari et al., 2014], changing the biological pump via nutrient control [Sigman et al., 2010], or southern ocean wind stress [Franois et al., 1997]. These theories share similar features: from interglacial conditions, a reduction in planetary temperature triggers a change in an ocean-relevant process; consequently altered ocean behaviours sequester CO₂ in the deep ocean, reducing atmospheric CO₂ concentration and acting as a positive feedback to the initial temperature change. However, predicting these trigger points and calculating appropriate atmospheric CO₂ reduction rates (rather than just total CO₂ reduction) over a full glacial cycle remains infeasible.

Broecker et al. [2015] notes that ocean-only mechanisms for the glacial CO₂ cycle necessitate a deep-sea carbonate preservation event during deglaciation. However, no such event is seen in ocean sediment records.

Reconciling oceanic observations with theory would be possible with a variable CO₂ flux into the ocean-atmosphere reservoir — Broecker et al. [2015] suggest that a previously hypothesised, glacially-induced variability in volcanic emissions would be suitable.

We have discussed two features of the glacial CO₂ record that volcanic CO₂ emissions could help explain: first, the long drawdown of CO₂ over ~100 kyr (ie. Earth’s climate system has a memory on the order of 10s-of-kyr), and second, increased CO₂ during deglaciation. How can volcanic CO₂ emissions perform these roles?

Recent work suggests volcanic CO₂ emissions change in response to glacial cycles [Huybers and Langmuir, 2009, Tolstoy, 2015, Burley and Katz, 2015]: subaerial volcanic CO₂ emissions respond to glaciation within a few thousand years [Huybers and Langmuir, 2009, Kutterolf et al., 2013, Rawson et al., 2015], and mid-ocean ridge (MOR) CO₂ emissions respond to changing sea level with a 10s-of-kyrs delay [Burley and Katz, 2015].

This MOR delay occurs, according to our previous chapter, because changing sea-level causes a CO₂ anomaly in mantle melt at about 60 km below the MOR, where hydrous melting abruptly becomes silicate melting. This CO₂ anomaly subsequently takes tens of thousands of years to be carried to the MOR axis by the melt transport.

Conceptually, as shown in figure 3.1, MOR CO₂ emissions that lag sea-level by 30–50 kyrs would act to create high atmospheric CO₂ concentration in periods of low insolation. This lagged MOR CO₂ emissions response gives the Earth system a memory on the 50 kyr timescale that could act to drive glacial cycles from 40 kyr cycles to a multiple of this period. If so, such glacials would have sawtooth profile; entering a glacial under insolation forcing, with a hiatus in ice sheet growth as increasing insolation and low CO₂ concentration counteract each other, followed by a deeper glacial as insolation reduces, then a large deglaciation as both insolation and CO₂ increase.

By contrast, variable subaerial volcanic CO₂ emissions (with a few thousand year lag) are unlikely to change the period of glacial cycles, acting instead as a positive feedback on changes in ice volume [Huybers and Langmuir, 2009] *e.g.* increasing CO₂ during deglaciation.

The lagged MOR CO₂ response’s effect on glacial cycles was first investigated in Huybers and Langmuir [2017] using coupled differential equations to parameterize global ice volume, average temperature, and atmospheric CO₂ concentration. Ice volume changes at a rate proportional to both the current temperature and ice volume to the third power (the latter gives a maximum and minimum bounding ice volume). Temperature varies according to insolation, temperature, and atmospheric CO₂ concentration. Atmospheric CO₂ concentration varies according to average temperature, subaerial volcanism and MOR volcanism (based on Burley and Katz [2015] calculations). These equations represent a coupled, non-linear oscillator, and generate glacial cycles at a multiple of the obliquity period.

These results are intriguing, however there are limits in their physical representation. For instance, they have: 1) an insolation forcing timeseries with no seasonal or spatial component; 2) a negative ice feedback proportional to the volume of the ice sheet cubed, inducing symmetrical variability rather than sawtooth behaviour; 3) no isostatic litho-

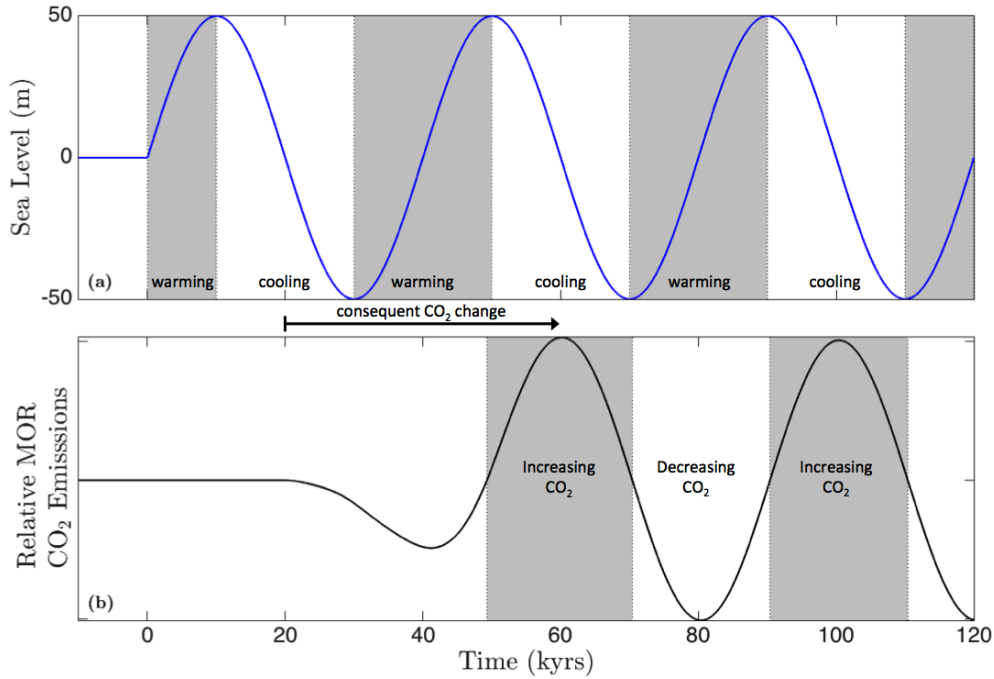


Figure 3.1: (a) Sinusoidal sea level change and (b) consequent global MOR CO₂ emissions for a 40 kyr lag (using chapter 2 calculations the emissions are, roughly, proportional to minus the rate of change of sea-level offset by the lag time). Sea level is treated as an independent input in this figure. The grey shading denotes a warming climate in panel (a) and increasing CO₂ in panel (b). MOR CO₂ emissions oppose the SL change when grey regions overlap white regions between the two panels; MOR lag of 30–50 kyr gives regimes that oppose 40 kyr sea level more than they reinforce it.

spheric response to the ice sheet. These simplifications remove potentially important physical mechanisms from the model glacial system.

A more complete representation of the Earth system would allow more detailed consideration of the key physics. The work in this chapter builds on [Huybers and Langmuir \[2017\]](#) by extending the modelling framework to a low complexity Earth system model. We ask what properties the volcanic CO₂ response to glacial cycles must have to alter the period of a glacial cycle?

We extend a simplified climate model from [Huybers and Tziperman \[2008\]](#) which focused on accurate treatment of orbital forcing, using an Energy Balance Model (EBM) coupled with an ice sheet model. The EBM calculates daily insolation to resolve the counteracting effects of orbital precession on ice sheets: hotter but shorter summers. The [Huybers and Tziperman \[2008\]](#) model demonstrates 40 kyr glacial cycles in response to insolation forcing. To maintain their focus on orbital effects, they did not consider the radiative effects of varying atmospheric CO₂ and water vapour; they assumed an

atmosphere of constant composition. From that framework we extend to a system of three component models: energy balance, ice sheet growth, and CO₂ concentration in the atmosphere. Our model does not aim to be a perfect representation of the climate; rather it focuses on approximating key features and feedbacks such that we can calculate Earth's glacial state over several glacial cycles.

Previous models of glacial cycles have ranged from simple, abstracted systems [Imbrie and Imbrie, 1980] to detailed representations of ice sheets and climate physics [Abe-Ouchi et al., 2013] — our model complexity is partway along this spectrum, considering the essential physics acting on a pseudo-2D system. However, even Abe-Ouchi et al. [2013] omit the carbon cycle, using imposed CO₂ concentrations rather than a dynamic system. No model has yet fully coupled an explicit representation of the solid-earth carbon cycle to physical representations of the Earth's climate. This work presents such a fully coupled model using a low-complexity physical representation. The full insolation forcing is used to drive an Earth system response in CO₂ concentration, temperature, and ice sheet configuration.

We will show that this model, when forced by the observed CO₂ record, calculates sea-level timeseries that closely match the historical record. When CO₂ evolves freely, the model has no ~ 100 kyr sea level variability until we include the lagged MOR CO₂ feedback; it is necessary to have a CO₂ feedback process with a period similar to or greater than the default 40 kyr glacial cycle in order to disrupt that cycle. We will show that the variation in MOR CO₂ emissions has the potential to generate sawtooth glacials.

The importance of volcanism in glacial cycles depends on both the percentage variations in volcanic emissions during glacial cycles and the background volcanic CO₂ emissions rate. There are uncertainties in both these quantities for MOR and subaerial systems. This uncertainty guides the modelling choices in made here. Rather than attempt a single exact estimate of global volcanic effects, we instead consider a range of volcanic effects. We define the threshold at which volcanism changes the pacing of glacial cycles, and compare this to estimates of these volcanic quantities. If the threshold values are orders of magnitude outside of estimates of these quantities, it would be strong evidence that volcanic CO₂ variability is not a important mechanism in glacial cycles. Our model

scales linearly with changes in baseline volcanic emissions and volcanic variability, so our results can be readily reinterpreted if such estimates are updated.

As mentioned above, our preference in this work is to consider the Earth's climate as naturally driven by the 40 kyr obliquity cycle — as seen in the early-Pleistocene record [although see [Raymo et al., 2006](#)] — with an internal Earth system feedback that locked the Earth into a 100 kyr mode after the mid-Pleistocene transition. However, we highlight that it is not agreed upon [[Maslin, 2016](#)] that late-Pleistocene ~ 100 kyr glacial cycles are driven by deglaciations on every second or third obliquity cycle (40 kyr period) [[Huybers and Wunsch, 2005](#)]; some argue that the precession index (23 kyr period oscillations in a 100 kyr envelope) causes deglaciations on every fourth or fifth precession maxima [[Raymo, 1997](#)] or for a combined effect [[Huybers, 2011](#)]. With these reservations in mind, we proceed to outline our study.

Section [3.2](#) introduces the three component models used to generate our results and discusses their coupling. Section [3.3](#) contains demonstrations of conceptually important model behaviour and the key model results: section [3.3.1](#) discusses how sea level period controls the maximum atmospheric CO₂ anomaly induced by MOR volcanoes. Section [3.3.2](#) illustrates the basic 2D dynamics of the model's EBM and ice sheet. Section [3.3.3](#) demonstrates our model's agreement with historical sea-level data when forced by the ice core CO₂ record. Section [3.4](#) shows the model behaviour with a dynamic CO₂ cycle and investigates volcanic interactions with glacial cycles: section [3.4.1](#) investigates the climate effects of different MOR lag times under simplified orbital forcing and discusses the importance of different timescale CO₂ feedbacks. Section [3.4.2](#) demonstrates model behaviour for a range of potential CO₂ feedbacks, showing the circumstances under which ~ 100 kyr cycles occur. Section [3.5](#) discusses the significance of assumptions and simplifications made in the model and the meaning of our results. Section [3.6](#) summarises my findings and offers some conclusions.

3.2 The Model System

The research question we ask, regarding the pacing of glacial cycles, requires that the model must run for 100's of thousands of years. To be capable of this, the model must

use a reduced complexity representation of the climate system.

The model treats the Earth's climate as a record of ice sheet volume (equivalently, sea level), temperature, and the CO₂ concentration in the atmosphere. We consider 2D models of ice and temperature, modelling a line from the equator to north pole.

Independent variables are time t and latitude ϕ . Temperature T is a function of t, ϕ , changing due to insolation S , ice (*i.e.* surface albedo), atmospheric CO₂ concentration, current temperature (controls longwave infrared emissions), and the temperature gradient with latitude. Ice sheet thickness h is a function of t, ϕ . It changes as ice flows under its own weight and accumulates/melts according to local temperature. Integrating h over latitude ϕ — with an assumed ice sheet width — gives total ice volume V . The CO₂ concentration in the atmosphere C is a function of t , varying in response to three processes: T -dependent changes in the surface system (*i.e.* atmosphere, biosphere, and ocean) partitioning of CO₂, V -dependent changes in subaerial volcanism (SAV), and V -dependent changes in mid-ocean ridge (MOR) volcanism. The dependencies of these components are shown graphically in figure 3.1.

These components are described by the following differential equations

$$\frac{\partial T(t, \phi)}{\partial t} = f_T \left(S, h, C, T, \frac{\partial T}{\partial \phi} \right) , \quad (3.1)$$

$$\frac{\partial h(t, \phi)}{\partial t} = f_h \left(\frac{\partial h}{\partial \phi}, T \right) , \quad (3.2)$$

$$\frac{dC(t)}{dt} = f_C \left(\frac{\partial T}{\partial t}, \frac{dV}{dt} \right) , \quad (3.3)$$

where functions f_i determine the rate of change of variable i . The system of equations (3.1)–(3.3) is driven by variation in insolation, S , computed using Berger and Loutre [1991]. All other variables evolve in response to the internal state of the model. Conceptually, this matches the Earth system: internal dynamics affected by the external driving force of variable insolation.

Having discussed the way these component models will be linked, I now describe each model in detail.

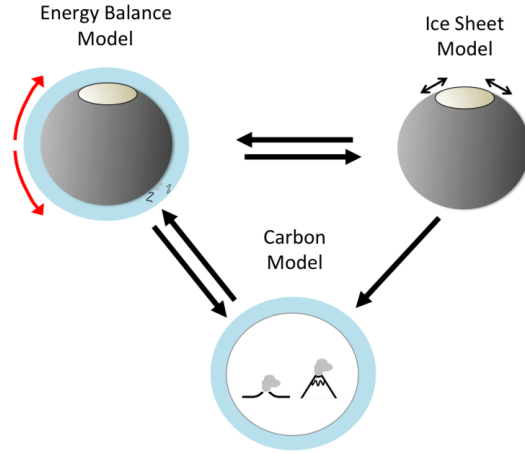


Figure 3.1: Component models and their interactions. Black arrows between models show information flow. Energy balance (*i.e.* temperature) is affected by carbon concentration in the atmosphere and the extent of the ice sheet. The ice sheet is affected by temperature only. Carbon concentration in the atmosphere is affected by the rate of change of temperature and sea level (determined by the ice sheet).

3.2.1 Energy Balance Model

To calculate planetary temperature and the annual ice accumulation/melting we use an Energy Balance Model (EBM) based on [Huybers and Tziperman \[2008\]](#). This model calculates insolation (and consequent temperature changes) at daily intervals, thus explicitly modelling the seasonal cycle and its effect on ice sheet accumulation/melting. Importantly, this includes the counteracting effects of orbital precession on ice sheets: hotter but shorter summers.

First, we will give an overview of the overall model and explain the method for including radiative forcings to represent CO₂, water vapour, lapse rate, and cloud effects. Subsequently, we fully detail the model's equation system.

3.2.1.1 EBM Overview

The EBM tracks energy in the atmosphere, ground surface, and subsurface; this is encompassed in:

$$c_a \frac{\partial T_a}{\partial t} = S_a + I_a + F_s + D_a \quad , \quad (3.4)$$

$$c_s \frac{\partial T_s}{\partial t} = S_s + I_s - F_s + F_{ss} \quad , \quad (3.5)$$

$$c_{ss} \frac{\partial T_{ss}}{\partial t} = -F_{ss} \quad , \quad (3.6)$$

where a, s, ss subscripts denote atmospheric, surface and subsurface quantities respectively, c is heat capacity ($\text{Jm}^{-2}\text{K}^{-1}$), S is the solar radiation (shortwave), I is net infrared longwave radiation, F is sensible heat flux (W/m^{-2}), and D_a is meridional heat flux. See table 3.1 for parameter values.

We modify this EBM to include radiative forcings from atmospheric composition and a temperature-dependent precipitation, detailed in 3.A.1. The atmospheric composition forcings represent CO_2 , water vapour, lapse rate, and cloud effects. These radiative forcings are treated with two terms: one for the CO_2 forcing, and another for the aggregate effects of water vapour, lapse rate and cloud forcings. Both terms are changes in the mean height at which the atmosphere becomes transparent to longwave radiation and emits to space, thus adjusting the longwave energy balance.

The net longwave radiation balance of the atmosphere I_a has three terms representing, respectively, the longwave emissions from the ground (absorbed by the atmosphere), emissions from the atmosphere to the ground, and emissions from the atmosphere into space. Applying the collective radiative forcings to I_a gives

$$I_a = \sigma T_s^4 - (\epsilon_a \sigma (T_a - \Gamma_m H_{as})^4 + R_{\text{DLW}}) - \epsilon_a \sigma (T_a + \Gamma_m (H_{ul} + \Delta z_C + \Delta z_{\text{WLC}}))^4, \quad (3.7)$$

where σ is the Stefan-Boltzmann constant, ϵ_a is atmospheric emissivity, T_a is the temperature of the middle atmosphere, Γ_m is the temperature profile in the atmosphere dT/dz , H_{as} is the middle-atmosphere-to-surface height, H_{ul} is the default middle-atmosphere-to-upper-layer height, Δz_C is the change in upper layer height due to CO_2 concentration in the atmosphere, and Δz_{WLC} the change in upper layer height modelling the parameterised water vapour, lapse rate, and cloud feedbacks.

Let us pause to consider the system this EBM describes. It models a latitudinal strip of land and the atmosphere above it, assuming atmosphere with well-mixed, homogenous composition and a linear temperature profile with height. The ground surface is flat, except when influenced by ice sheets. Ice sheets both elevate the surface (adding the height of the ice sheet to the bedrock level), and depress it (isostatic compensation). Surface albedo has two values in the model, representing ice and bare ground. Latitude-dependent

forcings are the variable surface albedo, insolation, CO₂ and the WLC parameterisation. Meridional heat transport occurs as a single parameterised term whose value is a sum of oceanic and atmospheric transport on Earth.

However, our model lacks an ocean and cannot include any effects based on longitudinal variations, thus excluding physical processes from calculation such as ocean thermal inertia reducing seasonality, the disruption of the Rossby wave over the Laurentide ice sheet [Roe and Lindzen, 2001], and precipitation based on the integrated history of an air mass. This flat, landlocked model can be considered a ‘cue-ball Earth’ simulation; capable of representing the Earth in continental regimes far removed from oceanic influence. Outside of such regimes, we expect the model to capture broad trends, but not as accurately.

To validate this reformulation of the Huybers and Tziperman [2008] EBM, we compare our model against present-day climate, and perform a CO₂-doubling experiment.

Figure 3.2 shows our model’s calculation of preindustrial conditions and the average surface temperature for 1950-80 [Berkeley Earth Surface Temperatures]. To approximate our model’s land-only, zero-relief Earth, the land temperatures are on a transect of data points closest to 52E — a continental regime with minimal ocean influence and low relief. Annual mean, maximum, and minimum temperatures are well aligned between our model and the data. The largest errors are near the equator, presumably owing to our model lacking latent heat transport, Hadley cell circulation, a representation of the low land fraction near the equator (*i.e.* no longitudinal heat transport) and because of our no-flux equatorial boundary condition. However, the seasonal temperature range is accurately captured across latitudes (except the polar coast, where oceanic buffering effects slightly reduce the annual temperature range), and the mean model temperature is within 1 K of the observed record at the high latitudes (55-75N) most relevant to ice sheet dynamics.

Figure 3.3 shows an experiment in which we double CO₂ from preindustrial conditions, holding atmospheric CO₂ concentration constant and running the model to equilibrium temperature. We calculate an increase in annual average atmospheric temperature of 3.7 K, with equatorial warming of 3 K and polar warming of 5 K. These results place our model within the range of GCM predictions for CO₂-doubling.

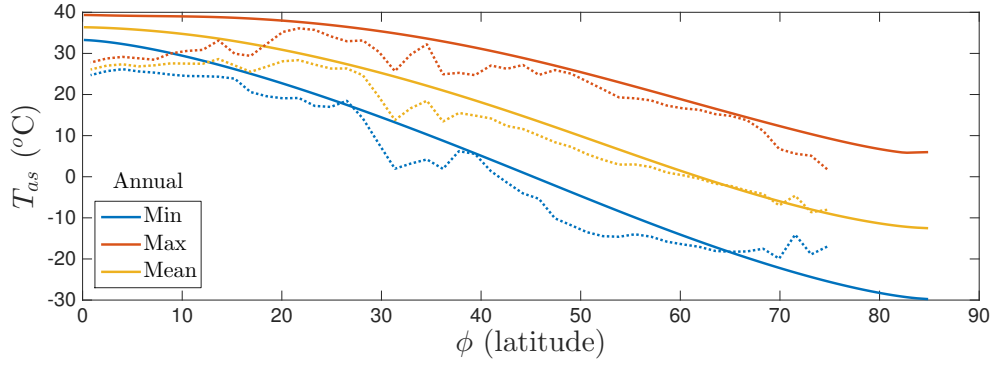


Figure 3.2: Annual mean, maximum, and minimum surface air temperatures for our model (solid lines) and average 1950-80 land data (dashed lines) [Berkeley Earth Surface Temperatures]. Model uses fixed modern insolation, and preindustrial CO₂ concentration. Temperature data is based on a transect of land points closest to 52E. This representative transect was chosen as it is low-elevation land, removed from oceanic influences, thus replicating our zero relief, ocean-free EBM. Furthermore, this region hosted at ice sheet at the LGM.

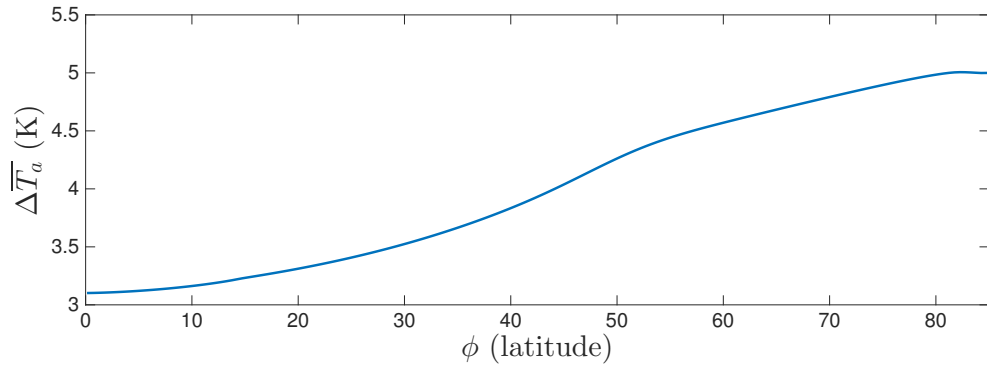


Figure 3.3: Change in annual average atmosphere temperature for a doubling of CO₂ from 280 to 560 ppmv under ice-free conditions with present-day insolation. The global mean temperature change is 3.7 K.

Importantly, the EBM includes an ice melting scheme — whereby if ice-covered ground reaches 0°C, ice melts according to the available thermal energy — giving the annual ice accumulation/melting at each latitude, an input for our ice sheet model.

3.2.1.2 EBM Equation System

The EBM is constructed around energy balance equations for the middle atmosphere (3.4), ground surface (3.5), and subsurface (3.6), repeated below:

$$\begin{aligned}
 c_a \frac{\partial T_a}{\partial t} &= S_a + I_a + F_s + D_a \ , \\
 c_s \frac{\partial T_s}{\partial t} &= S_s + I_s - F_s + F_{ss} \ , \\
 c_{ss} \frac{\partial T_{ss}}{\partial t} &= -F_{ss} \ ,
 \end{aligned}$$

where (as previously) a , s , ss subscripts define atmospheric, surface and subsurface quantities; T is temperature, c is heat capacity ($\text{Jm}^{-2}\text{K}^{-1}$), S is the solar radiation (shortwave), I is infrared longwave radiation, F is the sensible heat flux, and D_a is the meridional heat flux. Parameter values for the model are in table 3.1. All the RHS quantities are Wm^{-2} and are detailed below.

Solar radiation is treated as reflecting between the ground and a single atmospheric layer. The atmosphere has reflectivity R , absorption A , and transmissivity T — these sum to 1. The ground has reflectivity (equivalently, albedo) α , which has two values representing ice/non-ice conditions. Thus

$$S_a = AS + \frac{TAS\alpha}{1 - \alpha R} , \quad (3.8)$$

$$S_s = TS \frac{1 - \alpha}{1 - \alpha R} , \quad (3.9)$$

where the ground-atmosphere reflections are included as the sum of a geometric series. The fraction of solar radiation absorbed by the Earth system is $(S_s + S_a)/S$, giving 43.6% or 38.2% depending on whether α is set to ice or non-ice conditions. The model atmosphere has a single values for shortwave reflectivity and transmissivity, whereas real atmospheric reflectivity should vary with latitude due to increased cloud cover at high latitudes [Donohoe and Battisti, 2011]. Higher reflectivity at high latitude would 1) make variable insolation a weaker driver of glacial cycles, and 2) reduce the albedo effect of ice sheets, which are stronger in our model than in GCMs.

The infrared components are treated as imperfect black body radiators, giving

$$I_s = \epsilon_a \sigma T_{as}^4 - \sigma T_s^4 , \quad (3.10)$$

$$I_a = \sigma T_s^4 - \epsilon_a \sigma T_{as}^4 - \epsilon_a \sigma T_{ul}^4 , \quad (3.11)$$

where ϵ_a is the longwave atmospheric emissivity, σ is the Stefan-Boltzmann constant, T_{as} is the atmospheric temperature at the ground surface and T_{ul} at upper atmosphere. The atmospheric temperatures are related to the middle atmosphere temperature by a constant moist adiabatic lapse rate Γ_m of 6.5 K/km. The alternative of a spatially and temporally varying lapse rate requires assumptions about the global hydrological cycle

that we choose to circumvent. Applying the lapse rate to the previous equations gives

$$I_s = \epsilon_a \sigma T_{as}^4 - \sigma (T_a + \Gamma_m H_{as})^4 , \quad (3.12)$$

$$I_a = \sigma T_s^4 - \epsilon_a \sigma (T_a + \Gamma_m H_{as})^4 - \epsilon_a \sigma (T_a + \Gamma_m H_{ul})^4 , \quad (3.13)$$

where H_{ul} is the distance from the middle atmosphere to the upper atmosphere, H_{as} is the distance from the middle atmosphere to the ground surface, which varies with thickening ice sheets and bed depression. The upper atmosphere is defined as the height the atmosphere becomes optically thin to IR radiation and varies with C to represent radiative CO₂ forcing (see section 3.A.2).

Sensible heat flux scales linearly with the temperature difference between adjacent surfaces:

$$F_{ss} = K_s (T_{ss} - T_s) , \quad (3.14)$$

$$F_s = K_{ss} (T_s - (T_a + \Gamma_m H_{as})) , \quad (3.15)$$

where K is the coefficient parameterising the heat flux.

The meridional heat transport scales with the meridional heat gradient,

$$D_a = \frac{\partial}{\partial \phi} \left(-K_a \left| \frac{\partial T_a}{\partial \phi} \right| \frac{\partial T_a}{\partial \phi} \right) , \quad (3.16)$$

and this transport is tuned to a reasonable value by selecting K_a . We follow the 1000 J/K per degree latitude used in [Huybers and Tziperman \[2008\]](#).

To get to the energy available for melting ice the energy balance model is run for a year, with 1-day explicit timesteps to account for seasonality. At each timestep, the energy flux in/out of the ground surface is calculated; this energy flux changes the surface temperature or melts ice according to the local conditions. The thickness of ice melted is then calculated assuming constant ice density on the ice sheet's upper surface.

Finally, the model needs precipitation to accumulate ice. Precipitation is dependent on temperature as described in equation (3.25). At each timestep, wherever the atmospheric temperature at the ground surface is below freezing, this precipitation falls as snow and

creates an ice sheet. Where atmosphere is above freezing, the precipitation has no effect on the ice thickness or energy balance.

Table 3.1: Parameters used for the energy balance model.

Variable	Value	Description
α_g	0.3	land albedo
α_i	0.8	ice albedo
Γ_m	6.5 K/km	moist adiabatic lapse rate
ϵ_a	0.85	longwave atmospheric emissivity
ρ_l	900 kg/m ³	ice density
ρ_w	1000 kg/m ³	water density
ρ_a	1.5 kg/m ³	surface air density
σ	5.67×10^{-8} W/(m ² K ⁴)	Stefan-Boltzmann constant
C_p	2100 J/(kg K)	specific heat capacity of water
C_{air}	1.5 J/(kg K)	specific heat capacity of air
C_a	$5000\rho_a C_{air}$ J/(m ² K)	atmospheric heat capacity
C_s	$5\rho_i C_p$ J/(m ² K)	surface heat capacity
C_{ss}	$10\rho_i C_p$ J/(m ² K)	subsurface heat capacity
g	9.8 m/s ²	gravitational acceleration
H_{as}	5 km	height of middle atmosphere above sea-level
H_{ul}	2 km	upper atmosphere thickness
K_s	5 W/(m ² K)	Thermal transmittance, surface–atmosphere, the sensible heat flux coefficient
K_{ss}	2 W/(m ² K)	thermal transmittance, surface–subsurface
K_a	1000/(° lat) J/K	meridional heat flux coefficient
L_v	2.5×10^6 J/kg	latent heat of vaporization
L_m	3.34×10^6 J/kg	latent heat of melting
L_s	2.84×10^6 J/kg	latent heat of sublimation
S	1365 W/m ²	solar constant
A	0.2	shortwave absorption of atmosphere
R	0.3	shortwave reflection of atmosphere
T	0.5	shortwave transmission of atmosphere

3.2.2 Ice Sheet Model

Conceptually, our ice model combines the EBM’s annual ice accumulation/melting with ice flow under gravity and isostatic lithospheric adjustments. We calculate both the evolution of ice thickness across latitudes $h(t, \phi)$ and the global ice volume $V(t)$. The former is used by the EBM for ground height and reflectivity, and the latter is used to calculate volcanic responses to glaciation and sea level.

We use a vertically-integrated 1D model for h , following the [Huybers and Tziperman \[2008\]](#) model exactly, except we use a higher grid resolution and smaller timesteps.

As with the EBM, we begin with a conceptual overview, and then present the numerical equations that satisfy this conceptual system

3.2.2.1 Ice Sheet Overview

The ice model calculates the thickness of a northern hemisphere ice sheet flowing according to Glen’s Law, with an accumulation or ablation of ice at each latitude calculated according to the EBM. It assumes incompressible ice, temperature-independent ice deformability, and the ‘shallow ice’ approximation whereby deformation is resisted only by horizontal shear stress, including basal stress. The ground surface is initially flat, and deforms to maintain local isostatic equilibrium in each gridcell. Basal sliding is included via a shearable sediment layer, such that the base of the ice sheet can move with respect to the bedrock.

We calculate ice volume from the vertically-integrated 1D ice model by assuming that ice sheet width is 60% of Earth’s circumference at each latitude ϕ — a reasonable approximation at high northern latitudes. Ice volume is expressed in eustatic meters sea-level equivalent (msle) by dividing ice sheet volume by the ratio of ice to water density and the surface area of the ocean. Over glacial cycles, thermal expansion of the oceans is negligible at $< 1\%$ of glacial sea level change [McKay et al., 2011] and we ignore it in our sea level calculation.

3.2.2.2 Ice Sheet Equation System

Our ice sheet model begins with a PDE for ice thickness, h , deriving from conservation of mass

$$\frac{\partial h}{\partial t} = B - \frac{\partial}{\partial x} (\bar{u}h) \quad , \quad (3.17)$$

where B is the net accumulation rate (precipitation minus melting) in metres of ice per second, \bar{u} is the depth-averaged ice velocity, and x is distance along a line of latitude. Combining equation (3.17) with the shallow-ice conservation of momentum equation,

Glen's Law, and a variable bed height gives

$$\frac{\partial h}{\partial t} = B + \frac{\partial}{\partial x} \left(\frac{2A(-\rho_i g)^n}{n+2} \left| \frac{\partial(h+H)}{\partial x} \right| \frac{\partial(h+H)}{\partial x} (H+h)^{n+2} + u_b h \right) , \quad (3.18)$$

where A is the ice deformability constant in $\text{Pa}^{-3}\text{s}^{-1}$, ρ_i is ice density, g is gravitational acceleration, n is the exponent relating stress to strain in Glen's law, H is the height of the ground surface and u_b is the horizontal (sliding) speed of the base of the ice sheet. The sliding speed is calculated by

$$u_b = \frac{2D_o a}{(m+1)b} \left(\frac{\rho_i g h \left| \frac{\partial h}{\partial x} \right|}{2D_o \mu} \right)^m \cdot \left[1 - \left(1 - \frac{b}{a} \min\left(h_s, \frac{a}{b}\right) \right)^{m+1} \right] , \quad (3.19)$$

where D_o is the reference sediment deformation rate, m is the exponent in the stress-strain relationship, μ is the sediment reference viscosity, $a = \rho_i g h |\partial h / \partial x|$, the shear stress imparted to the sediment by ice flow above it, and $b = g(\rho_s - \rho_w) \tan(\phi_s)$ the rate of increase of shear strength with depth in sediment. Parameter values are given in table 3.2.

Finally, the bed height variation is calculated as a local relaxation to isostatic equilibrium

$$\frac{\partial H}{\partial t} = \frac{1}{\tau_b} \left(H_{eq} - H - \frac{\rho_i h}{\rho_b} \right) , \quad (3.20)$$

where τ_b is the bed relaxation timescale, H_{eq} is the equilibrium bed height, and ρ_b is the bedrock density. The importance of our selected bed relaxation timescale is explored in section 3.A.5.

Equation (3.18) is solved with a semi-implicit Crank-Nicolson scheme, a 0.5 degree latitudinal grid (56 km) and a two year timestep.

Table 3.2: Parameters used for the ice sheet model.

Variable	Value		Description
ρ_b	3370	kg/m ³	bedrock density
ρ_i	910	kg/m ³	ice density
ρ_s	2390	kg/m ³	saturated sediment bulk density
ϕ_s	22°	degrees	angle of internal friction
A	7.7×10^{-29}	1/(Pa ³ s)	deformability of ice
D_o	2.5×10^{-14}	s ⁻¹	reference sediment deformation rate
m	1.25		exponent in sediment stress-strain relationship
n	3		exponent in Glen's Law
h_{sed}	10	m	thickness of sediment layer
H_{eq}	0	m	equilibrium height above sea level
τ_b	5000	years	bed relaxation timescale
u_o	3×10^9	Pa/s	sediment reference viscosity

3.2.3 Carbon Model

The last component of our model calculates the CO₂ concentration in the atmosphere over time, responding to changes in climate configuration and volcanic emissions. Unlike our other model components the carbon system is not based on published work, so this section carefully justifies the elements of our carbon system, rather than presenting an essential summary and the system of equations as separate components. We will consider the CO₂ influences in turn, and discuss their timescale and magnitudes.

Glacial–interglacial CO₂ variations are not fully understood, and certainly cannot be replicated from first principles. Therefore we circumvent the accounting of all sources and sinks of CO₂. We instead parameterise atmospheric CO₂ concentration, C , as proportional to average global temperature, matching a well-established feature of reconstructed Pleistocene climate records [Cuffey and Vimeux, 2001, Sigman et al., 2010].

This carbon–temperature feedback accounts for all potential feedbacks in the surface carbon system, such as ocean–atmosphere equilibration and biosphere changes, and aggregates them to a single feedback parameter. This simplification allows us to be agnostic about the causes of these CO₂ changes and to enforce agreement with the observed correlation between CO₂ and ice volume in the Pleistocene. However, it fails to capture, for example, state dependency (a Kelvin change in average planetary temperature changes atmospheric CO₂ by a fixed amount, regardless of the current temperature). This may be important given recent suggestions of a lower limit on C during glacial cycles [Galbraith

and Eggleston, 2017] and several plausible non-linear components partitioning CO₂ in the surface system. These include, but are not limited to, hysteresis in the ocean overturning circulation [Weber et al., 2007], iron fertilisation [Watson et al., 2000], plant growth being non-linearly temperature dependent, and seafloor and permafrost methane clathrate release [MacDonald, 1990]. Despite these complications, the overall linear C, T relationship in the Pleistocene suggests our formulation is a good representation of leading order behaviour.

We have tested whether this modelled temperature–CO₂ feedback is significantly different when implemented as an equilibrium equation or a linear kinetic equation (see section 3.A.6). We found no meaningful differences and therefore choose to implement the simpler equilibrium formulation in the model.

We also include changes to atmospheric CO₂ from volcanic emissions as separate, independent terms, giving a carbon equation:

$$\frac{\partial C(t)}{\partial t} = \gamma_T \frac{\partial \bar{T}_s}{\partial t} + \gamma_{\text{MOR}} f_{\text{MOR}} \left(\frac{\partial V}{\partial t} \right) + \gamma_{\text{SAV}} f_{\text{SAV}} \left(\frac{\partial V}{\partial t} \right) , \quad (3.21)$$

where $f_{\text{SAV}}, f_{\text{MOR}}$ are functions that map sea level history to current CO₂ emissions for global subaerial and mid-ocean ridge volcanism respectively. The γ_i are coefficients that represent the sensitivity of C to changes in the Earth system. The γ_T term denotes the sensitivity to changes in surface temperature; this is interpreted physically as the net effect of surface system (*i.e.* atmosphere, biosphere, and ocean) partitioning of CO₂ between the atmosphere and other reservoirs. γ_T has units of CO₂ mass per Kelvin change in (annual and spatial) average planetary temperature, stated in ppmv/K for convenience (7.81 GtCO₂ = 1 ppmv change in atmospheric CO₂ concentration). The γ_{MOR} and γ_{SAV} coefficients are C sensitivity to changes in sea level caused by variable MOR and subaerial volcanic CO₂ emissions. These coefficients state the peak change in annual volcanic CO₂ emissions resulting from a given rate of sea level change, and thus have units of Mtonnes CO₂ per year per cm/yr change in sea level.

Volcanic CO₂ emissions have distinct timescales for subaerial and MOR volcanic systems. MOR CO₂ emissions follow the results in chapter 2, responding to glacial sea-level change with a tens-of-thousands-of-years lag. Subaerial volcanism responds comparatively

fast to changes in nearby ice sheets, with field evidence [Rawson et al., 2015, Kutterolf et al., 2013] showing responses in approximately 4 kyrs.

As shown in figure 3.4, we use an approximate Green’s function representation of each system where the rate of change of global ice volume (directly proportional to sea level) produces a change in CO₂ emissions at a later time. The γ_{MOR} and γ_{SAV} coefficients scale the height of these Green’s functions. The reasoning behind the imposed temporal patterns and magnitude of volcanic response is explained below.

The MOR Green’s function is the $\mathcal{G}_{\text{CO}_2}$ calculated in our previous chapter for a delta function in \dot{S} . There are no published observational constraints on MOR CO₂ response to glaciation that can support or reject this model. However, records of sea-floor bathymetry are consistent with a sea-level-driven MOR eruption volume model [Crowley et al., 2015b] that shares many features with the my CO₂ emissions model (though see Olive et al. [2015]).

As explained in chapter 2, sea-level change causes a CO₂ anomaly in mantle melt at about 60 km depth below the MOR. This CO₂ anomaly is subsequently carried by magma to the MOR axis. The MOR Green’s function’s magnitude and lag time are determined by the mantle permeability K_0 , a physical property that controls how quickly mantle melt percolates through the residual (solid) mantle grains. The mantle permeabilities assumed in this chapter are within the accepted range [Connolly et al., 2009a], and give CO₂ travel times in agreement with the ²³⁰Th disequilibria in MORB [Jull et al., 2002a].

Figure 3.4c shows example MOR CO₂ emissions responses for a range of mantle permeabilities. They show similar features: a decrease in CO₂ emissions lasting 10s-of-kyrs that lags the causative sea-level increase by 10s-of-kyrs. The total change in CO₂ emissions (*i.e.* the integral of figure 3.4c) is the same for all permeabilities, as established in section 2.3.2.

In subsequent sections, we discuss behaviour in terms of the ‘MOR lag’ rather than mantle permeability, as the former has a more direct interpretation that is relatable to other model components (as in fig 3.1).

MOR CO₂ emissions dissolve into intermediate ocean waters, delaying entry into the atmosphere by a few hundred years. This delay is much smaller than both the MOR lag

time and the uncertainties therein; hence we neglect it.

The SAV Green's function has a temporal pattern based on the observation-derived eruption volume calculations in [Rawson et al. \[2015, 2016b\]](#); these show a large increase in eruptive volume per unit time (volume flow rate) 3–5 kyrs after deglaciation, followed by a few kyrs of low eruptive volume per unit time, then a return to baseline activity. This timing is consistent with other studies that report an increase of subaerial arc volcanism that lags behind deglaciation by ~ 4 kyrs [[Jellinek et al., 2004](#), [Kutterolf et al., 2013](#)]. Therefore, the volume-flow-rate timeseries of [Rawson et al. \[2015\]](#) represents the temporal response of SAV accurately.

However, this is the response of a single volcano, and we need to model the global volcanic system. The planet's volcanoes experience different glacial coverage during an ice age, so the change in a single volcano's volume-flow-rate is not a valid basis for a global aggregate. Therefore, we want to adjust the magnitude of volume-flow-rate change, while keeping the temporal response pattern.

We create a representative global value for the volume-flow-rate change by using the eruption frequency datasets of [Siebert and Simkin \[2002\]](#) and [Bryson et al. \[2006\]](#), as compiled in [Huybers \[2011\]](#). To do this, we assume that eruption frequency is proportional to eruptive volume per unit time. This is an oversimplification, however eruption frequency is the only available constraint on global subaerial volcanic behaviour over a glacial cycle (erosion, reworking, and burial of volcanic units causes great difficulties in eruption volume calculations prior to the past few thousand years). Eruption frequency increases by at least $\sim 50\%$ during deglaciation. Next, we consider how to calculate the SAV CO₂ emissions.

To relate SAV eruption volume per unit time to CO₂ emissions there are three regimes to consider: if increased SAV volcanic eruption volume during deglaciation is entirely due to venting of pre-existing magma reservoirs, there would be direct proportionality between CO₂ flux and eruption volume; at the other extreme, if the eruption-volume increase is entirely due to enhanced melting of a CO₂-depleted mantle there is, to leading order, no correlation between eruption volume and CO₂ flux (see section [2.A.1](#)). Finally, if there is variable melting of a carbon-bearing phase (either mantle or metamorphism of a crustal

rock unit [Goff et al., 2001]) there will be a correlation between eruption volume and CO₂, but of unknown strength and with a dependence on location. For lack of information to guide us, we model SAV CO₂ emissions as directly correlated to the rate-of-change of ice volume. This leaves considerable uncertainty in the coefficient γ_{SAV} .

Furthermore, as discussed in section 2.6, it is unclear if hotspots have a glacially-driven variability. Their deep melting systems [Harðardóttir et al., 2017, Yuan and Romanowicz, 2017, Zhao, 2001] and extensive magma chamber systems [Harðardóttir et al., 2017, Larsen et al., 2001] mean they are affected by the same processes as SAV (and will not respond like MOR). Therefore we expect them to have a similar response timescale SAV; however, most hotspots are oceanic the pressure change will be caused by sea level rather than ice sheets. Thus I expect hotspots (if they have any glacially-driven CO₂ variability) to be a negative feedback acting simultaneously with arc volcanism, thus increasing the uncertainty in the appropriate value of γ_{SAV} .

Above, we have described the logic leading to our Green's function representations of MOR and subaerial volcanism. The physics-driven and data-driven calculations in this logic prescribe the percentage change in CO₂ emissions in response to rate-of-sea-level-change. We multiply the percentage value by the average annual volcanic emissions to get Green's functions in units of MtCO₂/year per cm/yr. Therefore, the Green's functions' magnitudes have uncertainty from both the calculated percentage change and the default emissions value.

Annual MOR CO₂ emissions have large uncertainties, with papers stating 2-standard-deviation lower bounds of 15–46 MtCO₂/yr, and upper bounds of 88–338 MtCO₂/yr from geochemical analyses [Marty and Tolstikhin, 1998, Resing et al., 2004, Cartigny et al., 2008, Dasgupta and Hirschmann, 2010]. The most recent estimates by Le Voyer et al. [2017] are MOR CO₂ emissions of 18–141 MtCO₂/yr. The 91 MtCO₂/yr estimate used in Burley and Katz [2015] is fairly central in that range and for consistency I continue to use that value in this thesis.

Annual SAV CO₂ emissions are also uncertain. Studies estimate SAV CO₂ emissions are within $\pm 15\%$ of MOR CO₂ emissions [Marty and Tolstikhin, 1998, Fischer, 2008], much less than the uncertainty in each value. For simplicity, we set background SAV CO₂

emissions as equal to MOR CO₂ emissions.

We assume that the solid Earth has no net effect on atmospheric concentration of CO₂, C , over the late Pleistocene, and therefore when SAV or MOR volcanism are at baseline emissions (*i.e.* 0% in figure 3.4(b,c)) they do not affect C . Any increase or decrease from average volcanic CO₂ emissions acts to increase or decrease C . Physically, this assumes the weathering drawdown of CO₂ balances the time-average of volcanic emissions, and that any variations in the weathering rate are at the sub-ka timescale (captured by γ_T) or negligible on the 1 Ma timescale.

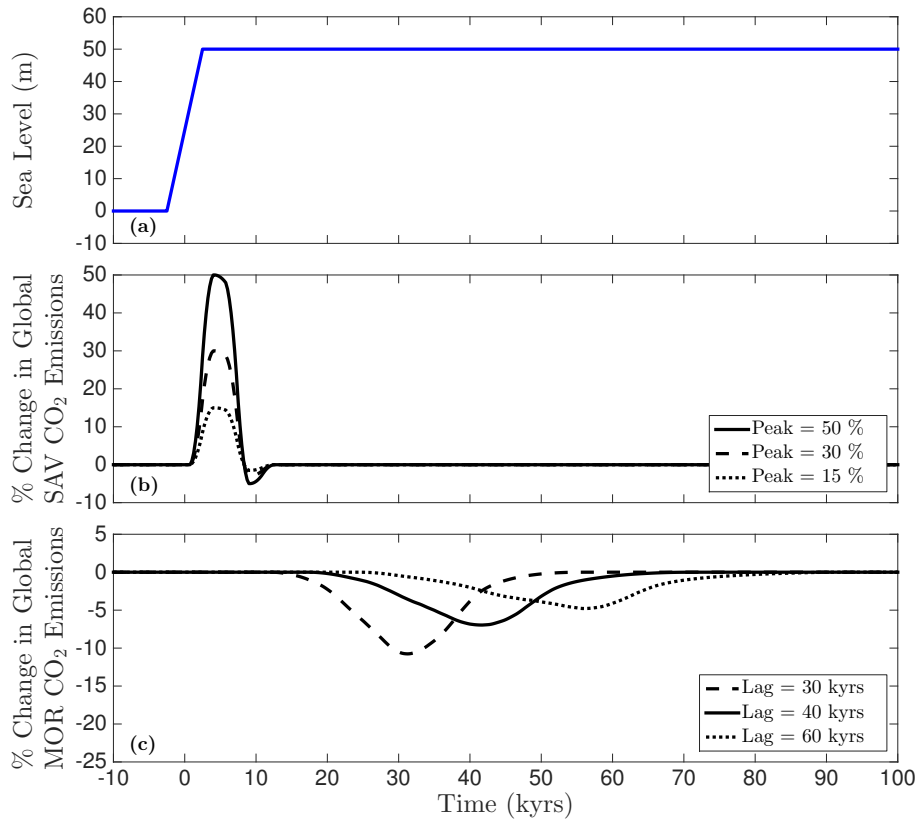


Figure 3.4: Toy deglaciation event with plots of (a) sea level, and the consequent CO₂ emissions of (b) subaerial and (c) MOR volcanism. γ_{MOR} and γ_{SAV} set the peak values of the emissions in panels (b),(c). The integrals of CO₂ emissions curves in panel (c) are all equal.

The volcanic Green's functions assume that all volcanic CO₂ variations directly change CO₂ concentration in the atmosphere. However, we might expect, for example, an extra 5 Mt/yr of volcanic CO₂ to be partially absorbed by the ocean such that atmospheric CO₂ mass does not increase at 5 Mt/yr. For modern oceans it is calculated that 15–30% of CO₂ added to the atmosphere remains after 2 kyr [Archer et al., 2009]. However, such calculations are state dependent; both the decay timescale and equilibrium airborne fraction vary with the injected CO₂ mass and the initial ocean state. There are no

estimates of the decay timescale or equilibrium airborne fraction on glacial timescales, nor glacial–interglacial ocean models from which one could be extracted. For simplicity, plots in this paper assume that all volcanic CO₂ remains in the atmosphere, however it is perhaps fairer to discount emissions by a constant factor — this discount is discussed in the conclusions section in terms of the of volcanic emissions required for certain climate behaviour.

Finally, we highlight a feature of the volcanic response that is important for understanding C evolution over time in equation (3.21): the total change in MOR CO₂ emitted (the integral of curves in figure 3.4c) is directly proportional to the amplitude of sea level change. For a detailed explanation, recall chapter 2.3.2.

Therefore the amplitude of changes in atmospheric CO₂ concentration ΔC caused by volcanism, for a single change in sea-level, are directly proportional to the amplitude of sea-level changes ΔV (section 3.3.1 illustrates the more complex scenario of periodic sea-level). By comparison, C changes due to surface system feedbacks are proportional to changes in mean atmospheric temperature \bar{T} . C determines radiative CO₂ forcing and thus this forcing depends upon past variations in ice volume V and \bar{T} . Furthermore, the effective insolation forcing depends on planetary albedo (*i.e.* ice sheet extent). Consequently, the balance of climate forcings in the model varies as the amplitude of changes in ice sheet volume, extent, and mean atmospheric temperature vary.

Note that we only model a single variable volcanic process — CO₂ emissions — yet other glacially-driven volcanic changes could affect climate. We discussed these previously in chapter 2.4.

These other potential glacially-driven volcanic effects have large uncertainty and complex underlying physical processes. We choose to not include them; they would increase model complexity and lead to an excess of uncertain parameters with overlapping timescales.

Having defined the component models, we now describe the coupling between these components and how the combined model is initialised.

3.2.4 Coupling and Initialising the Model

The three component models operate on different timescales and hence it is not immediately clear how to best couple them together. Careful consideration of timescales will inform our choice.

The fastest changes in the model are the seasonal changes in insolation and temperature, setting the shortest timestep in the model at 10^{-2} years. Taking such small timesteps for a full million years would be prohibitively expensive, so we use the simplification that 1) annual averages of thermal quantities are accurate drivers of ice sheet flow and carbon change (for example, we calculate ice sheet growth using the annual average melting/accumulation rate), and 2) subsequent years are very similar. Consequently we use the EBM model to calculate the equilibrium temperature and precipitation/melting distribution for the current CO_2 concentration and ice sheet configuration. We then hold temperature and precipitation constant while running the carbon and ice sheet models. After small changes in C and ice configuration we run the EBM again, calculating a new temperature and precipitation/melting distribution to drive further changes in C and ice.

The timescale for these ‘small changes’ in ice and C will clearly be greater than a year. In testing the model, we found a timescale on the order of 200 years was suitable. Shorter timescales do not alter V or C significantly.

For the results presented here, the ice model was run for intervals of 250 years, with two-year timesteps. The carbon concentration in the atmosphere is updated every 250 years, then the EBM is run for five years to update the temperature and precipitation/melting distribution in preparation for continuing the ice model. The model has converged for all these values — see appendix 3.A.4. To initialise the model at a particular time in the past, the insolation is computed for that time, and the CO_2 concentration is taken from ice core data. These are both held constant while the EBM and ice sheet come into equilibrium. Subsequently, the model is advanced using the timestepping described above.

The range of fully-defined initialisation times are limited by the atmospheric CO_2 record, which extends back 800 kyrs [Bereiter et al., 2015] (insolation is well defined for 10s-of-Myrs [Berger and Loutre, 1991, Laskar et al., 2004]).

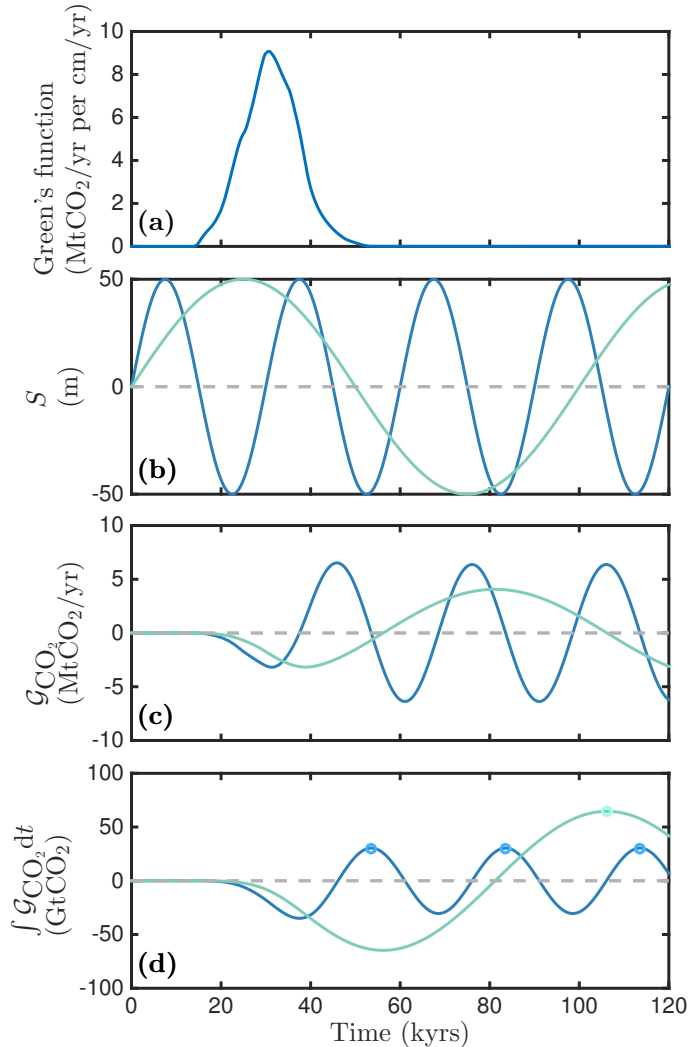
We could use earlier start times by solving an inverse problem to define starting C : use a range of initial C values and match the resulting equilibrium ice sheet volume to a proxy sea-level record. However the difficulties and objections such a method raises would distract from my core investigation.

3.3 Results: Basic Model Behaviour

3.3.1 Mid-Ocean Ridge CO₂ Response to Sinusoidal Sea Level

This section demonstrates how global MOR CO₂ emissions respond to sinusoidal sea-level changes, neglecting climate feedbacks from that CO₂ change.

Figure 3.1: MOR CO₂ emissions driven by sinusoidal sea level of 50 m amplitude, no climate feedbacks. This figure illustrates how the results of figure 3.2 are constructed. Panel (a) shows a Green’s function for the global MOR system. Panel (b) shows two sea-level timeseries with different periods, colours in the next two panels match their causative sea-level timeseries. Panel (c) shows the change in global MOR CO₂ emissions rate, and panel (d) the consequent total change in atmospheric CO₂, with the maximum values marked. Double these values is the peak-to-peak magnitude — the ‘maximum cumulative MOR CO₂ emissions’ defined in the text. To guide the reader, the two examples from this plot are marked in figure 3.2b. Note that the longer sea-level period causes a smaller change in $\mathcal{G}_{\text{CO}_2}$, but considerably larger changes in atmospheric CO₂.



As shown in figure 3.1, sinusoidal sea-level causes a sinusoidal variability in relative MOR CO₂ emissions rate (MtCO₂ per year relative to baseline MOR emissions). When these relative CO₂ emissions are positive, MORs are increasing the CO₂ concentration in the atmosphere; when negative, CO₂ concentration in the atmosphere is decreasing. Therefore, taking the integral (with respect to t) of the relative MOR CO₂ emissions rate gives the total change in atmospheric CO₂ mass caused by MORs, which is also sinusoidal (figure 3.1d). The peak-to-trough magnitude of this sinusoid (after a transient windup period) is the ‘maximum cumulative MOR CO₂ emissions’ — the maximum CO₂ mass

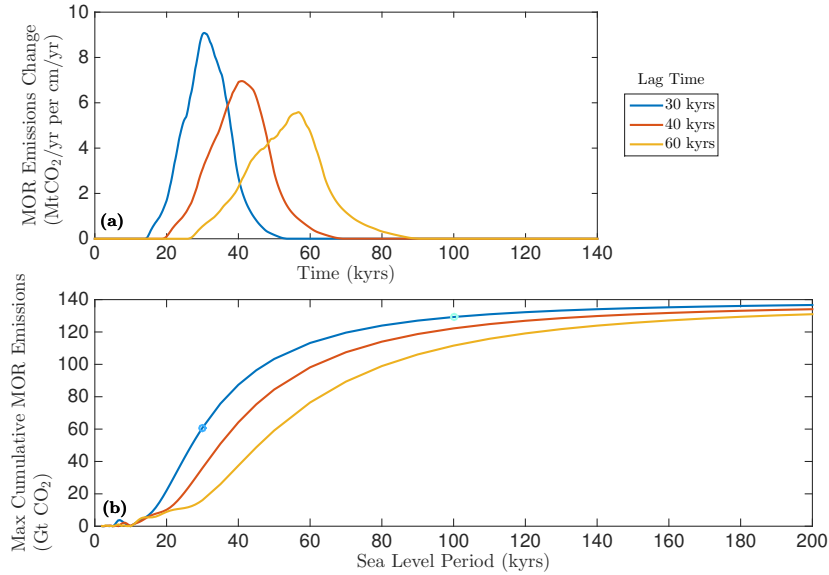


Figure 3.2: MOR CO₂ emissions driven by sinusoidal sea level of 50 m amplitude, no climate feedbacks. Panel (a) shows Green’s functions for the global MOR system with different lag times; stated as the global MOR emissions change in MtCO₂/yr per cm/yr rate-of-change in sea level. The γ_{MOR} values are those predicted from [Burley and Katz \[2015\]](#) for the lag times shown: 9.2, 7.1, 5.6 MtCO₂/yr per cm/yr rate-of-change of sea-level. Panel (b) shows the maximum cumulative MOR CO₂ emissions. The pair of blue circles mark the two values calculated in figure 3.1. 7.81 GtCO₂ = 1 ppmv C change, so maximum values in panel (b) are equivalent to 18 ppmv.

that variable CO₂ emissions add the atmosphere.

Figure 3.2b shows maximum cumulative MOR CO₂ emissions across a range of sinusoidal sea-level periods, for the three MOR lag times shown in figure 3.2a. The maximum cumulative MOR CO₂ emissions vary with sinusoidal sea-level frequency, meaning that MOR CO₂ emissions can have significantly larger effects on C if the period of sea level change increases. The physical reason for this behaviour is that the mantle melt (and associated CO₂ anomaly) arriving at the MOR at any given time is an amalgamation of mantle melts generated at the base of the melting region across a range of times (the width of the Green’s functions in figure 3.2a) in the past. If this range of times is greater than the sinusoidal sea-level period then CO₂ anomalies of opposing effect arrive at the MOR simultaneously, reducing variability in MOR CO₂ emissions (see [Burley and Katz \[2015\]](#)). Therefore, as shown in figure 3.2, sinusoidal sea-level periods shorter than the Green’s function width cause small amplitude cumulative MOR CO₂ emissions.

For sinusoidal sea-level periods much larger than the Green’s function width, the cumulative MOR CO₂ emissions reach a constant value; this can be understood by the

reservoir interpretation discussed in section 2.3.2.2. When sea level falls, the depth of first melting under the MOR increases, creating new melt in a deeper section of mantle, and extracting the carbon from that mantle. The change in depth of first melting (and thus the volume of mantle decarbonated) is proportional to the amplitude of sea-level change. Therefore the maximum possible CO₂ injected into the atmosphere is determined by the amplitude of sea-level change, and different period sinusoidal-sea-levels have different effectiveness at reaching this maximum. Sea-level periods much longer than the Green's function width allow this mantle volume to degas its carbon and emit CO₂ from the MOR without interference from opposing CO₂ anomalies. Thus longer sea-level periods converge to the maximum possible CO₂ release into the atmosphere.

Our arguments above state that maximum cumulative MOR CO₂ emissions will have near-zero values for sea-level periods much less than the width of the MOR Green's function, and converge to a large value for sea-level periods greater than the width of the MOR Green's function. The widths of our Green's functions in figure 3.2a are approximately 30–60 kyrs and, consequently, figure 3.2b demonstrates significant changes in the amplitude of cumulative emissions over glacial-cycle-relevant changes in sea-level period. For example, MOR systems with 40 kyr lag driven by 40, 80, 120 kyr sea-level period have maximum cumulative emissions of 64, 104, 126 Gt CO₂, corresponding to a doubling of MOR-derived CO₂ deviations when sea level changes from early-Pleistocene to late-Pleistocene periodicity.

This result is robust for any MOR system with a lag likely to destabilise 40 kyr glacial cycles (30–50 kyr): 1.4–2.5× increases in maximum cumulative MOR CO₂ emissions if sea level periodicity increases to ~100 kyrs. See appendix 3.A.7 for generalised mathematical treatment. Whilst MOR CO₂ emissions remain a small part of the overall glacial CO₂ cycles, this is a mechanism for MOR volcanism to reinforce ~100 kyr glacial cycles if they occur.

Our SAV Green's function width is 3.5 kyrs, much less than glacial sea-level periods, thus our calculated cumulative SAV CO₂ emissions do not vary significantly with sea-level period.

3.3.2 Dynamics of Coupled EBM & Ice Sheet

This section illustrates the ice sheet which underlies the model output, prior to the later results sections displaying abbreviated summaries of this physical system. We check that the system has reasonable values over glacial cycles.

Figure 3.3 shows the physical state of the ice sheet and snow precipitation over an 800 kyr model run that replicates historical glacial cycles by forcing the model with both historic insolation and the ice-core CO_2 record (see section 3.3.3 for further details). The ice sheet has a maximum elevation of 1.4 km and maximum thickness of 1.9 km, a reasonable average of Laurentide and Eurasian ice-sheets. The precipitation shows a reduction in snowfall over thick, poleward ice sheets due the temperature scaling (equation (3.25)). Lowest latitude snowfall occurs 38–48°N, with the interglacial value similar to present-day central continental regimes. Global temperature (weighted average by area) changes by 5–7 K; unfortunately data does not constrain mean global temperature well over geological times, but this value is in reasonable agreement with the local temperature proxies that exist for $\delta^{18}\text{O}$ [Kawamura et al., 2007], Ca/Sr [Beck et al., 1992], alkenones [Pelejero et al., 1999], or fossilised biomes [Rind and Peteet, 1985].

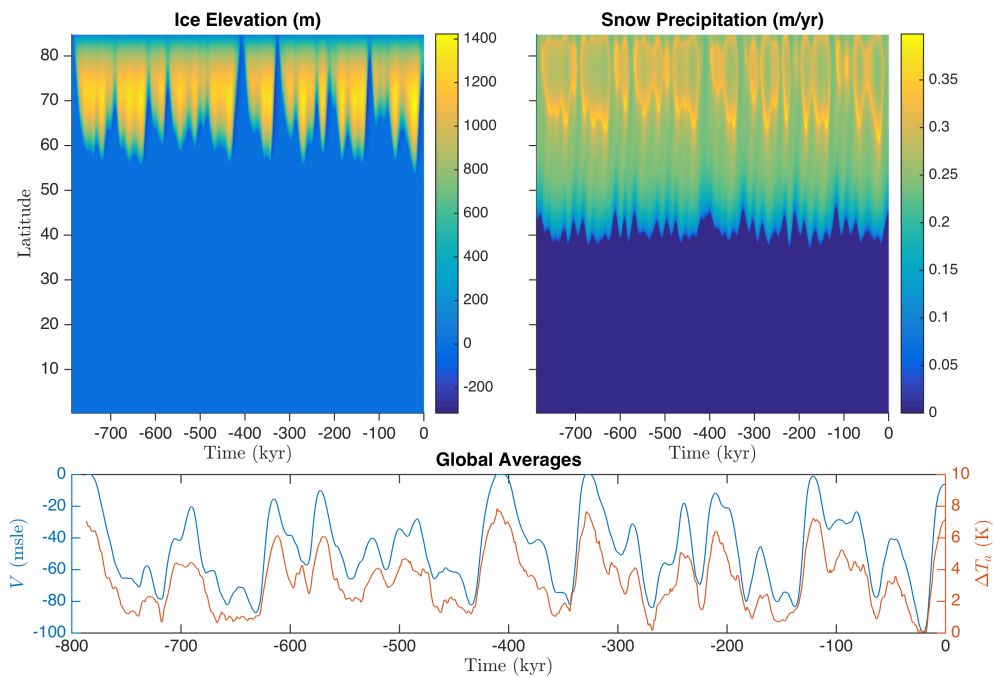


Figure 3.3: Plots showing Ice sheet configuration and precipitation over time (upper panels), and the change in global sea-level and mean temperature (lower panels). Data shown is a replication of historic glacial cycles (described in section 3.3.3).

3.3.3 Forcing with Historical CO₂ Values

In this section we consider a forcing based on reconstructed atmospheric CO₂ concentration, C , and insolation. For this scenario C is set to ice core values, rather than evolving according to equation (3.21). The scenario has two purposes: 1) validating our EBM and ice sheet model — the calculated ice sheet volume V should approximate reconstructed sea-level data, and 2) demonstrating our model’s V response to ~ 100 kyr C cycles — a benchmark for V when subsequent sections calculate C according to equation (3.21). These are both discussed below.

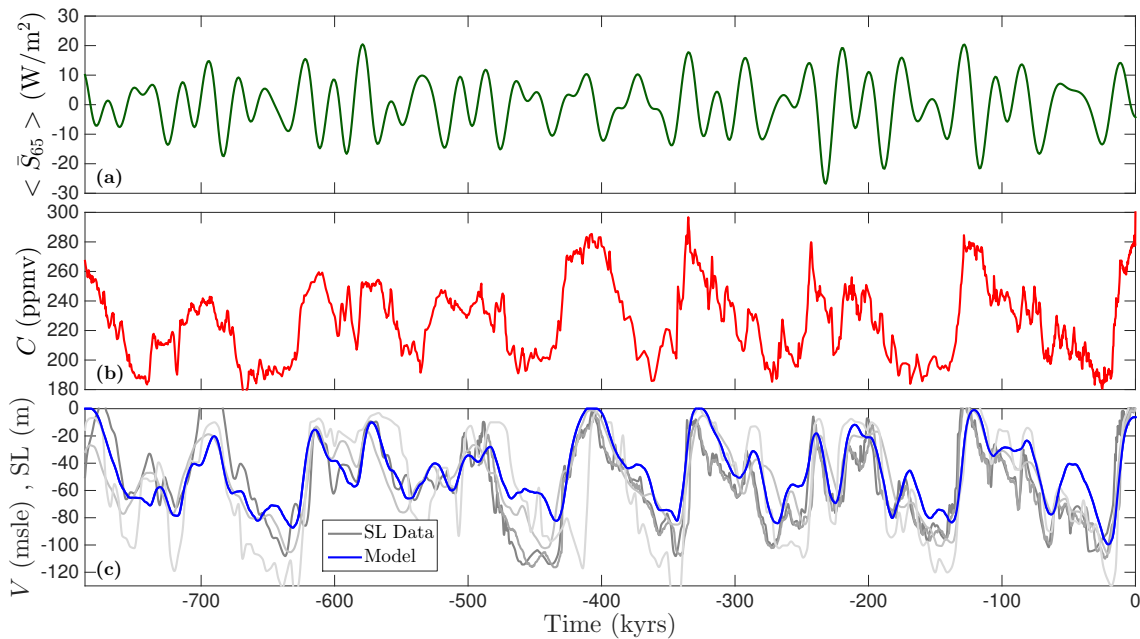


Figure 3.4: Model driven by insolation and ice core CO₂ values. Panel (a) shows mean summer half-year insolation at 65°N as deviation from the mean [Berger and Loutre, 1991]. Panel (b) shows atmospheric CO₂ concentration [Bereiter et al., 2015]. Panel (c) shows model ice volume V in metres sea level equivalent and reconstructed sea level from several sources. From dark to light grey these are Rohling et al. [2009], Elderfield et al. [2012] as compiled in Martinez-Boti et al. [2015], maximum probability Red-Sea record from Grant et al. [2014], and the $\delta^{18}\text{O}$ record decomposed into a sea level component by van de Wal et al. [2011] and Siddall et al. [2010]. Discrete Fourier transform of V gives power of 49.5% at 80–120 kyr periodicity, 23.4% at 40 kyr periodicity and 5.6% at 23 kyr periodicity.

Figure 3.4a and 3.4b show the insolation and C timeseries, and figure 3.4c shows the calculated ice volume V (blue). Ice volume is correlated to both insolation and C , as expected. Furthermore, the calculated ice volume is a good fit to reconstructed sea-level records (grey). The model’s most significant difference from sea-level records is a lower variability at high frequencies; part of this difference is noise in the data but part is probably rapid changes in ice sheets that our model does not capture. Despite this,

overall the timeseries in figure 3.4c are similar.

This similarity suggests the radiative forcings our model adds to Huybers and Tziperman [2008] are reasonable; we calculate realistic ice sheet configurations for actual insolation and C values. There are uncertainties in our WLC radiative forcing parameter (water vapour, lapse rate and clouds — discussed in section 3.A.3) due to the range in the tuning GCM cohort’s climate sensitivities. Across the plausible WLC forcing range, the maximum glacial varies from 75 m to 104 m. Changing WLC forcing does not introduce any novel model behaviour nor change the timing of turning points in V . Therefore we have confidence that our model behaviour is not contingent on peculiarly specific values of WLC forcing, and that our chosen value is physically plausible.

Figure 3.4c is a diagnostic for real-world glacial cycles in our model, demonstrating the ice volume timeseries that results from late-Pleistocene C and insolation. Our model calculates powers in the ice volume timeseries, at the 23, 41, and ~ 100 kyr periods of 5.6%, 23.4%, and 49.5% respectively, similar to the average of the displayed sea level data (4%, 10%, 55%). In section 3.4.2, we compare Fourier transforms of the ice volume timeseries from figure 3.4c and our full model system (forced purely by insolation, with C determined by equation (3.21)).

3.3.4 Forcing with Individual Historical Values

Another useful benchmark of model behaviour is forcing with just the insolation (constant CO_2 , 240 ppmv), and just the reconstructed atmospheric CO_2 concentration (constant insolation, 800 kyr average), and comparing to the result of section 3.3.3

In figure 3.5, our model calculates that CO_2 is the predominant influence on ice volume for the past 800 kyr¹. Table 3.1 quantifies this, showing that the power spectrum under both forcings is a weighted sum of, roughly, 70% CO_2 -only and 30% insolation-only spectra.

This is a somewhat surprising result, as the calculations of W/m^2 forcing are significantly larger for insolation than CO_2 at the canonical 65N latitude ($\pm 15 \text{ W}/\text{m}^2$ for mean half-year insolation, $\pm 4 \text{ W}/\text{m}^2$ for CO_2). However, this is not an apples-to-apples com-

¹To be clear, this is not a statement of causality; an imposed CO_2 timeseries does not address the reason for that CO_2 variation.

parison as CO_2 forcing is positive for the whole year, and insolation is highly seasonal. Furthermore, insolation at the top of the atmosphere is not the energy retained by the Earth system, which in our model is 43.7% of the top-of-atmosphere forcing for ice-covered ground (38.2% for non-icy ground, see section 3.2.1.2), reducing the effective insolation forcing on the Earth system to 6.5 W/m^2 , still 60% larger than the CO_2 forcing.

This dominant CO_2 effect suggests an emergent property in the model whereby the year-round CO_2 forcing has a much larger effect on ice-sheets than mean half-year insolation of a similar magnitude. This could be due to a magnifying effect from year-round coherent forcing, or it could be that the 65N metric does not accurately reflect the forcing on ice sheets². Controls on ice sheet balance are discussed further in section 3.A.8.

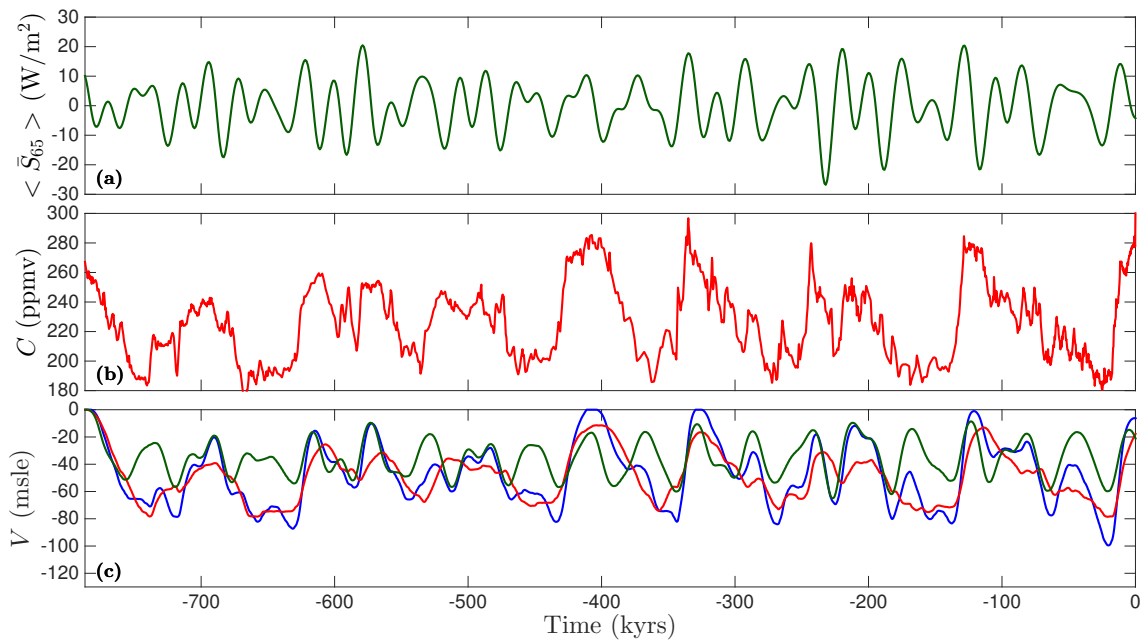


Figure 3.5: Model driven by insolation and ice core CO_2 values. Panels (a), (b) are identical to figure 3.4 — half-year insolation at 65N and atmospheric CO_2 concentration. Panel (c) shows model ice volume V in metres sea level equivalent for both forcings (blue), CO_2 -only (red) and Insolation-only (green).

²I don't think it is a coincidence that 65N is both the chosen forcing latitude and the most poleward latitude you can calculate without using more complicated formulations that handle polar-night / midnight-sun ($90^\circ - \max(\text{obliquity}) = 65.5^\circ\text{N}$).

Drivers	Power			Variance
	23 ka	40 ka	100 ka	
Inso-only	14%	70%	3%	190
CO ₂ -only	1%	4%	67%	340
Both	6%	23%	50%	550

Table 3.1: Diagnostic values for ice volume timeseries in figure 3.5

3.4 Results: Volcanic Interactions

Having explored the basic behaviour of the C-VICE model, the subsequent sections show the effects of including volcanism and a dynamically varying CO₂ concentration to the model.

3.4.1 Varying Mid-Ocean Ridge Lag

In this section we determine which MOR lag times disrupt the 40 kyr glacial cycles in the model, under simplified pure obliquity insolation forcing. This is a quantitative test of figure 3.1’s hypothesis that 30–50 kyr lags are capable of disrupting 40 kyr glacial cycles.

For this section, insolation is set to a 41 kyr sinusoidal obliquity variation, with eccentricity and precession fixed at their average values over the last 500 kyrs. Atmospheric CO₂ concentration is only affected by MOR CO₂ emissions; the temperature and subaerial-volcanism terms in eqn (3.21) are set to zero. However, the cumulative MOR CO₂ emissions change C by about 9 ppmv for 100 m sinusoidal sea-level at 41 kyr (see figure 3.2b), far less than the 100 ppmv glacial–interglacial C change. Therefore MOR sensitivity to sea-level γ_{MOR} is increased to 10 \times the values predicted in [Burley and Katz \[2015\]](#), facilitating C change up to about 90 ppmv.

Figure 3.1a shows the changes in ice volume periodicity for different MOR lag times over a 1.64 Myr model run, these results are presented as the power spectrum of ice volume (*i.e.* Discrete Fourier Transform ‘DFT’ of V). Figure 3.1b shows the final 300 kyrs of V for a subset of these results. For lag times less than 20 kyrs the V cycle remains at 40 kyrs, phase-locked to the insolation forcing. Increasing lags across 20–35 kyr gives the V DFT a subsidiary peak at progressively longer periods. For 40 kyr lag time the V cycle transitions to 80 kyr cycles (80 kyr term is six times the power of 40 kyr term). This

transition occurs because there are low points in C counteracting every second obliquity-driven deglaciation attempt, giving the ice volume timeseries shown in figure 3.1b. For lag times >40 kyr, V cycles have about equal power between 40 kyr and a >80 kyr cycle. For a 60 kyr MOR lag, there is a dominant cycle at 120 kyr.

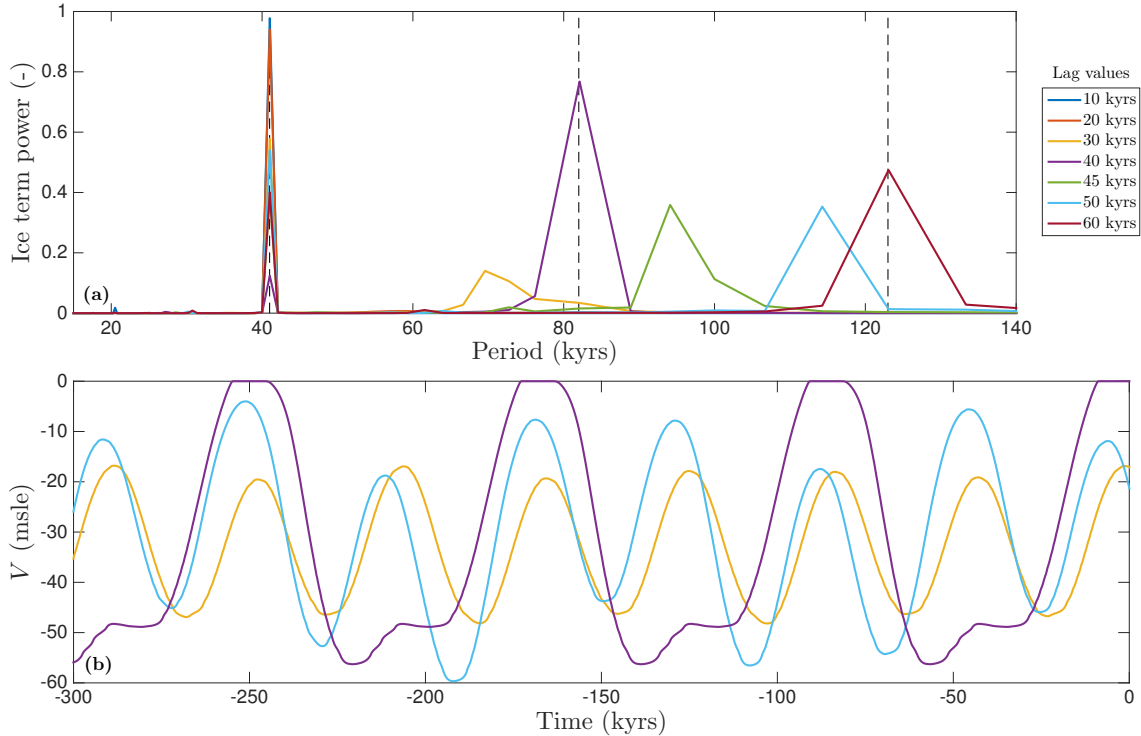


Figure 3.1: Model for different MOR lag times. Results use obliquity-only insolation, with γ_{MOR} non-zero and $\gamma_{\text{T}}, \gamma_{\text{SAV}} = 0$. Panel (a) shows the strength of DFT terms for the ice volume timeseries. The power spectra terms sum to unity. Panel (b) shows select ice volume timeseries over the final 300 kyrs of the model run. The dotted lines mark the 41 kyr obliquity period and its multiples. The mantle permeability range represented by the MOR lag values is 10^{-11} – $10^{-8.5}$ m² at 1% porosity.

We highlight two features of these results: firstly, they show that lag times < 20 kyr do not influence the periodicity of glacial cycles. This implies that C feedbacks operating at less than the < 20 kyr timescale (hereafter, short-timescale) do not affect the periodicity of glacial cycles.

We term these short-timescale feedbacks because they are shorter than the obliquity period (*i.e.* the default glacial cycle period). This is an important distinction, short-timescale feedbacks act on an intra-cycle basis, modulating the magnitude of glacial cycles and — in tandem with insolation — controlling the timing of peak climates (see the offset of different coloured sine peaks in figure 3.1b). However, the short-timescale feedbacks carry little information from one glacial cycle to the next and are therefore ineffective at

disrupting obliquity-linked 40 kyr cycles.

Thus, short-timescale C feedbacks only affect the magnitude of ice and temperature changes during glacial cycles; this is true for both negative C feedbacks (*i.e.* acts to oppose sea-level change) shown in this section and positive C feedbacks (see figures 3.A.10 and 3.A.11). Consequently, the model's glacial cycles are sensitive to the net C change caused by short-timescale C feedbacks, but relatively insensitive to how the C change is distributed on very short timescales. This helps justify our lumping surface system carbon feedbacks into a single parameter, and suggests we can be agnostic about how carbon feedbacks are distributed over short timescales if the net carbon change is correct (*i.e.* our model can have inaccurate γ_T and γ_{SAV} , provided that their collective effect on C is accurate). This reduces concerns about the uncertainty of the amplitude of SAV's CO₂ response to glacial cycles.

Secondly, these results largely support the concept that 30–50 kyr lags can disrupt 40 kyr glacial cycles. A smaller range of $\simeq 40$ kyr lag times generate sustained glacial cycles with 80 kyr periods and $\simeq 60$ kyr lag times generate glacial cycles with 120 kyr periods. Of these lag times, the 40 kyr MOR lag causes the most power in the ~ 100 kyr period band, and thus is the optimal lag for introducing ~ 100 kyr glacial cycles into an obliquity-dominated Earth system. To streamline results and discussion, we use this optimal 40 kyr lag time in subsequent sections. However, under real orbital forcing with power across a range of frequencies we expect a small range of lags to be similarly effective at disrupting 40 kyr cycles, because exact (anti-)resonance with 40 kyr orbital cycles will be a relatively less important effect.

These results provide us with the optimal MOR lag time for creating ~ 100 kyr glacial cycles, and demonstrate that our model system has no inherent 100 kyr periodicity until MOR CO₂ responses are introduced as an intercycle feedback. With the MOR lag time chosen, we now consider the effects of varying the strength of terms in our CO₂ feedback equation (3.21).

3.4.2 Full Model Behaviour

In this section all terms in our CO₂ model (eqn (3.21)) are active; atmospheric CO₂ concentration, C , varies according to our parameterised surface system and volcanic effects. Insolation forcing includes obliquity, precession, and eccentricity. We refer to this as the ‘full model’ configuration. We explore model behaviour by varying all three sensitivity parameters in the CO₂ equation (appendix 3.A.9 shows the model with only single carbon terms active). We first observe behaviour with timeseries plots, then use Fourier transforms of ice volume, V , to highlight the changing periodicity of ice volume as C feedback parameters are changed. Our benchmark for ~ 100 kyr cycles is figure 3.4c — the V timeseries calculated by our model when forced by both an imposed, ice-core CO₂ timeseries and insolation. We compare our DFT terms from the full model to this ‘ice core replication’ benchmark to determine if the model is producing ~ 100 kyr cycles.

Figure 3.2 shows how the full model varies with increasing γ_{MOR} . For $\gamma_{\text{MOR}} = 14$ MtCO₂/yr per cm/yr the model has reasonable amplitude C cycles (~ 80 ppmv) and generates V cycles with significant 100 kyr periodicity. Thus the amplitude of C cycles are reasonably close to late-Pleistocene values when the ‘full model’ is close to replicating the ice core ~ 100 kyr glacial cycles (this trend holds across sensitivity factor values). Increasing γ_{MOR} increases the magnitude of C cycles and adds greater 100 kyr variability. We now consider the periodicity of these model runs across a parameter sweep in the model’s three sensitivity factors γ_{T} , γ_{SAV} , and γ_{MOR} .

As mentioned above, we quantify the magnitude of the 40 kyr and ~ 100 kyr periodicities in ice volume by comparing them to the same periodicities (over the same time interval) in the model ice core replication shown in figure 3.4c. Specifically, we apply a discrete Fourier transform to each of these V timeseries and sum the terms in the frequency bands corresponding to 40 kyr and 80–120 kyr periodicity, then divide the ‘full model’ value by the ice core replication value — if the result is above 1 then there is more power present (in that frequency band) in the full model than there was in the calculated ice volume for Late-Pleistocene conditions. This parity criterion is marked with a red contour line in figure 3.3. For ~ 100 kyr cycles the minimum MOR emissions sensitivity to meet this parity criterion is $\gamma_{\text{MOR}} = 11$ MtCO₂/yr per cm/yr.

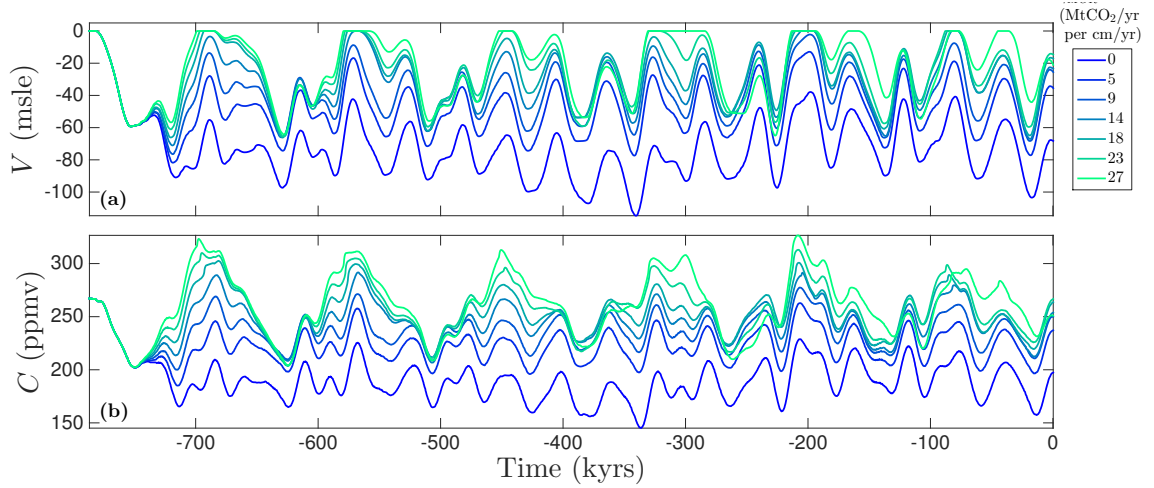


Figure 3.2: Increasing the sensitivity of MOR CO₂ emissions to sea level γ_{MOR} , with $\gamma_{\text{T}} = 10$ ppmv/K, $\gamma_{\text{SAV}} = 18$ MtCO₂/yr per cm/yr change in sea level. Panel (a) is ice volume in metres sea level equivalent. Panel (b) is CO₂ concentration in the atmosphere. The change dominant period occurs in both V and C as γ_{MOR} is increased, and occurs for the full time of the model run.

Figure 3.3 shows 40 kyr periodicity decreasing in strength for increasing γ_{MOR} , whilst the ~ 100 kyr periods increase in strength. This matches the predictions in prior sections and the behaviour in figure 3.2; MOR CO₂ emissions with a lag of 40 kyrs oppose every second obliquity cycle and create a stable feedback with an 80–120 kyr glacial cycle.

The trends in γ_{MOR} values that cause the full model to reach and exceed the parity criterion for ~ 100 kyr V cycles is as predicted in prior sections. Recall that MOR CO₂ emissions variations are directly proportional to the magnitude of sea-level change, and positive short-timescale intra-cycle feedbacks like γ_{T} and γ_{SAV} increase sea-level change. Therefore, the required γ_{MOR} value to match the parity criterion decreases as γ_{T} or γ_{SAV} increase. When trading off between γ_{T} and γ_{SAV} , a lower γ_{SAV} gives a lower minimum γ_{MOR} to reach parity for ~ 100 kyr cycles, shown by the top-right panel in figure 3.3 having the red parity contour reach lower γ_{MOR} values than in the lower-right panel.

For very high γ_{T} or γ_{SAV} , the V cycle amplitude increases. Runaway positive feedbacks in this limit (from larger ice sheets and decreasing temperatures) lead to a permanent glaciation, akin to a ‘Snowball Earth’. It is not clear if such runaway scenarios are reasonable representations of a marginal stability in the Earth system, or a model failure (*i.e.* parameterized feedbacks and forcings becoming inaccurate in very cold, low CO₂ conditions that have no parallel in the Pleistocene record). The largest stable γ_{T} values give model runs with sea-level changes of 85–100 metres, so our full model captures glacial

cycles with physical conditions similar to historical glacial cycles. Therefore we do not believe we are missing parameter space relevant to the Pleistocene.

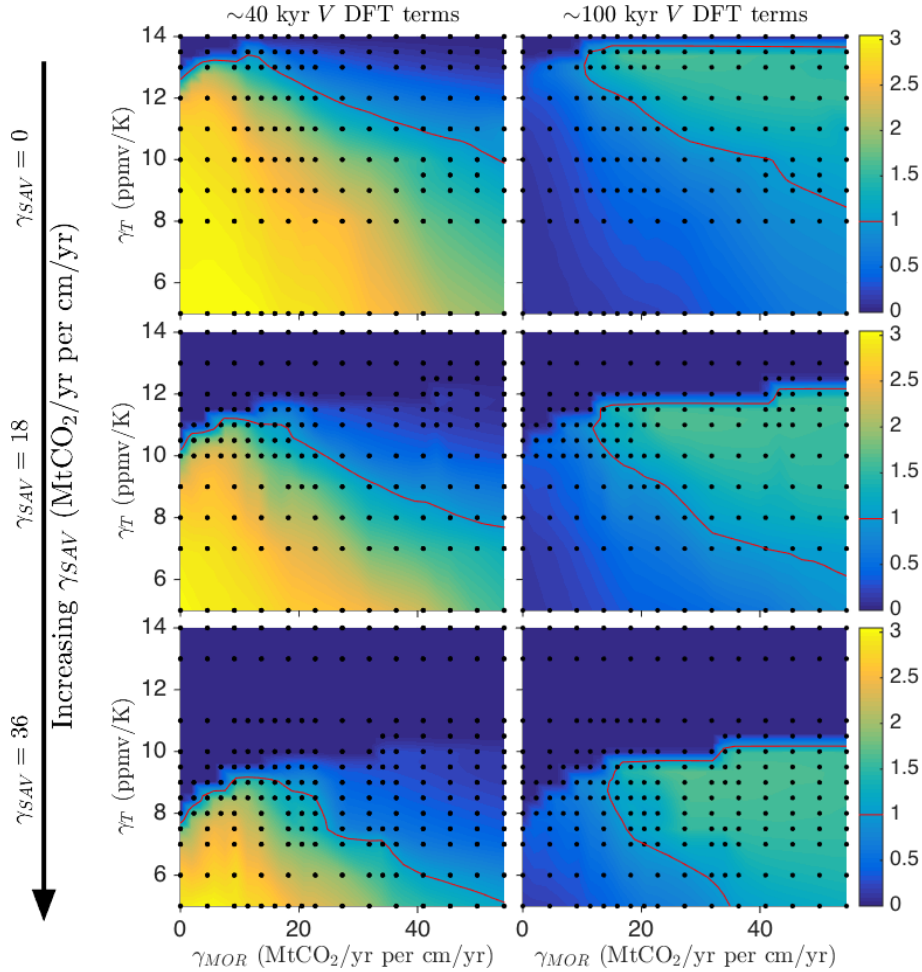


Figure 3.3: Periodicity of model runs for the last 787 kyr with $\gamma_{SAV} = 0, 18, 36$ MtCO₂/yr per cm/yr change in sea level for the three rows. Plots show the strength of terms in the discrete Fourier transform of ice volume relative to the model output in figure 3.4(a). The left plots show 40 kyr terms, the right plots 80–120 kyr terms. The red contour marks where the full model matches our modelled glacial replication. Dark blue marks where the model enters a runaway glacial event, we chose not to plot these as FFTs are not valid for timeseries that have a sharp change in periodicity partway through.

The power spectra for the full model at parity (*i.e.* near the red contour in figure 3.3) have power in the 23/41/100 kyr bands of 3%, 35%, and 50% respectively. Compared to our figure 3.4 ice core replication (5.6%, 23%, 50%), or sea-level data (4%, 10%, 55%) the full model is underpowered in the precessional band, and overpowered in the obliquity band. Despite this, the full model spectra (at parity) are a reasonable match for glacial cycles.

Overall, the full model system can switch from 40 kyr glacial cycles to ~ 100 kyr cycles, the calculated ~ 100 kyr cycles are stable (figure 3.2), and the minimum required

sensitivity of MOR CO₂ emissions to sea level is $\gamma_{\text{MOR}} = 11 \text{ MtCO}_2/\text{yr}$ per cm/yr change in sea level (figure 3.3). This γ_{MOR} requires MOR CO₂ emissions at the upper end of a 95% confidence interval (see section 3.5) according to most prior work, thus this γ_{MOR} value is possible, but not likely.

3.5 Discussion

We have presented a simplified model of climate through glacial–interglacial cycles. The model comprises three variables — temperature, ice sheet volume, and CO₂ concentration in the atmosphere — these evolve according to equations based on the physics of insolation, heat transfer in the atmosphere and Earth’s surface, radiative CO₂ forcing, ice flow under stress, proposed MOR CO₂ emissions processes, and parameterizations of the surface carbon system, subaerial volcanic CO₂ emissions, and water vapour plus cloud forcing. The model calculates glacial-interglacial behaviour with insolation as the sole driver of the system and CO₂ concentration in the atmosphere as an internal feedback. Although the model captures important and fundamental physics, it neglects many processes that may affect the results, which we discuss below.

We treat the atmosphere as a single layer and parameterise the net upward and downward longwave greenhouse effects. The parameterisation gives the overall energy balance between space, atmosphere, and ground but ignores changes in the internal atmospheric temperature structure. It is possible that important features are missed in this simplification, but our model does calculate reasonable present-day temperature distributions, seasonality (figure 3.2), CO₂-doubling scenarios (figure 3.3), and glacial replications (figure 3.4).

The ice model assumes a flat topography, distorted only by isostasy, and assumes no longitudinal variations in ice. Flat, low-lying topography suppresses initial ice formation and ignores the complexity of advancing ice sheets across the terrain of North America and Europe, but figure 3.4 shows our model replicating reconstructed sea-level timeseries, suggesting that the simplification is reasonable nonetheless. The computational complexity of the global 3D temperature and ice models required to relax these simplifying assumptions are too computationally expensive for Ma-scale studies; previous work on

glacial ice sheets made similar simplifications [Tarasov and Peltier, 1997, Fowler et al., 2013].

We do not explicitly include oceans in our model, they are implicitly incorporated into the temperature-dependent surface system term in equation (3.21). However, oceanic effects (that we have neglected) should reduce volcanism-driven C variations — extra absorption/venting of CO_2 to/from oceans when the atmospheric CO_2 concentration is out of equilibrium with the surface ocean. These are significant shortcomings, however there are no published ocean models that allow us to explicitly model oceanic CO_2 effects by dynamically replicating glacial-to-interglacial oceanic transitions. We believe the clear simplifications we make are better than building an ad-hoc ocean model. It would be an improvement to the current work if the qualitative ideas of glacial oceanic changes (iron fertilisation of the South Atlantic, shifting latitudes of southern ocean westerlies, changing relative deepwater formation rates in the North Atlantic vs. Antarctica, etc...) were included in an ocean model that makes quantitative changes to atmospheric CO_2 concentration.

We consider volcanic CO_2 emissions in our modelling, yet other glacially-driven volcanic changes could affect climate, such as subaerial aerosols, MOR hydrothermal flux, and Fe flux. It is not clear if including these extra volcanic effects in a model would affect the switch to ~ 100 kyr glacial cycles. If future research reveals any to have large climate feedbacks on 10's-of-kyr timescales, that would impact the conclusions of this work.

Our model is a deterministic system and, unlike geological records of glacial cycles, has no noise on (*e.g.*) < 200 year timescales. However, noise does not effect our model's conclusions. When we introduce noise in input parameters, we see no change in qualitative model behaviour (appendix 3.A.10).

Even after accounting for simplifications, our model gives insight into glacial–interglacial behaviour. Previous work takes dependent variables in the earth system (temperature, atmospheric CO_2 concentration, ice extent) and uses them as independent driving variables — clearly shortcomings when considering the highly coupled glacial system whose key features emerge on the 10s-of-kyrs timescale. This model addresses those features, with space for uncertainties to be reduced or further mechanisms explored.

We see a sharp distinction between climate feedbacks acting at significantly less than the glacial period (short-timescale feedbacks) and those acting at or above the glacial timescale. Short-timescale C feedbacks are intracycle effects that modulate the magnitude of each glacial, but because they carry little information from one glacial cycle to the next, are ineffective at changing overall glacial periodicity.

Our model finds transitions from 40 kyr cycles to ~ 100 kyr cycles as we increase MOR CO_2 emissions response to rate-of-sea-level-change (*i.e.* increasing γ_{MOR}). There is no significant 100 kyr variability without the intercycle feedback from MORs. The transition mechanism is atmospheric CO_2 concentration (influenced by MOR CO_2 emissions) acting to suppress a glacial–interglacial transition triggered by insolation. The subsequent increase in sea-level periodicity from 40 kyrs to 80–120 kyrs approximately doubles the magnitude of MOR CO_2 variability (fig 3.2), and short-timescale C feedbacks reinforce the new cycle and produce large C changes that dominate insolation such that only every second or third obliquity cycle causes major deglaciation.

This transition mechanism inherently generates sawtooth patterns in V (fig 3.1b), describing a growing ice sheet, interrupted growth (when C and insolation are in opposition), followed by further growth, and then a large deglaciation.

Our model’s transition to 80–120 kyr glacial cycles is broadly consistent with the coupled oscillator model of Huybers and Langmuir [2017], suggesting analogous behaviour may govern our system.

Under optimal conditions the model transitions to ~ 100 kyr cycles at $\gamma_{\text{MOR}} = 11 \text{ MtCO}_2/\text{yr}$ per cm/yr change in sea level. Physically this corresponds to MOR emissions of $91 \text{ MtCO}_2/\text{yr}$ changing up to $\pm 12\%$ across a glacial cycle, or (recalling that our γ_{MOR} is linear in baseline emissions and percentage change) a scaled equivalent *e.g.* $137 \text{ MtCO}_2/\text{yr}$ changing up to $\pm 8\%$. Are these volcanic numbers feasible? For our specified MOR lag time, we predict $\gamma_{\text{MOR}} = 8\%$ with little room for error (uncertainties in the model inputs would not change predicted γ_{MOR} by ± 1 percentage point), thus we must ask if $137 \text{ MtCO}_2/\text{yr}$ is a reasonable baseline global MOR CO_2 emissions rate.

It is worth considering global MOR CO_2 emissions in some detail, given the diverse literature. There are two approaches to estimating global MOR CO_2 flux, all based around

measuring an element that has a constant ratio to CO₂ in volcanic eruptions, then using that fact (plus other assumptions) to calculate CO₂ emissions: 1) use the concentration of an element in ocean water to infer the rate of MOR CO₂ emissions. The element must have a known lifetime in the ocean (preferably with no non-volcanic inputs). 2) use the concentration of an element in volcanic rocks to infer the CO₂ concentration in the source mantle. Then apply a melting fraction to generate an erupting mantle composition from the source mantle, and multiply by the volume of mantle erupted per year to calculate the rate of MOR CO₂ emissions. The first approach has a single method, ³He in the oceans, which has settled to values of 0–134 MtCO₂/yr [Resing et al., 2004] and 18–176 MtCO₂/yr [Marty and Tolstikhin, 1998] (2 std.dev.). Updated ³He flux values from Bianchi et al. [2010] would change these values to 0–101, and 9–93 MtCO₂/yr respectively. For the second approach, the most recent work combining ratios of Nb, Rb and Ba for melt inclusions calculates 18–141 MtCO₂/yr (2 std.dev.)³ [Le Voyer et al., 2017]. Work using the undegassed Siqueiros melt inclusions calculates 29–53 MtCO₂/yr (2 std.dev.) [Saal et al., 2002a] (the Siqueiros melt inclusions may be highly depleted, implying their derived global emissions value is an underestimate) and volcanic glasses give 88–158 MtCO₂/yr (2 std.dev.) [Michael and Graham, 2015]. There could be systematic error in some of these measurements, particularly given the sensitivity of the latter approaches to the assumed average mantle melt fraction used to generate MOR basalts (*i.e.* erupting mantle composition) from the MOR mantle source [Cartigny et al., 2008, Dasgupta and Hirschmann, 2010, Le Voyer et al., 2017], as I discussed previously in section 2.A.5. Furthermore, none of these studies include uncertainty in the degree of melting in their random error, so errors are likely underestimated. Using the latest melting models, Keller et al. [2017] calculate a range of 53–110 MtCO₂/yr for CO₂ concentration in the MOR mantle source is 100–200 ppmw. Extrapolating linearly (a vast simplification) to a 2- σ range in CO₂ concentration of 27–247 ppmw [Le Voyer et al., 2017] gives 14–135 MtCO₂/yr. Our required emissions of 137 MtCO₂/yr is at the high end of the 95% confidence interval for some of these studies, therefore it is possible, although not likely, that the global MOR CO₂

³However, this paper does not give the crust density they use to calculate emissions from their source mantle CO₂ concentration. Assuming a crustal density of 2900 kg/m³ [Carlson and Raskin, 1984] and using their stated values of 27–247 ppmw, $F = 0.1$, and 21 km³/yr crustal production gives emissions of 16–150 MtCO₂/yr, rather than 18–141 MtCO₂/yr.

emissions rate is large enough to disrupt glacial cycles, assuming no oceanic moderation of volcanic emissions.

However, if we assume volcanic CO₂ variability's effect on C is damped by oceanic absorption/emission, then the required MOR parameters are outside the expected range. This 'oceanic damping' logic is based on the idea that the surface ocean and atmospheric CO₂ are in equilibrium, and that any attempt to change the atmospheric CO₂ concentration is opposed by changes in ocean chemistry. Such logic represents anthropogenic carbon changes well, but glacial cycles probably involve changes in the physical ventilation of the oceans, making the comparison inexact; modern models are a worst case scenario. Regardless, modern Earth system models [Archer et al., 2009] suggest a factor of 4 increase in required background MOR emissions — necessitating 548 MtCO₂/yr, outside the upper limits of MOR CO₂ emissions. Even a factor of 1.5 increase would require unreasonable MOR CO₂ emissions. Therefore despite the uncertainty in oceanic CO₂-damping effects, background MOR CO₂ emissions are very unlikely to meet the requirements for ~100 kyr cycles after accounting for ocean absorption.

The magnitude of changes in MOR and SAV CO₂ emissions are proportional to the magnitude of sea-level change, and MOR CO₂ emissions increase for longer period sea level changes. Therefore, if MOR CO₂ emissions are part of the transition mechanism from 40 to 100 kyr glacial cycles, the model suggests the following: 1) transitioning to ~100 kyr glacial cycles will increase the magnitude of CO₂, sea-level, and temperature changes — including warmer interglacial periods, and 2) a relatively large sea level change should precede the transition to longer glacial cycles.

This process of volcanic CO₂ emissions altering glacial cycles is consistent with the results of Tzedakis, P.C. et al. [2017], where the summer insolation required to trigger full deglaciation increases across -1.5 Ma to -0.6 Ma (after accounting for discount rate, whereby deglaciation has a lower insolation threshold the longer an ice sheet has existed). Their discount rate is conceptually consistent with ice sheet instability as explained in Clark and Pollard [1998], Abe-Ouchi et al. [2013], however the changing insolation threshold is not readily explained by existing theories. A plausible explanation is a feedback cycle whereby an increase in the magnitude of sea-level changes leads to increased volcanic

CO₂ emissions response (thus amplifying CO₂ and temperature variations), that further amplifies the next sea-level cycle. This eventually changes the period of sea-level cycles as MOR CO₂ emissions variability becomes larger, leading to further increases in MOR CO₂ emissions and even larger sea-level cycles, until the system reaches a new steady state with large, long period sea-level cycles. The feedback between volcanism and sea-level would take several glacial cycles to reach a new equilibrium, consistent with the 900 kyr transition time proposed in [Tzedakis, P.C. et al. \[2017\]](#).

3.6 Summary

I have presented a 2D model system ‘C-VICE’ that calculates the Earth climate over the past 800 kyrs; a system with ice sheets, CO₂ concentration in the atmosphere and other forcings evolving in response to imposed insolation changes. I demonstrated a match to current planetary temperatures and GCM CO₂ doubling forecasts. When driven with observed CO₂, the model reproduces the glacial sea-level record.

My main research interest was quantifying the mid-ocean ridge (MOR) CO₂ emissions sensitivity to sea-level change necessary to induce ~ 100 kyr glacial cycles, thus assessing the plausibility of volcanic mechanisms for creating an Earth system climate response not linearly related to insolation forcing.

The C-VICE model has no intrinsic 100 kyr variability until the lagged response of MOR’s CO₂ emissions to sea level change is included; default behaviour is 40 kyr glacial cycles. We calculate that MOR CO₂ variability, above a threshold sensitivity to sea-level change, causes glacial cycles at a multiple of insolation’s 40 kyr obliquity cycle. These ~ 100 kyr cycles are asymmetric, and occur at both 80 kyr and 120 kyr periods, replicating features of the late-Pleistocene glacial record.

However, even under optimal conditions, ~ 100 kyr cycles require MORs’ CO₂ emissions response be 11 MtCO₂/yr per cm/yr rate of sea-level change, 50% higher than the expected 7.3 MtCO₂/yr per cm/yr. This requires background MOR CO₂ emissions of 137 MtCO₂/yr, within the 95% confidence interval of (some) estimates of MOR CO₂ flux. However, under less optimal conditions where oceanic effects moderate MOR emissions’ effect on C , required baseline MOR CO₂ emissions are over 200 MtCO₂ per year — highly

improbable. This suggests that MOR CO₂ emissions are not, in isolation, responsible for glacial cycles > 40 kyrs.

Of course, MOR CO₂ emissions do not act in isolation, and there are relevant glacial mechanisms that do not operate in our model, including regolith erosion [Clark and Pollard, 1998], secular CO₂ decline [Pagani et al., 2010, Hönisch et al., 2009], and switching modes in ocean ventilation [Franois et al., 1997, Toggweiler, 1999]. These mechanisms may interact with our existing processes to allow glacial cycles at lower MOR CO₂ variability. However, adding such mechanisms would increase model complexity; furthermore, these mechanisms are not precisely defined and would necessitate a wide range of representative models and parameter sweeps. Thus it is unlikely that a mixed mechanism hypothesis for ~100 kyr glacial cycles can be tested until each mechanism is more precisely defined.

Our model system highlights other important features. First, we calculate that the net changes in atmospheric CO₂ concentration caused by MOR volcanism will approximately double when sea-level periods increase from 40 kyrs to 100 kyrs. Therefore, if a ~100 kyr glacial cycle occurs, MOR volcanism acts to reinforce that periodicity.

Second, our model makes a distinction between intracycle and intercycle feedbacks. An intracycle feedback is a process with a timescale less than half the glacial cycle period; therefore acting within a glacial cycle. Intracycle feedbacks affect the magnitude of glacial cycles, but cannot change the glacial periodicity. This result will hold for any feedback process with constant sensitivity.

Third, we found that MOR systems with a 40 kyr lag between sea-level change and consequent CO₂ emissions generate 100 kyr cycles at the lowest γ_{MOR} . However, any intercycle feedback in the Earth system can potentially generate ~100 kyr cycles, and we calculate significant power at ~100 kyr for MOR lags of 30–80 kyrs. Therefore the proposed volcanic mechanism for 100 kyr glacial cycles is not dependent on a peculiarly specific MOR lag value (equivalently, a particular mantle permeability).

Finally, without strong MOR CO₂ emissions sensitivity, our model defaults to an obliquity-linked glacial cycle with a 40 kyr period; precession's 23 kyr cycle has little effect on the ice sheet. This result is in agreement with previous work considering integrated summer forcing, and is the first time that 40 kyr response has been shown dominant

in a model with radiative feedbacks. Therefore our model opposes the hypothesis that precession-linked glacial cycles may have occurred before the mid-Pleistocene transition, with anti-phase changes in Antarctic and Greenland ice mass at the 23 kyr period leaving a predominant 41 kyr signal in the $\delta^{18}\text{O}$ record [Raymo et al., 2006].

The model's conclusion could be sensitive to some of our simplifications, such as the oceans' interaction with volcanic emissions on glacial timescales and the climate effect of other variable volcanic elements. However, these effects are all beyond current understanding and it is hard to predict their effect on our model. Complete understanding of glacial cycle dynamics will require models including several of the mechanisms currently proposed in literature.

Appendix

3.A Supporting Materials

3.A.1 EBM Modifications

We make two major changes to the EBM scheme of [Huybers and Tziperman \[2008\]](#): adding longwave radiative forcings based on atmospheric composition, and creating a variable precipitation based on local temperature. These are explained below.

First we discuss our longwave radiative modifications; adding forcings representing CO₂, water vapour, lapse rate, and cloud effects. These radiative forcings are treated with two terms: one for the CO₂ forcing, and another for the aggregate effects of water vapour, lapse rate and cloud forcings. We add these forcings to a single-layer atmosphere that has an imposed linear temperature profile dT/dz of 6.5 K/km. The base of the atmosphere is at the ground surface (land or the top of an ice sheet). The upper surface of the atmosphere is the mean height at which the atmosphere becomes transparent to longwave radiation and allows longwave emissions to escape to space. In the model's neutral state, this is 6.5 km above sea level, well within the troposphere's linear temperature profile. Therefore, changes in the height of the mean emissions layer will change its temperature; this changes the power of longwave emissions to space according to the Stefan-Boltzmann law.

Greenhouse gas forcing occurs because such gases alter the height at which atmosphere becomes transparent to longwave radiation. Our model scheme is guided by this physics; implementing top-of-atmosphere forcing by altering the height of the emissions layer.

The upward longwave (ULW) radiative CO₂ forcing is derived from [Myhre et al. \[1998\]](#)

global mean forcing,

$$\bar{R}_{\text{ULW}} = \lambda \log_2 \left(\frac{C}{C_0} \right) , \quad (3.22)$$

where \bar{R}_{ULW} is the global average radiative forcing (we use R instead of typical forcing terminology ‘ F ’ to avoid confusion with the EBM’s heat flux terms), λ is CO₂ sensitivity in W/m² per CO₂-doubling, and $C_0 = 280$ ppmv is the reference concentration of CO₂ in the atmosphere. We follow the conclusions of [Stap et al. \[2014\]](#) and [Köhler et al. \[2010\]](#) for greenhouse forcing in the Pleistocene and assume a 30% increase in CO₂ forcing magnitude from synchronous increases in other greenhouse gases. Thus λ is 4.85 W/m² per CO₂-doubling.

We convert this global average forcing to a latitude-dependent forcing R_{ULW} by changing the height (and therefore temperature) of the atmospheric layer emitting longwave radiation to space — details are given in appendix [3.A.2](#). A reasonable summary is to consider a global temperature change of the emitting layer ΔT (assumes dT/dz independent of ϕ), changing Stefan-Boltzmann emissions by $(T_{ul} + \Delta T)^4 - T_{ul}^4$. Upper atmosphere temperature T_{ul} varies with ϕ , and the forcing is thus latitude-dependent. This forcing is applied to the net infrared energy balance of the atmosphere in equation [3.24](#) below.

DLW is parameterized to match the calculations in [Cai and Tung \[2012\]](#) of longwave CO₂ forcing at the bottom of the atmosphere in a 2D GCM. Our parameterised equation is a logistic function and an exponential

$$R_{\text{DLW}} = K \left(\frac{1}{1 + e^{(a-\phi)/b}} + \frac{e^{(-\phi/c)}}{3} \right) , \quad (3.23)$$

where K is the maximum forcing, $a = 30^\circ$ is the latitude of the logistic function turning point, b scales the width of the logistic function’s growth region and c scales the e-fold length of the decreasing exponential. For a given CO₂ concentration, K is equal to the maximum value of R_{ULW} .

We model the combined global energy balance effects of water vapour, lapse rate and clouds as a radiative longwave forcing, varying linearly with changes in \bar{T}_a from preindustrial conditions. This combined forcing is a parameterisation such that our model matches

the climate sensitivity of general circulation models for a CO₂ doubling from preindustrial conditions — details are given in section 3.A.3. We extrapolate from CO₂ doubling experiments and assume that the net water vapour, lapse rate, and cloud feedback is also linear for glacial–interglacial climate changes; literature does not yet have significant statistical proof or opposition to this assertion [Bony et al., 2015, Braconnot and Kageyama, 2015, Harrison et al., 2015, Hopcroft and Valdes, 2015, Harrison and Bartlein, 2016]. Having defined our radiative forcings, we now incorporate them into the EBM longwave balance.

The net longwave radiation balance of the atmosphere I_a has three terms representing, respectively, the longwave emissions from the ground (absorbed by the atmosphere), emissions from the atmosphere to the ground, and emissions from the atmosphere into space. Applying the collective radiative forcings to I_a gives

$$I_a = \sigma T_s^4 - (\epsilon_a \sigma (T_a - \Gamma_m H_{as})^4 + R_{DLW}) - \epsilon_a \sigma (T_a + \Gamma_m (H_{ul} + \Delta z_C + \Delta z_{WLC}))^4, \quad (3.24)$$

where σ is the Stefan-Boltzmann constant, ϵ_a is atmospheric emissivity, T_a is the temperature of the middle atmosphere, Γ_m is the temperature profile in the atmosphere dT/dz , H_{as} is the middle-atmosphere-to-surface height, H_{ul} is the default middle-atmosphere-to-upper-layer height, Δz_C is the change in upper layer height due to CO₂ concentration in the atmosphere, and Δz_{WLC} the change in upper layer height modelling the parameterised water vapour, lapse rate, and cloud feedbacks.

Finally, we consider the EBM’s precipitation model. Precipitation rate is used to track snowfall in the EBM, with snow falling when the atmosphere at ground level is below 0°C (precipitation above 0°C is ignored).

We change the Huybers and Tziperman [2008] model’s fixed 1 m/yr precipitation rate to a temperature-dependent precipitation rate, calculated at each timestep and gridcell in the EBM. This more realistic precipitation model was introduced to limit the growth of very large ice sheets (equivalent to > 150 m sea-level change) that occurred under the fixed precipitation rate, driven by unrealistically high 1 m/yr snowfall on 3 km thick ice

sheets at 70-80N. Our precipitation model is

$$P = \begin{cases} P_c e^{(\frac{T}{20}-1)} & \text{if } \phi \geq 50^\circ \\ P_c e^{(\frac{T_{50}}{20}-1)} & \text{if } \phi < 50^\circ \end{cases}, \quad (3.25)$$

where P is precipitation in m/yr, $P_c = 2$ m/yr is a scaling constant, T is surface air temperature in Celsius and T_{50} is temperature at 50° latitude. The $T/20$ scaling and P_c value are derived from an exponential best-fit to the ERA-interim reanalysis product (D. Battisti – pers. comm.). Physically, this exponential parameterisation represents the decreasing vapour saturation of colder air leading to reduced precipitation [Pierrehumbert et al., 2007], although we skip the details of why air remains near vapour saturation and the complexity of tracking moisture from source to sink. Using T_{50} to determine precipitation below 50° enforces mid-latitude deserts. What about the tropics? Across glacial-to-interglacial conditions our model has lowest-latitude snowfall occurring between 38-48N; thus the parameterisation does not artificially reduce tropical snowfall — the tropics are snow-free even in glacial conditions.

Equation (3.25) has the consequence that thick, cold ice sheets become drier during a glacial period, as expected (see figure 3.3).

3.A.2 Calculating Radiative CO₂ Forcing

The reference model for the radiative CO₂ effect uses a combination of line-by-line, narrow-band and broad-band radiative transfer schemes [Myhre et al., 1998] that produces the simple parameterisation of equation (3.22) with a logarithmic scaling. Here we describe how this radiative forcing is incorporated into our energy balance model.

Equation (3.22)'s forcing \bar{R}_{ULW} is a planetary average, if applied uniformly it would overestimate radiative CO₂ forcing at the poles and underestimate near the equator. We instead calculate the change in the average temperature of the emitting layer of the atmosphere $\Delta\bar{T}$ required to match \bar{R}_{ULW} . Then we convert $\Delta\bar{T}$ to an equivalent change in height of the emitting layer (*i.e.* the height above which the atmosphere is optically thin to IR radiation). This is consistent with the physics of higher CO₂ concentrations

making the atmosphere optically thicker to IR radiation.

This is derived below, beginning with a perturbation to a default state ‘0’.

$$F_0 + \bar{R}_{\text{ULW}} = \epsilon_a \sigma (T_0 + \Delta\bar{T})^4 , \quad (3.26)$$

$$F_0 + \lambda \text{Ln}(C/C_0) = \epsilon_a \sigma (T_0 + \Delta\bar{T})^4 , \quad (3.27)$$

where F_0 is the unperturbed longwave radiative flux to space, T_0 is the mean temperature of the emitting layer of the atmosphere, and \bar{R}_{ULW} is from eqn (3.22). Thus the perturbation is:

$$\lambda \text{Ln}(C/C_0) = \epsilon_a \sigma (4T_0^3 \Delta\bar{T} + 6T_0^2 \Delta\bar{T}^2 + 4T_0 \Delta\bar{T}^3 + \Delta\bar{T}^4) . \quad (3.28)$$

Equation (3.28) is fourth order in $\Delta\bar{T}$ and thus computationally expensive. However, $\Delta\bar{T} \ll 0.1\bar{T}$ thus terms above second order change the RHS by less than 1%, and we instead solve a quadratic in $\Delta\bar{T}$. Thus equation (3.28) becomes:

$$\Delta\bar{T} = \frac{-T_0^2 \pm \sqrt{T_0^4 - \frac{3\lambda}{2\epsilon_a \sigma} \text{Ln}(C/C_0)}}{3T_0} . \quad (3.29)$$

Finally, using the linear temperature profile $\Delta\bar{T} = -\Gamma_m \Delta z_C$, discarding the nonsensical solution and rearranging

$$\Delta z_C = \frac{T_0}{3\Gamma_m} \left(1 - \sqrt{1 - \frac{3\lambda}{2\epsilon_a \sigma T_0^4} \text{Ln}(C/C_0)} \right) , \quad (3.30)$$

where Δz_C is the change in height of the emissive layer of the atmosphere and is constant with respect to latitude. To illustrate how equation (3.30) relates to climate: if $C > C_0$ then $\text{Ln}(C/C_0)$ is positive, the square root is a small positive number, and Δz_C is positive — thus the emitting layer becomes higher and colder, reducing radiative emissions to space, and forcing the planet to warm to re-establish equilibrium (as expected for an increase in CO_2).

3.A.3 Calculating Other Radiative Forcing

Over glacial–interglacial cycles CO_2 forcing is not the only significant radiative effect, there are contributions from water vapour, lapse rate, and clouds (subsequently WLC). Unlike CO_2 forcing, the WLC contributions do not have well-established, simple parameterised equations (see equation (3.22)) to predict their effects. In this section we discuss how WLC forcings are incorporated into our model.

The most detailed modelling of WLC effects on planetary temperature comes from general circulation models forecasting the global warming over the next 100 years, and we can extract a parameterisation from these models. Parameterisation is required because the actual water vapour, lapse rate, and cloud schemes in GCMs are too computationally expensive for our model goals. Fortunately these models' results can be compiled into the following equation, assuming each mechanism operates as an independent linear perturbation feedback on average planetary temperature.

$$\Delta\bar{T}_a = \lambda_0\Delta\bar{R}_{\text{ULW}} + f_{\text{net}}\Delta\bar{T}_a \quad , \quad (3.31)$$

$$\Delta\bar{T}_a = \lambda_0\Delta\bar{R}_{\text{ULW}} + f_{\text{wv}}\Delta\bar{T}_a + f_{\text{lr}}\Delta\bar{T}_a + f_{\text{c}}\Delta\bar{T}_a + f_{\text{a}}\Delta\bar{T}_a \quad , \quad (3.32)$$

where Δ denotes a change in a quantity, f_x are unitless feedback parameters operating: f_{net} in total, f_{wv} from water vapour, f_{lr} from lapse rate, f_{c} from clouds, and f_{a} from surface ice albedo. R_{ULW} and T_a are as defined previously.

Using equation 3.32 GCMs show f_{net} range 0.49–0.73. Our model's $\lambda_0\Delta\bar{R}_{\text{ULW}}$ and f_{a} under modern insolation conditions comparable to GCM runs are 1.08 K per CO_2 doubling and 0.273 respectively. With these we calculate the cumulative water vapour, lapse rate, and cloud feedbacks f_{WLC} required for our model to be in line with GCM f_{net} values using $f_{\text{net}} = f_{\text{WLC}} + f_{\text{a}}$. This gives a f_{WLC} range 0.22–0.46.

Now we consider how to incorporate this WLC feedback in our model. f_{WLC} cannot be directly used in our EBM because it describes the equilibrium state — the increase in equilibrium average planet temperature from WLC effects per Kelvin increase in average planet temperature from other effects — rather than a forcing that causes the equilibrium

state. We calculate a longwave radiative forcing that will have the equivalent effect on equilibrium temperature $\bar{R}_{\text{WLC}} = f_{\text{WLC}}/\lambda_0$; this global average radiative forcing is included in the model by the same procedure described in section 3.A.2. This method assumes WLC radiative effects can be linearly superimposed with longwave CO₂ forcing. Having chosen the method, we must select a f_{WLC} value from within the available range.

We select a value of $f_{\text{WLC}} = 0.42$ to optimise the model's replication of the sea level record when forced with ice core CO₂ values (see figure 3.4); the model's overall feedback is 0.69, at the upper end of the GCMs' range.

To summarise, our WLC parameterisation creates a mean global forcing proportional to the current deviation from mean preindustrial temperature. The mean global forcing in this parameterisation is chosen to match the climate sensitivity of GCMs for CO₂-doubling experiments, giving us high confidence of accuracy on this metric.

However, we extrapolate assuming the forcing is linear with respect to temperature across the full glacial–interglacial climate variability; literature does not yet have significant statistical proof or opposition to this assertion [Bony et al., 2015, Braconnot and Kageyama, 2015, Harrison et al., 2015, Hopcroft and Valdes, 2015, Harrison and Bartlein, 2016]. The good match we obtain to sea-level records in figure 3.4 supports this assertion.

The WLC forcing is applied by changing the mean height of longwave emissions to space. Consequently, WLC forcing has the same latitudinal pattern as CO₂ forcing. Is this accurate for each of the three components?

For water vapour it is probably reasonably accurate; the mechanism of changing atmospheric concentration affecting the longwave optical thickness of the atmosphere applies to both CO₂ and H₂O. Although H₂O has a less homogenous distribution across latitudes, which may introduce some differences.

Lapse rate affects longwave emissions by changing dT/dz , causing a forcing equivalent to changing the height of the emissions layer. Assuming that the change in lapse rate is latitude independent, the lapse rate effect is physically consistent with WLC forcing. However, it is not clear that changes in lapse rate will be latitude independent.

Cloud forcing is the least understood of these feedbacks [Soden and Held, 2006, Stocker, 2013], but it is likely that high latitudes experience greater cloud forcing feedbacks [Cronin

and Tziperman, 2015], unlike our WLC forcing. Furthermore, clouds affect both the longwave and shortwave radiation balance, and we only represent a longwave effect. A cloud model calculating changes to the atmospheric shortwave parameters would interact with insolation (*e.g.* an increase in low-altitude high-latitude clouds increases shortwave reflectivity, therefore changes in insolation would have a reduced effect at high latitude); potentially creating emergent behaviours that are not captured our model. The redeeming feature of our cloud parameterisation is that it matches the average global cloud forcing of a GCM cohort.

We believe our WLC forcing model represents radiative water vapour forcing and lapse rate forcing well, but cloud forcing poorly. In the Soden and Held [2006] model comparison, water vapour, lapse rate and cloud feedbacks are, respectively, 1.8, -0.84, and $0.68 \text{ Wm}^{-2}\text{K}^{-1}$. Therefore we capture the effect of the largest forcing contributions. We believe this represents a reasonable approximation for our low-complexity modelling framework.

3.A.4 Model Timestep and Resolution

This section verifies our choices of timestep and grid-spacing, showing that the model has converged at the limits chosen.

Figure 3.A.1 demonstrates that reducing the interval over which the ice model is run (between EBM recalculating temperature) from 250 to 100 years does not change model results. Therefore the interval has converged for our chosen value of 250 yrs.

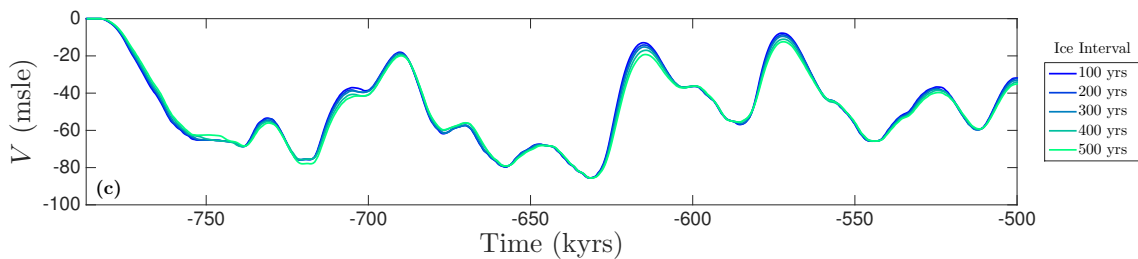


Figure 3.A.1: Effect of varying ice model interval.

Figure 3.A.2 demonstrates that reducing our ice model timestep from 5 years to 1 year does not significantly affect the results (and that 10 year timesteps create transient instabilities). Therefore the timestep has converged for our chosen value of 2 yrs.

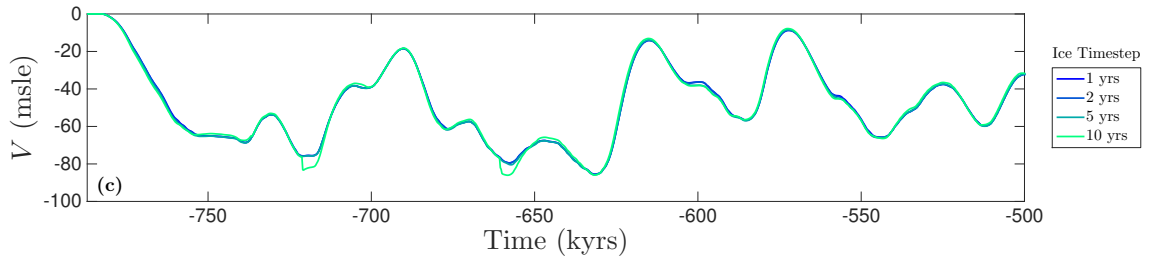


Figure 3.A.2: Effect of varying ice model timestep.

Figure 3.A.3 demonstrates that the model’s latitudinal grid has largely converged for our chosen value of 0.5° (56 km). There are accuracy gains made by using a finer, 0.25° grid, however this leads to unacceptable increases in the model’s run time. Specifically, the ice model scales with the square of the number of grid-cells, which might be manageable; however, increasing grid resolution necessitates smaller timesteps when calculating meridional heat transport in the EBM (to maintain stability in the explicit solution), leading to a scaling power of roughly 3.7. This would increase our model runtimes from 10 hours to over 130 hours.

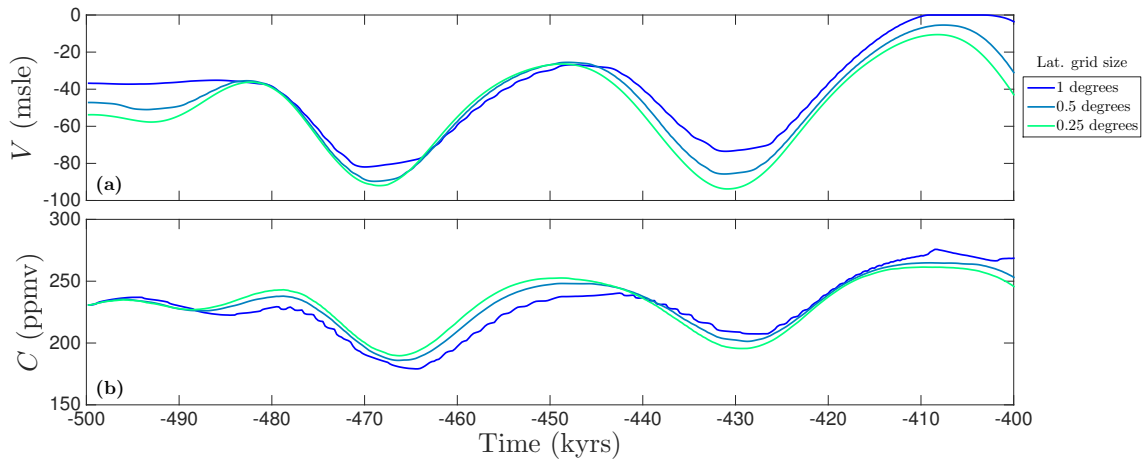


Figure 3.A.3: Effect of varying model’s latitudinal grid size (1 degree = 111 km). Uses a ‘full model’ configuration.

3.A.5 Varying Bed Relaxation Timescale: τ_b

This section explores how changes to the bed relaxation timescale (equivalently, the lithospheric rebound timescale) affect our model behaviour. Other models have calculated ~ 100 kyr cycles (at fixed CO_2 concentration) due to the lithospheric depression providing a positive feedback to ice retreat, such that the ice sheet becomes unstable to orbital perturbations when large. We explore our model’s parameter space to see if we replicate

this finding.

Figure 3.A.4 shows the model under pure insolation forcing with fixed 220 ppmv CO₂, for a range of bed relaxation timescales, τ_b , that span more than the range of uncertainty in this parameter. The bed relaxation times all produce 40 kyr cycles, suggesting that our model formulation does not support bed depression as a mechanism for ~ 100 kyr glacial cycles.

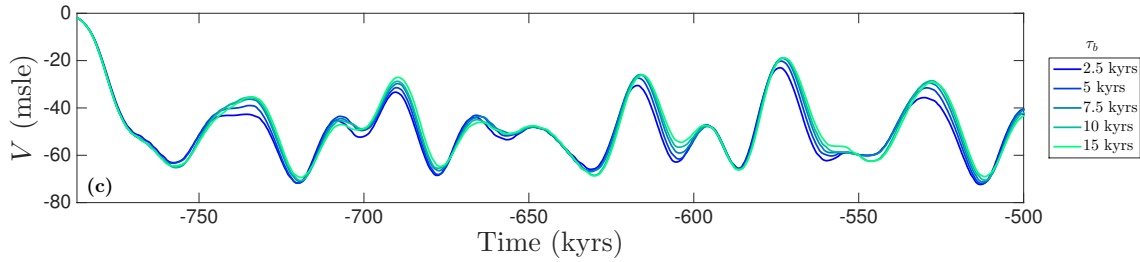


Figure 3.A.4: Effect of varying the lithospheric rebound timescale τ_b . For these runs, $C = 220$ ppmv, and all insolation terms are active. In the rest of this thesis, $\tau_b = 5$ kyrs.

Why is this? Compared to the original 1D models that proposed this mechanism [Oerlemans, 1980, Pollard, 1982, Clark and Pollard, 1998], C-VICE is more grounded in physical processes. They used imposed mass balances parameterised from peak daily insolation; we use direct models of (annual average) melting rate and precipitation based on an EBM with daily-resolution.

However, compared to more recent publications [*e.g.* Ganopolski and Calov, 2011, Abe-Ouchi et al., 2013], we are missing several physical processes. They use 3D ice sheets that can lose mass due to East–West flow and calving, and ice retreat is enhanced with a non-linear feedback such as dust deposition, proglacial lakes, or parameterised ice streams. These changes collectively act to enhance deglaciation, and provide stability tipping-points that are not present in my model.

One could also criticise our lithospheric depression for operating on a strictly local basis — an isostatic balance in each gridcell — rather than a viscoelastic force balance with a characteristic horizontal lengthscale. However, the differences between these model formulations are small [Abe-Ouchi et al., 2013], and local isostatic balance is sufficient for 3D ice models to generate 100 ka glacial cycles, suggesting that solving a non-local force balance is not necessary.

Finally, the thickness of our ice sheet is smaller than most reconstructions of the Lau-

rentide ice sheet (2 km vs. $\simeq 2.6$ km). It is not unreasonable to think the slightly increased lithospheric depression resulting from a thicker ice sheet could trigger a positive feedback sufficient for full deglaciation, however tests show this is not the case. In figure 3.A.5, model runs with varying bedrock density (thus changing equilibrium bed height for a given ice load, following eqn. 3.20) remain at 40 kyr cycles even when bed depression is enhanced by 65%.

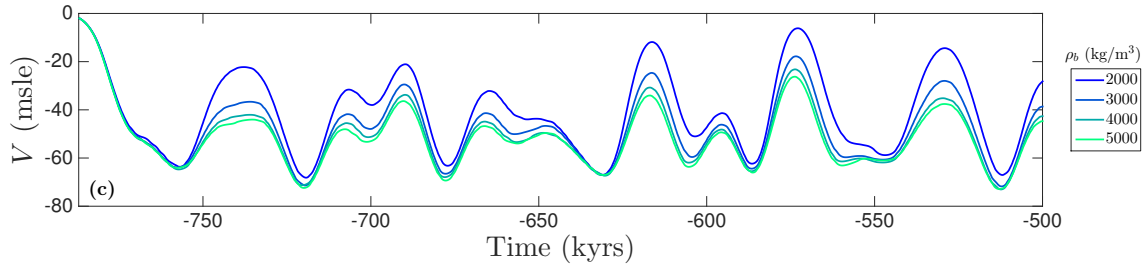


Figure 3.A.5: Effect of varying the bedrock density ρ_b , and thus bed depression. For $\rho_b = 2000$ bed depression is 65% greater than for our normal model (for an equivalent ice sheet). For these runs, $C = 220$ ppmv, and all insolation terms are active. In the rest of this thesis, $\rho_b = 3370$ kyrs.

Overall, we find that no plausible lithospheric rebound timescale induces insolation-driven ~ 100 kyr cycles in our model. It appears that this is because we do not prescribe non-linear forcing feedbacks that cause catastrophic retreat under certain circumstances. However, our model does produce ice sheet retreat rates in line with the glacial record under full forcing (see figure 3.4), so our lack of catastrophic feedbacks is not necessarily a deficiency.

3.A.6 Linear Kinetics

Our carbon model uses an equilibrium formulation, whereby the carbon concentration in the atmosphere is, at every timestep, adjusted according to the average global temperature. This section discusses the formulating the temperature feedback on carbon concentration as a linear kinetic equation.

Linear kinetics assume that a variable, at each timestep, has an equilibrium value. The variable approaches its equilibrium value at a rate directly proportional to the difference between the current value and the equilibrium value; thus the rate-of-change of the variable (the kinetics) is linearly related to the magnitude of disequilibrium.

The rate of change implemented at each timestep is therefore

$$\frac{dC}{dt} = (C_{\text{equil}} - C) \frac{1}{\tau_C} , \quad (3.33)$$

where τ_C is the equilibration half-life, and C_{equil} is the equilibrium carbon concentration in the atmosphere, as calculated in equation (3.21): $C_{\text{equil}} = C_0 + \gamma_T(\bar{T}_s - \bar{T}_{s0})$ with $_0$ denoting values at the start of a model run.

The advantage of linear kinetics is we can separate the ice timestep from the C equilibration timescale. The equilibrium model assumed perfect equilibrium in 250 years, similar to a equilibration half-life of 100 years, which we test below.

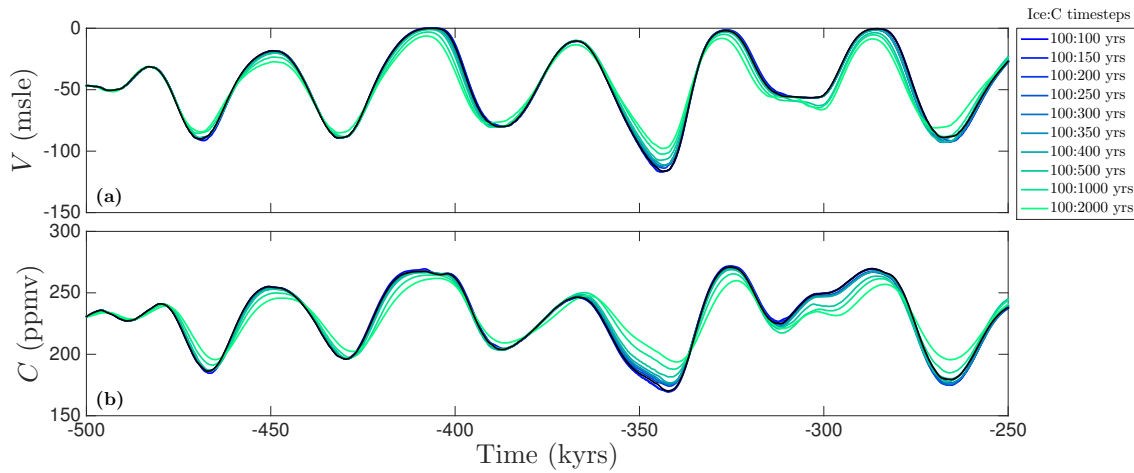


Figure 3.A.6: Effect of varying model’s carbon timescale τ_C under linear kinetics. For the blue-green lines, the ice timestep is 100 years, and the CO_2 equilibration half-life varies from 100–2000 years. The black line marks the default model used in this chapter: an equilibrium CO_2 model with 250 year intervals. Plots use a ‘full model’ configuration.

Figure 3.A.6 demonstrates the effect of changing the CO_2 equilibration half-life for a model with ice timestep of 100 years. There is very little effect for increasing the half-life from 100 to 400 years, and a moderate effect for increases from 400 to 2000 years. The linear kinetics models are all close to the default CO_2 model used in this chapter (the black line in Fig. 3.A.6).

Therefore the C-VICE model is relatively unaffected by using a temperature–carbon feedback based on linear kinetics or equilibrium, and I use the conceptually simpler equilibrium model for my main results.

3.A.7 Convolution: Analytical Solution for Sinusoidal Sea Level

In section 3.3.1, we investigate the effect of sinusoidal sea-level on MOR emissions and explain the results in terms of physical processes. However, results in figure 3.2 can be understood by the mathematical properties of a simplified system: convolving triangular functions, (approximately our MOR Green's functions) with sine functions (rate of change of sea level). This simplified system allows us to define short period and long period regimes precisely, unlike the physical argument. This section details an exact analytical solution for this simplified system, and shows that the results align with our physical explanation

We define a triangle function $T(x-d)$ with width $2d$ beginning at $x=0$, where d is the mid-point of the triangle. Similarly, boxcar functions of width d are denoted by $B(x-d)$, where d is the mid-point of the boxcar. Sea level is a sine function with amplitude A and period P . Thus the convolution of rate-of-change-of-sea-level with the triangle function is:

$$T(t) * Ak \cos(kt) = T(t) * \frac{\partial A \sin(kt)}{\partial t} , \quad (3.34)$$

where $k = 2\pi/P$. Applying the general convolution property $f * g' = f' * g$,

$$T(t) * Ak \cos(kt) = (B(t-d/2) - B(t-3d/2)) * A \sin(kt) . \quad (3.35)$$

Repeating this step, and taking the derivative of a Heaviside function (the edges of the boxcar functions) as a Dirac delta function gives:

$$T(t) * Ak \cos(kt) = [\delta(t) - 2\delta(t-d) + \delta(t-2d)] * -\frac{A}{k} \cos(kt) , \quad (3.36)$$

which is evaluated to give the percentage change in MOR CO₂ emissions rate

$$T(t-d) * Ak \cos(kt) = -\frac{A}{k} [\cos(kt) - 2\cos(k(t-d)) + \cos(k(t-2d))] . \quad (3.37)$$

Integrating this and simplifying gives the cumulative change in atmospheric CO₂

$$C = \frac{AP^2}{\pi^2} \sin^2\left(\frac{d\pi}{P}\right) \sin\left(\frac{2\pi}{P}(d-t)\right) . \quad (3.38)$$

Equation (3.38) is zero for $P = d/n$ where $n \in \mathbb{Z}_{>0}$. Therefore the largest sea-level period for which $C = 0$ is half the width of the triangle function (*i.e.* $P = d$), matching the end of the small period region in figure 3.2.

The maxima of equation (3.38) occur for $\partial C/\partial t = 0$ and are all equal, thus we can consider the first maxima as representative, given by:

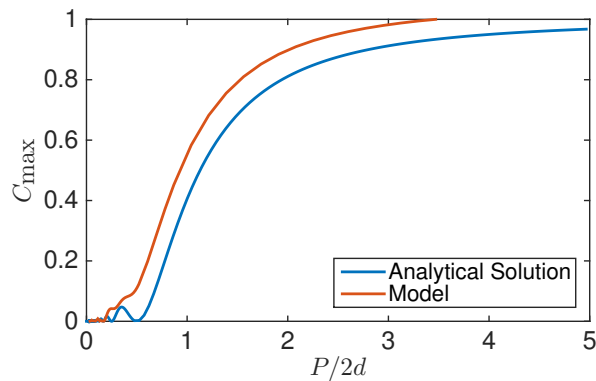
$$t = \frac{4d\pi + P\pi}{4\pi} \quad (3.39)$$

Substituting eqn.(3.39) into eqn. (3.38) gives an expression for the maxima of C

$$C_{\max} = \frac{AP^2}{\pi^2} \sin^2\left(\frac{d\pi}{P}\right) , \quad (3.40)$$

which has $\lim_{P \rightarrow \infty} = d^2$ via the squeeze theorem. Therefore the maximum amplitude of the change in atmospheric CO₂ concentration is proportional to the width of the triangle function. Figure 3.A.7 shows that the normalised behaviour of equation (3.40) is similar to our volcanic Green's functions.

Figure 3.A.7: Normalised maximum cumulative CO₂ emissions for the analytical solution of equation (3.40), and the actual volcanic Green's function from 3.2. The x-axis is sinusoidal sea level period divided by the width of the Green's function.



However, MOR volcanism actually converges to a single value, independent of the Green's function width, therefore this proposed d^2 scaling represents a divergence between our Green's functions of MOR CO₂ emissions and the triangle function approximation. The difference is readily explained. As seen in figure 3.2a, for longer MOR lag times, the

right-hand-side of the Green's function triangle becomes increasingly concave compared to a hypothetical, symmetrical triangle function, causing less emissions than would be expected from the triangle function approximation. This difference is such that the Green's functions all have the same total emissions in the long sea-level period limit.

Alternatively, explaining in physical terms, recall that sea-level-driven variable MOR CO₂ emissions are caused by the changing depth of first mantle melting. A low sea level means a deeper depth of first melting, effectively flushing out CO₂ that would occupy mantle at that depth and inserting it into the atmosphere (see section 2.3.2.2). There is a fixed density of CO₂ in that mantle, and thus a finite maximum CO₂ mass that a given amplitude of sea-level change can insert into the atmosphere, regardless of its period. Long-period sinusoidal sea level changes $P \gg d$ remove all the interference effects in upwelling melts arriving at the MOR and therefore all long-period sea level changes converge towards this same maximum CO₂ mass, regardless of MOR lag.

3.A.8 Controls on Ice Sheet Mass Balance

This section illustrates the ice sheet mass balance in this model, and discusses metrics that should influence it. We conclude that the metrics best correlated with ice dynamics are fixed-latitude forcings, and that more physically-motivated metrics considered in this section are significantly flawed.

Figure 3.A.8 shows snapshots of the ice sheet advancing, at maximum extent, and retreating. The ice sheet has a central region flowing outwards to either melt at the sheet's southern edge or calve off into the polar ocean. Ice flow acts to transport ice from areas of accumulation to areas of ablation. The mass balance is determined by total snow precipitation over the ice sheet and melting at the nose of the ice sheet; we will discuss these in turn.

Total snow precipitation is a function of the extent of the ice sheet and the mean snowfall over the ice sheet. Snowfall is dependent on atmospheric temperature (see equation (3.25)), and therefore influenced by insolation, CO₂ concentration, and the mean height of the ice sheet. Whilst these influences are complexly non-independent, a reasonable proxy is the mean forcing over the ice sheet.

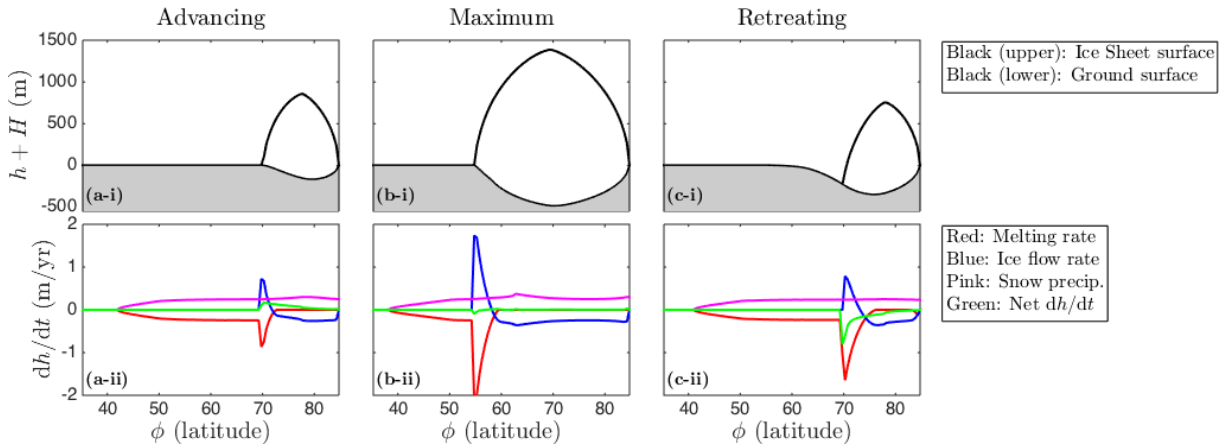


Figure 3.A.8: Model driven by insolation and ice core CO_2 values. Columns (a), (b), and (c) show an ice sheet advancing, at maximum extent, and retreating. The upper row shows the ice sheet configuration: the thickness of the ice sheet h plus the bedrock height H . The lower row shows annual mean m/yr effects of melting, ice flow, and snow precipitation, plus their total sum. To be clear, the ‘ice flow’ represents the m/yr effect on ice thickness in a particular grid-cell, not the horizontal flow rate.

Total melting is a function of the excess energy available at the southern edge of the ice sheet. This energy is provided by local radiative forcing and meridional heat transport. It is hard to construct a proxy for meridional heat transport from input parameters, but we should expect forcing at the edge of the ice sheet to correlate with the melting rate.

Therefore we have arguments for two different forcing metrics controlling the ice sheet’s mass balance: mean forcing over the whole ice sheet, and forcing at the ice sheet’s edge. However, as shown in figure 3.A.9 neither of these correlates with ice volume (nor rate-of-change-of-ice-volume, although this is not shown); neither can multi-linear regression create a physically plausible predictor from a combination of these forcings and ice extent.

This failure occurs because whilst these forcings (mean ice sheet and ice edge) are important in controlling the ice sheet’s mass balance, the key physical driver is not their absolute value, but their value relative to the conditions that would make the ice sheet stable. Without knowing the stability criteria⁴ for the current ice sheet configuration, it is not possible to make a good predictor from these two forcings.

For contrast, forcing at a fixed latitude over time (*e.g.* insolation at 65°N) captures information about changes to the Earth system that will move the ice sheet away from stability.

⁴By stability criteria we mean that the current ice sheet will be stable under multiple possible combinations of insolation and CO_2 concentration. Considering this in terms of phase space analysis, the evolution of the ice sheet depends how the actual combination of forcings compares to a stable criterion.

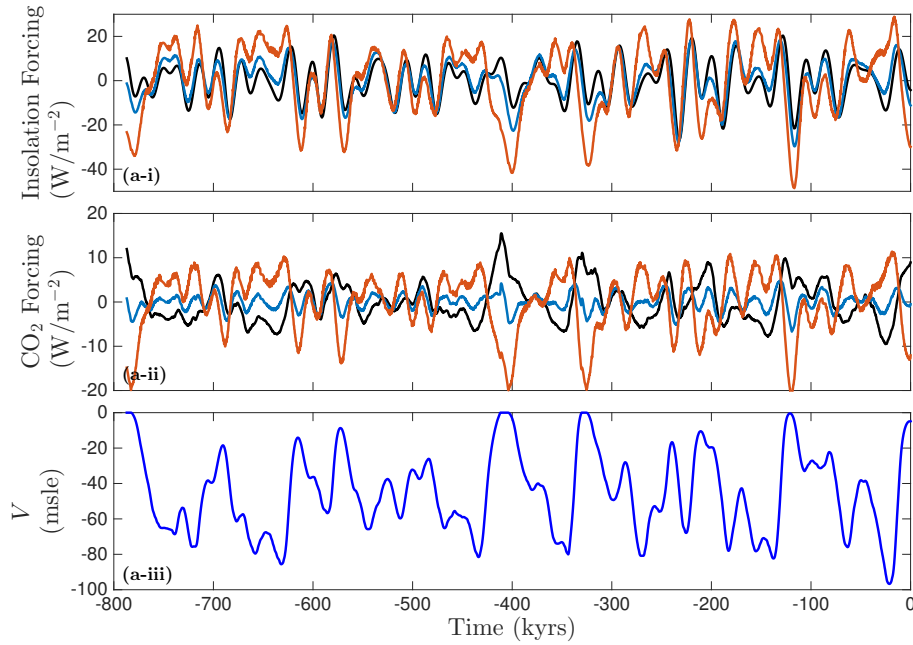


Figure 3.A.9: Model driven by insolation and ice core CO_2 values. Rows show the relative summer-half year forcing for **(i)** insolation; **(ii)** CO_2 ; and row **(iii)** shows ice volume in metres sea level equivalent. In forcing plots, the dark blue line shows the mean ice sheet forcing (latitudinal average), the red line shows the forcing at the southern edge of the ice sheet, and the black line is the summer-half year 65°N forcing — either CO_2 or insolation as appropriate. The key message is that the black lines are the best predictors of sea level.

Therefore, fixed, high-latitude forcings are better metrics of ice sheet change than forcings which physically track the ice sheet like mean-ice-sheet-insolation or insolation-at-the-ice-sheet’s-edge. For this reason, the canonical 65°N forcing is used throughout the rest of this thesis.

3.A.9 Tuning C Feedback Strength

Equation (3.21) for carbon concentration in the atmosphere C has three terms with corresponding sensitivity factors γ_T , γ_{MOR} , γ_{SAV} controlling how much C will change in response to changes in planetary temperature and sea level. In this section we run the model with only one CO_2 feedback term active, varying its corresponding sensitivity parameter, for each of the three feedback terms. The insolation forcing includes obliquity, precession, and eccentricity. This demonstrates how the model behaves (with reconstructed insolation) when a particular CO_2 feedback is dominant.

Figure 3.A.10 shows the model with C responding only to changes in global average temperature: $\gamma_T \neq 0$ and $\gamma_{\text{MOR}}, \gamma_{\text{SAV}} = 0$. The amplitude of the glacial cycles increases

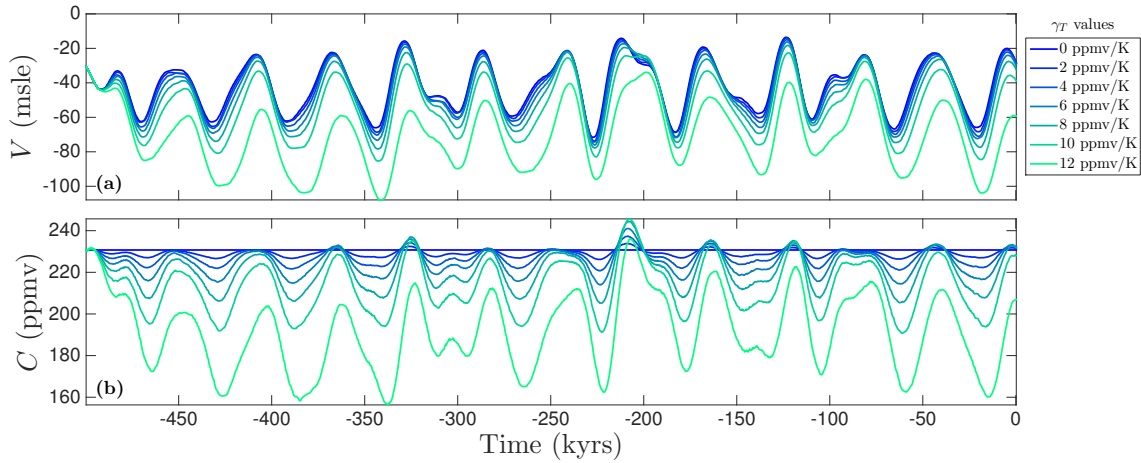


Figure 3.A.10: Increasing CO₂ temperature sensitivity parameter γ_T with volcanic CO₂ effects turned off: $\gamma_{MOR}, \gamma_{SAV} = 0$. Panel (a) is ice volume in metres sea level equivalent. Panel (b) is CO₂ concentration in the atmosphere.

with increasing positive feedback between C and temperature, until the model enters a runaway glacial for $\gamma_T > 12$ ppmv/K.

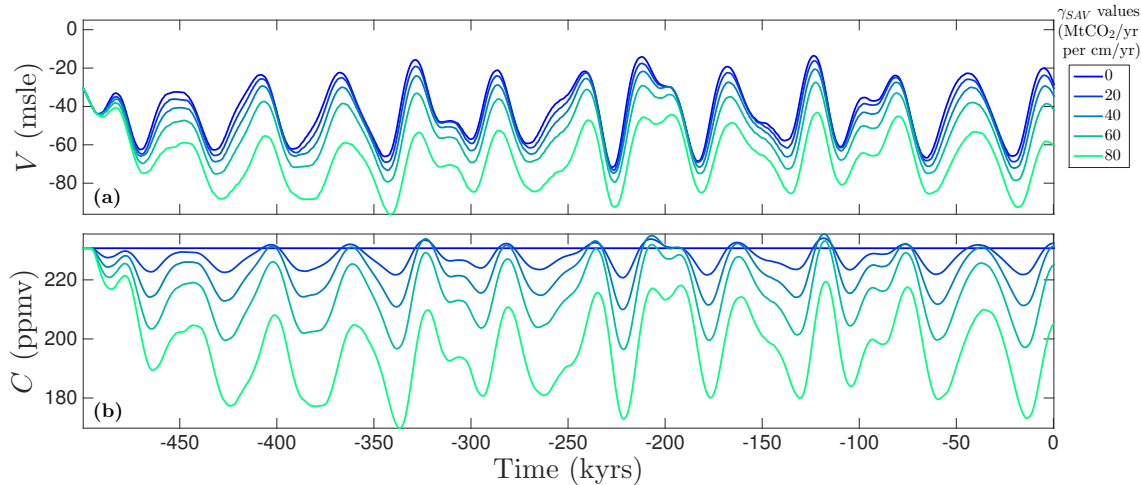


Figure 3.A.11: Increasing SAV CO₂ sensitivity to sea-level γ_{SAV} with other CO₂ effects turned off: $\gamma_T, \gamma_{MOR} = 0$ MtCO₂/yr per cm/yr. Panel (a) is ice volume in metres sea level equivalent. Panel (b) is CO₂ concentration in the atmosphere. The values in the legend are roughly equivalent to the peak increase in SAV CO₂ emissions flux caused by a deglaciation where $\dot{V} = 1$ cm/yr.

Figure 3.A.11 has C changing with variable SAV only: $\gamma_{SAV} \neq 0$ and $\gamma_T, \gamma_{MOR} = 0$. SAV CO₂ emissions lag the ice cycle by about 4 kyrs, and cause a runaway glacial for $\gamma_{SAV} \geq 90$ MtCO₂/yr per cm/yr. As expected from the discussion of short-timescale feedbacks in section 3.4.1, both V and C timeseries in figure 3.A.11 are similar to figure 3.A.10, and neither changes the dominant period of glacial cycles.

Figure 3.A.12 has C changing with variable MOR CO₂ emissions only (40 kyr MOR

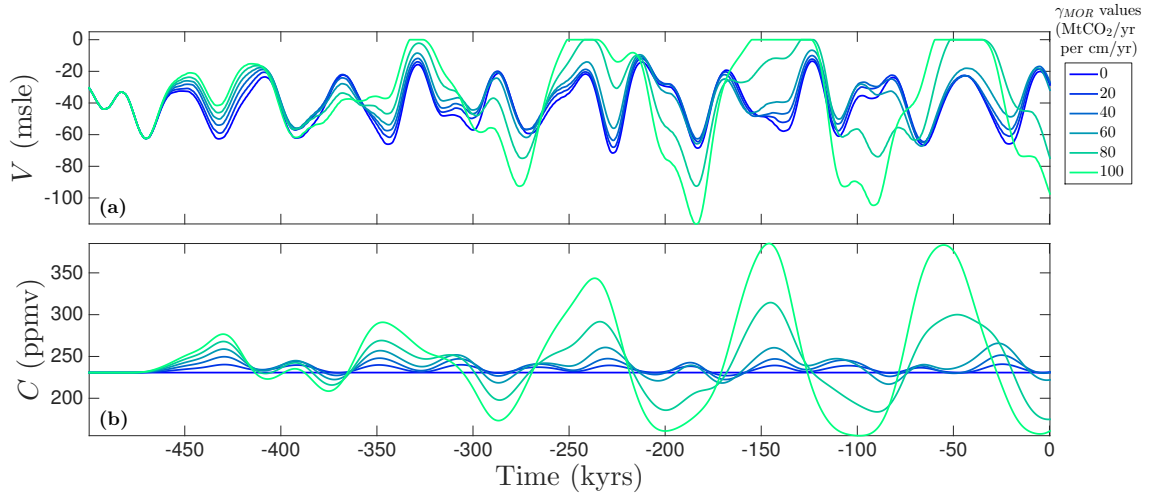


Figure 3.A.12: Increasing MOR CO_2 sensitivity to sea-level γ_{MOR} with other CO_2 effects turned off: $\gamma_{\text{T}}, \gamma_{\text{SAV}} = 0$. Panel (a) is ice volume in metres sea level equivalent. Panel (b) is CO_2 concentration in the atmosphere. The values in the legend are roughly equivalent to the peak decrease in MOR CO_2 emissions flux caused by a deglaciation where $\dot{V} = 1 \text{ cm/yr}$.

lag time): $\gamma_{\text{MOR}} \neq 0$ and $\gamma_{\text{T}}, \gamma_{\text{SAV}} = 0$. As with γ_{T} and γ_{SAV} , increasing the C sensitivity parameter γ_{MOR} increases the amplitude of C cycles. However, the response in ice volume is more complex; as γ_{MOR} is increased, different maxima and minima in V become more extreme or suppressed. This occurs because, as in section 3.4.1, the MOR-based variability in C opposes some insolation-driven changes in V (and reinforces others). As γ_{MOR} increases further, the model moves towards glacial cycles at a multiple of the obliquity cycle: for $\gamma_{\text{MOR}} = 80 \text{ MtCO}_2/\text{yr per cm/yr}$ a $\sim 100 \text{ kyr}$ oscillation dominates in the final 300 kyrs of C (fig 3.A.12b).

These results for varying C terms in eqn (3.21) are consistent with our suggestion that feedbacks need at least a 30 kyr lag time to disrupt 40 kyr glacial cycles. This reinforces the conclusions from exploring varying MOR lag times in section 3.4.1.

Collectively, the results presented in this section imply that variable MOR CO_2 emissions can change both the amplitude and periodicity of glacial cycles in C and V , and the short-timescale carbon feedbacks from subaerial volcanism and the surface system only change the amplitude of glacial cycles. However, as highlighted in section 3.2.3, increased amplitude of sea level change causes increased amplitude of MOR CO_2 emissions; therefore (when all CO_2 feedbacks are active in the model) the short-timescale feedbacks will affect MOR's CO_2 emissions and thus affect when the model generates $\sim 100 \text{ kyr}$ cycles.

3.A.10 Model Response to Noise

The main text establishes the behaviour of the model as a deterministic system. We showed the model tends toward 40 kyr glacials driven by insolation cycles, but transitions to glacials at a multiple of the 40 kyr cycle if the MOR CO_2 emissions response to sea-level change is increased. This section explores the model response to noise, evaluating if the model's glacial cycles are stable to stochastic forcing of key variables. Geological records show considerable noise at $\lesssim 500$ year periods. Would such noise affect model behaviour?

To test this, we add Gaussian white noise to a parameter, randomly changing its value at each timestep in the model. The noise timeseries was created using MATLAB's `wgn` function. We applied this model perturbation independently to insolation (change solar constant) and precipitation rate (change P_c).

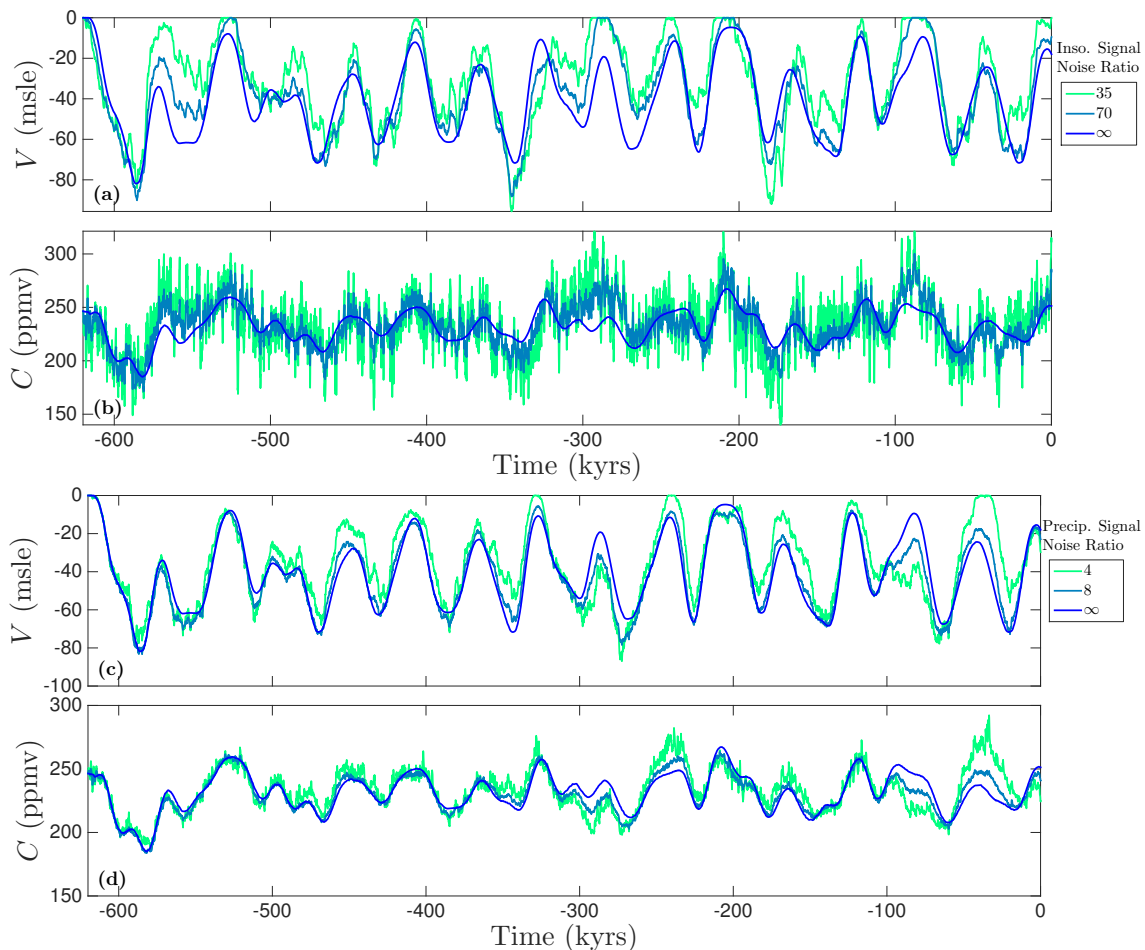


Figure 3.A.13: Model runs with increasing white noise added to insolation (upper pair) and precipitation (lower pair). In each pair the upper panel is ice volume in metres sea level equivalent and the lower panel is CO_2 concentration in the atmosphere. Noise is calculated by MATLAB's `wgn` function with random seed 400. Signal to noise ratio is the standard deviation of the noise divided by default value of the perturbed parameter.

Figure 3.A.13 shows the results of stochastic forcing in both insolation (fig 3.A.13a,b) and precipitation (fig 3.A.13c,d). Both forcings show high-frequency perturbations in V and C , despite the different physical mechanisms behind the perturbations. Insolation forcing changes the shortwave energy flux, thus changing Earth's temperature and consequently causing both ice sheet growth/retreat and (via the γ_T carbon feedback term) C changes. Precipitation forcing changes annual snowfall and thus directly affects ice sheet growth/retreat. The change in ice sheet extent changes surface albedo and consequently Earth's temperature, leading to C changes.

The stochastic forcings have no significant effect on SAV or MOR CO₂ emissions in the model, as the high-frequency variations in sea level (with a mean of zero) cancel out by the mechanism explained in section 3.3.1.

Neither insolation nor precipitation forcing significantly alters the 40 kyr glacial cycle. These results hold for a range of random seeds and signal-to-noise ratios. Therefore high frequency noise similar to or greater than the geological record does not affect the key conclusions of this study.

Chapter 4

Final Conclusions

4.1 Summary

This thesis began with the question “*could glacial cycles and volcanism form a feedback loop?*”; the work subsequently presented showed theoretical evidence that mid-ocean ridge volcanism (MOR) is affected by glacial cycles in a manner that alters MOR CO₂ emissions, and demonstrated in a low-complexity Earth system model that these CO₂ emissions could push the glacial system into a ~100 kyr cycle, whereby deglaciations occur every second or third obliquity cycle (80 or 120 kyrs).

Therefore the answer to the question is yes, glacial cycles and volcanism **could** form a feedback loop, although it is by no means certain that they form a feedback loop where volcanism is a dominant control on the pacing of glacial cycles.

Let us consider why. From the work in chapter 2, I have confidence that MOR CO₂ emissions do change in response to glacial cycles, and that the total effect is on the order of 130 Gt CO₂. This is sufficient to affect global climate through CO₂'s longwave forcings. However, as discussed in chapter 3, simulated glacial–interglacial cycles remain pinned at 40 kyr periodicity until the cumulative MOR CO₂ emissions are about 160 Gt. Volcanic emissions in this range are not impossible — they are at the upper end of a 95% confidence interval — but it would be rather fortuitous to assume reality lies at the extreme ends of a probability distribution just to make a hypothesis true. Uncertainties related to oceanic absorption of volcanic CO₂ emissions over glacial cycles further increase uncertainty, although they probably increase the required total volcanic CO₂ emissions

beyond any reasonable confidence interval. Therefore I conclude that the mechanism is possible, but current evidence and understanding cannot verify or reject the hypothesis that volcanic CO₂ emissions variability, in isolation, controls the pacing of glacial cycles.

Of course, MOR CO₂ emissions do not act in isolation, and there are relevant glacial mechanisms that do not operate in my model, including regolith erosion [Clark and Pollard, 1998], secular CO₂ decline [Pagani et al., 2010, Hönlisch et al., 2009], and switching modes in ocean ventilation [Franois et al., 1997, Toggweiler, 1999]. These mechanisms may interact and couple with our existing processes to allow glacial cycles at lower MOR CO₂ variability. However, these mechanisms are not precisely defined and thus their effects are hard to predict until further research can quantify their mechanisms.

Therefore, this thesis adds a new theory to the canon of Pleistocene glacial cycles, providing a physical foundation to a hypothesis first suggested in the literature in Huybers and Langmuir [2009]. It is by no means a proven hypothesis, but it is plausible.

Below, I discuss the detail of my work, highlight discoveries outside of the main question and potential current and future avenues to confirm model predictions.

4.1.1 Model Results and Predictions

My thesis presented work covering two major areas: mantle dynamics and paleoclimate modelling.

For the former, I presented a model of the transport of a highly incompatible element through the mid-ocean ridge (MOR) melting system. I showed that a physically consistent representation of the MOR system predicts changing sea level will cause a change in the emissions rate of highly incompatible elements.

Specifically, there will be a change in emissions rate that lags the causative sea-level change by 35–80 kyrs and (for historical sea-level changes) varies the emissions rate by up to 5–12%. The range in these figures is due to the uncertainty in a physical property of the mantle called permeability, which determines how fast the fluid mantle can percolate upwards through the residual solid for a given driving force. Semi-independent data constraints like uranium-series disequilibria support the lag time I derive by physical modelling.

Applying this incompatible-element model to CO₂ emissions from the MOR suggests that historical sea-level variation changed the CO₂ mass in the surface system by up to 130 Gt compared to steady-state emissions in the absence of varying sea level.

The model predicts the variation of any incompatible element in the melt, thus it is possible for future experimental work to test the model by looking at highly incompatible elements in volcanic glass over time — a project I suggest could be performed given the recently reported glasses in seafloor sediments [Langmuir \[2014\]](#).

Furthermore, the model draws out a physical prediction for degree of melting scaling with spreading rate, and having a different relationship between maximum degree of melting (under a MOR) and the average-degree-of-melting-of-extracted-melts. This is relevant to the ongoing petrology debate on this topic [*e.g.* [Dalton et al., 2014](#), [Niu, 2016](#)], providing a F vs. U_0 prediction to compare data against. My model is simple and fast; easily converted into code ‘tool’ for non-specialists.

For the latter — paleoclimate modelling — I presented a pseudo-2D Earth model, coupling dynamic component models for energy balance, ice sheet dynamics, and CO₂ concentration in the atmosphere; forced by insolation alone. The energy balance determines temperature according to the current insolation, ice sheet configuration and CO₂ concentration in the atmosphere; the ice sheet flows under its own weight, depresses the lithosphere beneath it, and melts/accumulates according the local temperature and precipitation conditions determined in the energy balance model; the CO₂ concentration in the atmosphere varies with average planetary temperature (a parameterisation of CO₂ partitioning in the surface system) and volcanic CO₂ outputs.

The C-VICE model is a physics-based representation of the Earth system that is capable of replicating the observed sequence of glacial cycles when forced by both insolation and (reconstructed) CO₂ timeseries. Whilst it is not the first model to achieve this dynamically (by which I mean a physical model system responding to driving forces throughout the simulation) [[Ganopolski and Calov, 2011](#)], it is certainly the simplest model to do so¹. Other, non-dynamic replications of the observed glacial sequence have either used

¹The ‘Earth models of intermediate complexity’ (EMICs) that sometimes replicate glacial cycles contain a minimum of 20+ component models [[Ganopolski et al.](#)], and are linked to 3D ice simulations that are also non-trivial.

rules-based systems to trigger switches between states [*e.g.* Paillard and Parrenin, 2004, Toggweiler, 2008] or used extrapolated behaviour from snapshots of a physical model [Abe-Ouchi et al., 2013].

Furthermore, C-VICE replicates the modern seasonal range and temperatures with latitude, and CO₂-doubling experiments in GCMs. However, these are merely model validations confirming the C-VICE implements a reasonable approximation of the key physics in the climate system; the model's real questions were about behaviour under dynamic atmospheric CO₂.

The C-VICE model predicts that the glacial system is strongly coupled to the obliquity cycle; thus glacial cycles occur with 40 kyr periods in the model. These 40 kyr cycles occur when atmospheric CO₂ is determined by processes with a feedback timescale of less than 30 kyrs, regardless of the strength of that feedback. Disruption of the 40 kyr cycles only occurs when there is a significant carbon feedback acting at ≥ 35 kyrs.

The reason for this disruption is due to the difference between intra-cycle feedbacks — acting on a timescale much less than the glacial cycle and thus transferring little information between cycles — and inter-cycle feedbacks. Only a process that affects a glacial parameter (like atmospheric CO₂) on an inter-cycle basis can couple with the insolation forcing to give a stable cycle at a longer period. I believe that this framework of inter-cycle (vs. intra-cycle) feedbacks is a useful conceptual tool for understanding glacial cycles and how forcings interact.

Variable MOR CO₂ emissions provide the inter-cycle carbon feedback, and are shown to do so when their emissions sensitivity to sea-level change is about 50% higher than my chapter 2 model and volcanic CO₂ emissions data predict. The large uncertainty in the data mean this 50% difference is not significantly improbable (*i.e.* $p < 0.05$). However, C-VICE does not include oceanic CO₂ buffering (there are no quantitative dynamic models of oceans across glacial cycles). As discussed above, this would likely increase the required emissions sensitivity beyond what is plausible.

C-VICE makes qualitative predictions about ~ 100 kyr glacial cycles and potential mechanisms for the Mid-Pleistocene transition. For instance, MOR-driven 100 kyr cycles lead to sawtooth patterns in atmospheric CO₂; increasing volcanic influence will cause

warmer interglacials with higher CO₂; and increased volcanic CO₂ during deglaciation is consistent the lack deep-sea carbonate preservation that is otherwise difficult to explain [Broecker et al., 2015].

With regards to the Mid-Pleistocene transition, we would 1) expect a preceding larger-than-average drop in sea-level change, or a small partial deglaciation, as this establishes a large MOR CO₂ pulse and 2) expect the feedback loop between MOR CO₂ and sea-level to stabilise over several glacial cycles (several hundred kyrs). Since I made this latter prediction — although before I published — Tzedakis, P.C. et al. [2017] showed evidence for the Mid-Pleistocene transition taking $\simeq 0.8$ Myrs, consistent with this prediction and no other glacial hypothesis (that I am aware of).

4.1.2 Reflections on Modelling Complex Systems

Mantle dynamics and paleoclimate modelling are disparate fields and there are many differences between them, but they have one important similarity: rich observational datasets that are themselves the result of complex interpretations (*i.e.* models), and generally represent some time- or spatial-average of the system's dynamics.

Therefore mantle and paleoclimate dynamics are underconstrained by data, and we have a non-uniqueness problem — it is generally possible to reconstruct the data with models of fundamentally different assumptions.

To give examples from each field: *i*) observed radioactive disequilibrium in erupted melts imposes a maximum time interval from when-that-melt-was-formed to when-that-melt-erupted; but these can be interpreted differently depending on the assumed partitioning of elements between phases, and whether melts are extracted by a fractional or batch process. (also: whether arc magma chemistry represents crustal or wedge processes). *ii*) the insolation and sea-level timeseries represents a termination on every second or third obliquity cycle [Huybers and Wunsch, 2005], fourth or fifth obliquity cycle [Ridgwell et al., 1999], or an incidental phase-locking with an internal Earth system oscillation [Gildor and Tziperman, 2000, Huybers, 2011], (also: the array of oceanic theories for CO₂ cycles).

Therefore there is a need for models that can develop causative mechanisms from underlying physics, rather than imposing convenient assumptions. Such models should

be derived from clear principles (and thus can be disproven if the underlying framework is later shown to be invalid). This has been the guiding principle in the models developed in this thesis.

Furthermore, it is insufficient for models to merely match a single observable at once. It is rather easy to force a model to obtain a desired result (intentionally or not) when fitting a single constraint. Far better for a model to simultaneously explain several observed trends and make falsifiable predictions in uncertain areas.

Indeed, such models are more than tools for chasing data fits. Models can ‘sharpen questions’ with their predictions: *e.g.* if we believe X and Y, we should see effect Z — subsequently observing Z increases our belief in X and Y, failure to observe Z means we need question our understanding of X and Y. This logic was seen in the first chapter of this thesis (section 1.2.2); if we believe that ice sheet dynamics are dominated by melting, and that peak summer insolation is a good metric of overall melting, then ice sheet volume changes should occur at the dominant 23 kyr cycles of peak daily insolation. This was not true, and on reconsidering we could see that overall melting energy was *i)* better approximated by 40 kyr cycles in integrated half year forcing, and *ii)* probably required tracking of internal Earth system oscillations.

All of these thoughts are effectively summarised as Bayesian inference: a model that takes assumptions from physical principles is more likely to be true than one that makes an arbitrary assumption, fitting more data is better than fitting less data, and we can’t be certain of data or hypotheses (and a suitable model can demonstrate faults by calculating a consequence of data/hypotheses that is obviously highly improbable).

Therefore I do not look to find certainty in my models, I look to find consequences of my assumptions, and to therefore better constrain the probable truths of the Earth system.

4.1.3 Concluding Remarks

There are no absolutes when working in fields where modelling is known to not explain all the observed features of the system under study. However, I am certain that the models I developed over the past few years have reduced uncertainty in the topics they address,

allowing future research to use my results with a realistic degree of confidence, or look at specific avenues to disprove my proposed mechanisms.

The research community can have confidence that MOR CO₂ emissions vary according to the mechanism I specified, and can reject models relying on increased melting rate inside the melting region.

My modelling supports this variation in CO₂ emissions having a non-trivial effect on glacial cycles, and shows that this is due to the long lag time (tens of thousands of years) between changing sea-level and consequent CO₂ emissions — an inter-cycle feedback.

However, I cannot be certain that these variable volcanic emissions change the pacing of glacial cycles from 40 kyr to 100 kyr periods. Therefore the answer to: “*could glacial cycles and volcanism form a feedback loop?*” is yes, but the importance of that feedback loop is not known. I think it likely that volcanic CO₂ emissions are part of a mixed set of mechanisms that collectively act to drive the pacing glacial cycles.

Therefore, as stated earlier in this chapter: this thesis adds a new theory to the canon of Pleistocene glacial cycles, providing a physical foundation to a hypothesis first suggested in the literature in [Huybers and Langmuir \[2009\]](#). It is by no means a proven hypothesis, but it is plausible.

Bibliography

- A. Abe-Ouchi, F. Saito, K. Kawamura, M. E. Raymo, J. Okuno, K. Takahashi, and H. Blatter. Insolation-driven 100,000-year glacial cycles and hysteresis of ice-sheet volume. *Nature*, 500(7461):190–193, Aug. 2013.
- J. L. Ahern and D. L. Turcotte. Magma migration beneath an ocean ridge. *Earth and Planetary Science Letters*, 45(1):115–122, Oct. 1979.
- D. Archer, M. Eby, V. Brovkin, A. Ridgwell, L. Cao, U. Mikolajewicz, K. Caldeira, K. Matsumoto, G. Munhoven, A. Montenegro, and K. Tokos. Atmospheric Lifetime of Fossil Fuel Carbon Dioxide. *dx.doi.org*, 37(1):117–134, Apr. 2009.
- G. Arrhenius. Sediments cores from the east Pacific. *Geologiska Föreningen i Stockholm Förhandlingar*, pages 115–118, 1953.
- S. Arrhenius. On the influence of carbonic acid in the air upon the temperature of the ground. *Phil. Mag.*, 41(251):237–276, 1896.
- P. Asimow and C. Langmuir. The importance of water to oceanic mantle melting regimes. *Nature*, 421(6925):815–820, 2003. doi: 10.1038/nature01429.
- G. Batchelor. *An Introduction to Fluid Mechanics*. Cambridge University Press, 1967.
- J. Bear and Y. Bachmat. *Introduction to modeling of transport phenomena in porous media*, volume 4. Springer Science & Business Media, 1990.
- J. W. Beck, R. L. Edwards, E. Ito, F. W. Taylor, J. Recy, F. Rougerie, P. Joannot, and C. Henin. Sea-surface temperature from coral skeletal strontium/calcium ratios. *Science*, 257(5070):644–648, 1992.
- B. Bereiter, S. Eggelston, J. Schmitt, C. Nehrbass-Ahles, T. F. Stocker, H. Fischer, S. Kipfstuhl, and J. Chappellaz. Revision of the EPICA Dome C CO₂ record from 800 to 600 kyr before present. *Geophysical Research Letters*, 42(2):542–549, Jan. 2015.
- A. Berger and M. F. Loutre. Insolation values for the climate of the last 10 million years. *Quaternary Science Reviews*, 10(4):297–317, Jan. 1991.
- A. Berger, M. F. Loutre, and C. Tricot. Insolation and Earth’s orbital periods. *Journal of Geophysical Research: Planets (1991–2012)*, 98(D6):10341–10362, June 1993.
- Berkeley Earth Surface Temperatures. Monthly mean land surface temperatures 1951–80, 1 degree grid. file: Raw_tavg_equalarea.nc. <http://berkeleyearth.org/data/m>. Accessed: 2017-05-03.

- D. Bianchi, J. L. Sarmiento, A. Gnanadesikan, R. M. Key, P. Schlosser, and R. Newton. Low helium flux from the mantle inferred from simulations of oceanic helium isotope data. *Earth and Planetary Science Letters*, 297(3-4):379–386, Sept. 2010.
- S. Bony, B. Stevens, D. M. W. Frierson, C. Jakob, M. Kageyama, R. Pincus, T. G. Shepherd, S. C. Sherwood, A. P. Siebesma, A. H. Sobel, M. Watanabe, and M. J. Webb. Clouds, circulation and climate sensitivity. *Nature Geoscience*, 8(4):261–268, Apr. 2015.
- J. W. Bown and R. S. White. Variation with Spreading Rate of Oceanic Crustal Thickness and Geochemistry. *Earth and Planetary Science Letters*, 121(3-4):435–449, Feb. 1994.
- P. Braconnot and M. Kageyama. Shortwave forcing and feedbacks in Last Glacial Maximum and Mid-Holocene PMIP3 simulations. *Philosophical Transactions of the Royal Society a-Mathematical Physical and Engineering Sciences*, 373(2054), 2015.
- W. S. Broecker and J. Donk. Insolation changes, ice volumes, and the O18 record in deep-sea cores. *Reviews of Geophysics*, 8(1):169–198, Feb. 1970.
- W. S. Broecker, J. Yu, and A. E. Putnam. Two contributors to the glacial CO₂ decline. *Earth and Planetary Science Letters*, 429(C):191–196, Nov. 2015.
- R. U. Bryson, R. A. Bryson, and A. Ruter. A calibrated radiocarbon database of late Quaternary volcanic eruptions. *eEarth Discussions*, 2006.
- M. I. Budyko, A. B. Ronov, and A. L. Yanshin. *History of the Earth's Atmosphere*. Springer Berlin Heidelberg, 1987.
- J. M. A. Burley and R. F. Katz. Variations in mid-ocean ridge CO₂ emissions driven by glacial cycles. *Earth and Planetary Science Letters*, 426:246–258, Sept. 2015.
- M. Cai and K.-K. Tung. Robustness of Dynamical Feedbacks from Radiative Forcing: 2 % Solar versus 2 x CO₂ Experiments in an Idealized GCM. *Journal of the Atmospheric Sciences*, 69(7):2256–2271, July 2012.
- R. L. Carlson and G. S. Raskin. Density of the Ocean Crust. *Nature*, 311(5986):555–558, 1984.
- P. Cartigny, F. Pineau, C. Aubaud, and M. Javoy. Towards a consistent mantle carbon flux estimate: Insights from volatile systematics (H₂O/Ce, delta D, CO₂/Nb) in the North Atlantic mantle (14 degrees N and 34 degrees N). *Earth and Planetary Science Letters*, 265(3-4):672–685, 2008.
- P. U. Clark and D. Pollard. Origin of the middle Pleistocene transition by ice sheet erosion of regolith. *Paleoceanography*, 13(1):1–9, Feb. 1998.
- N. Coltice, L. Simon, and C. Lecuyer. Carbon isotope cycle and mantle structure. *Geophysical Research Letters*, 31(5):–n/a, 2004.
- J. A. D. Connolly, M. W. Schmidt, G. Solferino, and N. Bagdassarov. Permeability of asthenospheric mantle and melt extraction rates at mid-ocean ridges. *Nature*, 462(7270):209–U83, 2009a.

- J. A. D. Connolly, M. W. Schmidt, G. Solferino, and N. Bagdassarov. Permeability of asthenospheric mantle and melt extraction rates at mid-ocean ridges. *Nature*, 462(7270):209–212, 2009b.
- C. P. Conrad and C. Lithgow-Bertelloni. How mantle slabs drive plate tectonics. *Science*, 298(5591):207–209, 2002.
- J. Croll. On the change in the obliquity of the ecliptic, its influence on the climate of the polar regions and on the level of the sea. *The London*, 1867.
- T. W. Cronin and E. Tziperman. Low clouds suppress Arctic air formation and amplify high-latitude continental winter warming. *Proceedings of the National Academy of Sciences*, 112(37):11490–11495, Sept. 2015.
- J. W. Crowley, R. F. Katz, P. Huybers, C. H. Langmuir, and S. H. Park. Glacial cycles drive variations in the production of oceanic crust. *Science*, 2015a. doi: 10.1126/science.1261508.
- J. W. Crowley, R. F. Katz, P. Huybers, C. H. Langmuir, and S.-H. Park. Glacial cycles drive variations in the production of oceanic crust. *Science*, 347(6227):1237–1240, Mar. 2015b.
- K. M. Cuffey and F. Vimeux. Covariation of carbon dioxide and temperature from the Vostok ice core after deuterium-excess correction. *Nature*, 412(6846):523–527, 2001.
- C. A. Dalton, C. H. Langmuir, and A. Gale. Geophysical and Geochemical Evidence for Deep Temperature Variations Beneath Mid-Ocean Ridges. *Science*, 344, 2014. doi: 10.1126/science.1249466.
- R. Dasgupta. Ingassing, storage, and outgassing of terrestrial carbon through geologic time. *Rev Mineral Geochem*, 2013.
- R. Dasgupta and M. M. Hirschmann. The deep carbon cycle and melting in Earth's interior. *Earth and Planetary Science Letters*, 298(1-2):1–13, Sept. 2010.
- R. Dasgupta, A. Mallik, K. Tsuno, A. C. Withers, and G. Hirth. Carbon-dioxide-rich silicate melt in the Earth's upper mantle. *Nature*, 2013.
- A. Donohoe and D. S. Battisti. Atmospheric and Surface Contributions to Planetary Albedo. *dx.doi.org*, 24(16):4402–4418, Aug. 2011.
- H. Elderfield, P. Ferretti, M. Greaves, S. Crowhurst, I. N. McCave, D. Hodell, and A. M. Piotrowski. Evolution of Ocean Temperature and Ice Volume Through the Mid-Pleistocene Climate Transition. *Science*, 337(6095):704–709, Aug. 2012.
- C. Emiliani. Pleistocene temperatures. *The Journal of Geology*, 1955.
- R. Ferrari, M. F. Jansen, J. F. Adkins, A. Burke, A. L. Stewart, and A. F. Thompson. Antarctic sea ice control on ocean circulation in present and glacial climates. *Proceedings of the National Academy of Sciences*, 111(24):8753–8758, June 2014.
- T. P. Fischer. Fluxes of volatiles (H₂O, CO₂, N₂, Cl, F) from arc volcanoes. *Geochemical Journal*, 42(1):21–38, Feb. 2008.
- A. C. Fowler, R. E. M. Rickaby, and E. W. Wolff. Exploration of a simple model for ice ages. *GEM - International Journal on Geomathematics*, 4(2):227–297, 2013.

- R. Francois, M. A. Altabet, E.-F. Yu, D. M. Sigman, M. P. Bacon, M. Frank, G. Bohrmann, G. Bareille, and L. D. Labeyrie. Contribution of Southern Ocean surface-water stratification to low atmospheric CO₂ concentrations during the last glacial period. *Nature*, 389(6654):929–935, Oct. 1997.
- E. D. Galbraith and S. Eggleston. A lower limit to atmospheric CO₂ concentrations over the past 800,000 years. *Nature Geoscience*, 2017.
- A. Gale, C. A. Dalton, C. H. Langmuir, Y. Su, and J. G. Schilling. The mean composition of ocean ridge basalts. *Geochemistry, Geophysics, Geosystems*, 14(3):489–518, Mar. 2013.
- A. Ganopolski and R. Calov. The role of orbital forcing, carbon dioxide and regolith in 100 kyr glacial cycles. *Climate of the Past*, 7(4):1415–1425, 2011.
- A. Ganopolski, R. Calov, R. Petoukhov, V. Brovkin, M. Willeit, and E. Bauer. CLIMBER-2 Model overview. <https://www.pik-potsdam.de/research/earth-system-analysis/models/climber/climber-2/climber-2>.
- M. C. Gardeweg, R. S. J. Sparks, and S. J. Matthews. Evolution of Lascar Volcano, Northern Chile. *Journal of the Geological Society*, 155(1):89–104, Feb. 1998.
- J. Geikie. *The great ice age and its relation to the antiquity of man*. 1874.
- T. Gerlach. Etna’s greenhouse pump. *Nature*, 351(6325):352–353, 1991.
- H. Gildor and E. Tziperman. Sea ice as the glacial cycles’ climate switch: Role of seasonal and orbital forcing. *Paleoceanography*, 2000.
- F. Goff, S. P. Love, R. Warren, D. Counce, J. Obenholzner, C. Siebe, and S. C. Schmidt. Passive infrared remote sensing evidence for large, intermittent CO₂ emissions at Popocatépetl volcano, Mexico. *Chemical Geology*, 177(1):133 – 156, 2001. doi: 10.1016/S0009-2541(00)00387-9.
- K. Grant, E. Rohling, C. B. Ramsey, H. Cheng, R. Edwards, F. Florindo, D. Heslop, F. Marra, A. Roberts, M. E. Tamisiea, et al. Sea-level variability over five glacial cycles. *Nature communications*, 5, 2014.
- A. P. Gysi and A. Stefansson. Experiments and geochemical modeling of CO₂ sequestration during hydrothermal basalt alteration. *Chemical Geology*, 306:10–28, 2012.
- T. Hammouda and S. Keshav. Melting in the mantle in the presence of carbon: Review of experiments and discussion on the origin of carbonatites. *Chemical Geology*, 418: 171–188, 2015.
- S. Harðardóttir, S. A. Halldórsson, and D. R. Hilton. Spatial distribution of helium isotopes in Icelandic geothermal fluids and volcanic materials with implications for location, upwelling and evolution of the Icelandic mantle plume. *Chemical Geology*, 2017.
- S. P. Harrison and P. J. Bartlein. What have we learnt from palaeoclimate simulations? *Journal of Quaternary Science*, 2016.

- S. P. Harrison, P. J. Bartlein, K. Izumi, G. Li, J. Annan, J. Hargreaves, P. Braconnot, and M. Kageyama. Evaluation of CMIP5 palaeo-simulations to improve climate projections. *Nature Climate Change*, 5(8):735–743, Aug. 2015.
- J. Hasenclever, J. P. Morgan, M. Hort, and L. H. Rüpke. 2D and 3D numerical models on compositionally buoyant diapirs in the mantle wedge. *Earth and Planetary Science Letters*, 311(1-2):53–68, 2011.
- J. Hasenclever, G. Knorr, L. H. Rüpke, P. Köhler, J. Morgan, K. Garofalo, S. Barker, G. Lohmann, and I. R. Hall. Sea level fall during glaciation stabilized atmospheric CO₂ by enhanced volcanic degassing. *Nature Communications*, 8, 2017.
- J. D. Hays, T. Saito, and N. D. Opdyke. Pliocene-Pleistocene sediments of the equatorial Pacific: their paleomagnetic, biostratigraphic, and climatic record. *GSA Bulletin*, 1969.
- J. D. Hays, J. Imbrie, and N. J. Shackleton. Variations in the Earth's orbit: Pacemaker of the ice ages. 1976.
- E. Hellebrand, J. E. Snow, H. Dick, and A. W. Hofmann. Coupled major and trace elements as indicators of the extent of melting in mid-ocean-ridge peridotites. *Nature*, 410(6829):677–681, 2001.
- I. J. Hewitt. Modelling melting rates in upwelling mantle. *Earth and Planetary Science Letters*, 300(3-4):264–274, 2010.
- B. Hönlisch, N. G. Hemming, D. Archer, M. Siddall, and J. F. McManus. Atmospheric carbon dioxide concentration across the mid-pleistocene transition. *Science*, 324(5934):1551–1554, 2009.
- P. O. Hopcroft and P. J. Valdes. How well do simulated last glacial maximum tropical temperatures constrain equilibrium climate sensitivity? *Geophysical Research Letters*, 2015.
- P. Huybers. Combined obliquity and precession pacing of late Pleistocene deglaciations. *Nature*, 480(7376):229–232, Dec. 2011.
- P. Huybers and C. Langmuir. Feedback between deglaciation, volcanism, and atmospheric CO₂. *Earth and Planetary Science Letters*, 286(3-4):479–491, Sept. 2009.
- P. Huybers and C. H. Langmuir. Delayed CO₂ emissions from mid-ocean ridge volcanism as a possible cause of late-Pleistocene glacial cycles. *Earth and Planetary Science Letters*, 2017.
- P. Huybers and E. Tziperman. Integrated summer insolation forcing and 40,000-year glacial cycles: The perspective from an ice-sheet/energy-balance model. *Paleoceanography*, 23(1):–n/a, 2008.
- P. Huybers and C. Wunsch. Obliquity pacing of the late Pleistocene glacial terminations. *Nature*, 434(7032):491–494, Mar. 2005.
- J. Imbrie and J. Z. Imbrie. Modeling the Climatic Response to Orbital Variations. *Science*, 207(4434):943–953, 1980.

- J. Imbrie, J. D. Hays, D. G. Martinson, A. McIntyre, and A. C. Mix. The orbital theory of Pleistocene climate: support from a revised chronology of the marine $\delta^{18}\text{O}$ record. 1984.
- A. M. Jellinek, M. Manga, and M. O. Saar. Did melting glaciers cause volcanic eruptions in eastern California? Probing the mechanics of dike formation. *Journal of Geophysical Research-Solid Earth*, 109(B9), 2004.
- M. Jull and D. McKenzie. The effect of deglaciation on mantle melting beneath Iceland. *Journal of Geophysical Research: Planets (1991–2012)*, 101(B10):21815–21828, Oct. 1996.
- M. Jull, P. B. Kelemen, and K. Sims. Consequences of diffuse and channelled porous melt migration on uranium series disequilibria. *Geochimica et cosmochimica acta*, 66(23):4133–4148, Dec. 2002a.
- M. Jull, P. B. Kelemen, and K. Sims. Consequences of diffuse and channelled porous melt migration on uranium series disequilibria. *Geochimica et Cosmochimica Acta*, 2002b.
- R. F. Katz. Magma Dynamics with the Enthalpy Method: Benchmark Solutions and Magmatic Focusing at Mid-ocean Ridges. *Journal of Petrology*, 49(12):2099–2121, Dec. 2008.
- R. F. Katz. Porosity-driven convection and asymmetry beneath mid-ocean ridges. *Geochemistry, Geophysics, Geosystems*, 11(11):n/a–n/a, 2010.
- R. F. Katz and S. M. Weatherley. Consequences of mantle heterogeneity for melt extraction at mid-ocean ridges. *Earth and Planetary Science Letters*, 2012.
- K. Kawamura, F. Parrenin, L. Lisiecki, R. Uemura, F. Vimeux, J. P. Severinghaus, M. A. Hutterli, T. Nakazawa, S. Aoki, J. Jouzel, et al. Northern Hemisphere forcing of climatic cycles in Antarctica over the past 360,000 years. *Nature*, 448(7156):912–916, 2007.
- P. B. Kelemen, N. Shimizu, and V. J. M. Salters. Extraction of mid-ocean-ridge basalt from the upwelling mantle by focused flow of melt in dunite channels. , *Published online: 29 June 1995; | doi:10.1038/375747a0*, 375(6534):747–753, June 1995.
- T. Keller and R. F. Katz. The role of volatiles in reactive melt transport in the asthenosphere. *Journal of Petrology*, 2016.
- T. Keller, D. A. May, and B. Kaus. Numerical modelling of magma dynamics coupled to tectonic deformation of lithosphere and crust. *Geophysical Journal International*, 2013.
- T. Keller, R. F. Katz, and M. M. Hirschmann. Volatiles beneath mid-ocean ridges: Deep melting, channelised transport, focusing, and metasomatism. *Earth and Planetary Science Letters*, 464:55–68, Apr. 2017.
- E. M. Klein and C. H. Langmuir. Global correlations of ocean ridge basalt chemistry with axial depth and crustal thickness. *Journal of Geophysical Research: Planets (1991–2012)*, 92(B8):8089–8115, July 1987.
- P. Köhler, R. Bintanja, H. Fischer, F. Joos, R. Knutti, G. Lohmann, and V. Masson-Delmotte. What caused Earth’s temperature variations during the last 800,000 years? Data-based evidence on radiative forcing and constraints on climate sensitivity. *Quaternary Science Reviews*, 29(1-2):129–145, Jan. 2010.

- Y. Kono, C. Kenney-Benson, D. Hummer, H. Ohfuji, C. Park, G. Shen, Y. Wang, A. Kavner, and C. E. Manning. Ultralow viscosity of carbonate melts at high pressures. *Nature Communications*, 5:5091, Oct. 2014.
- S. Kutterolf, M. Jegen, J. X. Mitrovica, T. Kwasnitschka, A. Freundt, and P. J. Huybers. A detection of Milankovitch frequencies in global volcanic activity. *Geology*, 41(2): 227–230, Feb. 2013.
- C. Langmuir. SeaVoice overview and rock sampling. AGU, 2014. URL https://voice.fas.harvard.edu/files/voice/files/voice_charlie_agu_2014.pdf.
- C. H. Langmuir, E. M. Klein, and T. Plank. Petrological systematics of mid-ocean ridge basalts: Constraints on melt generation beneath ocean ridges. *Geophysical Monograph Series*, 71:183–280, 1992a.
- C. H. Langmuir, E. M. Klein, and T. Plank. Petrological systematics of mid-ocean ridge basalts: Constraints on melt generation beneath ocean ridges. *AGU Monograph*, 71: 183–280, 1992b.
- C. Larsen, A. J. Newton, A. J. Dugmore, and E. G. Vilmundardottir. Geochemistry, dispersal, volumes and chronology of Holocene from the Katla volcanic silicic tephra layers system, Iceland. *Journal of Quaternary Science*, 16(2):119–132, Feb. 2001.
- J. Laskar, P. Robutel, F. Joutel, M. Gastineau, A. Correia, and B. Levrard. A long-term numerical solution for the insolation quantities of the Earth. *Astronomy & Astrophysics*, 428(1):261–285, Dec. 2004.
- G. Le Hir, Y. Donnadieu, and Y. Godd eris. The snowball Earth aftermath: Exploring the limits of continental weathering processes. *Earth and Planetary . . .*, 2009.
- M. Le Voyer, K. A. Kelley, E. Cottrell, and E. H. Hauri. Heterogeneity in mantle carbon content from CO₂-undersaturated basalts. *Nature Communications*, 8:14062, 2017.
- L. E. Lisiecki and M. E. Raymo. A Pliocene-Pleistocene stack of 57 globally distributed benthic delta O-18 records. *Paleoceanography*, 20(1):–n/a, 2005.
- D. C. Lund and P. D. Asimow. Does sea level influence mid-ocean ridge magmatism on Milankovitch timescales? *Geochemistry, Geophysics, Geosystems*, 12(12):n/a–n/a, 2011.
- G. J. MacDonald. Role of methane clathrates in past and future climates. *Climatic Change*, 1990.
- J. Maclennan, M. Jull, D. McKenzie, L. Slater, and K. Gr nvo ld. The link between volcanism and deglaciation in Iceland. *Geochemistry, Geophysics, Geosystems*, 3(11): 1–25, Nov. 2002.
- M. A. Martinez-Boti, G. L. Foster, T. B. Chalk, E. J. Rohling, P. F. Sexton, D. J. Lunt, R. D. Pancost, M. P. S. Badger, and D. N. Schmidt. Plio-Pleistocene climate sensitivity evaluated using high-resolution CO₂ records. *Nature*, 518(7537):49–+, 2015.
- B. Marty and I. N. Tolstikhin. CO₂ fluxes from mid-ocean ridges, arcs and plumes. *Chemical Geology*, 145(3-4):233–248, 1998.
- M. Maslin. In retrospect: Forty years of linking orbits to ice ages. *Nature*, 2016.

- N. P. McKay, J. T. Overpeck, and B. L. Otto Bliesner. The role of ocean thermal expansion in Last Interglacial sea level rise. *Geophysical Research Letters*, 38(14):n/a–n/a, July 2011.
- D. McKenzie. The Generation and Compaction of Partially Molten Rock. *Journal of Petrology*, 25(3):713–765, Aug. 1984.
- P. J. Michael and D. W. Graham. The behavior and concentration of CO₂ in the suboceanic mantle: Inferences from undegassed ocean ridge and ocean island basalts. *Lithos*, 236-237:338–351, Nov. 2015.
- J. L. Middleton, C. H. Langmuir, S. Mukhopadhyay, J. F. McManus, and J. X. Mitrovica. Hydrothermal iron flux variability following rapid sea level changes. *Geophysical Research Letters*, 43(8):3848–3856, Apr. 2016.
- M. Milankovitch. *History of radiation on the Earth and its use for the problem of the ice ages*. K. Serb. Akad. Beogr, 1941.
- K. J. Miller, W.-l. Zhu, L. G. J. Montesi, and G. A. Gaetani. Experimental quantification of permeability of partially molten mantle rock. *Earth and Planetary Science Letters*, 388:273–282, 2014.
- W. G. Minarik and E. B. Watson. Interconnectivity of Carbonate Melt at Low Melt Fraction. *Earth and Planetary Science Letters*, 133(3-4):423–437, July 1995.
- G. Myhre, E. J. Highwood, and K. P. Shine. New estimates of radiative forcing due to well mixed greenhouse gases. *Geophysical Research Letters*, 1998.
- Y. Niu. The Meaning of Global Ocean Ridge Basalt Major Element Compositions. *Journal of Petrology*, 57(11-12):2081–2103, 2016.
- Y. L. Niu and R. Hekinian. Spreading-rate dependence of the extent of mantle melting beneath ocean ridges. *Nature*, 385(6614):326–329, 1997.
- J. Oerlemans. Model Experiments on the 100,000-Yr Glacial Cycle. *Nature*, 287(5781):430–432, 1980.
- J. A. Olive, M. D. Behn, G. Ito, W. R. Buck, J. Escartin, and S. Howell. Sensitivity of seafloor bathymetry to climate-driven fluctuations in mid-ocean ridge magma supply. *Science*, 350(6258):310–+, 2015.
- M. Pagani, Z. Liu, J. LaRiviere, and A. C. Ravelo. High Earth-system climate sensitivity determined from Pliocene carbon dioxide concentrations. *Nature Geoscience*, 3(1):27–30, Jan. 2010.
- D. Paillard and F. Parrenin. The Antarctic ice sheet and the triggering of deglaciations. *Earth and Planetary Science Letters*, 227(3-4):263–271, Nov. 2004.
- C. Pelejero, J. O. Grimalt, S. Heilig, M. Kienast, and L. Wang. High-resolution UK 37 temperature reconstructions in the South China Sea over the past 220 kyr. *Paleoceanography*, 14(2):224–231, 1999.
- R. T. Pierrehumbert, H. Brogniez, and R. Roca. On the relative humidity of the Earth's atmosphere. *The General Circulation*, 2007.

- V. Pinel and C. Jaupart. Magma storage and horizontal dyke injection beneath a volcanic edifice. *Earth and Planetary Science Letters*, 2004.
- T. Plank, M. Spiegelman, C. H. Langmuir, and D. W. Forsyth. The meaning of “mean F”: Clarifying the mean extent of melting at ocean ridges. *Journal of Geophysical Research: Planets (1991–2012)*, 100(B8):15045–15052, Aug. 1995.
- D. Pollard. A simple ice sheet model yields realistic 100 kyr glacial cycles. *Nature*, 1982.
- D. Pollard. A coupled climate-ice sheet model applied to the Quaternary ice ages. *Journal of Geophysical Research: Oceans*, 1983.
- H. Rawson, J. A. Naranjo, V. C. Smith, and K. Fontijn. The frequency and magnitude of post-glacial explosive eruptions at Volcán Mocho-Choshuenco, southern Chile. *Journal of Volcanology . . .*, 2015.
- H. Rawson, T. Keller, K. Fontijn, D. M. Pyle, T. A. Mather, V. C. Smith, and J. A. Naranjo. Compositional variability in mafic arc magmas over short spatial and temporal scales: Evidence for the signature of mantle reactive melt channels. *Earth and Planetary Science Letters*, 456:66–77, Dec. 2016a.
- H. Rawson, D. M. Pyle, T. A. Mather, V. C. Smith, and K. Fontijn. The magmatic and eruptive response of arc volcanoes to deglaciation: Insights from southern Chile. *Geology*, 2016b.
- M. E. Raymo. The timing of major climate terminations. *Paleoceanography*, 1997.
- M. E. Raymo, L. E. Lisiecki, and K. H. Nisancioglu. Plio-pleistocene ice volume, Antarctic climate, and the global delta O-18 record. *Science*, 313(5786):492–495, 2006.
- D. W. Rees Jones, R. F. Katz, M. Tian, and J. F. Rudge. Thermal impact of magmatism in subduction zones. *ArXiv e-prints*, Jan. 2017.
- M. Regelous, C. G. Weinzierl, and K. M. Haase. Controls on melting at spreading ridges from correlated abyssal peridotite - mid-ocean ridge basalt compositions. *Earth and Planetary Science Letters*, 449:1–11, 2016.
- J. A. Resing, J. E. Lupton, R. A. Feely, and M. D. Lilley. CO₂ and ³He in hydrothermal plumes: implications for mid-ocean ridge CO₂ flux. *Earth and Planetary Science Letters*, 226(3-4):449–464, Oct. 2004.
- N. M. Ribe. The Generation and Composition of Partial Melts in the Earths Mantle. *Earth and Planetary Science Letters*, 73(2-4):361–376, 1985a.
- N. M. Ribe. The deformation and compaction of partial molten zones. *Geophysical Journal International*, 1985b.
- A. J. Ridgwell, A. J. Watson, and M. E. Raymo. Is the spectral signature of the 100 kyr glacial cycle consistent with a Milankovitch origin. *Paleoceanography*, 1999.
- D. Rind and D. Peteet. Terrestrial conditions at the last glacial maximum and climap sea-surface temperature estimates: Are they consistent? *Quaternary Research*, 24(1): 1–22, 1985.

- G. H. Roe and R. S. Lindzen. The Mutual Interaction between Continental-Scale Ice Sheets and Atmospheric Stationary Waves. *Journal of Climate*, 14(7):1450–1465, Apr. 2001.
- E. J. Rohling, K. Grant, M. Bolshaw, A. P. Roberts, M. Siddall, C. Hemleben, and M. Kucera. Antarctic temperature and global sea level closely coupled over the past five glacial cycles. *Nature Geoscience*, 2(7):500–504, July 2009.
- A. Rosenthal, E. H. Hauri, and M. M. Hirschmann. Experimental determination of C, F, and H partitioning between mantle minerals and carbonated basalt, CO₂/Ba and CO₂/Nb systematics of partial melting, and the CO₂ contents of basaltic source regions. *EPSL*, 2015.
- K. H. Rubin and J. M. Sinton. Inferences on mid-ocean ridge thermal and magmatic structure from MORB compositions. *Earth and Planetary Science Letters*, 260(1-2): 257–276, Aug. 2007.
- L. H. Rupke, J. P. Morgan, M. Hort, and J. Connolly. Serpentine and the subduction zone water cycle. *Earth and Planetary Science Letters*, 223(1-2):17–34, 2004.
- A. E. Saal, E. H. Hauri, C. H. Langmuir, and M. R. Perfit. Vapour undersaturation in primitive mid-ocean-ridge basalt and the volatile content of Earth’s upper mantle. *Nature*, 419(6906):451–455, Oct. 2002a.
- A. E. Saal, E. H. Hauri, C. H. Langmuir, and M. R. Perfit. Vapour undersaturation in primitive mid-ocean-ridge basalt and the volatile content of Earth’s upper mantle. *Nature*, 2002b.
- H. Sakai, T. Gamo, E. S. Kim, M. Tsutsumi, and T. Tanaka. Venting of carbon dioxide-rich fluid and hydrate formation in mid-Okinawa trough backarc basin. *Science*, 1990.
- V. Salters and A. Stracke. Composition of the depleted mantle. *Geochemistry, Geophysics, Geosystems*, 5(5):–n/a, 2004.
- W. P. Schellart. Quantifying the net slab pull force as a driving mechanism for plate tectonics. *Geophysical Research Letters*, 31(7), 2004.
- N. J. Shackleton and N. D. Opdyke. Oxygen isotope and palaeomagnetic stratigraphy of Equatorial Pacific core V28-238: Oxygen isotope temperatures and ice volumes on a 105 year and 106 year scale. *Quaternary research*, 1973.
- M. Siddall, B. Hoenisch, C. Waelbroeck, and P. Huybers. Changes in deep Pacific temperature during the mid-Pleistocene transition and Quaternary. *Quaternary Sci. Rev.*, 2010. doi: 10.1016/j.quascirev.2009.05.011.
- L. Siebert and T. Simkin. Volcanoes of the world: an illustrated catalog of holocene volcanoes and their eruptions. smithsonian institution, global volcanism program, digital information series. gvp-3,. 2002.
- D. M. Sigman, M. P. Hain, and G. H. Haug. The polar ocean and glacial cycles in atmospheric CO₂ concentration. *Nature*, 466(7302):47–55, 2010.
- G. E. Sigvaldason, K. Annertz, and M. Nilsson. Effect of glacier loading/deloading on volcanism: postglacial volcanic production rate of the Dyngjufjöll area, central Iceland. *Bulletin of Volcanology*, 54(5):385–392, July 1992.

- N. H. Sleep. Segregation of Magma from a Mostly Crystalline Mush. *Geological Society of America Bulletin*, 85(8):1225–1232, Aug. 1974.
- B. J. Soden and I. M. Held. An assessment of climate feedbacks in coupled ocean-atmosphere models. *Journal of Climate*, 19(14):3354–3360, July 2006.
- S. Solomon, D. Qin, M. Manning, Z. Chen, M. Marquis, K. Averyt, M. Tignor, and H. Miller. Ipcc, 2007: climate change 2007: the physical science basis. *Contribution of Working Group I to the fourth assessment report of the Intergovernmental Panel on Climate Change*, 2007.
- D. W. Sparks and E. M. Parmentier. Melt Extraction From the Mantle Beneath Spreading Centers. *Earth and Planetary Science Letters*, 105(4):368–377, Aug. 1991.
- M. Spiegelman and D. McKenzie. Simple 2-D models for melt extraction at mid-ocean ridges and island arcs. *Earth and Planetary Science Letters*, 83:137–152, May 1987.
- L. B. Stap, R. S. W. van de Wal, B. de Boer, R. Bintanja, and L. J. Lourens. Interaction of ice sheets and climate during the past 800 000 years. *Climate of the Past*, 10(6): 2135–2152, 2014.
- P. Sternai, L. Caricchi, D. Garcia-Castellanos, L. Jolivet, T. E. Sheldrake, and S. Castelltort. Magmatic pulse driven by sea-level changes associated with the Messinian salinity crisis. *Nature Geosci.*, advance online publication SP - EP -.
- T. e. a. Stocker. Climate Change 2013: The Physical Science Basis. Contribution of Working Group I to the Fifth Assessment Report of the Intergovernmental Panel on Climate Change . Technical report, 2013. 1535 pp.
- E. Stolper, D. Walker, B. H. Hager, and J. F. Hays. Melt segregation from partially molten source regions: The importance of melt density and source region size. *Journal of Geophysical Research: Planets (1991–2012)*, 86(B7):6261–6271, July 1981.
- A. Stracke, B. Bourdon, and D. McKenzie. Melt extraction in the Earth’s mantle: Constraints from U-Th-Pa-Ra studies in oceanic basalts. *Earth Plan. Sci. Lett.*, 244:97–112, 2006. doi: 10.1016/j.epsl.2006.01.057.
- L. Tarasov and W. R. Peltier. Terminating the 100 kyr ice age cycle. *Journal of Geophysical Research: Atmospheres*, 1997.
- J. R. Toggweiler. Variation of atmospheric CO₂ by ventilation. *Paleoceanography*, 1999.
- J. R. Toggweiler. Origin of the 100,000-year timescale in Antarctic temperatures and atmospheric CO₂. *Paleoceanography*, 23(2):n/a–n/a, June 2008.
- M. Tolstoy. Mid-ocean ridge eruptions as a climate valve. *Geophysical Research Letters*, 42(5):1346–1351, 2015.
- D. L. Turcotte and G. Schubert. *Geodynamics*. Cambridge University Press, 2nd edition, 2002.
- A. Turner, R. Katz, and M. Behn. Grain-size dynamics beneath mid-ocean ridges: Implications for permeability and melt extraction. *Geochem. Geophys. Geosys.*, 2015. doi: 10.1029/2014GC005692. in press.

- A. M. Tushingham and W. R. Peltier. Ice-3G: A new global model of Late Pleistocene deglaciation based upon geophysical predictions of post-glacial relative sea level change. *Journal of Geophysical Research: Planets*, 96(B3):4497–4523, Mar. 1991.
- Tzedakis, P.C., M. Crucifix, T. Mitsui, and E. W. Wolff. A simple rule to determine which insolation cycles lead to interglacials. *Nature*, 542(7642):427–+, 2017.
- E. Tziperman, M. E. Raymo, P. Huybers, and C. Wunsch. Consequences of pacing the Pleistocene 100 kyr ice ages by nonlinear phase locking to Milankovitch forcing. *Paleoceanography*, 21(4):1879, Dec. 2006.
- R. S. W. van de Wal, B. de Boer, L. J. Lourens, P. Koehler, and R. Bintanja. Reconstruction of a continuous high-resolution CO₂ record over the past 20 million years. *Climate of the Past*, 7(4):1459–1469, 2011.
- M. A. Velbel. Temperature dependence of silicate weathering in nature: How strong a negative feedback on long-term accumulation of atmospheric CO₂ and global warming? *Geology*, 1993.
- D. Walker, E. M. Stolper, and J. F. Hays. A numerical treatment of melt/solid segregation: Size of the eucrite parent body and stability of the terrestrial low-velocity zone. *Journal of Geophysical Research: Planets (1991–2012)*, 83(B12):6005–6013, Dec. 1978.
- A. J. Watson, D. Bakker, A. J. Ridgwell, and P. W. Boyd. Effect of iron supply on Southern Ocean CO₂ uptake and implications for glacial atmospheric CO₂. *Nature*, 2000.
- S. L. Weber, S. S. Drijfhout, and A. Abe-Ouchi. The modern and glacial overturning circulation in the Atlantic ocean in PMIP coupled model simulations. *Climate of the Past*, 2007.
- R. S. White, D. McKenzie, and R. K. Onions. Oceanic Crustal Thickness From Seismic Measurements and Rare-Earth Element Inversions. *Journal of Geophysical Research-Solid Earth*, 97(B13):19683–19715, 1992.
- C. R. Wilson, M. Spiegelman, P. E. van Keken, and B. R. Hacker. Fluid flow in subduction zones: The role of solid rheology and compaction pressure. *Earth and Planetary Science Letters*, 401:261–274, Sept. 2014.
- K. Yuan and B. Romanowicz. Seismic evidence for partial melting at the root of major hot spot plumes. *Science*, 357(6349):393–396, 2017.
- D. Zhao. Seismic structure and origin of hotspots and mantle plumes. *Earth and Planetary Science Letters*, 192(3):251–265, 2001.